A Digital Physics Method for Two Phase Flow

by

David M. Freed

B.S. Double, Nuclear Engineering and Chemical Engineering,
University of California at Berkeley (1991)

Submitted to the Department of Nuclear Engineering
in partial fulfillment of the requirements for the degree of

Doctor of Philosophy in Nuclear Engineering

at the

MASSACHUSETTS INSTITUTE OF TECHNOLOGY

May 1997

Author .....
Department of Nuclear Engineering
May 1997

Certified by .....
Kim Molvig
Associate Professor
Thesis Supervisor

Accepted by .....
Jeffrey P. Freidberg
Professor
Reader

Accepted by .....
Jeffrey P. Freidberg
Chairman, Departmental Committee on Graduate Students

A Digital Physics Method for Two Phase Flow

by
David M. Freed

Submitted to the Department of Nuclear Engineering
on April 1, 1997, in partial fulfillment of the
requirements for the degree of
Doctor of Philosophy

ABSTRACT

Digital Physics refers to a fully discrete, microdynamical system whose mean behavior recovers real continuum physics. The purpose of this project is to develop a Digital Physics method by which to model the flow of single-component fluids with a non-ideal-gas equation of state, such as liquids and two-phase mixtures. The new system, called the multiphase system, is built upon the framework of a previously developed Digital Physics system. This original Digital Physics system, the standard system, is used to simulate low Mach number flow of an ideal gas.

Previously, substantial performance improvements (compared to CFD numerical solvers) have been achieved with the standard system for hydrodynamic simulations of ideal gas flows. Hence the underlying motivation of this work is the development of a more efficient simulation tool for *detailed* two-phase flow investigation as compared to current numerical methods. Specifically, the multiphase system simulates the local instantaneous flow field including explicit representation of the interfaces.

The multiphase system contains significant extensions of the standard system, particularly a non-local operation allowing microscopic interactions at a distance, loosely mimicking a real liquid, while preserving exact (global) conservation of mass, momentum, and energy. It retains the advantages of Digital Physics compared to other lattice gas methods for flow modeling, such as Galilean invariance, elimination of the dynamic pressure anomaly, and a meaningful energy transport equation. In the multiphase system the energy degree of freedom has been extended to allow a consistent empirical thermodynamics suitable for a system with liquid-vapor coexistence. Thus in addition to correct hydrodynamic transport, the multiphase system achieves appropriate equations of state for the liquid and vapor phases; the current implementation employs a van der Waals thermodynamical system. The multiphase system does not model heat transfer, although heat transfer capability is anticipated to be a possible extension.

Results are presented for a variety of simulations using a 2D implementation of the multiphase system created as part of this thesis. These include measurements of shearwave decay, liquid soundspeed, and the equilibrium coexistence

curve. Two independent measurements of surface tension are made and found to be in agreement. Dynamical two phase experiments performed are spontaneous phase separation, Rayleigh-Taylor instability, and single bubble rise in a liquid column. It is found that the simulation results for the multiphase system agree well with theoretical and experimental results, and it is concluded that the key physical mechanisms are correctly captured. Furthermore, it is predicted that a 3D version of the multiphase system would be straightforward to implement, and could be used to investigate bubbly and slug flow for water at Reynolds numbers on order 10^4.

Thesis Supervisor: Kim Molvig
Title: Associate Professor, Nuclear Engineering Department

Acknowledgements

First and foremost, I would like to thank my thesis supervisor, Professor Kim Molvig, for his guidance, enthusiasm, encouragement, and patience. He helped steer me towards a rewarding, enjoyable project, and his remarkable physical intuition and creativity guided me through many rough spots. I feel very fortunate that I have had the opportunity to work with Professor Molvig (who yet believes that I can be turned into a physicist), and look forward to our continued collaboration.

I am also deeply grateful to Hudong Chen and Chris Teixeira, for countless discussions and assistance throughout this project. In many instances their previous work, some of it not yet published, was instrumental to my research.

I would like to thank EXA Corporation for financial support and for the kind use of their facilities. I would also like to thank the people at EXA, all of whom have graciously assisted me at one time or another.

I would like to thank the MIT Nuclear Engineering Department for financial support in the form of fellowships and research assistantships. I am also grateful for the many positive interactions I have had with various members of the NED faculty and staff.

I am lucky to have made many great friends during my graduate work, and I wish to express my gratitude to certain individuals with whom I have most closely shared my MIT experience. These are Brett Mattingly, Jeffrey Hughes, Kory Budlong Sylvester, Raj Gupta, and Stephen Friedenthal.

I am especially grateful to one Tanya L. Williams, whose companionship and support have meant a very great deal to me.

Finally, a special thanks to my parents, Arthur and Ninette, whose love and encouragement are deeply appreciated, now as much as always.

David M. Freed
April 1, 1997

Contents

List of Figures

List of Tables

Chapter 1

Introduction

This thesis presents a lattice gas method for detailed simulation of two phase hydrodynamics. The method is an example of the "Digital Physics" approach to the simulation of physical systems governed by continuum mechanics. This multiphase Digital Physics system will be referred to as the "multiphase system" for short.

This chapter provides a brief introduction to two phase flow, lattice gases, and where the current method is thought to fit into each of these expansive fields. A summational outline of the thesis is provided as well.

1.1 Applications and Current Methods of Two Phase Flow Modeling

Two phase flows of a gas-liquid mixture are extremely common, both in industrial processes and in nature. Chemical processes such as reaction or mass transfer are often carried out by contact of a liquid phase and a gas phase in a "chemical reactor." Over 60% of heat exchange equipment used in industrial processes involves two phase flow of one kind or another [1]. Large power production operations typically rely on boiling heat transfer, which results in a flowing two phase mixture of a liquid and its vapor. Study of the atmospheric and geohydrologic transport of materials often involves two phase flow. An important example is prediction of the fate of radioactive substances when evaluating disposal options. Another example is the petroleum industry, since methods of oil recovery typically involve multiphase flows.

One of the most active areas and important driving forces of two phase flow research for several decades has been the thermal-hydraulic design of nuclear reactors [2]. Safety and efficiency (in both the thermodynamic and economic sense) during normal operation require accurate prediction of two phase flow behavior. In addition, modeling of transient two phase flow is needed for safety analyses of possible accident conditions [3]. Especially in the latter case there is a diverse set of two phase flow problems that may come into play.

The most important feature of a two phase mixture is the presence of interfaces separating regions of one phase from regions of the other. Hence the flow has an internal structure, and the overall pattern characterizing the spatial distribution of the two phases is known

as the flow regime. For example, in vertical upflow through a conduit, the flow pattern is commonly regarded as belonging to one of the following flow regimes: bubbly flow, slug flow, churn (or froth) flow, or annular flow [4].

A basic problem in two phase flow modeling is that the important transfer mechanisms, between fluid and structure as well as between the two phases of the fluid, depend heavily on the flow regime. In turn it is often difficult to reliably predict the flow regime for a given system without direct experimental evidence. The fact that fluid properties, flow parameters, and system geometry are all influential in determining flow regime provides uncertainty in attempts to extrapolate from existing information [3].

In principle a two phase flow problem may be formulated in terms of the usual transport equations of single phase flow, with appropriate matching boundary conditions at the interfaces. With enough resolution this would allow direct computational prediction of the detailed flow dynamics, including the flow regime. Unfortunately this is far too computationally burdensome to be practical, except for the very smallest of systems. Indeed the resolution needed for an explicit calculation of this nature is currently achieved only for a very limited range of single phase systems, which of course do not have the added complexity of spatially and temporally varying internal boundary conditions.

Practical two phase flow modeling (say for a nuclear reactor core) therefore requires a "macroscopic" approach where the interfaces are not explicitly modeled at all, but their influence on local transfers is accounted for by somehow adjusting the parameters and properties of a simplified model. This is analogous to turbulence modeling in single phase flow, where the effects of turbulence are reflected in quantities such as the eddy viscosity. The

simplest and most common two phase flow model is the homogeneous equilibrium model (HEM), where the transport equations are solved for a single pseudo-fluid whose properties represent a mixture average of the two phases. The other approach is the separated flow model, in which each fluid is considered individually to some degree.

A very simple separated flow model is the drift flux model, which focuses mainly on the relative velocity difference (or slip velocity) between the two phases [5]. The drift flux model is especially useful because it requires modest computational work over that of the HEM, but can approximate flows where the fluids may have very different mean velocities. An example is annular flow, where an upflowing vapor core is surrounded by a liquid film whose net flow may be downward; here the homogeneous equilibrium model is clearly inadequate.

A more sophisticated separated flow model is the two fluid model, where the transport equations are written for each phase separately. Additional equations then describe interactions (such as rates of mass, momentum, and energy transfer) between the two phases and between each phase and the solid boundaries. Many forms of the two fluid concept exist, for example the energy transport equation may be written for the mixture while mass and momentum transport remain separate for each phase. The two fluid approach is common in current thermal hydraulics codes in the nuclear industry (e.g. [6]).

The choice of a model for a given system must strike a balance between computational speed and various degrees of accuracy and resolution. In all cases some level of fine grain detail is sacrificed, and the necessary approximations use information obtained empirically or semi-empirically. Most important in the choice and application of such information is knowledge of the flow regime. In correlating or theoretically formulating information used

in the parameters of the large-scale models, it is very useful to understand the physical mechanisms which govern the behavior in a certain flow regime and the transitions between flow regimes. It is in this capacity that modeling of smaller scale phenomena through theory, experiment, and fine grain computer simulation can play a valuable role. For example, correlations used in modeling bubbly or slug flow typically rely on prediction of the relative rise velocity of a single bubble.

Computational flow simulation in which the *exact* equations are solved as described above would offer a way, in compliment with experimental results, to intimately probe assumptions about basic physical mechanisms. To date the use of such simulations to investigate even relatively simple, small-scale two phase systems is quite limited because they are so computationally demanding. Progress in this direction has been made with the volume-of-fluid method [7, 8, 9] and the front tracking method [10] in the investigation of the motions of rising bubbles. Here the local instantaneous field equations (for incompressible fluids with no heat or mass transfer) are numerically solved, including an explicit dynamical representation of the interface as a discontinuity existing within specific volume elements. In one instance of recent work by Tomiyama, Sou, Zun, and Sakaguchi [11], 3D bubbly flow is simulated in a duct composed of $\sim 2(10^4)$ cells. However, the flow is strictly laminar ($Re < 100$), and values of certain relevant dimensionless quantities, particularly the Morton number, are far different than those representative of water. Nevertheless interesting phenomena have been studied with these methods, such as bubble deformation, lateral bubble migration, and patterns of bubble distribution resulting from the interaction of bubbles with the velocity profile of a shear flow.

The method presented here, the Digital Physics "multiphase system," recovers the exact equations for isothermal, compressible two phase flow. Its main usefulness, like any detailed simulation method, is expected to be found in the context of (a) providing insight into fundamental physical mechanisms important in two phase flow behavior, and (b) better resolving the fine grain details of subsystems whose effects must ultimately be incorporated in an approximate fashion into the coarse grain model for a large system. Moreover, the multiphase system is predicted to expand the range of two phase flow problems accessible to direct simulation of the detailed flow field including interfaces. This greater range refers to both the system size and the fluid properties, as represented through appropriate dimensionless quantities. The source of this optimism is an estimate of the computational performance of the multiphase system based on current commercial Digital Physics capabilities[1]. Simulation Reynolds numbers on order 10^4 are anticipated, which would allow study of, for example, effects of turbulence on bubble dynamics. At the same time Morton numbers appropriate for water can be achieved. In addition, it may be possible to extend the multiphase system to allow simulation of non-isothermal flows (with very little additional computational work).

1.2 Lattice Gases and Fluid Flow Simulation

What is the multiphase system, indeed what is Digital Physics? The term Digital Physics refers to a fully discrete microdynamical system where mass, momentum, and energy are exactly conserved, entropy production is assured by a local H-Theorem, and the mean be-

[1] A specific estimate is detailed in Section 5.2.

havior recovers real continuum physics. A Digital Physics system capable of simulating low Mach number, ideal gas hydrodynamics is the multispeed lattice gas automata introduced by Molvig, Donis, Myczkowski, and Vichniac [12], and further developed by Teixeira [13], Chen [14], and others [15, 16, 17, 18, 19]. This ideal gas Digital Physics method will be referred to throughout this thesis as the "standard system." The multiphase system is an extension of the standard system which supports a non-ideal-gas thermodynamics appropriate for two phase coexistence; hence it is essentially a type of lattice gas automata.

In its most basic form, a lattice gas automata consists of identical particles which move about with unit speed from node to node on a fixed regular lattice. Associated with each particle at any given time is a discrete velocity, also considered its *microstate*, which determines its direction of movement during the current step. Each complete update step consists of two events, a collision phase and a propagation (also called advection) phase. In the collision phase, particles have their velocities adjusted according to a set of *collision rules*; then the actual hopping to a new site comprises the propagation phase. At most one particle may exist at a given site with a given velocity, which is the "exclusion rule" of the lattice gas; hence a microstate is either occupied or unoccupied.

The collision rules are carefully constructed such that mass, momentum, and energy (and nothing else) are conserved for every collision. Of course when all particles have equivalent speed, then mass and energy are redundant. Collisions serve to randomize the local particle distributions, monotonically generating entropy such that the ensemble average occupation probability of any microstate has a value given by the local thermodynamic equilibrium[2].

[2]In a system with an exclusion rule it is a Fermi-Dirac equilibrium.

The fate of the (average) occupation probability of a given microstate during a complete update step can be expressed as a difference equation, called the *lattice update equation.* The lattice update equation is Taylor expanded in space and time to give the *microkinetic equation* of the lattice gas. Then the mass, momentum, and energy moments of the microkinetic equation may be expressed as differential equations containing local macroscopic quantities, such as density and velocity, varying in space and time. These are the mass, momentum, and energy transport equations which describe the long-wavelength, low frequency dynamical behavior of the system.

This is analogous to the derivation of the real transport equations of continuum fluid mechanics from the Boltzmann equation. The first order Knudsen number expansion of the kinetic equation gives the Euler equations, and the second order expansion gives the Navier-Stokes equations. However, due to the presence of only a finite set of discrete velocities on the lattice, the transport equations of the lattice system will be different than those of true continuum mechanics. These differences are referred to as *discreteness artifacts.* In particular, the momentum flux tensor is generally anisotropic in a fashion related to the structure of the lattice.

In 1986 it was recognized by Frisch, Hasslacher, and Pomeau [20] that a 2D hexagonal lattice results in an isotropic momentum flux tensor for the lattice gas. This gives a momentum transport equation for the basic lattice gas just described which is similar to that of real hydrodynamics, but which still retains certain other discreteness artifacts. Nonetheless the discovery of the isotropic momentum flux tensor touched off a flurry of research into extensions of the original system [21, 22, 23, 24, 25, 26], the general theory of lattice gas sys-

tems [27, 28, 29, 30], and the potential to use them for hydrodynamic simulation [31, 32, 33].

Immediately investigated, for example, was the opportunity to exploit inherent computational advantages of the lattice gas system [34], since each microstate could be represented by a single bit as the system evolved via simple logical and highly parallel operations. Shortly after the 2D hexagonal system was introduced, Frisch, Hasslacher, Lallemand, Pomeau, d'Humières, and Rivet [35] showed that the face-centered hypercube (FCHC) lattice also results in an isotropic momentum flux tensor, and moreover could be used to represent a 3D system. A concept inspired by lattice gas automata called the "lattice-Boltzmann method" was developed [36, 37, 38], where the discrete particles are replaced with floating-point numbers, resulting in a kind of hybrid between a lattice gas and an explicit finite-difference scheme. In the decade or so since the landmark paper of Frisch, Hasslacher, and Pomeau [20], many other interesting and important developments have been made[3].

Most of the resulting lattice gas models, it turns out, suffer from the additional discreteness artifacts, limiting their usefulness as flow simulation methods. In 1988, however, Molvig, Donis, Myczkowski, and Vichniac [12] showed that a lattice gas composed of particles with three different speeds, instead of just a single speed, could be designed to eliminate all discreteness artifacts from the momentum transport equation. By manipulating the distribution of particles amongst the different available speeds (or energies) in a particular way, correct momentum transport is recovered exactly. In addition, this *multispeed* model, where mass and energy are no longer redundant, has a well-defined energy transport equation, with an ideal gas relationship between internal energy and pressure. This is the standard system

[3]Many of the key early works can be found in collections edited by Doolen [39] and Monaco [40].

referred to above; certain discreteness artifacts remain in the energy transport equation, hence it is appropriate for simulating flows where heat transfer is not important.

The first demonstrations of the ability of the three-speed standard system to simulate quantitatively accurate 3D hydrodynamic behavior were presented in 1991 by Mujica [41] for flow past a flat plate, and in 1992 by Teixeira [13] for Poiseuille flow and flow past a circular cylinder. Teixeira [13] also showed that additional, higher particle speeds can be used to remove the energy transport artifacts, and that the FCHC lattice has the necessary symmetry properties to allow the inclusion of these higher speed particles[4]. Certain other extensions to the multispeed lattice gas have been made, including the use of multi-bit microstate populations [16] (hence no exclusion rule). Larger populations drastically reduce the noisiness of the method, allowing a much crisper realization of the local instantaneous field equations of hydrodynamics. In order to equilibrate the multi-bit population distributions, the collision process [42, 18] at each site is carried out as a series of bilinear scattering events, in which each event drives the distributions closer to equilibrium[5]. Moreover, this collision process can be modified in a way that alters the shear viscosity of the lattice gas from its nominal value, hence the viscosity may be "dialed in" within a certain allowable range [17]. These and certain other developments[6] have enabled the Digital Physics standard system to become a powerful tool for simulation of low Mach number flows[7] where it is acceptable to represent the fluid as an ideal gas.

[4]In fact he proves that the momentum flux tensor remains isotropic for *any* particle speed of integer value on the FCHC lattice.

[5]Which now has the usual Maxwell-Boltzmann form.

[6]In particular developments related to high Reynolds number flow are not discussed here as they are proprietary to EXA Corporation.

[7]For example state of the art simulations of automobile aerodynamics [43] and cavity flows [44].

The presence of interfaces is the difference between a simple fluid and a complex one, such as a multiphase or multicomponent fluid. Several ideas for lattice gas models of complex flows have been put forth. A two component model called the "immiscible lattice gas" (ILG) was introduced by Rothman and Keller [45] in 1988, and recently another two component model using a lattice Boltzmann method was conceived by Swift, Osborn, and Yeomans [46]. A lattice gas exhibiting a liquid-vapor transition was formulated by Appert and Zaleski [47]. Various implementations and extensions of these, particularly of the ILG, have been explored[26, 48]. Generally, however, these methods not only retain the discreteness artifacts of single speed models, they also tend to have a very limited range of fluid-fluid density ratio and other key two phase properties. Recent work based on the ILG explores the use of "stopped particles" (particles of zero velocity) as a degree of freedom by which to remove one of the artifacts [49], or to increase the density of one component relative to the other [50]. The result, however, is that large amounts of stopped particles severely limit the fluid velocity. Furthermore, the equation of state in such systems (i.e. the pressure-density relation) is quite unphysical, in fact the liquid is actually more compressible than the gas.

A particularly interesting concept was introduced by Shan and Chen [51] in 1993 in their multiphase lattice Boltzmann model. They formulated a non-local, nearest-neighbor interaction that mimics an interparticle "potential," and in the macroscopic limit yields a non-ideal-gas equation of state. The interaction alters the local value of momentum at a site in a way that reflects its neighborhood, but does so in a fashion that conserves momentum globally (i.e. over the lattice as a whole). The equation of state can be tuned by adjusting a parameter central to the non-local interaction, and two phase coexistence occurs when the

pressure-density relation exhibits a hysteresis such that two different densities are stable at the same pressure. This concept was used with a single speed lattice Boltzmann method, where discreteness artifacts in the momentum equation can be eliminated, but there is still no energy degree of freedom; hence any connection with two phase thermodynamics is hindered. Also, lattice Boltzmann methods are subject to numerical instabilities [52] because they use floating point values rather than discrete particles.

In the present work a discrete adaptation of the non-local interaction concept of Shan and Chen is developed as an extension to the Digital Physics standard system. This requires construction of an exact-integer version of the sitewise momentum adjustment process, the addition of a new microphysical feature to account for the energy associated with phase change, and several other developments which are detailed herein. The result is the first lattice gas method with correct momentum transport, two phase capability, a realistic equation of state for the gas and liquid phases, and the ability to achieve liquid-vapor density ratios sufficient for simulation of practical systems. Furthermore, the independent energy transport equation provides the potential to extend the method to include heat transfer. This work also contains the first application of a lattice gas method to the investigation of two phase bubble dynamics.

1.3 Outline of Analysis

The goals of this thesis are as follows. The first is to present the fundamental extensions which allow the multiphase system to obey a more general equation of state than that of an ideal gas,

specifically one which exhibits a region of two phase coexistence. The second is to show how to recover correct hydrodynamical behavior for the resulting individual bulk fluid phases. The third is to outline the potential for the multiphase system to provide quantitatively accurate simulation of real fluids, particularly water, in two phase flow situations of practical interest. The fourth is to present experimental results for a 2D version of the multiphase system which verify the theoretical predictions for the properties of the multiphase system, and demonstrate its ability to capture certain key physical mechanisms of two phase flow.

The content of this thesis is intended to introduce the fundamental advances leading to development of the multiphase system, and to investigate its properties primarily from the perspective of achieving correct two phase hydrodynamics. The multiphase system is in principle capable of modeling a variety of substances over a range of (equilibrium) thermodynamic conditions. The specific implementation presented here is intended to be as simple as possible but nonetheless suitable for an approximate representation of water. It is also a 2D version, but the extension of the multiphase system to 3D is entirely straightforward; 2D was used only to speed development of the fundamental algorithms by reducing computational requirements as much as possible.

A key limitation of the multiphase system at present is a maximum liquid to vapor density ratio of about 200. Another important limitation in the present implementation is the required use of an "isothermal condition", where all of the material in the system is imagined to be in immediate and instantaneous contact with a constant temperature reservoir. These restrictions are likely associated with the need for additional microphysics within the finite interfacial region. While heat transfer issues are beyond the scope of this project, the ability

to include heat transfer in the multiphase system is feasible if a way to eliminate the need for the isothermal condition can be found. The multiphase system does take important steps towards heat transfer capability. It includes a physically consistent representation of thermodynamical quantities, emphasized for example by the large difference in internal energy per unit mass between the vapor and liquid phases. Furthermore, it is believed that the energy transport analysis[8] provided in this thesis is sufficient to construct a method for single phase flow of a non-ideal-gas vapor or liquid including heat transfer, although this task has not been undertaken here.

The remainder of this document is organized as follows. In Chapter 2 a new operator, named the interaction operator, is introduced into the Digital Physics microsystem. The interaction operator is shown to provide a non-local interaction, in the form of a sitewise momentum and energy adjustment, which mimics the intermolecular forces in a real liquid. Chapter 3 discusses how the momentum piece of the interaction operator gives rise to non-ideal-gas behavior, and in particular can be used to achieve a thermodynamical system, such as a van der Waals system, appropriate for modeling two-phase coexistence. It also introduces the "microscopic internal energy" as a means to address the internal energy dependence in the multiphase system, which must account for the latent heat of the liquid-vapor phase transition. In Chapter 4, the moments of the resulting microkinetic equation are evaluated at the Euler level to provide constraints by which to remove discreteness artifacts. Correct momentum transport requires the same constraints as in the standard system. On the other hand the energy transport equation contains new artifacts, one of which must be removed

[8]The energy transport analysis for the standard system was done by Teixeria [13].

using the energy piece of the interaction operator. Although it is shown how to recover correct adiabatic energy transport for the multiphase system, in practice the isothermal condition is needed in the two phase simulation experiments.

Chapter 5 looks at the important thermodynamic and flow properties involved in modeling two-phase flow of water, and describes the relationship between macroscopic quantities in the lattice system and those of the real world. It also discusses predictions of the capabilities and limitations of a 3D, "engineering-scale" multiphase system for simulating flow systems of practical interest, and bubbly flow is identified as a promising application. Chapter 6 addresses key issues in selecting and implementing a specific multiphase system. These include solution of the system of constraints needed to remove artifacts, and a modified advection scheme required to stabilize the liquid phase due to its elevated soundspeed. Also included is a description of the algorithm used in the 2D simulations presented in this thesis. These experiments and the results are described in Chapters 7 and 8. In Chapter 7, the more basic behavior of the multiphase system is observed and compared to theoretical prediction. This includes single phase shearwave decay and soundwave propagation tests, spontaneous phase separation, and experiments which probe the equilibrium properties of two-phase systems at rest. Chapter 8 looks at simulations of two dynamic liquid-vapor systems: Rayleigh-Taylor instability, and single bubble rise in a column of liquid. Chapter 9 presents conclusions and further discussion of a few key issues.

Chapter 2

The Multiphase Microsystem

2.1 A Non-Local Interaction

This chapter begins the theoretical description of the multiphase system by introducing and describing its microdynamical nature. In particular, the goal is to show how the set of microscopic rules which constitute the standard system can be extended so as to achieve multiphase behavior in the macroscopic limit. The thermodynamics of the standard system are consistent with those of an ideal gas. The fundamental advance by which multiphase behavior will be brought about for the new system may be viewed as the existence of non-ideal-gas thermodynamics, which is a physically consistent basis. However, rather than imitating the highly complex molecular interactions which result in the real non-ideal-gas behavior of a substance, a simple, discrete microscopic procedure in the usual Digital Physics

fashion is desired. This chapter will be concerned with motivating and formulating such a microscopic procedure.

In a real fluid, the departure from ideal gas behavior is a result of the forces exerted on the fluid molecules by other fluid molecules. Due to these forces, at any instant in time the motion of a particular molecule is influenced by the relative types and positions of the molecules around it. In a gas, the molecules are far apart, and intermolecular forces are weak relative to the mean molecular kinetic energy. On the other hand the molecules of a liquid are held close together by attractive intermolecular forces and very short range repulsive ones, and these interparticle forces dominate the instantaneous molecular motions.

This physical picture points to the idea that to achieve a Digital Physics representation of a fluid with non-ideal-gas behavior, such as a liquid, an interaction should be introduced through which a lattice gas particle "feels" the other particles around it. Particularly within a liquid phase the interparticle interaction should be very strong. There is a fundamental difficulty with such a concept, which is illustrated in Figure 2.1. Consider the collection of particles drawn on the left-hand side. If these were the molecules of a real material, then the influence of one particle on another would depend on the distance between them. In a lattice gas, however, the system is spatially discrete; one can imagine drawing control volumes (shown by dashed lines) which fill space, and every particle belongs to exactly one of these unit cell microvolumes. Most significantly, all the particles of a cell are represented as existing at a central node, hence all information is lost concerning the precise locations of particles within a cell. Naturally the set of control volumes forms the lattice, and their central nodes are just the lattice sites, as shown on the right side of Figure 2.1.

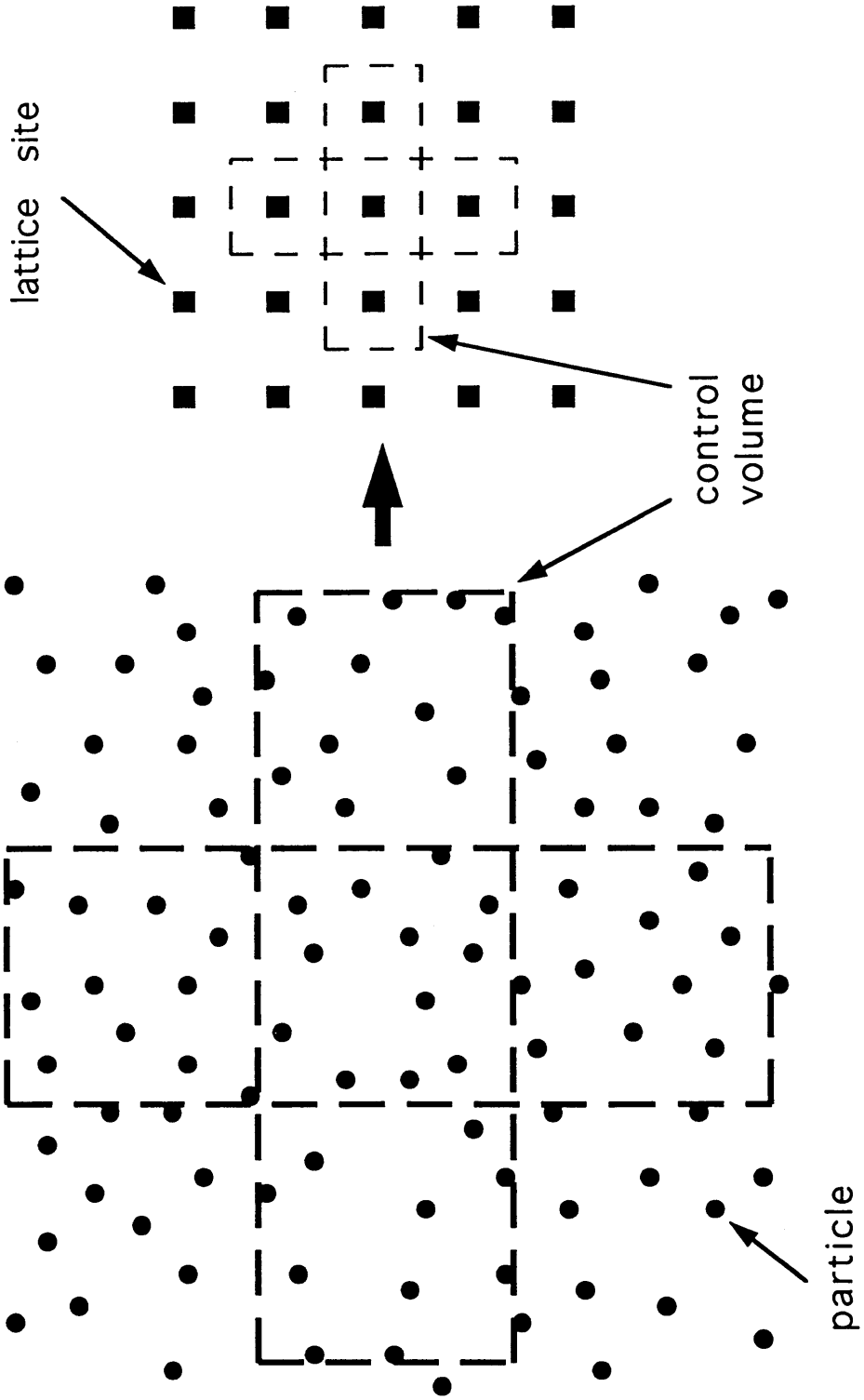

Figure 2.1: The lattice gas - a spacially discrete collection of particles.

In the lattice gas, precise particle locations by which interparticle distances could be determined are not available, instead there is only the discrete distances between lattice sites. This suggests replacing interactions between particles with interactions between sites, where now one site "feels" the other sites around it through their local macroscopic properties such as density. A conceptual illustration is provided in Figure 2.2; the first part shows forces between molecules of a liquid, the second shows momentum exchange between sites with different densities (indicated by the patterns). In particular, one can imagine momentum exchanges between pairs of sites which increase with the product of the densities of the pair. However when that product becomes very large (such as between the two highest density sites in Figure 2.2), the amount of momentum exchange begins to decrease, essentially representing repulsive forces at very high density. The physical interpretation is that a mean interparticle distance in a local neighborhood of lattice sites is found by examining the densities of those sites. Then variations over its neighborhood give rise to the forces experienced by a given site. In this way one can hope to capture the physics of a liquid through a *mean-field* approach in a spatially discrete system.

A distinguishing feature of such a lattice gas is the presence of a *non-local interaction*, since in carrying out the microdynamics at one site, information about other sites is employed. The implementation of such an interaction must be some new operation or set of operations which alters the microscopic population distribution of a site in response to the influence of its neighbors. Moreover, it is believed that in general such operations must locally alter one or more of the fundamentally conserved quantities - mass, momentum, and energy. A simple argument may be made for why this should be true. Consider the nature of the standard

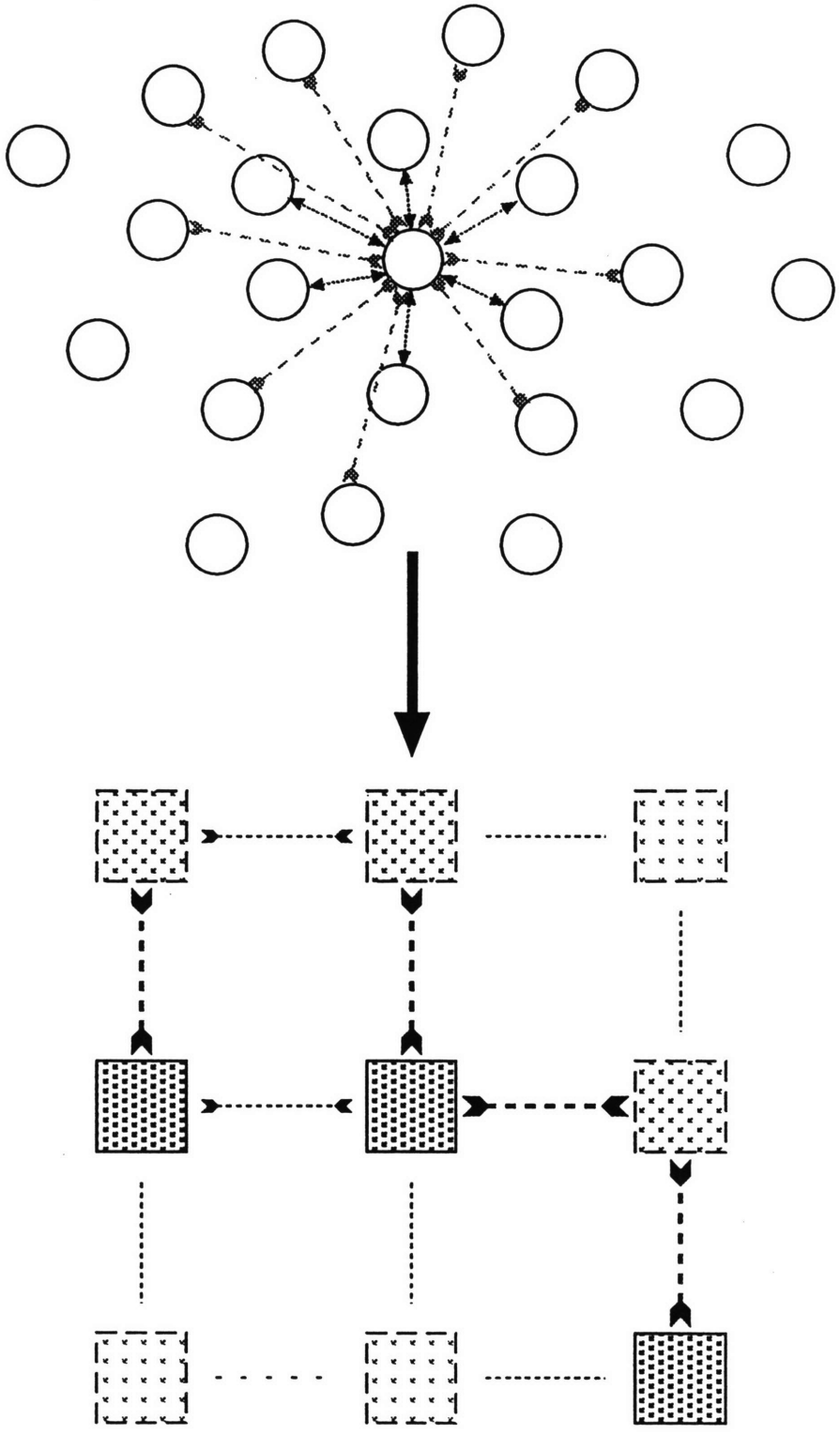

Figure 2.2: Creating a liquid in a lattice gas - from interactions between molecules to interaction between sites.

system, which consists of two operations, a propagation step and a collision step. The purpose of collisions is to force the distribution of particles at each site to be the Boltzmann distribution. This maximizes the local entropy for a given mass, momentum, and energy, which must be the only invariants of the collision process. At the completion of a successful collision process, the distributions are at (or very near) equilibrium, and the propagation step must act on these equilibrium distributions in order to recover hydrodynamics at the macroscopic level. Thus any other operation must act after the propagation step but prior to the collision step. However, if an operation acting at this time were to alter the distributions in some way but did not affect the invariants, there would be no net effect at all, since the following collision step would destroy any trace of the operation when it restores the equilibrium distributions.

Thus the purpose of the non-local interaction, indeed the only way it can be meaningful, is to break sitewise conservation of some combination of mass, momentum, and energy. In keeping with the principles of Digital Physics, however, exact integer conservation is required in a global sense, that is to say the total mass, momentum, and energy of the whole system must be constant in the absence of external influences. In order to ensure this, it is desirable to design the new operations to represent some sequence of events, each of which conserves mass, momentum, and energy individually. This implies that each hypothetical event is some sort of exact exchange process of one or more of these quantities. This concept is employed in Section 2.3 (and 4.2) when the precise nature of how to implement the non-local operations of the multiphase system is explored.

2.2 The Interaction Operator

In this section a general formalism for a Digital Physics system which can include the exchange of mass, momentum, and energy amongst neighboring sites will be developed. This formalism must provide a microscopic description of the system from which its macroscopic behavior can be derived. It is useful to first recall briefly some basic properties of the standard system, which forms the framework for the multiphase system. The underlying lattice is the 4D face-centered-hypercube (FCHC) lattice, which possesses certain necessary symmetry properties [27]. Particles move from one lattice site to another according to their discrete microscopic velocities during the propagation phase. Then particles at the same site exchange momentum and energy during the collision phase, where each collision event conserves mass, momentum, and energy exactly. For each site, the collisions cause the distribution of particles amongst the available velocities to be that representing local thermodynamic equilibrium[1]. The system evolves by repeated updates of propagation followed by collision. It is not very difficult to imagine that the system just described represents a discrete version of an ideal gas.

At least three different speeds of particles are required in order to recover correct momentum transport. The nominal (three-speed) version of the standard system contains particles of speed 0, 1, and 2. The speed of a particle is actually its microscopic kinetic energy $\varepsilon_j = mc_j^2/2$, where m is microscopic mass and c_j is the microscopic velocity magnitude. The microscopic velocity vector $\mathbf{c}_{ji}$ gives the direction and distance that a particle travels during

[1]A theoretical description of the original lattice gas collision operator is given by Frisch, Hasslacher, Lallemand, Pomeau, d'Humières, and Rivet [35]; the collision process developed for the multi-bit states of Digital Physics is discussed by Chen, Teixeira, and Molvig [19].

the propagation phase. The notation of Molvig, Donis, Myczkowski, and Vichniac [12] is continued here, using j to refer to the particle speed (or more generally species) and i to refer to a specific velocity available for that speed. The vectors representing the possible velocities for speed 0, 1, and 2 particles are shown in Figure 2.3 for a 2D mapping of the FCHC lattice. This set of vectors is the one actually used in the 2D implementation of the multiphase system for this thesis. The numbers by the arrows indicate the degeneracy or "weight" associated with a velocity; weights occur due to the representation of a 4D system in 2D.

The basic mathematical description of a lattice gas microsystem is its lattice update equation. The lattice update equation of the Digital Physics standard system[2] is

$$N_{ji}(\mathbf{x} + \mathbf{c}_{ji}, t+1) - N_{ji}(\mathbf{x}, t) = C_{ji} \tag{2.1}$$

where N_{ji} is the population of microstate ji at site $\mathbf{x}$ and time t, alternatively referred to as the microscopic distribution of state ji. As noted above $\mathbf{c}_{ji}$ is the velocity vector associated with microstate ji. C_{ji} represents the collision operator C acting on the population at microstate ji, which causes that population to take its equilibrium value N_{ji}^{EQ}.

A new operator, the interaction operator $\mathcal{I}$, is introduced as the formal representation of some non-local interaction within the Digital Physics microsystem. The interaction operator

[2]Which has the same basic form as the update equation for the original FHP lattice gas.

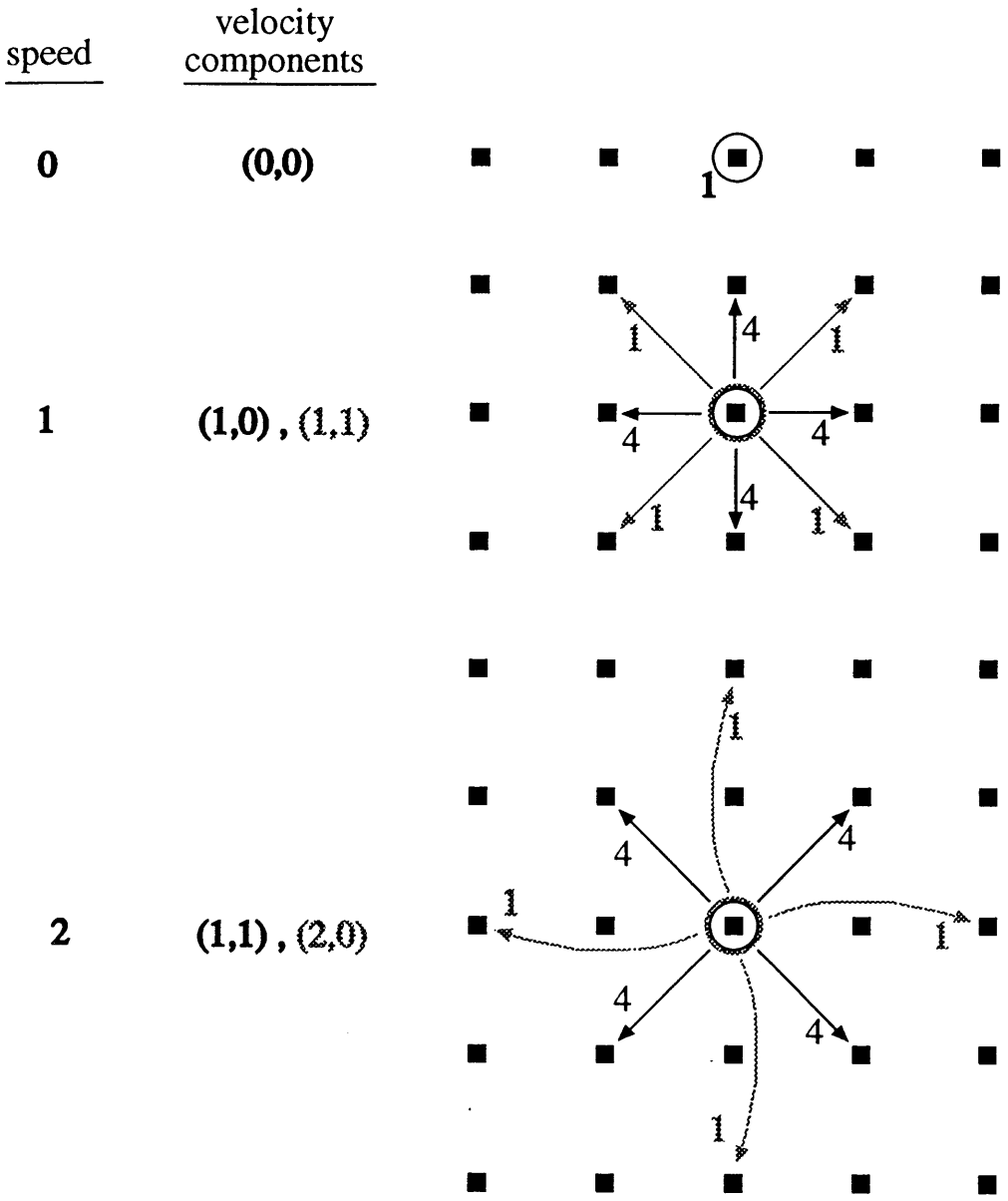

Figure 2.3: Velocity vectors for speed 0, 1, and 2 particles on the 2D mapping of the 4D face-centered hypercube (FCHC) lattice used in Digital Physics. Numbers by arrows are degeneracy or "weight" of a microstate in the 2D representation of the FCHC lattice.

is included in the above equation to generate a new lattice update equation:

$$N_{ji}\left(\mathbf{x}+\mathbf{c}_{ji},t+1\right)-N_{ji}\left(\mathbf{x},t\right)=C_{ji}+\mathcal{I}_{ji} \tag{2.2}$$

where $\mathcal{I}_{ji}$ is the interaction operator acting on the microscopic distribution N_{ji}. Unlike the collision operator, which is purely local since it depends only on the distributions at site $\mathbf{x}$, the interaction operator must somehow take into account information about the distributions at other sites in the vicinity.

To proceed it is helpful to get an idea of how the presence of this additional operator will affect the macroscopic dynamics of the system. A first order expansion (in Knudsen number, i.e. a small mean free path expansion) of the new lattice update equation gives

$$\partial_t N_{ji}+\mathbf{c}_{ji}\cdot\nabla N_{ji}=C_{ji}+\mathcal{I}_{ji} \tag{2.3}$$

where $N_{ji}\left(\mathbf{x},t\right)$ is abbreviated as N_{ji}, and then taking the mass, momentum, and energy moments:

$$\sum_{ji} m\left[\partial_t N_{ji}+\mathbf{c}_{ji}\cdot\nabla N_{ji}=C_{ji}+\mathcal{I}_{ji}\right] \tag{2.4}$$

$$\sum_{ji} m\mathbf{c}_{ji}\left[\partial_t N_{ji}+\mathbf{c}_{ji}\cdot\nabla N_{ji}=C_{ji}+\mathcal{I}_{ji}\right] \tag{2.5}$$

$$\sum_{ji} \varepsilon_j\left[\partial_t N_{ji}+\mathbf{c}_{ji}\cdot\nabla N_{ji}=C_{ji}+\mathcal{I}_{ji}\right] \tag{2.6}$$

which go over to

$$\partial_t\rho+\nabla\cdot\rho\mathbf{u}=\sum_{ji}\mathcal{I}_{ji} \tag{2.7}$$

$$\partial_t \rho \mathbf{u} + \nabla \cdot \underline{\underline{\mathbf{\Pi}}}_k = \sum_{ji} \mathcal{I}_{ji} \mathbf{c}_{ji} \tag{2.8}$$

$$\partial_t W + \nabla \cdot \mathbf{Q}_k = \sum_{ji} \mathcal{I}_{ji} \varepsilon_j \tag{2.9}$$

after employing the following definitions and relations:

$$\begin{aligned}
&m = \text{microscopic mass (hereafter taken to be unity)} \\
&\varepsilon_j = \frac{1}{2} m c_j^2 = \text{microscopic kinetic energy} \\
&\rho = \sum_{ji} m N_{ji} = \text{macroscopic mass (per unit volume)} \\
&\rho \mathbf{u} = \sum_{ji} m \mathbf{c}_{ji} N_{ji} = \text{macroscopic momentum (per unit volume)} \\
&\underline{\underline{\mathbf{\Pi}}}_k = \sum_{ji} m \mathbf{c}_{ji} \mathbf{c}_{ji} N_{ji} = P_k \underline{\underline{\mathbf{I}}} + g \rho \mathbf{u}\mathbf{u} = \text{momentum flux tensor} \\
&P_k = \text{isotropic pressure} \\
&W = \sum_{ji} \varepsilon_j N_{ji} = E + \frac{1}{2} \rho |\mathbf{u}|^2 = \text{total macroscopic energy (per unit volume)} \\
&E = \text{internal energy (per unit volume)} \\
&\mathbf{Q}_k = \sum_{ji} \varepsilon_j \mathbf{c}_{ji} N_{ji} = \text{energy flux} \\
&\sum_{ji} m C_{ji} = \sum_{ji} m \mathbf{c}_{ji} C_{ji} = \sum_{ji} \varepsilon_j C_{ji} = 0
\end{aligned} \tag{2.10}$$

Equations (2.7 - 2.9) express the "lattice Euler equations" for the multiphase system. They naturally look like those of the standard system, except for the terms involving the interaction operator $\mathcal{I}$. For the moment let us assume that the momentum flux tensor $\underline{\underline{\mathbf{\Pi}}}_k$ has the indicated form[3] which is identical to that of the standard system (as derived by Molvig, Donis, Myczkowski, and Vichniac [12]). The subscript "k" used with the momentum flux

[3]Actually the form given is for the zeroth order momentum flux tensor with $N_{ji} = N_{ji}^{EQ}$.

tensor, scalar pressure, and energy flux is meant to indicate that the given expressions for these quantities really represent only the "kinetic" contributions. Kinetic contribution or kinetic part denotes that part which is due to the conventional (ideal gas) part of the system and does not include the effects of the non-local interaction, which are entirely represented by the moments of the interaction operator written on the right-hand sides of these equations.

This is an important distinction since the non-local interaction is expected to provide a significant contribution to these quantities, indeed that is its function. Therefore the subscript "n" is used to indicate the so-called non-local contributions. The total quantities are the sums of the kinetic and non-local parts and will simply be written with no subscript, thus momentum flux $\underline{\underline{\mathbf{\Pi}}} = \underline{\underline{\mathbf{\Pi}}}_k + \underline{\underline{\mathbf{\Pi}}}_n$, scalar pressure $P = P_k + P_n$, and energy flux $\mathbf{Q} = \mathbf{Q}_k + \mathbf{Q}_n$. By definition these total quantities must satisfy the Euler equations written as

$$\partial_t \rho + \nabla \cdot \rho \mathbf{u} = 0 \tag{2.11}$$

$$\partial_t \rho \mathbf{u} + \nabla \cdot \underline{\underline{\mathbf{\Pi}}} = 0 \tag{2.12}$$

$$\partial_t W + \nabla \cdot \mathbf{Q} = 0 \tag{2.13}$$

Subtracting equations (2.11 - 2.13) from equations (2.7 - 2.9) gives

$$\sum_{ji} \mathcal{I}_{ji} = 0 \tag{2.14}$$

$$\sum_{ji} \mathcal{I}_{ji} \mathbf{c}_{ji} = \nabla \cdot \underline{\underline{\mathbf{\Pi}}}_k - \nabla \cdot \underline{\underline{\mathbf{\Pi}}} = -\nabla \cdot \underline{\underline{\mathbf{\Pi}}}_n \tag{2.15}$$

$$\sum_{ji} \mathcal{I}_{ji}\varepsilon_j = \nabla \cdot \mathbf{Q}_k - \nabla \cdot \mathbf{Q} = -\nabla \cdot \mathbf{Q}_n \tag{2.16}$$

These equations show that the mass moment of the interaction operator should vanish, and relate the momentum and energy moments to specific macroscopic quantities. It is therefore expected that local changes in momentum and energy, but not mass, will be required to occur between the propagation and collision steps. The way in which the amounts of these local changes in momentum and energy are calculated depends on the nature of the quantities $\nabla \cdot \underline{\underline{\mathbf{\Pi}}}_n$, the divergence of the non-local part of the momentum flux tensor, and $\nabla \cdot \mathbf{Q}_n$, the divergence of the non-local part of the energy flux. This analysis is dealt with mainly in the next two chapters.

For now the formal description of the interaction operator is continued by looking at how to implement the desired changes in local momentum and energy once they have been determined. In the Digital Physics system, with its discrete particles and discrete velocity states, it is natural to think of "pushing" a particle from one state to another. The momentum and energy of a site will be altered by sequences of pushes at that site, where each individual push provides a small, discrete change in momentum and/or energy. Given the large state space associated with multiple speeds on a FCHC lattice, there are generally going to be a very large number of ways to push particles around so as to cause a given total change in momentum and energy. It is therefore useful to define a set of pushes $\mathcal{P}(\Delta_n \rho \mathbf{u}, \Delta_n W)$ as any set that provides a momentum change of $\Delta_n \rho \mathbf{u}$ and an energy change of $\Delta_n W$ (where the subscript "n" denotes an effect of the non-local interaction). It is found then that $\mathcal{I}_{ji}$,

the interaction operator acting on the particles in state ji, can be written as

$$\mathcal{I}_{ji} = \sum_{\mathcal{P}} A_p \left[\delta_{ji}^{ji''(p)} - \delta_{ji}^{ji'(p)} \right] \tag{2.17}$$

where a push of type p flips a particle from direction ji' to direction ji'', A_p is the number of pushes of type p, and $\delta_{ji}^{ji''(p)}$ is a Krönecker delta function which is equal to one if $ji = ji''(p)$, and zero otherwise (and likewise for $\delta_{ji}^{ji'(p)}$). Substituting into equation (2.14),

$$\begin{aligned} \sum_{ji} \mathcal{I}_{ji} &= \sum_{ji} \sum_{\mathcal{P}} A_p \left[\delta_{ji}^{ji''(p)} - \delta_{ji}^{ji'(p)} \right] \\ = \sum_{\mathcal{P}} A_p \sum_{ji} \left[\delta_{ji}^{ji''(p)} - \delta_{ji}^{ji'(p)} \right] &= \sum_{\mathcal{P}} A_p (1-1) = 0 \end{aligned} \tag{2.18}$$

and it is seen that the mass moment vanishes as expected, since for every type of push the particles corresponding to direction ji' are subtracted and an equal number corresponding to direction ji'' are added. The total momentum change is found by substituting into the momentum moment of the interaction operator,

$$\begin{aligned} \sum_{ji} \mathbf{c}_{ji} \mathcal{I}_{ji} = \sum_{ji} \sum_{\mathcal{P}} A_p \left[\delta_{ji}^{ji''(p)} - \delta_{ji}^{ji'(p)} \right] \mathbf{c}_{ji} &= \sum_{\mathcal{P}} A_p \sum_{ji} \left[\delta_{ji}^{ji''(p)} - \delta_{ji}^{ji'(p)} \right] \mathbf{c}_{ji} \\ = \sum_{\mathcal{P}} A_p \left[\mathbf{c}_{ji''(p)} - \mathbf{c}_{ji'(p)} \right] &= \sum_{\mathcal{P}} A_p \mathbf{c}_p = \Delta_n \rho \mathbf{u} \end{aligned} \tag{2.19}$$

where $\mathbf{c}_p = \mathbf{c}_{ji''(p)} - \mathbf{c}_{ji'(p)}$ is the microscopic change in momentum due to push p. Likewise, the energy moment of the interaction operator gives

$$\sum_{ji} \varepsilon_j \mathcal{I}_{ji} = \sum_{ji} \sum_{\mathcal{P}} A_p \left[\delta_{ji}^{ji''(p)} - \delta_{ji}^{ji'(p)} \right] \varepsilon_j = \sum_{\mathcal{P}} A_p \varepsilon_p = \Delta_n W \tag{2.20}$$

where ε_p is the microscopic change in energy due to a push of type p.

The interaction operator as written in equation (2.17) has the appropriate form since its momentum and energy moments can be described as pushing operations which alter the momentum and energy at a site by specific amounts, while leaving the density unchanged. At this point it is useful to consider these new momentum and energy pushing operations as two separate entities, partly because they yield distinct macroscopic signatures, and partly because it is convenient to implement them as separate algorithms. In the following chapters, attention is turned towards the macroscopic considerations which govern the dynamically determined local instantaneous sitewise momentum and energy adjustments. First, this chapter further explores the formulation of the momentum pushing operation, which is the natural starting point of the non-local interaction.

2.3 The Interaction Force

This section addresses the concept of how to perform a sitewise momentum adjustment which inherently provides exact integer conservation of this quantity globally. It is useful to return to the idea of a sequence of hypothetical exchange events, each of which conserves momentum exactly. To make this concept more concrete, imagine that the particles throughout the lattice emit imaginary subparticles called "interactons" at each time step, and that the interactons emitted at one site are absorbed by the particles at other sites during the same time step. These particular interactons are massless and carry quanta of momentum. It is required that an equal number of these momentum-carrying subparticles are exchanged

between any pair of sites, where this number may depend on the local properties of those two sites such as density ρ and internal energy per unit volume E.

This construction suggests a pairwise "potential" $\mathcal{V}_{pair}$ between any two sites $\mathbf{x}_1$ and $\mathbf{x}_2$,

$$\mathcal{V}_{pair}(\mathbf{x}_1, \mathbf{x}_2) = G\psi(\mathbf{x}_1)\psi(\mathbf{x}_2) \tag{2.21}$$

where $\psi = \psi(\mathbf{x})$ will be referred to as the "interaction parameter," and $G = G(\mathbf{x}_1 - \mathbf{x}_2)$ is a coupling coefficient which in general is a function of separation distance. Equation (2.21) has essentially the same form given by Shan and Chen [51] in describing their interparticle potential (they refer to ψ as the "effective mass"). The pairwise potential $\mathcal{V}_{pair}$ indicates the number of interactons exchanged between two sites. This number depends on the local properties of the two sites in a fashion determined by the functional form of the interaction parameter ψ; the macroscopic considerations which determine this functional form are addressed in the next chapter.

Naturally the pairwise potential should decrease with separation distance. This can be accomplished by allowing the coupling constant G to decrease with increased distance between the sites. For simplicity and to minimize the range of the interaction (and corresponding computational effort), momentum exchange is allowed only between nearest neighbors, i.e. sites separated by a single velocity vector $\mathbf{c}_{ji}$, and G is treated as a constant that is absorbed into the interaction parameter ψ. It is further proposed that the momentum exchange between a site $\mathbf{x}$ and its neighbor at $\mathbf{x} + \mathbf{c}_{ji}$ is the pairwise potential $\mathcal{V}_{pair}$ (i.e. the number of interactons exchanged) multiplied by the velocity vector $\mathbf{c}_{ji}$ which separates them. This

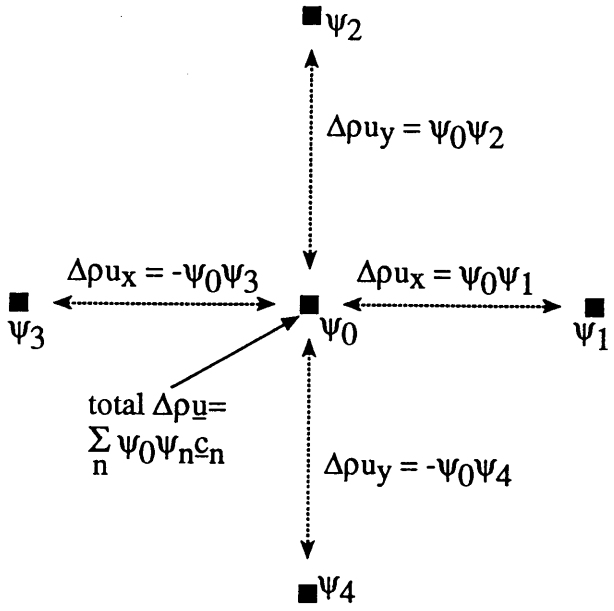

Figure 2.4: Illustration of non-local momentum adjustment process – the net momentum change of the center site is the neighborhood sum of the individual *exact integer* momentum exchanges.

implies that the total momentum change $\Delta_n \rho \mathbf{u}$ at site $\mathbf{x}$ may be calculated as the sum over the neighborhood,

$$\Delta_n \rho \mathbf{u} = \sum_{ji} \mathcal{V}_{pair}\left(\mathbf{x}, \mathbf{x} + \mathbf{c}_{ji}\right) \mathbf{c}_{ji} = \sum_{ji} \psi(\mathbf{x}) \psi\left(\mathbf{x} + \mathbf{c}_{ji}\right) \mathbf{c}_{ji} \equiv \mathbf{F}(\mathbf{x}) \Delta t \tag{2.22}$$

where the "interaction force" $\mathbf{F}$ has been introduced as equivalent to the local momentum change (which takes place over a time step Δt, thus $\mathbf{F}$ has units of force).

The interaction parameter ψ is a local macroscopic quantity determined dynamically for each site, then the momentum change at each site is calculated via the summation in equation (2.22). Figure 2.4 illustrates the momentum adjustment process, where it is pretended that

the nearest neighborhood for the site in the center consists of just the four other sites shown.[4] This scheme, using the interaction parameter ψ to represent local properties, is the specific implementation of the concept pictured in Figure 2.2. The way in which the momentum at a particular site is influenced by its neighborhood has now been precisely specified. The form of the interaction force $\mathbf{F}$ given in equation (2.22) is the same as that introduced by Shan and Chen [51], except that the Digital Physics version involves exact integer quantities.

It is straightforward to show that, as expected from its construction based on an exact exchange process, the interaction force conserves momentum globally. That is to say, the sum over all lattice sites of the momentum remains constant, because the sum over the lattice of the interaction force vanishes,

$$\sum_{\mathbf{x}} \mathbf{F}(\mathbf{x}) = 0 \tag{2.23}$$

Following Shan and Chen, this is verified by writing

$$\sum_{\mathbf{x}} \mathbf{F}(\mathbf{x}) = \sum_{\mathbf{x}} \sum_{ji} \psi(\mathbf{x}) \psi\left(\mathbf{x} + \mathbf{c}_{ji}\right) \mathbf{c}_{ji} \tag{2.24}$$

or, summing over $-\mathbf{c}_{ji}$ instead of $\mathbf{c}_{ji}$,

$$-\sum_{\mathbf{x}} \mathbf{F}(\mathbf{x}) = \sum_{\mathbf{x}} \sum_{ji} \psi(\mathbf{x}) \psi\left(\mathbf{x} - \mathbf{c}_{ji}\right) \mathbf{c}_{ji} \tag{2.25}$$

but one may equivalently sum over $\mathbf{x}' = \mathbf{x} - \mathbf{c}_{ji}$, which is indistinguishable from summing

[4]The algorithm actually used in the multiphase system involves the 12 nearest neighbors representing speed 1 and 2 directions on the 2D mapping of the FCHC lattice, as described in Section 6.4.

over $\mathbf{x}$, thus

$$\begin{aligned} -\sum_{\mathbf{x}'} \mathbf{F}(\mathbf{x}') &= \sum_{\mathbf{x}'} \sum_{ji} \psi\left(\mathbf{x}' + \mathbf{c}_{ji}\right) \psi(\mathbf{x}') \mathbf{c}_{ji} \\ &= \sum_{\mathbf{x}} \sum_{ji} \psi\left(\mathbf{x} + \mathbf{c}_{ji}\right) \psi(\mathbf{x}) \mathbf{c}_{ji} = \sum_{\mathbf{x}} \mathbf{F}(\mathbf{x}) \end{aligned} \tag{2.26}$$

and therefore equation (2.23) must be true.

Combining equations (2.19) and (2.22) gives an important result:

$$\sum_{p} A_p \mathbf{c}_p = \sum_{ji} \psi(\mathbf{x}) \psi\left(\mathbf{x} + \mathbf{c}_{ji}\right) \mathbf{c}_{ji} \tag{2.27}$$

This equation indicates that the presence of the non-local interaction is felt through the pushing of particles on each lattice site at every time step, causing sitewise changes in momentum which nonetheless conserve momentum globally. The same approach will be used later (Section 4.2) for the energy part of the non-local interaction. The next chapter begins to look in detail at the macroscopic behavior this method needs to achieve through the microdynamics of the multiphase system.

Chapter 3

Thermodynamics of the Multiphase System

3.1 A van der Waals Equation of State

An equation of state is formally defined as a relationship which expresses an intensive parameter, such as temperature T or pressure P, in terms of the independent extensive parameters of a system. It is often convenient to formulate from such relationships an expression which gives the dependence of the pressure P on the two properties density ρ (or volume V) and temperature T, and such an expression is commonly referred to as the equation of state. This practice will be followed, such that the equation of state refers to an expression for the pressure $P = P(\rho, T)$. As such, the equation of state is only defined for a substance in a

single phase.

We are interested in modeling a substance which can exist as a vapor, a liquid, or a mixture of these two phases in equilibrium. Part of a hypothetical equation of state for such a substance, the pressure-density curve along an isotherm, is shown in Figure 3.1. The left part of the curve represents the pure vapor; traveling along the curve in the direction of increasing density, the pressure increases approximately linearly. At point A a discontinuity occurs as the system becomes a two phase mixture of liquid and vapor. From point B the pressure once more increases, but much more sharply than before; this part of the curve represents the liquid, which is much less compressible than the vapor. Points A and B give the vapor and liquid densities and pressure of the equilibrium two phase mixture.

The real behavior over the two phase region between A and B is shown by the solid constant-pressure line, since phase transitions occur at constant temperature and pressure. However the pure vapor and liquid curves can be extended in an imaginary fashion, shown as the dashed line through the two-phase region. The point C on this line represents a non-equilibrium (and therefore unstable) state of intermediate density. The line containing C is a plot of a single continuous expression which describes both the liquid and vapor in the single phase regions, and corresponds to some important properties of the two-phase system. The van der Waals equation of state (used to draw Figure 3.1) is the classic example of this concept, and has proven to be useful in describing many aspects of the liquid-vapor phase transition [53]. An interesting property of the van der Waals equation is that in addition to being a simple empirical curve fit for a liquid-vapor system, it may be derived from a very simple molecular model.

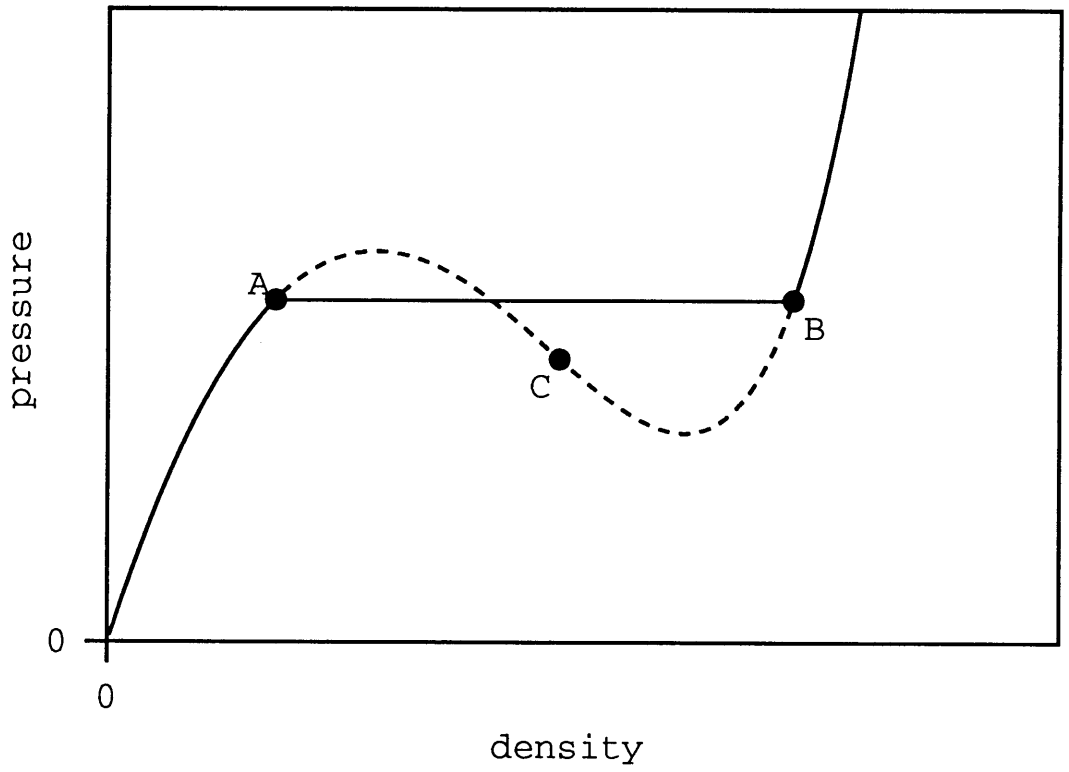

Figure 3.1: Example of a pressure-density isotherm for a substance which can exist as a vapor, a liquid, or a two-phase mixture.

This section shows how the momentum piece of the non-local interaction introduced in the previous chapter gives rise to a non-ideal-gas equation of state. In fact a great deal of flexibility over the equation of state results, and one which has the behavior illustrated in Figure 3.1 can be chosen. In this case it is expected that (for temperatures below the critical point) a first order phase transition will yield the coexistence of a high density region and a low density region, representing liquid and vapor phases. Fundamentally, two-phase coexistence occurs when it minimizes the total free energy of the system[1].

[1]It has yet to be proven, however, that a true free energy in the sense of a thermodynamic potential exists for this lattice gas system, hence terms such as "entropy" and "free energy" are used rather loosely in this work to represent local hydrodynamic quantities.

To begin the analysis the relevant relations just derived in Chapter 2 are restated:

$$\sum_{ji} \mathcal{I}_{ji} \mathbf{c}_{ji} = \sum_{\mathcal{P}} A_p \mathbf{c}_p = -\nabla \cdot \underline{\underline{\mathbf{\Pi}}}_n = \Delta_n \rho \mathbf{u} = \mathbf{F} \tag{3.1}$$

which equates the momentum moment of the interaction operator, the explicit form of the momentum pushing operation, the divergence of the non-local part of the momentum flux tensor, the local momentum change due to the non-local interaction, and the interaction force. The correct form of the total momentum flux tensor $\underline{\underline{\mathbf{\Pi}}}$ in a bulk phase (i.e. far from an interface) is

$$\underline{\underline{\mathbf{\Pi}}} = P\underline{\underline{\mathrm{I}}} + \rho \mathbf{u}\mathbf{u} = \underline{\underline{\mathbf{\Pi}}}_k + \underline{\underline{\mathbf{\Pi}}}_n \tag{3.2}$$

As shown in equation (2.10), the kinetic part of the momentum flux tensor, which is expected to be equivalent to the momentum flux tensor of the standard system [12], is

$$\underline{\underline{\mathbf{\Pi}}}_k = P_k \underline{\underline{\mathrm{I}}} + g \rho \mathbf{u}\mathbf{u} \tag{3.3}$$

It is also expected that, as in the standard system, the Galilean factor g can be set to unity through the "rate coefficients" which govern the energy dependent part of the distributions (this is proved in Section 4.1). Combining the last two equations therefore yields

$$\underline{\underline{\mathbf{\Pi}}}_n = P\underline{\underline{\mathrm{I}}} - P_k \underline{\underline{\mathrm{I}}} = P_n \underline{\underline{\mathrm{I}}} \tag{3.4}$$

for the non-local contribution to the momentum flux in a bulk phase region, and in view of

equation (3.1),

$$-\nabla \cdot P_n \underline{\underline{\mathrm{I}}} = \mathbf{F} = -\nabla P_n \tag{3.5}$$

This is consistent with the goal of using the non-local interaction to alter the pressure, and therefore the equation of state, while leaving the velocity-dependent terms of the momentum transport equation intact.

Returning to the form given for the interaction force $\mathbf{F}$ in equation (2.22), and using a first order Taylor expansion to substitute for the value of the interaction parameter ψ at neighbor $\mathbf{x} + \mathbf{c}_{ji}$,

$$\psi\left(\mathbf{x} + \mathbf{c}_{ji}\right) = \psi(\mathbf{x}) + \mathbf{c}_{ji} \cdot \nabla\psi(\mathbf{x}) + ... \tag{3.6}$$

gives

$$\begin{aligned} \mathbf{F} &= \sum_{ji} \psi \left[\psi + \mathbf{c}_{ji} \cdot \nabla\psi\right] \mathbf{c}_{ji} = \sum_{ji} \psi\nabla \cdot \psi \mathbf{c}_{ji}\mathbf{c}_{ji} \\ &= \psi\nabla \cdot \psi \sum_{j} \frac{c_j^2 d_j}{D} \underline{\underline{\mathrm{I}}} = \nabla \cdot \frac{\Gamma}{2}\psi^2 \underline{\underline{\mathrm{I}}} \end{aligned} \tag{3.7}$$

where the "interaction coefficient" Γ is defined as

$$\Gamma \underline{\underline{\mathrm{I}}} \equiv \sum_{ji} \mathbf{c}_{ji}\mathbf{c}_{ji} \tag{3.8}$$

and the following property of the FCHC lattice was used:

$$\sum_{ji} \mathbf{c}_{ji}\mathbf{c}_{ji} = \sum_{j} \frac{c_j^2 d_j}{D} \underline{\underline{\mathrm{I}}} \tag{3.9}$$

where d_j is the number of velocities states available to particles of type j, and D is the dimension of the lattice ($D = 4$ for the FCHC lattice, required in Digital Physics). From

equations (3.5) and (3.7),

$$P_n = -\frac{\Gamma}{2}\psi^2 \tag{3.10}$$

is the contribution to the scalar pressure from the non-local interaction. Thus the total pressure in a bulk phase will be

$$P = P_k - \frac{\Gamma}{2}\psi^2 \tag{3.11}$$

This expression gives the equation of state of the multiphase system in terms of the interaction parameter ψ.

The well-known van der Waals equation of state,

$$P_{vdw}(\rho, T) = \frac{\rho RT}{1 - \rho b} - a\rho^2 \tag{3.12}$$

is chosen as a simple (if crude) means by which to model a pure substance which can undergo a phase transition. The van der Waals equation of state is imposed on the multiphase system by combining equations (3.11) and (3.12) to solve for the interaction parameter ψ:

$$\psi = \sqrt{\frac{2}{\Gamma}\left(P_k - \frac{\rho RT}{1 - \rho b} + a\rho^2\right)} \tag{3.13}$$

This is the functional form of ψ required to determine the interaction force and implement the momentum pushing operation. The explicit form of the kinetic pressure P_k will be found in the next chapter, but for now it can be viewed with little error as the true ideal gas pressure, $P_k = \rho T$, in which case the interaction parameter may be written as $\psi = \psi(\rho, T)$. However, while the density ρ has a straightforward interpretation as the number of particles

at a given location, a meaningful definition of the temperature T must still be established. This will be addressed in the next section.

The van der Waals constants a and b must also be specified. These parameters play a role in many of the thermodynamic properties of the system, because they in part determine the so-called fundamental equation (also discussed in the next section). Values of the van der Waals constants have been determined for many substances, and they generally reflect a "best fit" of the van der Waals equation to various experimental data over a wide range of (for example) temperature and pressure conditions. Such empirical fits are typically fairly crude, since there are only two adjustable parameters in the van der Waals equation of state. For the purposes of this project, however, a van der Waals system is suitable to demonstrate key aspects of a two phase system. A more sophisticated equation of state, $P_{eos}(\rho, T)$, could be used to improve agreement of the thermodynamic properties of the model with the properties of a real substance, and in general the interaction parameter ψ would be found as

$$\psi(\rho, T) = \sqrt{\frac{2}{\Gamma}(P_k - P_{eos}(\rho, T))} \tag{3.14}$$

This method breaks down if the argument of the root is negative, which may occur when the pressure in the liquid is very large. This has not been found to be a limitation of any consequence for two-phase systems, since the kinetic pressure $P_k \cong \rho T$ in the liquid is inevitably much larger than the saturation pressure P_{sat} towards which the system is driven.

As mentioned, the equation of state provides a relationship between the pressure, density (or volume), and temperature of a substance. There is no such thing as an equation of

state for a two-phase mixture, however; in this case there is only one independent intensive thermodynamic property of the system, for example either pressure or temperature (an intensive property is one which does not depend on the size of the system). This is a result of the Gibbs Phase Rule, which states that the number of degrees of freedom is two plus the number of components minus the number of phases present. An equation of state can still be written for each phase individually; furthermore both phases must (at equilibrium) coexist at the same temperature and pressure, known as the saturation temperature T_{sat} and saturation pressure P_{sat}. The resulting pair of equations is

$$P_{sat} = \frac{\rho_g R T_{sat}}{1 - \rho_g b} - a\rho_g^2 = \frac{\rho_f R T_{sat}}{1 - \rho_f b} - a\rho_f^2 \tag{3.15}$$

where ρ_g and ρ_f are the equilibrium vapor and liquid densities, respectively. These are also thermodynamic properties of a two-phase mixture and must therefore depend on only one independent property. This leaves three unknowns in equations (3.15); for example when the saturation temperature T_{sat} is chosen as the independent property, the unknowns are the saturation pressure P_{sat}, the equilibrium vapor density ρ_g, and the equilibrium liquid density ρ_f. An additional equation is needed, and it comes from the equilibrium condition that the chemical potentials of each phase must be equal. This leads to the well known Maxwell equal area rule, which may be written as

$$\int_{\rho_g}^{\rho_f} \frac{P(\rho, T_{sat}) - P_{sat}}{\rho^2} d\rho = 0 \tag{3.16}$$

Equations (3.15) and (3.16) allow any three of the identified properties of a two-phase mixture

to be found as functions of the fourth.

3.2 The Internal Energy Relation

Calculation of the interaction parameter ψ so as to achieve a desired empirical equation of state is a key part of the multiphase system. However, the hydrodynamic system is not closed with just an equation of state. The set of independent hydrodynamic variables which are local properties on the lattice can be identified as follows: density ρ, velocity $\mathbf{u}$, pressure P, temperature T, and internal energy per unit volume E. Relationships between these variables are given, in general, by the mass, momentum, and energy transport equations, an equation of state, and another constitutive relation describing (for example) the dependence of the internal energy on density and temperature. The latter is the missing ingredient; an appropriate internal energy relation is needed. Moreover, a method by which it can be achieved in the Digital Physics framework must be developed.

It is clear that internal energy in the multiphase system cannot in general be that of the standard system, for which the internal energy per unit volume is

$$E = \frac{D}{2}\rho T \tag{3.17}$$

which is correct for a monatomic 4D ideal gas and which provides the definition of the temperature T for the standard system. Consider a two-phase mixture in equilibrium: the vapor and liquid regions, while at the same temperature T_{sat}, have vastly different specific

internal energies (far from the critical point), that of the liquid being much lower than that of the vapor.

An important goal of this work is to build into the method a consistent empirical thermodynamics at the macroscopic level which captures the correct dependencies of the internal energy and related quantities. A complete thermodynamical description of a system is given by its fundamental equation, one form of which is the Helmholtz free energy as a function of temperature T, volume V, and particle number N, $F = F(T, V, N)$. To derive a fundamental equation consistent with a van der Waals equation of state, the well known thermodynamic relations known as the Maxwell Relations are employed, beginning with one involving the Helmholtz free energy:

$$P = -\left[\frac{\partial F}{\partial V}\right]_T \Longrightarrow F = -\int P dV \tag{3.18}$$

Using $N = \rho V$ to rewrite the van der Waals equation of state (3.12) in terms of particle number N and volume V,

$$F(N, V, T) = -\int dV \left(\frac{NRT}{V - bN} - \frac{N^2 a}{V^2}\right) = -NRT \ln (V - bN) - \frac{N^2 a}{V} + \xi(T) \tag{3.19}$$

where the constant of integration is some function of temperature, $\xi(T)$. For convenience another function of temperature $\phi(T)$ is defined such that $\xi(T) = NRT \ln [N\phi(T)]$, which allows equation (3.19) to be written as

$$F(N, V, T) = -NRT \ln \left[\frac{V - bN}{N\phi(T)}\right] - \frac{N^2 a}{V} = -NRT \ln \left[\frac{\frac{1}{\rho} - b}{\phi(T)}\right] - N\rho a \tag{3.20}$$

Dividing by particle number N gives the Helmholtz free energy per unit mass f,

$$f(\rho,T) = -RT\ln\left[\frac{\frac{1}{\rho}-b}{\phi(T)}\right] - \rho a \tag{3.21}$$

Another of the Maxwell Relations gives the entropy S from the Helmholtz free energy F:

$$S = -\left[\frac{\partial F}{\partial T}\right]_{\rho} \tag{3.22}$$

Thus the entropy per unit mass s can be found from equation (3.21),

$$s(\rho,T) = -\left[\frac{\partial f}{\partial T}\right]_{\rho} = -\frac{RT\phi'(T)}{\phi(T)} + R\ln\left[\frac{\frac{1}{\rho}-b}{\phi(T)}\right] \tag{3.23}$$

where $\phi'(T) = \partial_T\phi(T) = d\phi(T)/dT$. The definition of the Helmholtz free energy F is $F \equiv U - TS$, where U is the total internal energy. Thus the internal energy per unit mass u is given by $u = f + Ts$, which yields

$$u(\rho,T) = -RT\ln\left(\frac{\frac{1}{\rho}-b}{\phi(T)}\right) - \rho a + T\left[-\frac{RT\phi'(T)}{\phi(T)} + R\ln\left(\frac{\frac{1}{\rho}-b}{\phi(T)}\right)\right] \tag{3.24}$$

or

$$u(\rho,T) = -\rho a - R\chi(T) \tag{3.25}$$

where

$$\chi(T) \equiv \frac{T^2\phi'(T)}{\phi(T)} \tag{3.26}$$

Equations (3.21), (3.23), and (3.25) give expressions for useful thermodynamic quantities

as functions of the van der Waals constants and an arbitrary function of temperature. Expressions for other quantities such as enthalpy and Gibbs free energy could be similarly obtained.

As identified earlier, the internal energy per unit mass $u(\rho, T)$ is of primary interest. Clearly its temperature behavior is determined by the function $\chi(T)$; to proceed this function must be specified. It is related to the constant volume heat capacity per unit mass c_v:

$$\begin{aligned} c_v \equiv \left[\frac{\partial u}{\partial T}\right]_\rho &= -R\frac{d\chi(T)}{dT} = c_v(T) \\ \Longrightarrow \chi(T) &= -\frac{1}{R}\int c_v(T)dT \end{aligned} \tag{3.27}$$

and it is apparent that one of the consequences of the van der Waals equation of state is that the constant volume heat capacity per unit mass does not depend on density. This necessarily introduces the assumption that the heat capacity of the liquid will be equal to the heat capacity of the vapor on a unit mass basis. For water, the constant volume heat capacity per unit mass of the saturated liquid, c_{vf}, is on order twice that of the saturated vapor, c_{vg}, over a fair range of temperatures. This need not concern us at the moment, however, since heat transfer is beyond the scope of this work. On the other hand complete flexibility exists regarding the temperature dependence of the constant volume heat capacity. It is convenient to assume that it is constant, which is often an acceptable approximation for small temperature changes. Then equation (3.27) gives

$$\begin{aligned} \chi(T) = -\frac{1}{R}\int c_v dT = -\frac{c_v T}{R} + A &= \frac{T^2\phi'(T)}{\phi(T)} \\ \Longrightarrow d\ln\phi(T) = -\frac{c_v}{R}d\ln T + \frac{A}{T^2}dT & \end{aligned} \tag{3.28}$$

where A is an integration constant. Integrating once more,

$$\ln \phi(T) = -\frac{c_v}{R} \ln \frac{T}{B} - \frac{A}{T} \tag{3.29}$$

where B is another integration constant.

The above expressions for the functions $\chi(T)$ and $\phi(T)$ can now be used in equations (3.21), (3.23), and (3.25) to get explicit forms for the Helmholtz free energy per unit mass f,

$$f(\rho, T) = -RT \ln \left(\frac{1}{\rho} - b \right) - \rho a - c_v T \ln \frac{T}{B} - AR \tag{3.30}$$

the entropy per unit mass s,

$$s(\rho, T) = R \ln \left[\left(\frac{1}{\rho} - b \right) \left(\frac{T}{B} \right)^{\frac{c_v}{R}} \right] + c_v \tag{3.31}$$

and the internal energy per unit mass u,

$$u(\rho, T) = c_v T - \rho a - AR \tag{3.32}$$

Equation (3.30) is essentially the fundamental equation of a van der Waals system with a temperature-independent constant-volume heat capacity, and will serve as the fundamental equation of the multiphase system. The analysis used to derive equations (3.30-3.32) is essentially the same as the treatment given by Fermi [54] for a van der Waals system. An analogous method could in principle be applied to any equation of state (supplemented by a heat capacity equation).

The formulation of the internal energy relation is completed by specifying the values of the constant volume heat capacity per unit mass c_v and the arbitrary constant A. The value of A sets the absolute energy scale of the system[2]; this could be done in such a way as to reflect the absolute scale used in the steam tables, which is set such that the internal energy of liquid water at the triple point is zero. It is more convenient and physically appealing to instead allow the multiphase system to collapse to the ideal gas physics of the standard system in the limit of zero density. This suggests $A = 0$, such that

$$u(\rho, T) = c_v T - \rho a \tag{3.33}$$

which gives

$$\lim_{\rho \to 0} u(\rho, T) = c_v T \tag{3.34}$$

which is the correct internal energy per unit mass for an ideal gas. Also, to force the internal energy relation to collapse to that of the standard system at zero density, the constant volume heat capacity is taken to be

$$c_v = \frac{D}{2} R = 2R \tag{3.35}$$

which gives

$$u(\rho, T) = 2RT - \rho a \tag{3.36}$$

Equation (3.36) will be referred to as the internal energy relation for the multiphase sys-

[2]The arbitrary constant B, which sets the absolute entropy scale, can be ignored for the current purposes.

tem. It was derived from an equation of state, the form of the constant volume heat capacity, and the absolute energy scale of the system. The hydrodynamic system is now complete, because the internal energy relation provides a meaningful definition of the temperature T in terms of fundamental local properties ρ and $u = E/\rho$:

$$RT = \frac{1}{2}(u + a\rho) \tag{3.37}$$

3.3 Properties of the Interface

Equations (3.30)-(3.32) each express one intensive thermodynamic property as a function of two others, as appropriate for a single phase substance. For an equilibrium two-phase mixture, however, there can be only one independent intensive property. This brings up the important issue that in the Digital Physics multiphase system, continuous relationships between macroscopic properties analogous to those for a single phase substance are required, even if the overall system happens to represent two-phase coexistence. Consider a site at some instant located somewhere in a bulk phase region, say within the liquid phase. The site does not know it is supposed to be liquid, nor does it have any immediate information as to whether or not a vapor phase exists somewhere else in the system; the particle distributions at the site are simply evolving according the microdynamical rules of the algorithm. The microdynamics depend upon the calculation of local quantities, particularly temperature $T = T(\rho, u)$ and kinetic pressure $P_k = P_k(\rho, u)$ such that the interaction parameter ψ can be determined from equation (3.13). Hence for any site at any instant, relationships

of this nature using two locally independent variables are necessary, whether or not the overall system is a two phase mixture. The Gibbs phase rule allowing a single independent parameter for a two phase system will be recovered in the *equilibrium* behavior of the system in a *macroscopic* (i.e. time and space averaged) sense.

Moreover, such relationships between local thermodynamic quantities must exist within the highly non-equilibrium interfacial region, which will have finite size and occupy some number of lattice sites. Non-equilibrium conditions will also occur due to fluctuations and transient behavior. In this version of the multiphase system, the thermodynamical relations derived above are simply followed in a continuous fashion even for non-equilibrium conditions, including highly inhomogeneous regions like that of the interface. This treatment[3] ignores the additional free energy associated with such a region, which within the interface is referred to as the surface excess free energy [56]. One might expect the fact that this free energy contribution is not explicitly included in the microdynamics to have consequences for the behavior of the interface; this point is discussed further in Section 5.2. It is nevertheless predicted that homogeneous liquid and vapor phase regions will exist, and will be driven towards the equilibrium thermodynamic properties close to those predicted for a van der Waals thermodynamic system.

A key property of a two phase system (or any system with a fluid-fluid interface) is the coefficient of surface tension[4] σ. The phenomena often called surface tension or interfacial tension is really a manifestation of the additional free energy just mentioned that exists

[3]Known as the *point-thermodynamic* approximation [55].

[4]Throughout this thesis, the coefficient of surface tension σ will be taken as the usual quantity divided by the liquid density ρ_f. This convention simplifies ensuing dimensionless analyses because surface tension scales directly with the liquid density.

within the interface [56, 55]. The source of the excess free energy is the intermolecular forces, or more precisely the variations in intermolecular forces that occur as the density varies continuously through the interface from its liquid value to its vapor value. The mean molecular spacing is larger in the interface than in the bulk liquid, and energy is required to move the molecules father apart. In the direction normal to the interfacial surface, a density gradient is established which maintains a balance of forces continuously from the liquid side to the vapor side. In the direction parallel to the interface, however, the density does not vary, and the increased molecular spacing results in a net tension force [56].

Consequently, the pressure tensor $\underline{\underline{P}}$ (which is the zero-velocity part of the momentum flux tensor $\underline{\underline{\Pi}}$) is not isotropic within the interface, because the "tension" contributes to the tangential components but not to the normal component. It is useful to consider a flat interface in the $x-y$ plane, hence normal to the z-direction. The pressure tensor $\underline{\underline{P}}$ is purely diagonal, and the tangential components are $P_{xx}(z) = P_{yy}(z) = P_T(z)$, while the normal component is $P_{zz} = P_N = P_o$, where P_o is the scalar pressure in either of the bulk phases. Then the coefficient of surface tension σ can be written in terms of these quantities [55],

$$\sigma\rho_f = \int_{INT}(P_N - P_T)dz \tag{3.38}$$

where the integration is performed over at least the width of the interface, or beyond since $P_N = P_T$ outside of the interface. This equation results from calculating the total work done, and hence the increase in free energy F, per unit area A, during an isothermal and reversible

change in the volume of the interface, and using the formal definition of surface tension [55]

$$\sigma\rho_f = \frac{\delta F}{\delta A} \tag{3.39}$$

It is possible to use equation (3.38) to understand the existence of surface tension in the multiphase system by finding expressions for the normal and tangential components of the pressure tensor. From equations (2.22) and (3.5), the form of the interaction force is

$$\mathbf{F} = \sum_{ji} \psi(\mathbf{x})\psi(\mathbf{x}+\mathbf{c}_{ji})\mathbf{c}_{ji} = -\nabla \cdot P_n \underline{\underline{\mathrm{I}}} \tag{3.40}$$

which implies that the total pressure tensor can be written as

$$\underline{\underline{\mathrm{P}}} = \sum_{ji} N_{ji}\mathbf{c}_{ji}\mathbf{c}_{ji} - \sum_{ji} \frac{1}{2}\psi(\mathbf{x})\psi(\mathbf{x}+\mathbf{c}_{ji})\mathbf{c}_{ji}\mathbf{c}_{ji} \tag{3.41}$$

where the first term is the usual kinetic part and the second is the contribution due to the non-local interaction. A second order Taylor expansion in space yields

$$\psi(\mathbf{x}+\mathbf{c}_{ji}) = \psi(\mathbf{x}) + \mathbf{c}_{ji}\cdot\nabla\psi(\mathbf{x}) + \frac{1}{2}\mathbf{c}_{ji}\mathbf{c}_{ji} : \nabla\nabla\psi(\mathbf{x}) \tag{3.42}$$

which gives for the non-local term

$$\begin{aligned} &-\frac{1}{2}\psi\sum_{ji}\left(\mathbf{c}_{ji}\mathbf{c}_{ji}\psi - \frac{1}{2}\mathbf{c}_{ji}\mathbf{c}_{ji}\mathbf{c}_{ji}\mathbf{c}_{ji} : \nabla\nabla\psi\right) \\ &\Longrightarrow -\frac{1}{2}\Gamma\psi^2\underline{\underline{\mathrm{I}}} - \frac{1}{4}\Gamma'(\psi\nabla^2\psi\underline{\underline{\mathrm{I}}} - 2\psi\nabla\nabla\psi) \end{aligned} \tag{3.43}$$

where Γ is given by equation (3.8) and Γ' is defined as

$$\Gamma'\Delta^{(4)} \equiv \sum_{ji} \mathbf{c}_{ji}\mathbf{c}_{ji}\mathbf{c}_{ji}\mathbf{c}_{ji} = \sum_{j} \frac{d_j c_j^4}{D(D+2)}\Delta^{(4)} \tag{3.44}$$

Neglecting velocity terms, the kinetic part of the pressure tensor is $P_k\underline{\underline{\mathrm{I}}}$, thus equation (3.41) becomes

$$\underline{\underline{\mathrm{P}}} = \left(P_k - \frac{1}{2}\Gamma\psi^2 - \frac{1}{4}\Gamma'\psi\nabla^2\psi\right)\underline{\underline{\mathrm{I}}} - \frac{1}{2}\Gamma'\psi\nabla\nabla\psi \tag{3.45}$$

Note that in the bulk regions where the properties are uniform and the derivatives vanish, equation (3.11) for scalar pressure P is recovered.

Local values of the pressure components for an arbitrary (2D) interface are $P_N = \hat{\mathbf{n}}\hat{\mathbf{n}} : \underline{\underline{\mathrm{P}}}$ and $P_T = \hat{\mathbf{t}}\hat{\mathbf{t}} : \underline{\underline{\mathrm{P}}}$, where $\hat{\mathbf{n}}$ and $\hat{\mathbf{t}}$ are unit normal and tangent vectors. Hence for the flat interface normal to the z-direction, the normal pressure component is

$$P_N = P_k - \frac{1}{2}\Gamma\psi^2 - \frac{3}{4}\Gamma'\psi\frac{d^2\psi}{dz^2} \tag{3.46}$$

and the tangential pressure component is

$$P_T = P_k - \frac{1}{2}\Gamma\psi^2 - \frac{1}{4}\Gamma'\psi\frac{d^2\psi}{dz^2} \tag{3.47}$$

Thus the difference between them is

$$P_N - P_T = -\frac{1}{2}\Gamma'\psi\frac{d^2\psi}{dz^2} \tag{3.48}$$

Finally, equation (3.38) gives

$$\sigma\rho_f = -\frac{1}{2}\Gamma' \int_{INT} \psi \frac{d^2\psi}{dz^2} dz \tag{3.49}$$

or in general (for a non-planar 2D interface)

$$\sigma\rho_f = -\frac{1}{2}\Gamma' \int_{INT} \psi \frac{\partial^2\psi}{\partial n^2} dn \tag{3.50}$$

where n is the local coordinate normal to the interface. Hence the surface tension in the multiphase system is related to the interaction parameter ψ and its spatial derivatives, which in turn depend on the imposed equation of state and the steady state density and energy profiles through the interface.

It is also possible to evaluate the effect of surface tension on the momentum transport equation within an interfacial region. As shown in equation (2.12), the time rate of change of momentum is equal (and opposite) to the divergence of the momentum flux tensor $\underline{\underline{\Pi}} = \underline{\underline{P}}$ + velocity terms. Hence the zero-velocity part of the momentum transport equation is

$$\begin{aligned} \nabla \cdot \underline{\underline{P}} &= \nabla \cdot (P_N \hat{\mathbf{n}}\hat{\mathbf{n}} + P_T \hat{\mathbf{t}}\hat{\mathbf{t}}) \\ &= \nabla P_N \cdot \hat{\mathbf{n}}\hat{\mathbf{n}} + P_N \hat{\mathbf{n}} \cdot \nabla \hat{\mathbf{n}} + P_N \hat{\mathbf{n}} \nabla \cdot \hat{\mathbf{n}} + \nabla P_T \cdot \hat{\mathbf{t}}\hat{\mathbf{t}} + P_T \hat{\mathbf{t}} \cdot \nabla \hat{\mathbf{t}} + P_T \hat{\mathbf{t}} \nabla \cdot \hat{\mathbf{t}} \end{aligned} \tag{3.51}$$

Noting that the curvature $\kappa = \nabla \cdot \hat{\mathbf{n}}$ and $\hat{\mathbf{t}} \cdot \nabla \hat{\mathbf{t}} = -\kappa \hat{\mathbf{n}}$, and that when the curvature is small

$\nabla\hat{\mathbf{n}} = \nabla \cdot \hat{\mathbf{t}} = \nabla P_T \cdot \hat{\mathbf{t}} \cong 0$, equation (3.51) becomes

$$\nabla \cdot \underline{\underline{\mathrm{P}}} = \frac{\partial P_N}{\partial n}\hat{\mathbf{n}} + P_N\kappa\hat{\mathbf{n}} - P_T\kappa\hat{\mathbf{n}} = \left[\frac{\partial P_N}{\partial n} + \kappa(P_N - P_T)\right]\hat{\mathbf{n}} \tag{3.52}$$

The first term on the right-hand side is the usual pressure gradient term. The other term is proportional to the curvature κ and results in a force related to surface tension, $\mathbf{F}_\sigma$. Using equation (3.48) it may be written

$$\mathbf{F}_\sigma = \kappa(P_N - P_T)\hat{\mathbf{n}} = -\frac{1}{2}\kappa\Gamma'\psi\frac{\partial^2\psi}{\partial n^2}\hat{\mathbf{n}} \tag{3.53}$$

When the interface is treated as a discontinuity, which is almost invariably the case, the interface curvature and coefficient of surface tension do not appear explicitly in the transport equations. Instead they occur as part of the "jump conditions" obeyed at the discontinuity, as discussed in Section 5.1 (where it is shown that in the limit of vanishing interface thickness, equation (3.53) gives the usual jump condition involving surface tension).

3.4 Microscopic Internal Energy

Despite the simplicity of the internal energy relation (3.36), it captures an essential physical feature, namely the large difference between the internal energy per unit mass of the saturated liquid, $u_f = 2RT_{sat} - \rho_f a$, and that of the vapor, $u_g = 2RT_{sat} - \rho_g a$ (hence the difference is $\Delta u = -a\Delta\rho$.) The multiphase system must be able to represent not only these

two different internal energies at the same temperature, but also the whole range in between, within which will exist the values of internal energy for interfacial regions. This cannot be achieved with the standard system, where the internal energy per unit mass is always proportional to the temperature, $u = 2RT$. This is natural because the particles of the standard system are like ideal gas molecules which contribute only their energy of motion to the local energy moment.

In order to have a range of internal energies for a given temperature, an internal degree of freedom must be provided. This is addressed by introducing a *microscopic internal energy*[5], ε_j^I, a discrete amount of energy carried by a particle of type j in addition to its kinetic energy ε_j^K. Thus the total microscopic energy ε_j^T is

$$\varepsilon_j^T = \varepsilon_j^K + \varepsilon_j^I \tag{3.54}$$

The total local internal energy moment will now be the sum of a kinetic term and a non-kinetic term, similar to the way the total pressure is the sum of kinetic and a non-local pieces. It is shown later how the relative contributions to the energy moment can be adjusted to achieve the correct macroscopic values of internal energy as required by equation (3.36).

The absolute energy scale of the multiphase system has been specified by the decision to let the internal energy relation collapse to that of an ideal gas in the limit of zero density. The benefit of this choice is that in the ideal gas limit no microscopic internal energy contribution

[5]The original concept of microscopic internal energy in a multispeed lattice gas is due to Teixeira and Molvig [57], where it was developed in the context of altering the ratio of specific heats of an ideal gas in the standard system.

is required, and the multiphase system reverts to the standard system. It happens that any non-kinetic contribution to the internal energy must always be negative, since an ideal gas has the maximum internal energy for a given temperature (this also clear from the internal energy relation (3.36)). Therefore, *negative* microscopic internal energies are needed, in order to lower the macroscopic internal energy from that of the ideal gas. The physical interpretation of a negative internal energy contribution is the presence of attractive intermolecular bonds. Intermolecular forces are very strong in liquids compared to gases, and the resulting bonds can be thought of as storing negative energy, since energy is required to break the bonds while energy is given up when the bonds are formed. In the multiphase system, a site with higher density will have a higher fraction of particles with negative microscopic internal energy. An interesting result of the choice of absolute energy scale is that for water at conditions far from the critical point, the latent energy of vaporization is greater than the energy of the saturated vapor taken in an absolute sense: $u_{gf} > u_g \cong 2RT$. This means that the internal energy per unit mass of the saturated liquid, u_f, will be negative. There is nothing unphysical about a negative internal energy; it is a consequence of the fact that the absolute energy scale is lower for the multiphase system compared to that of the steam tables.

In Section 5.6 the van der Waals thermodynamical system will be compared to the properties of water, and in Section 6.1 particular choices of new species with both internal and kinetic microscopic energies are explored. The next chapter looks in detail at how the presence of microscopic internal energy, a fundamental property needed to achieve the desired thermodynamics of the multiphase system, affects the macroscopic transport equations of the multispeed lattice gas.

Chapter 4

The Multiphase Euler Equations and Artifact Removal

4.1 The Mass and Momentum Moment Equations

The equations of motion of a fluid result from the mass, momentum, and energy moments of the kinetic equation where the distributions of the fluid particles are maintained in local thermal equilibrium at all times. The Euler equations describe the motion of an ideal (i.e. non-viscous) fluid, and result from the moments of the kinetic equation expanded to first order in Knudsen number, $\kappa \propto \lambda/L$, where λ is the mean free path and L is a macroscopic scale length. This is the meaning of the expansion used to generate equation (2.3) from the lattice update equation (2.2). The moments of equation (2.3), shown in microscopic form as

equations (2.4-2.6) and in rough macroscopic form as equations (2.7-2.9), give the so-called lattice Euler equations for the multiphase system.

To begin, the lattice moment equations are rewritten:

$$\partial_t \sum_{ji} N_{ji}^{EQ} + \nabla \cdot \sum_{ji} \mathbf{c}_{ji} N_{ji}^{EQ} = 0 \tag{4.1}$$

$$\partial_t \sum_{ji} \mathbf{c}_{ji} N_{ji}^{EQ} + \nabla \cdot \sum_{ji} \mathbf{c}_{ji}\mathbf{c}_{ji} N_{ji}^{EQ} = -\nabla \cdot \underline{\underline{\mathbf{\Pi}}}_n \tag{4.2}$$

$$\partial_t \sum_{ji} \varepsilon_j^T N_{ji}^{EQ} + \nabla \cdot \sum_{ji} \varepsilon_j^T \mathbf{c}_{ji} N_{ji}^{EQ} = -\nabla \cdot \mathbf{Q}_n \tag{4.3}$$

where the moments of the interaction operator were substituted for via equations (2.14)-(2.16). Also, the microscopic energy ε_j of the standard system has been replaced by the total microscopic energy $\varepsilon_j^T = \varepsilon_j^K + \varepsilon_j^I$ because of the inclusion of a microscopic internal energy. It should also be noted that for simplicity the particle mass m has been taken to be always unity.

In this section and the next, each of the moment terms in the lattice Euler equations will be carefully evaluated. By comparing the results to the true Euler equations, the coefficients in the expansion of the equilibrium microscopic distribution function, N_{ji}^{EQ} (shown below), will be found. Moreover, the conditions required to remove artifacts will be identified, where artifacts are any unphysical attributes of the equations of motion, which arise due to the discreteness of the system.

The equilibrium microscopic distribution function N_{ji}^{EQ} expanded to third order in velocity (actually Mach number) contains all of the terms relevant to the transport equations and

has the following form [13]:

$$N_{ji}^{EQ} = N_j[1 - \gamma_0(\mathbf{c}_{ji} \cdot \mathbf{u}) + \frac{1}{2}\gamma_0^2(\mathbf{c}_{ji} \cdot \mathbf{u})^2 - \left(\alpha_2 + \beta_2\varepsilon_j^T\right) \\ -\frac{1}{6}\gamma_0^3\left(\mathbf{c}_{ji} \cdot \mathbf{u}\right)^3 + \gamma_0\left(\mathbf{c}_{ji} \cdot \mathbf{u}\right)\left(\alpha_2 + \beta_2\varepsilon_j^T\right) - \gamma_2\left(\mathbf{c}_{ji} \cdot \mathbf{u}\right) + \mathcal{O}(\mathbf{u}^4)] \tag{4.4}$$

The Lagrange multipliers for mass, momentum, and energy have been expanded as $\alpha = \alpha_0 + \alpha_2$, $\gamma = \gamma_0 + \gamma_2$, and $\beta = \beta_0 + \beta_2$, respectively, where coefficients with subscript "0" are constant with respect to velocity and those with subscript "2" are proportional to the square of the velocity. The zero-velocity or isotropic distribution function, N_j, is given by

$$N_j = r_j \exp\left(-\alpha_0 - \beta_0\varepsilon_j^T\right) \tag{4.5}$$

where r_j is the rate coefficient associated with species j. These rate coefficients, plus coefficients α_0 and β_0 (which will hereafter be considered part of the set of rate coefficients as well), are adjusted to achieve the desired energy-exchange behavior of the system, as shown in Section 4.3. The four remaining coefficients, γ_0, γ_2, α_2, and β_2, are associated with the velocity dependence of the equilibrium microscopic distribution function N_{ji}^{EQ}, and (as mentioned) will be solved for by comparing the lattice Euler equations to the real Euler equations.

It is useful at this point to define the isotropic moment (where isotropic is meant to imply no velocity dependence) of a microscopic parameter x_j:

$$\langle x \rangle = \sum_j x_j d_j N_j \tag{4.6}$$

where d_j is the number of lattice velocities available to a particle of species j. It is also useful to note three identities of the FCHC lattice:

$$\sum_{ji} x_j = \sum_j x_j d_j \tag{4.7}$$

$$\sum_{ji} \mathbf{c}_{ji}\mathbf{c}_{ji} = \sum_j \frac{d_j c_j^2}{D}\underline{\underline{\mathrm{I}}} \tag{4.8}$$

$$\sum_{ji} \mathbf{c}_{ji}\mathbf{c}_{ji}\mathbf{c}_{ji}\mathbf{c}_{ji} = \sum_j \frac{d_j c_j^4}{D(D+2)}\Delta^{(4)} \tag{4.9}$$

where $\underline{\underline{\mathrm{I}}}$ is the two-dimensional isotropy tensor and $\Delta^{(4)}$ is the four-dimensional isotropy tensor. Combining the last two of these with equation (4.6) gives the following useful relations:

$$\sum_{ji} x_j \mathbf{c}_{ji}\mathbf{c}_{ji} N_j = \sum_j \frac{x_j d_j c_j^2 N_j}{D}\underline{\underline{\mathrm{I}}} = \sum_j \frac{x_j d_j 2\varepsilon_j^K N_j}{D}\underline{\underline{\mathrm{I}}} = \frac{2}{D}\langle x\varepsilon^K\rangle\underline{\underline{\mathrm{I}}} \tag{4.10}$$

$$\sum_{ji} x_j \mathbf{c}_{ji}\mathbf{c}_{ji}\mathbf{c}_{ji}\mathbf{c}_{ji} N_j = \sum_j \frac{x_j d_j c_j^4 N_j}{D(D+2)}\Delta^{(4)} = \frac{4}{D(D+2)}\langle x\varepsilon^K\varepsilon^K\rangle\Delta^{(4)} \tag{4.11}$$

To proceed, the expanded form of N_{ji}^{EQ} given above is substituted into the lattice moment equations, beginning with the mass moment,

$$\sum_{ji} N_{ji}^{EQ} = \sum_{ji} N_j + \sum_{ji} N_j \frac{1}{2}\gamma_0^2 \mathbf{c}_{ji}\mathbf{c}_{ji} : \mathbf{u}\mathbf{u} - \sum_{ji} N_j \left(\alpha_2 + \beta_2 \varepsilon_j^T\right) \tag{4.12}$$

Note that moments over odd powers of the velocity vector $\mathbf{c}_{ji}$ vanish. From the definition of

the density, $\rho \equiv \sum_{ji} N_{ji}$, and application of the above relations,

$$\rho = \sum_{ji} N_{ji}^{EQ} = \langle 1 \rangle + \frac{1}{D}\gamma_0^2 \langle \varepsilon^K \rangle |\mathbf{u}|^2 - \alpha_2 \langle 1 \rangle - \beta_2 \langle \varepsilon^T \rangle \tag{4.13}$$

Grouping terms by velocity order yields two equations,

$$\rho = \langle 1 \rangle = \sum_j N_j d_j \tag{4.14}$$

$$\frac{1}{D}\gamma_0^2 \langle \varepsilon^K \rangle |\mathbf{u}|^2 - \alpha_2 \rho - \beta_2 E = 0 \tag{4.15}$$

where the definition of the internal energy per unit volume was used,

$$E \equiv \sum_j \varepsilon_j^T d_j N_j = \langle \varepsilon^T \rangle \tag{4.16}$$

Equation (4.15) requires that all the mass is retained in the zero order term.

Moving on to the mass flux (i.e. momentum) term,

$$\begin{aligned}
\rho \mathbf{u} &\equiv \sum_{ji} \mathbf{c}_{ji} N_{ji}^{EQ} \\
&= -\sum_{ji} N_j \gamma_0 \mathbf{c}_{ji}\mathbf{c}_{ji} \cdot \mathbf{u} - \sum_{ji} N_j \frac{1}{6}\gamma_0^3 \mathbf{c}_{ji}\mathbf{c}_{ji}\mathbf{c}_{ji}\mathbf{c}_{ji} \vdots \mathbf{uuu} \\
&+ \sum_{ji} N_j \gamma_0 (\alpha_2 + \beta_2 \varepsilon_j^T) \mathbf{c}_{ji}\mathbf{c}_{ji} \cdot \mathbf{u} - \sum_{ji} N_j \gamma_2 \mathbf{c}_{ji}\mathbf{c}_{ji} \cdot \mathbf{u} \\
&= -\frac{2}{D}\gamma_0 \langle \varepsilon^K \rangle \mathbf{u} - \frac{1}{6}\gamma_0^3 \frac{4}{D(D+2)} \langle \varepsilon^K \varepsilon^K \rangle (3|\mathbf{u}|^2 \mathbf{u}) \\
&+ \frac{2}{D}\gamma_0 \alpha_2 \langle \varepsilon^K \rangle \mathbf{u} + \frac{2}{D}\gamma_0 \beta_2 \langle \varepsilon^K \varepsilon^T \rangle \mathbf{u} - \frac{2}{D}\gamma_2 \langle \varepsilon^K \rangle \mathbf{u}
\end{aligned} \tag{4.17}$$

where the relation $\Delta^{(4)}(\mathbf{uuu}) = 3|\mathbf{u}|^2\mathbf{u}$ has been used. Again this gives two equations,

$$\rho\mathbf{u} = -\frac{2}{D}\gamma_0\langle\varepsilon^K\rangle\mathbf{u} \tag{4.18}$$

$$\begin{aligned} &-\frac{1}{6}\gamma_0^3\frac{4}{D(D+2)}\langle\varepsilon^K\varepsilon^K\rangle(3|\mathbf{u}|^2\mathbf{u}) + \frac{2}{D}\gamma_0\alpha_2\langle\varepsilon^K\rangle\mathbf{u} + \frac{2}{D}\gamma_0\beta_2\langle\varepsilon^K\varepsilon^T\rangle\mathbf{u} - \frac{2}{D}\gamma_2\langle\varepsilon^K\rangle\mathbf{u} = 0 \\ &\Longrightarrow -\frac{1}{D+2}\gamma_0^3\langle\varepsilon^K\varepsilon^K\rangle|\mathbf{u}|^2 + \gamma_0\alpha_2\langle\varepsilon^K\rangle + \gamma_0\beta_2\langle\varepsilon^K\varepsilon^T\rangle - \gamma_2\langle\varepsilon^K\rangle = 0 \end{aligned} \tag{4.19}$$

Equation (4.18) gives, as in the standard system,

$$\gamma_0 = -\frac{\rho D}{2\langle\varepsilon^K\rangle} \tag{4.20}$$

Proceeding to the kinetic part of the momentum flux in the momentum transport equation,

$$\begin{aligned} \underline{\underline{\Pi}}_k &\equiv \sum_{ji}\mathbf{c}_{ji}\mathbf{c}_{ji}N_{ji}^{EQ} \\ &= \sum_{ji}N_j\mathbf{c}_{ji}\mathbf{c}_{ji} + \sum_{ji}N_j\frac{1}{2}\gamma_0^2\mathbf{c}_{ji}\mathbf{c}_{ji}\mathbf{c}_{ji}\mathbf{c}_{ji} : \mathbf{uu} - \sum_{ji}N_j\mathbf{c}_{ji}\mathbf{c}_{ji}\left(\alpha_2 + \beta_2\varepsilon_j^T\right) \\ &= \frac{2}{D}\langle\varepsilon^K\rangle\underline{\underline{\mathrm{I}}} + \frac{2\gamma_0^2\langle\varepsilon^K\varepsilon^K\rangle}{D(D+2)}\left(2\mathbf{uu} + |\mathbf{u}|^2\underline{\underline{\mathrm{I}}}\right) - \frac{2}{D}\alpha_2\langle\varepsilon^K\rangle\underline{\underline{\mathrm{I}}} - \frac{2}{D}\beta_2\langle\varepsilon^K\varepsilon^T\rangle\underline{\underline{\mathrm{I}}} \\ &= P_k\underline{\underline{\mathrm{I}}} + g\rho\mathbf{uu} \end{aligned} \tag{4.21}$$

where the relation $\Delta^{(4)}(\mathbf{uu}) = 2\mathbf{uu} + |\mathbf{u}|^2\underline{\underline{\mathrm{I}}}$ has been used. The last line, as shown in equation (3.3), matches the form of the kinetic part of the momentum flux which was claimed to be expected (in Section 2.2) by analogy with the standard system, and that assumption is now

seen to be correct. Equating **uu** terms gives

$$g\rho = \frac{4\gamma_0^2\langle\varepsilon^K\varepsilon^K\rangle}{D(D+2)} \tag{4.22}$$

where the Galilean coefficient g must be equal to unity in order to recover correct hydrodynamics. This requirement gives the Galilean invariance constraint,

$$\langle\varepsilon^K\varepsilon^K\rangle = \frac{D(D+2)\rho}{4\gamma_0^2} = \frac{D+2}{D}\frac{\langle\varepsilon^K\rangle^2}{\rho} \tag{4.23}$$

which is identical to the result for the three-speed standard system. Thus the presence of a microscopic internal energy has no effect on the formal condition for Galilean invariance.

Equation (4.21) gives the kinetic part of the isotropic pressure P_k:

$$P_k = \frac{2}{D}\langle\varepsilon^K\rangle \tag{4.24}$$

In order for the pressure to be retained in the zero order velocity term (thereby avoiding a "dynamic pressure anomaly"), the following relation must also be satisfied:

$$\frac{1}{2}\rho|\mathbf{u}|^2 - \frac{2}{D}\alpha_2\langle\varepsilon^K\rangle - \frac{2}{D}\beta_2\langle\varepsilon^K\varepsilon^T\rangle = 0 \tag{4.25}$$

and the Galilean invariance condition (4.23) was used to substitute for the isotropic moment $\langle\varepsilon^K\varepsilon^K\rangle$.

From equations (4.20) and (4.23) and a little manipulation, equation (4.15) becomes

$$\frac{1}{2}\rho|\mathbf{u}|^2 - \frac{2}{D}\langle\varepsilon^K\rangle\alpha_2 - \frac{2}{D}\frac{\langle\varepsilon^K\rangle}{\rho}\beta_2 E = 0 \tag{4.26}$$

and equation(4.19) becomes

$$\frac{1}{2}\rho|\mathbf{u}|^2 - \frac{2}{D}\alpha_2\langle\varepsilon^K\rangle - \frac{2}{D}\beta_2\langle\varepsilon^K\varepsilon^T\rangle = \frac{4}{\rho D^2}\gamma_2\langle\varepsilon^K\rangle^2 \tag{4.27}$$

Comparing the last equation to equation (4.25) indicates that they can only be nontrivially satisfied if γ_2 vanishes, thus

$$\gamma_2 = 0 \tag{4.28}$$

Subtraction of equation (4.26) from equation (4.25) gives

$$\begin{aligned} &\frac{2}{D}\frac{\langle\varepsilon^K\rangle}{\rho}\beta_2 E - \frac{2}{D}\beta_2\langle\varepsilon^K\varepsilon^T\rangle = 0 \\ &\Longrightarrow \beta_2\left(\langle\varepsilon^K\rangle E - \rho\langle\varepsilon^K\varepsilon^T\rangle\right) = 0 \end{aligned} \tag{4.29}$$

The two solutions to this equation are $\langle\varepsilon^K\varepsilon^T\rangle = \langle\varepsilon^K\rangle E/\rho$ or $\beta_2 = 0$. It is expected that, at most, only one of these at a time may be physically consistent. In the limit of the standard system, $\langle\varepsilon^K\rangle = \langle\varepsilon^T\rangle = \langle\varepsilon\rangle = E$, and the first solution reduces to $\langle\varepsilon^2\rangle = E^2/\rho$. This contradicts the Galilean invariance condition (4.23), which reduces to $\langle\varepsilon^2\rangle = (1+2/D)(E^2/\rho)$. The multiphase system should collapse to the standard system in the low density limit, and it is therefore necessary to throw out the first solution and choose the $\beta_2 = 0$ solution. In

this case equations (4.26) and (4.25) both reduce to

$$\frac{1}{2}\rho|\mathbf{u}|^2 - \frac{2}{D}\alpha_2\langle\varepsilon^K\rangle = 0 \tag{4.30}$$

which may be solved for the last remaining expansion coefficient,

$$\alpha_2 = \frac{D}{4}\frac{\rho|\mathbf{u}|^2}{\langle\varepsilon^K\rangle} \tag{4.31}$$

The forms of the solutions for the velocity dependent expansion coefficients are analogous to those found for the standard system, except that it is no longer as convenient to write them as functions of temperature T. Having evaluated the terms in the mass and momentum transport equations, energy transport is considered in the next section, where the presence of microscopic internal energy plays a more explicit role.

4.2 The Energy Moment Equation

Many of the above results will be used in evaluating the terms in the energy transport equation, beginning with the moment over total microscopic energy ε_j^T:

$$\begin{aligned} W &\equiv \sum_{ji} \varepsilon_j^T N_{ji}^{EQ} \\ &= \sum_{ji} \varepsilon_j^T N_j + \sum_{ji} \varepsilon_j^T N_j \frac{1}{2}\gamma_0^2 \mathbf{c}_{ji}\mathbf{c}_{ji} : \mathbf{uu} - \sum_{ji} \varepsilon_j^T N_j \left(\alpha_2 + \beta_2 \varepsilon_j^T\right) \\ &= \langle \varepsilon^T \rangle + \frac{1}{D}\gamma_0^2 \langle \varepsilon^K \varepsilon^T \rangle |\mathbf{u}|^2 - \alpha_2 \langle \varepsilon^T \rangle - \beta_2 \langle \varepsilon^T \varepsilon^T \rangle \\ &= E + \frac{D\rho^2 |\mathbf{u}|^2 \langle \varepsilon^K \varepsilon^T \rangle}{4\langle \varepsilon^K \rangle^2} - \frac{D\rho |\mathbf{u}|^2 E}{4\langle \varepsilon^K \rangle} \end{aligned} \tag{4.32}$$

The total energy per unit volume is $W = E + (1/2)\rho|\mathbf{u}|^2$, which implies

$$\frac{D\rho^2 |\mathbf{u}|^2 \langle \varepsilon^K \varepsilon^T \rangle}{4\langle \varepsilon^K \rangle^2} - \frac{D\rho |\mathbf{u}|^2 E}{4\langle \varepsilon^K \rangle} = \frac{1}{2}\rho |\mathbf{u}|^2 \tag{4.33}$$

which may be rearranged to give

$$D\rho \langle \varepsilon^K \varepsilon^T \rangle = DE\langle \varepsilon^K \rangle + 2\langle \varepsilon^K \rangle^2 \tag{4.34}$$

Using the identities $\langle \varepsilon^K \varepsilon^T \rangle = \langle \varepsilon^K \varepsilon^K \rangle + \langle \varepsilon^K \varepsilon^I \rangle$ and $E = \langle \varepsilon^K \rangle + \langle \varepsilon^I \rangle$, this becomes

$$\begin{aligned} D\rho \left(\frac{D+2}{D} \frac{\langle \varepsilon^K \rangle^2}{\rho} + \langle \varepsilon^K \varepsilon^I \rangle \right) &= D\langle \varepsilon^K \rangle^2 + D\langle \varepsilon^K \rangle \langle \varepsilon^I \rangle + 2\langle \varepsilon^K \rangle^2 \\ \Longrightarrow (D+2)\langle \varepsilon^K \rangle^2 + D\rho \langle \varepsilon^K \varepsilon^I \rangle &= (D+2)\langle \varepsilon^K \rangle^2 + D\langle \varepsilon^K \rangle \langle \varepsilon^I \rangle \\ \Longrightarrow \langle \varepsilon^K \varepsilon^I \rangle &= \frac{\langle \varepsilon^K \rangle \langle \varepsilon^I \rangle}{\rho} \end{aligned} \tag{4.35}$$

Here another constraint has been derived, which will be referred to as the mechanical energy condition. The physical interpretation of this constraint is that all of the mechanical energy, $(1/2)\rho|\mathbf{u}|^2$, originates from the microscopic kinetic energy, ε_j^K, with no contribution from the microscopic internal energy ε_j^I. This is seen most clearly by evaluating their moments:

$$\begin{aligned}\sum_{ji}\varepsilon_j^K N_{ji}^{EQ} &= \langle\varepsilon^K\rangle + \frac{D\rho^2|\mathbf{u}|^2\langle\varepsilon^K\varepsilon^K\rangle}{4\langle\varepsilon^K\rangle^2} - \frac{D\rho|\mathbf{u}|^2\langle\varepsilon^K\rangle}{4\langle\varepsilon^K\rangle} \\ = \langle\varepsilon^K\rangle + \frac{D+2}{D}\frac{\langle\varepsilon^K\rangle^2}{\rho}\frac{D\rho^2|\mathbf{u}|^2}{4\langle\varepsilon^K\rangle^2} - \frac{D}{4}\rho|\mathbf{u}|^2 &= \langle\varepsilon^K\rangle + \frac{1}{2}\rho|\mathbf{u}|^2\end{aligned} \tag{4.36}$$

$$\begin{aligned}\sum_{ji}\varepsilon_j^I N_{ji}^{EQ} &= \langle\varepsilon^I\rangle + \frac{D\rho^2|\mathbf{u}|^2\langle\varepsilon^K\varepsilon^I\rangle}{4\langle\varepsilon^K\rangle^2} - \frac{D\rho|\mathbf{u}|^2\langle\varepsilon^I\rangle}{4\langle\varepsilon^K\rangle} \\ = \langle\varepsilon^I\rangle + \frac{\langle\varepsilon^K\rangle\langle\varepsilon^I\rangle D\rho|\mathbf{u}|^2}{4\langle\varepsilon^K\rangle^2} - \frac{D}{4}\rho|\mathbf{u}|^2\frac{\langle\varepsilon^I\rangle}{\langle\varepsilon^K\rangle} &= \langle\varepsilon^I\rangle\end{aligned} \tag{4.37}$$

It is interesting but not altogether surprising that the velocity dependence of the total energy per unit volume should be completely associated with the kinetic energy moment, while the distribution of microscopic internal energy must be constrained to be isotropic.

Finally, the last remaining moment is the kinetic part of the energy flux:

$$\begin{aligned}\mathbf{Q}_k &\equiv \sum_{ji}\mathbf{c}_{ji}\varepsilon_j^T N_{ji}^{EQ} \\ &= \sum_{ji} N_j\gamma_0\varepsilon_j^T\mathbf{c}_{ji}\mathbf{c}_{ji}\cdot\mathbf{u} - \sum_{ji} N_j\frac{1}{6}\gamma_0^3\varepsilon_j^T\mathbf{c}_{ji}\mathbf{c}_{ji}\mathbf{c}_{ji}\mathbf{c}_{ji}\!:\!\mathbf{uuu} \\ &+ \sum_{ji} N_j\gamma_0\varepsilon_j^T\left(\alpha_2+\beta_2\varepsilon_j^T\right)\mathbf{c}_{ji}\mathbf{c}_{ji}\cdot\mathbf{u} - \sum_{ji} N_j\gamma_2\varepsilon_j^T\mathbf{c}_{ji}\mathbf{c}_{ji}\cdot\mathbf{u} \\ &= \frac{\rho\langle\varepsilon^K\varepsilon^T\rangle}{\langle\varepsilon^K\rangle}\mathbf{u} + \frac{D^2\rho^3\langle\varepsilon^K\varepsilon^K\varepsilon^T\rangle}{4(D+2)\langle\varepsilon^K\rangle^3}|\mathbf{u}|^2\mathbf{u} - \frac{D\rho^2\langle\varepsilon^K\varepsilon^T\rangle}{4\langle\varepsilon^K\rangle^2}|\mathbf{u}|^2\mathbf{u}\end{aligned} \tag{4.38}$$

Using equation (4.34) to substitute for isotropic moment $\langle \varepsilon^K \varepsilon^T \rangle$,

$$\begin{aligned} \mathbf{Q}_k &= \left(E + \frac{2}{D} \langle \varepsilon^K \rangle \right) \mathbf{u} + \left(\frac{D^2 \rho^3 \langle \varepsilon^K \varepsilon^K \varepsilon^T \rangle}{4(D+2)\langle \varepsilon^K \rangle^3} - \frac{\rho D E}{4\langle \varepsilon^K \rangle} - \frac{\rho}{2} \right) |\mathbf{u}|^2 \mathbf{u} \\ &= \left(E + P_k + g' \frac{1}{2} \rho |\mathbf{u}|^2 \right) \mathbf{u} \end{aligned} \tag{4.39}$$

where the term g' is the energy Galilean invariance coefficient. It was given for the standard system by Molvig, Donis, Myczkowski, and Vichniac [12], and in the multiphase system (i.e. in the presence of microscopic internal energy) it takes the form

$$g' = \frac{D^2 \rho^2 \langle \varepsilon^K \varepsilon^K \varepsilon^T \rangle}{2(D+2)\langle \varepsilon^K \rangle^3} - \frac{DE}{2\langle \varepsilon^K \rangle} - 1 \tag{4.40}$$

This implies the following constraint in order to achieve the physically correct condition of $g' = 1$:

$$\langle \varepsilon^K \varepsilon^K \varepsilon^T \rangle = \frac{\langle \varepsilon^K \varepsilon^K \rangle}{\rho} (E + 2P_k) \tag{4.41}$$

Although the condition by which to eliminate the g' artifact has been derived, it will not be used in this work, mainly because this artifact is third order in velocity and should be small at low Mach number. In order to design a Digital Physics system with correct energy transport at Mach numbers of order unity, the constraint which removes the g' artifact would have to be satisfied via additional particle speeds and rate coefficients, as shown for the standard system by Teixeira [13].

Of greater concern for the current multiphase system is the potential artifact associated with the first order velocity part of the energy transport, namely the presence of the kinetic pressure instead of the total pressure in equation (4.39). In the liquid phase, the kinetic

pressure is much greater than the total pressure, and would dominate the energy flux in an unphysical way. There is no obvious constraint that can be satisfied via rate coefficients by which to remove this "kinetic pressure artifact." Instead, it is observed that the total pressure P includes a contribution from the momentum moment of the interaction operator. The removal of the kinetic pressure artifact must involve the energy moment of the interaction operator.

The construction of the energy piece of the non-local interaction proceeds in a fashion completely analogous to that of the momentum piece presented in Sections 2.3 and 3.1. Recalling the relevant relations derived in Chapter 2,

$$\sum_{ji} \mathcal{I}_{ji} \varepsilon_j^T = \sum_{\mathcal{P}} A_p \varepsilon_p = -\nabla \cdot \mathbf{Q}_n = \Delta_n W = \Phi \tag{4.42}$$

where the interaction rate of work Φ has been introduced (which, like the interaction force $\mathbf{F}$, is named for its units). The correct form of the total energy flux in a bulk phase is

$$\mathbf{Q} = (E + P)\mathbf{u} + \mathcal{O}(\mathbf{u}^3) = \mathbf{Q}_k + \mathbf{Q}_n \tag{4.43}$$

and in light of equation (4.39),

$$\mathbf{Q}_n = (E + P)\mathbf{u} - (E + P_k)\mathbf{u} = P_n \mathbf{u} \tag{4.44}$$

Using equation (3.10) to substitute for the non-local contribution to the pressure P_n,

$$\Phi = \nabla \cdot \left(\frac{\Gamma}{2} \psi^2 \mathbf{u} \right) \tag{4.45}$$

An energy pushing operation must be constructed such that equation (4.45) is satisfied. As with the interaction force, allowing the interaction rate of work Φ to be non-vanishing means breaking sitewise energy conservation. It is required, however, that energy is conserved globally for an adiabatic system. For this reason a scheme based on the exchange of imaginary subparticles is once again employed. It is imagined that there is another type of interacton, which carries only energy quanta instead of momentum quanta. A direction dependent scalar quantity $Y_{ji}(\mathbf{x})$ is defined as the interaction energy parameter, and represents the number of energy interactons given off by the particles at site $\mathbf{x}$ in direction ji. The number of interactons received by the particles at site $\mathbf{x}$ with direction ji must then be $Y_{ji}(\mathbf{x} - \mathbf{c}_{ji})$, and the net number of energy interactons accrued at site $\mathbf{x}$ for all directions is therefore

$$\begin{aligned} &\sum_{ji} \left[Y_{ji}(\mathbf{x} - \mathbf{c}_{ji}) - Y_{ji}(\mathbf{x}) \right] \\ &= \sum_{ji} -\mathbf{c}_{ji} \cdot \nabla Y_{ji}(\mathbf{x}) = -\nabla \cdot \sum_{ji} \mathbf{c}_{ji} Y_{ji}(\mathbf{x}) \end{aligned} \tag{4.46}$$

where a first order Taylor expansion in space was used to obtain the gradient. Comparing this expression to equation (4.45) suggests letting Y_{ji} take the form

$$Y_{ji} = \frac{\Gamma}{2} \frac{\psi^2 N_{ji}^{EQ}}{\rho} \tag{4.47}$$

and taking the net energy gain to be the negative of the net number of interactons. The local change in energy is then

$$\nabla \cdot \sum_{ji} \mathbf{c}_{ji} \frac{\Gamma}{2} \frac{\psi^2 N_{ji}^{EQ}}{\rho} = \nabla \cdot \frac{\Gamma}{2} \frac{\psi^2}{\rho} \sum_{ji} \mathbf{c}_{ji} N_{ji}^{EQ} = \frac{\Gamma}{2} \nabla \cdot \psi^2 \mathbf{u} \tag{4.48}$$

which matches the desired result. Thus a means by which to calculate the energy change at a site due to the non-local interaction has been formulated:

$$\Phi(\mathbf{x}) = \sum_{ji} [Y_{ji}(\mathbf{x}) - Y_{ji}(\mathbf{x} - \mathbf{c}_{ji})] = \sum_{\mathcal{P}} A_p \varepsilon_p \tag{4.49}$$

where the interaction energy parameter Y_{ji} is a local quantity given by equation (4.47), and is analogous to the interaction parameter ψ. Physically, the change in sign used to derive equation (4.48) implies that an energy interacton carries a quanta of work done on the particle emitting it, and work done by the particle receiving it, due to the non-local interaction; therefore the arrival of an interacton provides an energy reduction.

Equation (4.49) summarizes the calculation and implementation of the energy part of the non-local interaction needed to remove the kinetic pressure artifact and restore correct adiabatic energy transport. It is necessary to show that the sitewise energy adjustment calculated in this fashion conserves energy globally. The total energy of the system must be constant if the sum over the lattice of the interaction rate of work Φ vanishes, and this is verified by writing

$$\sum_{\mathbf{x}} \Phi(\mathbf{x}) = \sum_{\mathbf{x}} \sum_{ji} [Y_{ji}(\mathbf{x}) - Y_{ji}(\mathbf{x} - \mathbf{c}_{ji})] \tag{4.50}$$

but summing over $-\mathbf{c}_{ji}$ instead of $\mathbf{c}_{ji}$, and substituting $\mathbf{x}-\mathbf{c}_{ji}$ for $\mathbf{x}$, gives for the right-hand side

$$\sum_{\mathbf{x}-\mathbf{c}_{ji}} \sum_{-ji} [Y_{-ji}(\mathbf{x}-\mathbf{c}_{ji}) - Y_{-ji}(\mathbf{x})] = \sum_{\mathbf{x}} \sum_{ji} [Y_{ji}(\mathbf{x}-\mathbf{c}_{ji}) - Y_{ji}(\mathbf{x})] = -\sum_{\mathbf{x}} \Phi(\mathbf{x}) \qquad (4.51)$$

and therefore

$$\sum_{\mathbf{x}} \Phi(\mathbf{x}) = -\sum_{\mathbf{x}} \Phi(\mathbf{x}) = 0 \qquad (4.52)$$

As discussed in the next chapter, it turns out that interfacial regions in the multiphase system require an isothermal condition in order to remain intact. This means that in general the ability to restore correct energy transport cannot be taken advantage of, except in the case of a single phase fluid. The derivation of the energy component of the non-local interaction is nevertheless an important result because it will serve to allow correct energy transport, and therefore heat transfer capability, in future extensions of the current system which eliminate the need for the isothermal restriction. Furthermore, in Section 7.2 the validity of the energy adjustment scheme is demonstrated by measuring the soundspeed of a pure liquid, which is a function of the form of the energy flux.

4.3 Constraints and Rate Coefficients

This section looks at the last remaining expansion coefficients, those associated with the zero-velocity part of the equilibrium distribution function N_{ji}^{EQ}, namely α_0, β_0, and the other rate coefficients r_j. These parameters are functions of density ρ and internal energy

per unit volume E only, and determine the distribution of particles amongst the available species.

The number of coefficients needed is equal to the number of constraints imposed upon the energy-exchange part of the distribution function. There are four such constraints for the multiphase system as developed here: mass conservation, energy conservation, the Galilean invariance condition (4.23), and the mechanical energy condition (4.35). These four constraints can be expressed in terms of the zero-velocity distributions N_j:

$$\rho = \langle 1 \rangle = \sum_j N_j d_j \tag{4.53}$$

$$E = \langle \varepsilon^T \rangle = \sum_j N_j d_j \varepsilon_j^T \tag{4.54}$$

$$\langle \varepsilon^K \varepsilon^K \rangle = \frac{D+2}{D} \frac{\langle \varepsilon^K \rangle^2}{\rho} = \sum_j N_j d_j \varepsilon_j^K \varepsilon_j^K \tag{4.55}$$

$$\langle \varepsilon^K \varepsilon^I \rangle = \frac{\langle \varepsilon^K \rangle \langle \varepsilon^I \rangle}{\rho} = \sum_j N_j d_j \varepsilon_j^K \varepsilon_j^I \tag{4.56}$$

The true unknowns, α_0, β_0, and the r_j's, are introduced via equation (4.5), which may be rewritten as

$$n_j = \frac{N_j}{\rho} = r_j \frac{exp(-\alpha_0)}{\rho} exp\left(-\beta_0 \varepsilon_j^T\right) = r_j y z^{\varepsilon_j^T} \tag{4.57}$$

which includes the useful parameters $y \equiv exp(-\alpha_0)/\rho$ and $z \equiv exp(-\beta_0)$. Dividing equations (4.53)-(4.56) by density ρ, and using the internal energy per unit mass $u = E/\rho$, they can

be rewritten explicitly in terms of the true unknowns:

$$1 = \sum_j d_j r_j y z^{\epsilon_j^T} \tag{4.58}$$

$$u = \sum_j d_j \epsilon_j^T r_j y z^{\epsilon_j^T} \tag{4.59}$$

$$\frac{D+2}{D}\left(\sum_j d_j \epsilon_j^K r_j y z^{\epsilon_j^T}\right)^2 = \sum_j d_j \epsilon_j^K \epsilon_j^K r_j y z^{\epsilon_j^T} \tag{4.60}$$

$$\left(\sum_j d_j \epsilon_j^K r_j y z^{\epsilon_j^T}\right)\left(\sum_j d_j \epsilon_j^I r_j y z^{\epsilon_j^T}\right) = \sum_j d_j \epsilon_j^K \epsilon_j^I r_j y z^{\epsilon_j^T} \tag{4.61}$$

The key observation gleaned from this form of the system of constraints is that the rates, and therefore the zero-velocity distributions, depend only on the internal energy per unit mass u. The total number of unknowns must be four, of course, and therefore two independent rate coefficients are needed (along with y and z) to close this system. A minimum of four different species are needed, and in principle one may choose any two of these with which to associate the independent rates, although a physically acceptable solution to the system is not guaranteed and must be checked for. If there were less than four species, there would be no way to adjust the distributions to satisfy the four constraints; however there may be more than four species, indeed it is found that this is preferred. It is also apparent that at least one of the species must have both kinetic and internal microscopic energies, or equation (4.56) cannot be nontrivially satisfied. The choice of species and the solution to this system of equations will be discussed in detail in Section 6.1.

The theoretical development of the multiphase system so far is now briefly summarized. A

momentum pushing step and an energy pushing step representative of a non-local interaction have been introduced, and are to be included in the lattice update algorithm along with the usual propagation and collision steps of the standard system. The new steps break sitewise momentum and energy conservation but conserve these quantities globally. The relationship of these new steps to a new operator, the interaction operator, included in the lattice update equation has been formally derived. It was shown how the momentum and energy pushing steps influence the mean dynamical behavior of the Digital Physics system; specifically, how their presence allows the multiphase system to behave with a non-ideal-gas equation of state and an accompanying thermodynamically consistent relation for the internal energy. These attributes allow the system, in principle, to represent a vapor, a liquid, or a two-phase mixture. Calculation procedures were specified for the amount of momentum pushing needed to achieve a particular equation of state, such as a Van der Waals equation of state, and the amount of energy pushing needed to recover correct adiabatic energy transport. Finally, a system of equations for the rate coefficients was derived, which must be satisfied to eliminate artifacts and achieve correct hydrodynamics.

Chapter 5

Application to Real Flow Systems

5.1 Two Phase Flow Equations

The purpose of the method introduced here, the multiphase system, is to provide *detailed* simulation of two phase flow, including explicit representation of interfaces. This is achieved by recovering the local instantaneous field equations of two phase flow, where each lattice site represents a control volume within the flow system. Assuming there are no external influences except a body force $\mathbf{g}$ due to gravity, the standard form of these equations on a control volume basis is as follows [58]:

$$\partial_t \rho + \nabla \cdot \rho \mathbf{u} = 0 \tag{5.1}$$

$$\partial_t (\rho \mathbf{u}) + \nabla \cdot (\rho \mathbf{u}\mathbf{u}) = -\nabla P - \rho \mathbf{g} + \nabla \cdot \underline{\underline{\tau}} \tag{5.2}$$

$$\partial_t \left[\rho\left(u + \frac{1}{2}|\mathbf{u}|^2\right)\right] + \nabla \cdot \left[\left(h + \frac{1}{2}|\mathbf{u}|^2\right)\rho\mathbf{u}\right] = \xi \tag{5.3}$$

where $h = u + P/\rho$ is the enthalpy per unit mass, and ξ represents the viscous energy dissipation term (note that u is internal energy per unit mass whereas $\mathbf{u}$ is velocity). The viscous stress tensor $\underline{\underline{\tau}}$ is given by

$$\underline{\underline{\tau}} = \mu[\nabla\mathbf{u} + (\nabla\mathbf{u})^T] + \left(\eta - \frac{2}{3}\mu\right)(\nabla \cdot \mathbf{u})\underline{\underline{\mathrm{I}}} \tag{5.4}$$

where μ and η are the usual transport coefficients of shear and bulk viscosity. To form a closed system the transport equations must be accompanied by appropriate thermodynamic relations involving pressure and temperature, for example $P = P(\rho, T)$ and $T = T(\rho, e)$.

The set of equations just described is identical to that for single phase flow, because each individual phase of the two phase mixture obeys the standard fluid mechanics equations. There are, however, key attributes which distinguish two phase flow. The required thermodynamic relations must span a much wider range of conditions because the two phases coexist with very different densities and internal energies. The interfaces between phases are typically represented as boundaries of discontinuity, across which exist certain matching conditions. These "jump" conditions involve the local velocity and stress components of the fluids on either side of the interface, and may be written as $\Delta\mathbf{u} = 0$ and $\Delta P = \kappa\sigma\rho_f$,[1] where κ is the local curvature of the interface, and $\sigma\rho_f$ is the surface tension of the liquid.

When the interface is of finite volume rather than a discontinuity, the transport equations are explicitly different for two phase flow, because the zero-velocity pressure tensor $\underline{\underline{\mathrm{P}}}$ is non-

[1]The shear stress jump condition is usually zero as well, unless there are gradients in the surface tension.

isotropic in the interface, as shown in Section 3.3. Hence there are terms due to interfacial tension which vanish in the bulk phase regions but are non-zero within the interface. Replacing ∇P in equation (5.2) with $\nabla \cdot \underline{\underline{P}}$, and using equations (3.52) and (3.53), the momentum transport equation in the presence of a finite-volume interface can be rewritten as

$$\partial_t(\rho \mathbf{u}) + \nabla \cdot (\rho \mathbf{u}\mathbf{u}) = \left(-\frac{\partial P_N}{\partial n} + \frac{1}{2}\kappa\Gamma'\psi\frac{\partial^2 \psi}{\partial n^2} \right) \hat{\mathbf{n}} - \rho \mathbf{g} + \nabla \cdot \underline{\underline{\tau}} \tag{5.5}$$

In the limit that the interface thickness dn becomes small, the velocity components within the interface become equal, and the jump condition $\Delta \mathbf{u} = 0$ is recovered. Moreover, the divergence of the pressure tensor $\nabla \cdot \underline{\underline{P}}$ within the interface vanishes, thus

$$\frac{\partial P_N}{\partial n} = \frac{1}{2}\kappa\Gamma'\psi\frac{\partial^2 \psi}{\partial n^2} \tag{5.6}$$

Integrating across the interface and using equation (3.50),

$$\Delta P = \int_{INT} \frac{1}{2}\kappa\Gamma'\psi\frac{\partial^2 \psi}{\partial n^2} dn = \kappa\sigma\rho_f \tag{5.7}$$

where $P = P_N$ is the scalar pressure in a bulk phase. Hence the correct jump condition for the normal stress at the interface is also recovered as expected. If the profile of the interaction parameter through the interface, $\psi(n) = \psi[\rho(n), u(n)]$, is a function only of the thermodynamic state of the system and not the flow conditions, then equation (5.7) predicts a material surface tension coefficient. Terms related to the interfacial tension must also be included in the energy transport equation for a finite-volume interface (the analysis is beyond

the scope of this work).

The ability of the current method to recover the equations of two phase flow is now summarized. The Euler (non-viscous) portions of the transport equations for the bulk phases of the multiphase system were detailed in Chapter 4, where it was shown how correct hydrodynamic transport is obtained at the Euler level (first order expansion in Knudsen number). At present an isothermal condition, discussed in the next section, is used whenever interfaces are present. Section 6.3 shows that the multiphase system recovers the correct form of the viscous stress tensor. Section 3.1 showed how an empirical thermodynamic relation for the pressure of each phase is achieved in the multiphase system by dynamically calculating the interaction parameter ψ used in the non-local momentum exchanges between nearest neighbors. The other necessary thermodynamic relation, derived in Section 3.2 and referred to as the internal energy relation, is achieved by dynamically adjusting the particle distributions through energy-exchange collisions, detailed in Sections 6.1 and 6.4.

Despite the fact that the interface will have finite volume, an important question is whether the physics of the jump conditions normally employed for interfaces is properly captured. The velocity jump condition appears trivial; however, it has been found that generally it is not met, instead there are so-called spurious velocities which can also influence the dynamics of the vapor phase. As it happens this is not important for simulations where the vapor may be considered essentially void space; then the interface is a free surface and the velocity matching conditions are meaningless. On the other hand the matching condition for the normal stress component (which is the scalar pressure P) involving surface tension is critical. The existence of interfacial tension due to the non-local interaction and its effect on

momentum transport was discussed in Section 3.3. In Section 7.7 it is verified that surface tension is observed and has the correct effect on pressure.

As noted repeatedly the interface in the multiphase system is not a discontinuity, instead it is a region of lattice sites over which there is a steep variation in local density. It is desirable to have the thickness of this interfacial region as small as possible, since physically this length should be small compared to any other characteristic length in the flow system. When this is achieved, the density gradient through the interface is necessarily very large, particularly if the ratio of densities between the phases is large. In the presence of such gradients the basic assumptions of slowly varying macroscopic quantities used in deriving the lattice transport equations are not necessarily valid. There are, therefore, some fundamental issues concerning the prediction of local properties within the interfacial region. From the viewpoint of hydrodynamic simulation this may have limited relevance, since the interface will typically be a very small fraction of the system volume.

5.2 Basic Limitations

There are many applications for two-phase flow modeling, involving a wide range of flow systems, fluid substances, and physical phenomena. As just described, the bulk phases of a two-phase flow obey the Navier-Stokes equations just like single-phase flow, but the interface position is in general a complicated function of space and time. Hence many physical features in addition to those of single phase flow may come into play. These include buoyancy forces on the low density phase, surface tension effects, mass transfer between phases, nucleation

of one phase from the other, a host of heat transfer phenomena, and different interactions of each phase with solid boundaries. The spatial distribution of the phases in the two phase mixture, which in flow through a conduit is known as the flow regime, heavily influences the relative importance of and interactions between all of these effects.

A benefit of using a microdynamical system to model complex flows such as a liquid/vapor mixture is that the interface evolves naturally, and may become arbitrarily complex in shape without extreme degradation of accuracy or computational performance. The same benefit applies to arbitrary geometry of solid boundaries. By building upon the concepts introduced in this project, there is the potential for developing Digital Physics methods which can correctly capture the fluid flow phenomena essential for the study and modeling of important problems, such as two-phase pressure drop and heat transfer behavior in various flow regimes, and prediction of flow regime transitions. However, the multiphase system as introduced in this work is not yet suitable for accurately reproducing all of the behavior in two-phase flow systems of practical interest. This is due to several limitations of the current implementation. First is the isothermal condition, and thus the inability to properly model heat transfer. Second is an upper limit of liquid to vapor density ratio of about 200. Third is the over-simplified boundary condition at fluid-solid interfaces. Fourth is practical limits on system size and simulation time, which provide upper limits to the fundamental dimensionless flow quantities such as the Reynolds number.

The isothermal requirement stems from the observation that the interface tends to dissolve in the presence of normal (adiabatic) energy transport. This is a strong indication that the microdynamics of the interface are not correct, and that the theory relating the macro-

scopic bulk phase properties to the non-local microdynamical operations is not adequate within the interfacial region. The most likely source of the problem is that the additional free energy which should exist in the interface due to the presence of a density gradient is being ignored (as mentioned in Section 3.2). Providing this excess free energy may require some sort of simultaneous mass, momentum, and energy diffusion process in the interface, essentially a further generalization of the non-local momentum and energy exchange operations introduced in this work. Some observations which suggest this conjecture have been made in the course of this work. For now it is noted that, as seen in the results of the experiments presented in Chapters 7 and 8, the bulk phases appear to be well behaved and to have macroscopic properties close to those predicted by the preceding analyses. Thus the multiphase system has been relegated to a constant temperature condition, for which the precise algorithm is described in Section 6.4, and one must proceed with caution when measuring macroscopic quantities such as velocity in and near the interface.

The liquid to vapor density ratio limit exists because one begins to observe steady-state "flip failure" in the interfacial region when the density ratio is greater than about 200. Flip failure means that the required momentum (and/or energy) adjustment at a given site cannot be accomplished; the way in which flip failure is handled microdynamically is discussed in Section 6.4. The presence of a sufficient fraction of flip failure is observed to alter the pressure of the system, and therefore the density ratio and all other properties. Persistent flip failure threatens to sabotage the flow dynamics, even beyond any thermodynamic effects, because the amount of flip failure will be a function of local velocity and interface orientation. It is thought that flip failure at large density ratio could be avoided by manipulating the structure

of the vapor side of the interface so as to provide a smoother transition in density between the bulk vapor and the interior of the interface, but a suitable means by which to do this has not been devised[2]. The solution to this problem is likely related to the previous one - the additional piece of microdynamics with which to include and adjust the excess free energy of the interface should also allow adjustment of the interfacial density profile.

The solid boundary issue refers to the fact that no attempt has been made to account for the physics of the interactions of the separate phases with a solid surface. This would be an important influence in, for example, flow of a two-phase mixture through a porous medium. It is likely that issues involving liquid-solid versus vapor-solid interactions, such as wettability and contact angle, could be approached through a further theoretical treatment of the non-local operations near a solid. For example, the interaction parameter ψ attributed to a solid site during the calculations for a fluid site could be somehow adjusted to properly account for true energies of interaction between particular solid and fluid phases.

As regards system size, the code used in this thesis is a 2D version of the method, meant for proof-of-principle, not large simulations. Indeed the performance of the present "lab-scale" code is vastly slower than what would be possible with an optimized version running on a commercial-strength computer. Instead it is worthwhile to consider the simulations that could be done with an "engineering-scale" multiphase system, defined as a 3D, optimized implementation of the algorithms introduced here. Based on current commercial Digital Physics capabilities [59], it is estimated that a single 300 MHz processor would provide a

[2]Schemes such as altering the size of the neighborhood over which the non-local interactions are calculated have been attempted.

performance of $5(10^4)$ voxel - time steps per second. This assumes that a voxel - time step in the multiphase system takes twice as long as for the standard system; this is based mainly on the increased size of the collision list. It is interesting that the non-local momentum and energy exchange steps of the multiphase system, detailed in Section 6.4, are typically very fast relative to the rest of the update procedure. The reason is that at any given time, most of the system consists of bulk phases with uniform properties, where the instantaneous values of the interaction force are very small (indeed they arise only through the fluctuations), hence very few momentum (and energy) exchanges are required. Apparently this is an advantage of the mean field theory approach of this method.

Returning to the issue of practical system sizes, let us assume a 32 processor machine. Then if one is willing to wait one week for simulation results which require 10000 time steps (a generous number), then the system size can be on order 10^8 voxels (i.e. lattice sites). This would allow, for example, a tube of diameter $\tilde{D} = 200$ and length $\tilde{L} = 3000$, or one with $\tilde{D} = \tilde{L} = 500$ lattice sites.

5.3 Multiphase Fluid Properties

This section describes the ranges of fluid properties which may exist in the multiphase system, which eventually must be related to the physical world through the dimensionless quantities which govern a particular two-phase flow system. The fluid properties and flow parameters generally of interest are shown in Table 5.1. Also given for each is the approximate range of values attainable in the multiphase system (in lattice units); these ranges apply to both

Property	Symbol	Approx. Range (lattice units)
density	ρ	10^5–10^{10}
velocity magnitude	$\|\mathbf{u}\|$	0–0.3
kinematic viscosity	ν	0.005–0.2
gravitational constant	g	0–1
liquid soundspeed	c_s	1–3
surface tension coefficient (divided by liquid density)	σ	0.07–0.23

Table 5.1: Fluid and flow properties in the multiphase system.

liquid and vapor. Their meaning in terms of standard dimensionless numbers will be explored shortly.

The lower limit on density of (10^5) was determined experimentally and assures equilibration of the state populations through the collision process (particularly for the vapor where some microstates carry only a small fraction of the particles at a site). The upper limit of $(10)^{10}$ corresponds (roughly) to 32-bit microstates. Macroscopically the absolute lattice densities are unimportant because they cancel out of relevant dimensionless quantities. The maximum flow speed of 0.3 is based on the low Mach number requirement (for the vapor) and on stability (for the liquid). The lower limit of 0.005 for the kinematic viscosity, achieved by collisional over-relaxation (a microdynamical process discussed later), is based practically on stability, but more fundamentally on the notion that it is undesirable to have a viscosity so small that the system attempts to form flow structures within a single cell which cannot be realized. The upper viscosity limit of 0.2 just reflects the natural value of the system, in the absence of over-relaxation; it could be raised if desired by collisional under-relaxation. Each of the above constraints is a property only of the microdynamics; the next chapter

looks in detail at the collision operation and issues of stability.

From a microdynamical view the gravitational constant, an external body force, could range from zero to order unity. However, there is also an important macroscopic consideration - the action of gravity should not cause unphysically large density variation with height due to compression. This restriction will be quantified later, but it essentially introduces the liquid soundspeed c_s as another important property. Details of soundspeed calculation are given in Section 7.2; the range listed (1-3) corresponds to systems with liquid to vapor density ratios 10-100. The last property is the coefficient of surface tension (divided by liquid density) σ, which is a function of the equation of state of the system through the interaction parameter ψ. The range given, $0.07 - 0.23$, corresponds to the observations presented in Section 7.7, again for systems with density ratios 10-100. In the multiphase system the surface tension increases with equilirium density ratio (i.e. decreases with temperature) which is physically correct.

In the conversion from lattice units to real units, one employs the concept that the behavior of a system depends entirely on a particular set of dimensionless quantities. The required set of dimensionless quantities varies for different physical systems, or may even vary for different values of quantities within the same system. The idea is that for some cases of interest, the simulation method can correctly reproduce all of the necessary dimensionless quantities, thereby accurately mimicking the dimensionlessly equivalent physical system.

5.4 Motion of a Rising Bubble

The ability of the multiphase system to achieve the correct values for a set of dimensionless quantities must be discussed in the context of a specific flow scenario. Given the various constraints and limitations discussed above, an application for which the engineering-scale multiphase system would be particularly suitable is the study of bubbles rising in a column of liquid. Furthermore, bubble dynamics may be studied qualitatively with the present 2D implementation. One advantage of this system is the existence of a substantial amount of experimental work and analysis[3]. Another advantage is that a lot of interesting physics takes place even at low and moderate bubble Reynolds numbers, due to the interaction between drag and deformation of the bubble, and the interactions between bubbles.

The dynamics of a rising bubble are governed by the locally varying competition between inertial forces, viscous forces, buoyancy forces, and surface tension forces. The problem of interest is to determine for a single bubble, in an infinite medium with no net flow, how the terminal bubble velocity U_b varies with bubble volume V_b, and with fluid properties such as surface tension per unit density σ and liquid kinematic viscosity ν. The physical mechanisms at work may be described as the buoyancy of the bubble, the inertia of the bubble, the drag on the bubble, and the deformation of the bubble as controlled by surface tension. A sufficient set of dimensionless quantities which characterize this system are the bubble Reynolds number Re, the Eotvos number Eo, and the Morton number (or property

[3]In two phase flow experiments, most investigators use a *two component* two phase system such as air and water, and these results are typically applied to *single component* two phase systems, under the assumption that the only difference in the flow mechanics will be due to differences in fluid properties. The same assumption will be made here, though in the other direction.

group) M, defined as:

$$Re \equiv \frac{U_b d_e}{\nu} \tag{5.8}$$

$$Eo \equiv \frac{g d_e^2}{\sigma} \tag{5.9}$$

$$M = \frac{g \nu^4}{\sigma^3} \tag{5.10}$$

where the equivalent bubble diameter d_e is used,

$$d_e \equiv \left(\frac{6 V_b}{\pi} \right)^{1/3} \tag{5.11}$$

It has been assumed that the liquid to vapor density ratio is sufficiently large that the vapor density may be neglected in the buoyancy terms. There are several other dimensionless numbers commonly employed to describe bubble rise, including bubble drag coefficient C_D, Weber number We, and Froude number Fr, all of which may be formed by combinations of the above three quantities. In particular the drag coefficient is often useful, and is given by

$$C_D = \frac{4}{3} \frac{g d_e}{U_b^2} \tag{5.12}$$

which is obtained by equating the buoyancy force to the drag force for a bubble at terminal velocity,

$$V_b g = \frac{1}{2} A_b U_b^2 C_D \tag{5.13}$$

where the projected area of the bubble is taken to be $A_b = \pi d_e^2 / 4$.

The following is a brief summary of bubble rise velocity behavior based on a survey of

Temp. (C)	ν	σ	$M = g\nu^4/\sigma^3$
20	$1.0(10^{-6})$	$7.3(10^{-5})$	$2.5(10^{-11})$
250	$1.3(10^{-7})$	$3.3(10^{-5})$	$7.8(10^{-14})$

Table 5.2: Key properties of low and high temperature water.

the literature [60, 61, 62, 63, 64]. In order to provide quantitative illustrations, the "wave analogy" correlation proposed by Mendelson [65] and extended by Jamialahmadi, Branch, and Müller-Steinhagen [66] has been adopted, because it is simple and fits experimental data in the literature quite well (details of the wave analogy are given in Appendix B). The correlation gives the rise velocity as a function of equivalent diameter and fluid properties. With some manipulation this essentially allows determination of one dimensionless quantity, such as bubble Reynolds number, as a function of two others, such as Morton number and Eotvos number.

Two systems of practical interest are considered, water at low temperature (20 C) and high temperature (250 C). The significant differences between them for purposes of this analysis are that the high temperature water has a smaller viscosity by about a factor of eight and and smaller surface tension by about a factor of two. Table 5.2 lists values from the standard Steam Tables of kinematic viscosity ν and surface tension over density σ for water at these two temperatures; it also lists the resulting Morton numbers. The predicted terminal bubble rise velocity in a liquid of infinite extent, U_b, as a function of equivalent diameter d_e, calculated from the wave analogy correlation, is plotted in Figure 5.1 for water at 20 C and 250 C. Also shown are corresponding Reynolds numbers. The rise curve for 20 C water is replotted in Figure 5.2 with some additional details explained below.

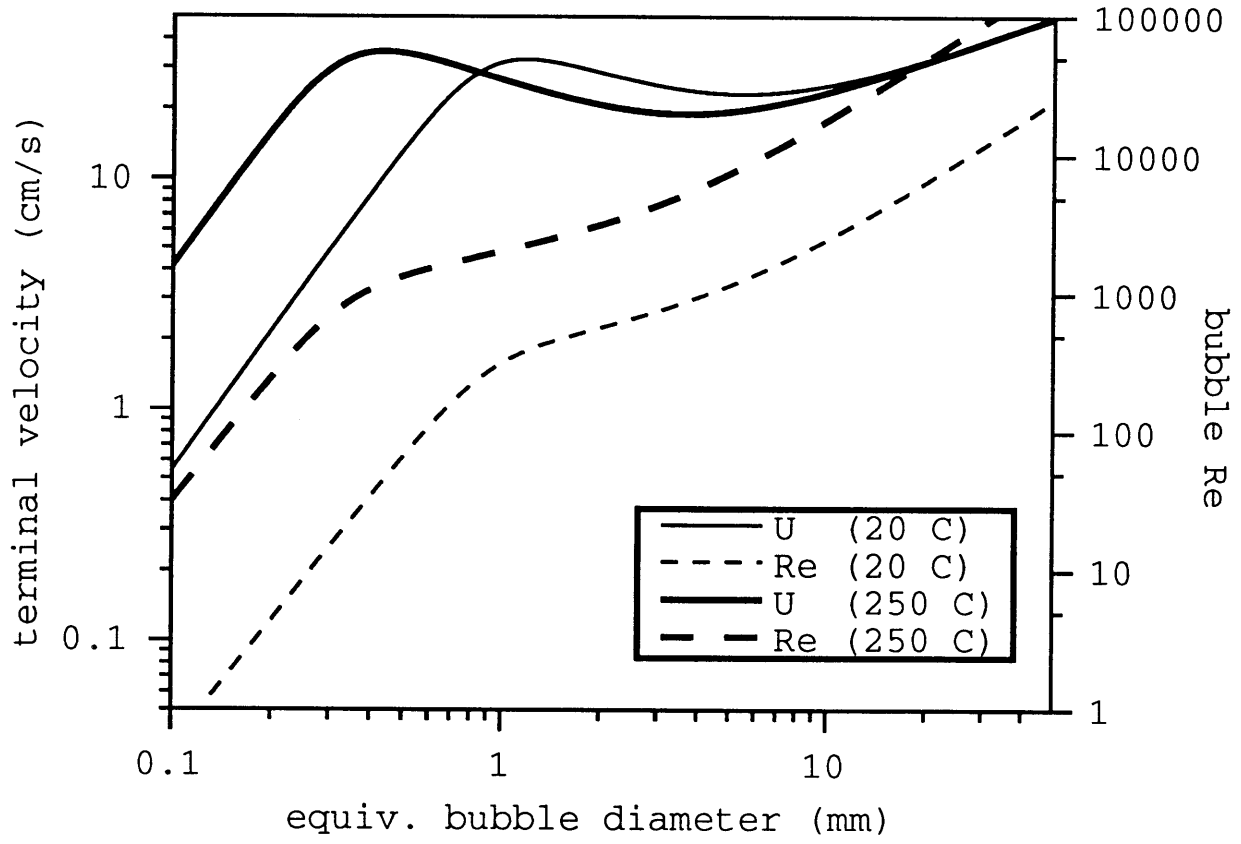

Figure 5.1: Bubble rise behavior for low-temperature water (20 C) and high-temperature water (250 C) based on the wave analogy correlation.

When a bubble is very small it is spherical and rises slowly, and buoyancy and viscous forces dominate the behavior. For a "solid" bubble where the surface is not free to move, the drag is equivalent to that of Stokes flow past a sphere [67], $C_D = 24/Re$, whereas for a "fluid" bubble internal circulation requires a correction (due to Hadamard [68]). Most systems contain contaminants which accumulate at the surface, resulting in solid bubbles. The range of small spherical bubbles will be called region I; this region is defined as obeying Stokes equation (to within five percent), shown as the light dashed line in Figure 5.2. For low temperature water, region I includes bubbles with diameters of up to about 0.5 mm, for which $Re \cong 70$. For high temperature water region I extends only to bubble diameters of

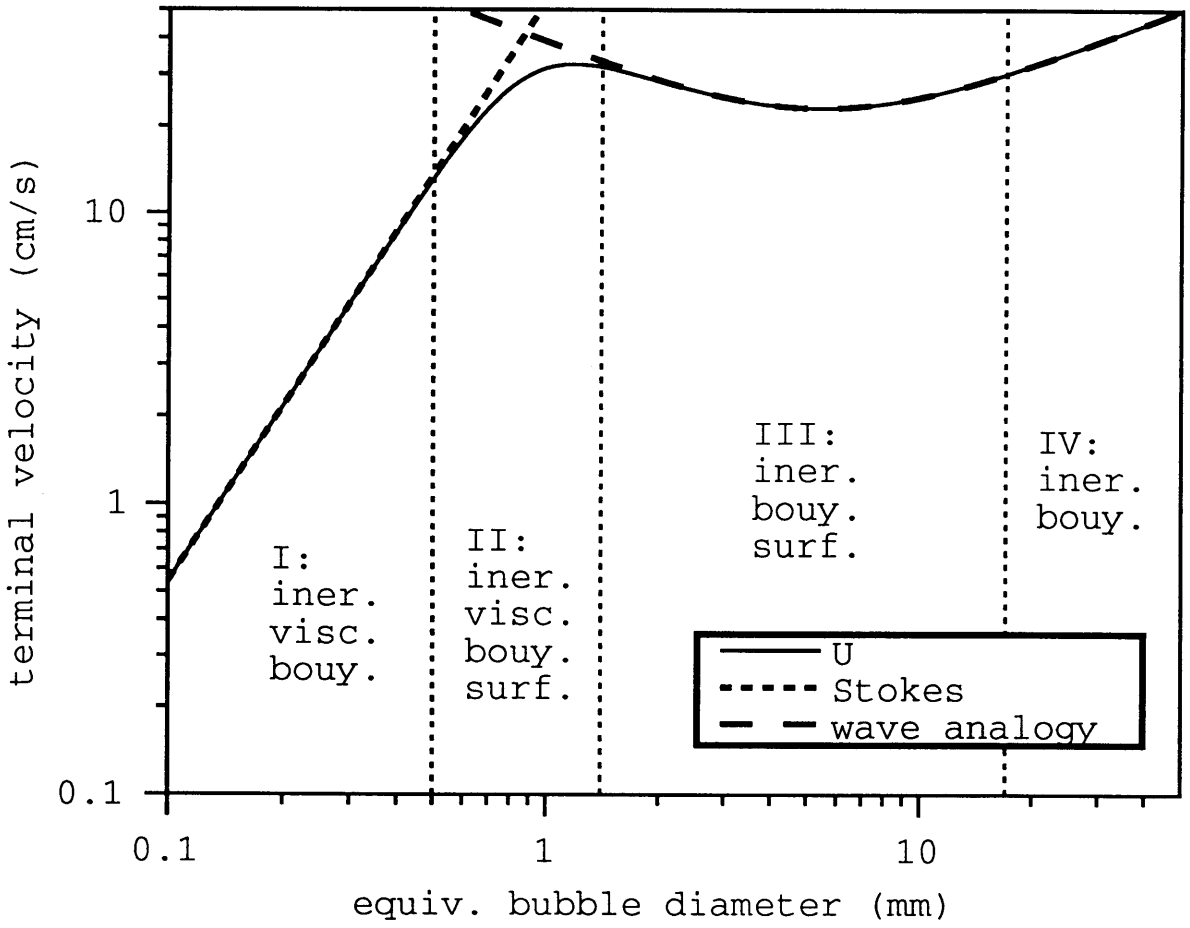

Figure 5.2: Bubble rise behavior for 20 C water showing various regions of the characteristic rise curve.

about 0.2 mm, for which $Re \cong 250$.

For somewhat larger bubbles, increased velocity leads to increased drag and the bubble deforms to become an oblate ellipsoid. The amount of deformation depends on the relative strength of the surface tension forces to the other forces. For still larger bubbles, the drag becomes controlled entirely by bubble shape. At this point viscous forces no longer play a role, so the behavior is essentially independent of Reynolds number. The heavy dashed line in Figure 5.2 is the "wave" piece of the correlation, and indicates the part of the curve where

viscous forces are not significant.

The range of bubble diameters where all of the forces are important, in between the purely Stokes and purely wave pieces of the velocity plot, will be called region II. The boundary between region II and region III is calculated based on five percent error between the total velocity and just the wave piece. In the low temperature system region II is (in mm) $0.5 < d_e < 1.4$, with Reynolds number in the range $70 < Re < 450$; for the high temperature system region II is $0.2 < d_e < 0.5$ and $250 < Re < 1300$. Within region II, the velocity reaches a maximum and then decreases with bubble diameter; for a fluid with lower viscosity this maximum is more pronounced, whereas a much more viscous fluid would not exhibit the maximum at all.

For very large bubbles, the ellipsoid shape gives way to a spherical cap. The drag becomes constant, and the velocity increases as the square root of the equivalent diameter. That surface tension no longer plays a role can be understood physically to mean that the bubble cannot deform any further. The transition from region III to region IV is taken to occur when the $U_b \sim \sqrt{d_e}$ relationship is realized to within five percent error. For low temperature water, region III is $1.4 < d_e < 16.8$ and $450 < Re < 5100$, while for high temperature water the ranges are $0.5 < d_e < 11$ and $1300 < Re < 20000$. In region III the bubble velocity passes through a minimum, then begins to increase once again with bubble size as deformation becomes more difficult and the shape approaches a spherical cap. The dependence of velocity on volume to the one sixth power in region IV is the well known result of Davies and Taylor [69].

To summarize the analysis given above, Table 5.3 lists the values of equivalent bubble

region	20 C water			250 C water		
boundary:	I-II	II-III	III-IV	I-II	II-III	III-IV
d_e (mm)	0.50	1.4	17	0.20	0.5	11
Re	70	450	5100	250	1300	20000
Eo	0.034	0.26	38	0.012	0.074	36

Table 5.3: Summary of bubble size regions.

diameter, Reynolds number, and Eotvos number which occur at the boundaries between the four identified regions, for both 20 C and 250 C water. These regions are also identified in Figure 5.2, along with the forces that control the bubble rise velocity within each region. An important conclusion is that except for very small bubbles, rise velocity does not depend on Reynolds number, since viscous forces do not have a significant effect in regions III and IV. More specifically, the behavior of bubbles in these regions is determined by a relationship between just two dimensionless quantities, neither of which contain viscosity, such as Eotvos number Eo and drag coefficient C_D. Indeed the wave piece of the wave analogy correlation, which describes regions III and IV, can be written explicitly as a relationship between Eo and C_D (as shown in Appendix B).

Some additional comments about rising bubbles are in order. It is commonly observed that they tend to develop a horizontal velocity component and trace out a zigzag or helical path, even in the absence of net liquid flow. This is surmised to be due to the influence of the wake, which experiences Karman vortex shedding [70]. A steam bubble in water is actually at a slightly higher temperature than the surrounding liquid, even when the liquid is at the saturation temperature, because the pressure of the steam is higher than that of the liquid due to surface tension. This is important in understanding the nucleation of bubbles at a

hot surface, and is not accounted for in the multiphase system with its isothermal condition. Of course for air bubbles in water there is no such temperature difference, and in any case it should not directly affect the bubble velocity. It is shown later (Section 7.7) that vapor bubbles in the multiphase system are in fact at an elevated pressure compared to the liquid, and the pressure difference is used to measure the surface tension according to Laplace's Law.

For bubbles rising in a container such as a tube of diameter D, there is the additional physical mechanism of wall shear, the effect of which will depend on the dimensionless quantity d_e/D. As this ratio increases, the shear causes the bubble to rise more slowly; for $(d_e/D) > 0.6$ [5] it becomes a "Taylor bubble," and slug flow exists[4]. When many bubbles are present, they will affect each others motion in complicated ways and tend to coalesce. The influence of the presence of many bubbles is often expressed using the void fraction α, which is the time-averaged fraction of cross-sectional area occupied by vapor. As void fraction increases, bubble agglomeration occurs more quickly, and for $\alpha > 0.25$ [4] slug flow occurs.

Finally, for vapor bubbles rising in a flowing liquid, the velocity profile of the liquid is important in determining the behavior of a single bubble and the "phase distribution" when many bubbles are present. If the flow is vigorous enough then turbulent forces become important as well because they cause breakup of large bubbles, allowing a "dispersed bubble" flow regime to exist with void fractions up to $\alpha \cong 0.5$ [4]. Therefore the Reynolds number

[4]In slug flow, bullet nosed cylindrical bubbles which nearly fill the tube rise along with slugs of liquid between them, while a thin layer of liquid flows down around them.

of the liquid is very important for general two-phase bubbly flow.

5.5 The Multiphase System Applied to Bubbles Rising in Water

Returning to the problem of just a single bubble rising in a stagnant liquid, one can attempt to find sets of simulation parameters which are dimensionlessly equivalent to the low and high temperature water systems. In the process of matching the relevant dimensionless quantities, it is often necessary to refer to dimensional quantities which have both a "lattice" and a "real world" representation. When needed to avoid ambiguity, the notation $\tilde{x}$ will be used to refer to a variable in the lattice world, as opposed to just x for the real world. The dimensions of the former are always lattice cells, time steps, and particle mass. Naturally these correspond to length, time, and mass[5]. Unless otherwise noted the dimensions of real world quantities are always in SI units (meters, seconds, and kilograms).

The purpose of this analysis is to find values of lattice gravitational constant $\tilde{g}$, liquid viscosity $\tilde{\nu}$, and surface tension per unit density $\tilde{\sigma}$ which will give a lattice bubble velocity $\tilde{U}_b$ and a lattice equivalent bubble diameter $\tilde{d}_e$ that are within acceptable ranges for the multiphase system. The first three of these are properties which are fixed for a specified system, while the latter two are the dependent and independent variables of interest in a bubble rise experiment.

[5]Explicit lattice temperature units are not needed, since the lattice temperature may always be scaled by the universal gas constant R to give $\tilde{R}\tilde{T}$, which has units of (length/time)^2.

It is convenient to introduce the following formalism: a starred quantity x^* is the ratio of a lattice variable $\tilde{x}$ in lattice units to a real variable x in SI units. Then for any dimensionless number that is to be matched for the real and lattice systems, the same combination of starred quantities must be equal to unity. Taking the Eotvos number for example,

$$Eo = \frac{g d_e^2}{\sigma} = \frac{\tilde{g}\tilde{d}_e^2}{\tilde{\sigma}} \Longrightarrow \frac{g^*(d_e^*)^2}{\sigma^*} = 1 \tag{5.14}$$

The Morton number M is often used in correlating bubble rise data [62, 63] because it involves only the fluid properties. From the form of the Morton number, one may write

$$g^*(\nu^*)^4/(\sigma^*)^3 = 1 \tag{5.15}$$

which may be combined with equation (5.14) and solved for d_e^* to give

$$d_e^* = (\nu^*)^2/\sigma^* \tag{5.16}$$

From the form of the Reynolds number,

$$U_b^* = \nu^*/d_e^* = \sigma^*/\nu^* \tag{5.17}$$

The quantities d_e^* and U_b^* may be written simply as d^* and U^*, since they represent the length and velocity conversions applicable to any length and velocity comparison between the lattice system and the real system it is intended to represent. Another useful quantity is the time conversion $t^* = d^*/U^*$.

For the high temperature water system, the information from Tables 5.1 and 5.2 implies that the possible ranges of ν^* and σ^* are $3.8(10^4) < \nu^* < 1.5(10^6)$ and $2.1(10^3) < \sigma^* < 7.0(10^3)$ for water at 250 C. From equation (5.16) this gives a range of length conversions of $1.1(10^9) < d^* < 2.1(10^5)$, which means that the largest real value a lattice unit can represent is $1/[2.1(10^5)]$ meters or about 5 microns! Surely a requirement of 2000 cells per centimeter prohibits a practical bubble rise system. Moreover, the time conversion for this system would be $t^* = d^*/U^* = (\nu^*)^3/(\sigma^*)^2 \cong 10^6$ time steps per second, which is prohibitively slow. Hence it is quite troublesome to match all three dimensionless quantities (Re, M, Eo) for the case of water at 250 C.

The situation improves considerably for water at 20 C. Taking $\tilde{\sigma} = 0.17$ (which corresponds to the nominal system with density ratio $r_\rho = 40$), and the minimum viscosity $\tilde{\nu} = 0.005$, gives $\sigma^* = 2.3(10^3)$ and $\nu^* = 5.0(10^3)$. Hence $g^* = 2.0(10^{-5})$, and the lattice gravity must be set to $\tilde{g} = 2.0(10^{-4})$ (which is within acceptable range). The length conversion is now $d^* = 1.1(10^4)$, or about 110 cells per cm, which is quite reasonable. The velocity conversion is $U^* = \sigma^*/\nu^* = 0.46$ (or $U^* = \sqrt{d^* g^*}$ which gives the same result). This implies that the maximum lattice velocity of 0.3 corresponds to a real velocity of 0.65 m/s. Also, the time conversion is $t^* = 1.1(10^4)/0.46 = 2.4(10^4)$ time steps per second.

Figure 5.1 shows that the rise velocity does not exceed about 0.3 m/s until the bubble is greater than 2 cm; for large bubbles $U_b \cong \sqrt{g d_e}$ [69]. Thus the largest bubble that could be represented without exceeding the maximum lattice velocity of 0.3 (when there is no net liquid flow) is $d_e = U_b^2/g = 4.3$ cm; this bubble has an equivalent diameter of about 500 cells. Assuming a simulated tube of $\tilde{D} = \tilde{L} = 500$, the bubble would fill the tube and would

therefore be a "Taylor bubble" and rise with a slug flow velocity that is substantially smaller than the infinite media velocity. Therefore even larger tubes and Taylor bubbles could be used without exceeding the maximum lattice velocity.

On the other end of the size scale, very small bubbles in the multiphase system cannot support the interface, which tends to be about 4-5 cells thick. The minimum lattice bubble diameter was found experimentally to be about 12 lattice units, which is about 1.1 mm according to the above length conversion. It is therefore expected that the engineering-scale multiphase system could simulate single bubbles rising in low temperature water with a range of equivalent diameters $1.1 < d_e < 43$ mm. The preceding analysis shows that to adjust this range towards simulation of smaller bubbles, one merely needs to raise the lattice viscosity from its minimum value.

The fact that the identified range of bubble sizes is nearly beyond region II for low temperature water, and well beyond it for high temperature water, suggests a reevaluation of the high temperature water case in such a way as to neglect the viscous forces. Ignoring ν^* (i.e. not matching Reynolds number) provides an additional degree of freedom, for example the length scale conversion can now be set to that of the low temperature water system: 110 cells per cm, or $d_e^* = 1.1(10^4)$. Again using $\tilde{\sigma} = 0.17$ gives $\sigma^* = 5.2(10^3)$, and equation (5.14) leads to $g^* = 4.3(10^{-5})$. The conversion from lattice to real velocity is found to be $U^* = \sqrt{d^* g^*} = 0.69$, so the maximum real velocity is $0.3/0.69 = 0.44$ m/s. This occurs for a bubble with $d_e = 1.9$ cm; hence the expected simulation range for high temperature water is $1.1 < d_e < 19$ mm.

The minimum bubble size, due once more to the minimum lattice bubble diameter of

12 cells, is large enough to justify the assumption that viscous forces can be neglected (see Table 5.3). The real viscosity represented by this system can still be determined. From equation (5.17), $\nu^* = d^* U^* = 7.6(10^3)$, and assuming the "best" lattice viscosity of $\tilde{\nu} = 0.005$, the real viscosity is $\nu = 6.6(10^{-7})$ m^2/s. According to Table 5.2 this is five times too high for water at 250 C. Thus the Reynolds number of the simulation in this formulation will be too low by a factor of five, but it will not affect the (no flow) single bubble rise simulations.

On the other hand the Reynolds number will matter for simulation of a system with many bubbles, or one where the liquid is flowing (or both). Viscous forces will be important in bubble interactions, because now the behavior of the wakes of the bubbles is very significant. When there is net flow of the system through a tube, the liquid velocity profile depends on the Reynolds number of the liquid and strongly affects the trajectories and shapes of bubbles, and hence the phase distribution (e.g. wall-peak or core-peak bubble pattern). Viscous stresses will also be of primary importance in the breakup of bubbles due to turbulence at high enough Reynolds numbers[6].

Some conclusions can be drawn from the above discussion. For high temperature water, the multiphase system can achieve the correct density ratio, but cannot achieve the correct dimensionless representation of inertial, viscous, surface tension, and buoyancy forces simultaneously with a practical system size. Basically the reason is that the Morton number $M = g\nu^4/\sigma^3$ of water at 250 C is very small, $M = 7.8(10^{-14})$, and to achieve this in a simulation the strength of gravity must be lowered so much that the length and velocity

[6]The liquid Reynolds number is typically incorporated into a mixture Reynolds number [4], $Re_M = DU_M/\nu$, where mixture velocity $U_M = U_L(1-\alpha)+U_G\alpha$, U_L is the mean liquid velocity, and U_G is the mean vapor velocity (which will be the mean liquid velocity plus the mean bubble rise velocity).

scales are sacrificed. One approach is to compromise the viscosity, which is appropriate for a bubble with diameter greater than a half millimeter rising in infinite media. Another possibility would be to find a way to increase the lattice surface tension (or lower lattice viscosity, which may not be desirable for other reasons).

For low temperature water, the multiphase system can achieve all three correct dimensionless quantities (Re, Eo, and M), with a length scaling of about a hundred cells per centimeter, which is appropriate for rising bubbles and perhaps other flow scenarios as well. Moreover, when the bubble Reynolds number is correct then the liquid (and mixture) Reynolds numbers must also be correct. Naturally the quantities d_e/D and void fraction α must be correct as well since length and velocity scale linearly. This implies that the engineering-scale multiphase system can be expected to accurately capture many of the key physical mechanisms that govern bubbly two-phase flow of water at room temperature. However, several caveats must be mentioned.

First, the density ratio is incorrect; fortunately this is not important for flow systems where the vapor may be represented as void space, and the density ratio need only be large enough to provide this approximation. This certainly is not the case when the stresses of the vapor on the liquid at the interface are important. Second, Reynolds number is limited by available computational power, as in any simulation method. The largest achievable value in the multiphase system is $Re = D(0.3)/(0.005) = 60D$, and D will depend on the system size that can be simulated in a reasonable amount of time. Third, the thickness of the interface is not negligible, especially for small bubbles, which could influence void fraction dependent processes. Lastly, there are (as mentioned) the spurious velocities near the interface, which

could cause unphysical effects.

Returning for a moment to the issue of maximum Reynolds number, $Re = 60D$, it is worth noting that one of the most important features of the engineering-scale multiphase system is the possibility for simulating turbulent bubbly flow. This claim is based on the previous estimate (Section 5.2) of a system size of 10^8 lattice cells. One may wish, for example, to simulate flow in a tube with a large enough length to diameter ratio L/D to allow some development of the flow regime. A tube with $D = 200$ and $L = 3000$ cells can be used, giving $L/D = 15$, and a Reynolds number $Re = 12000$ (although this is still a relatively small L/D, the boundary conditions at the flow entrance and exit can be set up in such a way as to enhance the development of fully turbulent flow). In some cases perhaps a much squatter tube could be used for simulations of flow that does not require much development, for example $D = L = 500$; then the maximum Reynolds number is $Re = 30000$. These Reynolds numbers would allow investigation of the complex effects of turbulent forces on bubble dynamics.

Some final thoughts are in order regarding the issue of converting from lattice units to real units. It is instructive to introduce the Mach number $M_a = |\mathbf{u}|/c_s$, where $\mathbf{u}$ is a velocity of interest. The fundamental properties that determine the kinematic viscosity ν are the soundspeed c_s and the mean free path λ, $\nu \cong c_s\lambda$. The Reynolds number may therefore be rewritten as

$$Re = M_a \left(\frac{L}{\lambda}\right) \tag{5.18}$$

where L is some appropriate length. Water at 20 C has a mean free path $\lambda \cong 7(10^{-10})$

meters. The lattice system has some minimum allowable kinematic viscosity, which was specified as 0.005, and the liquid phase has (typical) soundspeed $c_s \cong 2$, giving a mean free path of $\tilde{\lambda} \cong 2.5(10^{-3})$ lattice cells. Thus the length conversion on the basis of mean free path would be about $3(10^{-7})$ meters per lattice cell. This would, of course, restrict the method to simulation of very small flow systems - a system on the scale of millimeters would exceed the most generous plausible computational limits. Consequently the basic dimensionless quantity L/λ must be much smaller in the lattice system than in the real world. In order to achieve the correct Reynolds number, therefore, it is necessary to make the lattice Mach number much higher than the real Mach number. This is also necessary from the point of view of simulation time, since the higher lattice flow velocity allows proportionally fewer time steps.

The bubble drag coefficient (equation (5.12)) is basically just a Froude number, which may be written in general as $Fr = gL/|\mathbf{u}|^2$. Using the Mach number to recast the Froude number,

$$Fr = \frac{gL}{c_s^2 M_a^2} = \frac{D_g}{M_a^2} \tag{5.19}$$

where another dimensionless quantity has been defined, $D_g = Lg/c_s^2$, which will be referred to as the dimensionless gravitational compression. Physically it represents the fractional density change of a substance due to gravity acting over a height L. Since the Mach number of the lattice system is typically elevated as much as possible to maximize Reynolds number, a consequence when attempting to achieve a certain Froude number at the same time is that the dimensionless gravitational compression of the lattice system must be much higher than that of the real world. This is acceptable so long as it does not become so large that

it causes strong density variations in a system where they should be negligible. This is the source of an additional macroscopic restriction on lattice gravitational constant g, referred to earlier. The choice of criterion depends on the system; if for example no more than five percent change in density over a column of liquid of height $\tilde{L} = 500$ is acceptable, then $\tilde{g} < (0.05)(2)^2/500 = 4(10^{-4})$ is required.

5.6 Van der Waals Thermodynamics

This section describes how the choice of a system based on the van der Waals equation of state affects the ability to model water from a thermodynamic viewpoint. It is a property of a van der Waals system (detailed in Appendix A) that the dimensionless thermodynamic quantities related to two-phase coexistence depend on a single dimensionless parameter, which will be referred to as the universal van der Waals parameter Z,

$$Z \equiv \frac{a}{bRT} \tag{5.20}$$

The quantities that depend only on the universal parameter Z include the following:

- density ratio $r_\rho \equiv \rho_f/\rho_g$
- reduced temperature $T^* \equiv RT/RT_{crit}$
- reduced pressure $P^* \equiv P/P_{crit}$
- dimensionless latent energy of vaporization $u^* \equiv (u_g - u_f)/RT$

- dimensionless latent entropy of vaporization $s^* \equiv (s_g - s_f)/R$
- dimensionless volume-work of vaporization $w^* \equiv (P/RT)(1/\rho_g - 1/\rho_f) = P\Delta v/RT$
- dimensionless liquid and vapor soundspeeds $c_s/\sqrt{RT}$

where $\Delta v \equiv v_g - v_f$ is the volume change of vaporization. In this section the temperature and pressure are always taken to be the saturation values corresponding to a two-phase mixture.

Once any one of the dimensionless quantities listed above is specified, all of the others are determined, hence a single parameter governs all of the important two-phase thermodynamical behavior of this system. The van der Waals system is therefore likely to provide a rather crude approximation to the thermodynamic properties of any real substance. Since the focus of the project is on water, it is worthwhile to examine how the properties of saturated water compare, in dimensionless fashion, to those of a van der Waals system. The basis of comparison is chosen to be the liquid to vapor density ratio r_ρ. Figure 5.3 shows the parameter Z as a function of equilibrium liquid to vapor density ratio for the van der Waals system, and also gives the saturation temperature of water for which a given density ratio exists. Figures 5.4-5.9 compare the van der Waals system to water[7] by showing each of the above dimensionless quantities plotted as a function of density ratio. The agreements are not quantitatively correct, with some quantities differing consistently by a factor of two or more. Nevertheless the correct trends are captured over a wide range of conditions.

[7]All data for water was taken from the Steam Tables. Values of quantities for the van der Waals system were found by numerical solution of equations (3.15) and (3.16).

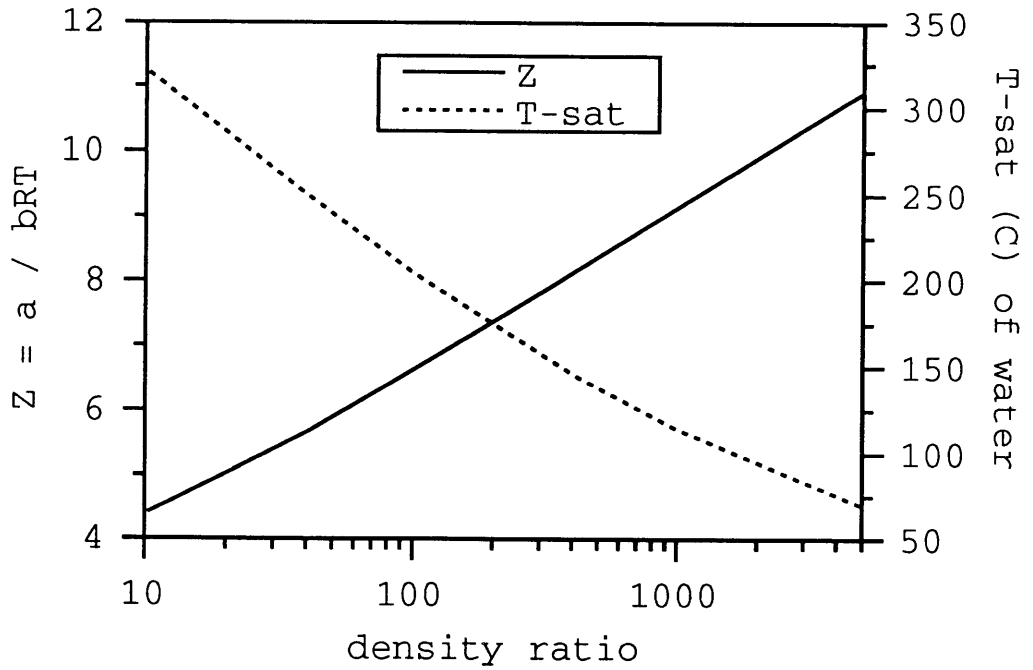

Figure 5.3: Universal van der Waals parameter $Z = a/bRT$, and saturation temperature of water, versus equilibrium liquid to vapor density ratio.

The lack of quantitative agreement is not a concern in this work. The example of a van der Waals thermodynamical system used in this project is sufficient to show the important features which characterize the multiphase system. In practice a much more accurate empirical thermodynamical model for a specific substance, such as one based on the fundamental equation for water given in the Steam Tables, could be used (as noted in Chapter 3). The present goal is just to demonstrate that the multiphase system is in fact able to represent a consistent two phase thermodynamical system, especially since this is crucial for eventually including heat transfer capability.

The key point of this analysis is that, along with the density ratio, a very significant requirement imposed by thermodynamics on the multiphase system involves the dynamic range of the internal energy per unit mass $\tilde{u}$. This is because the system must be able to

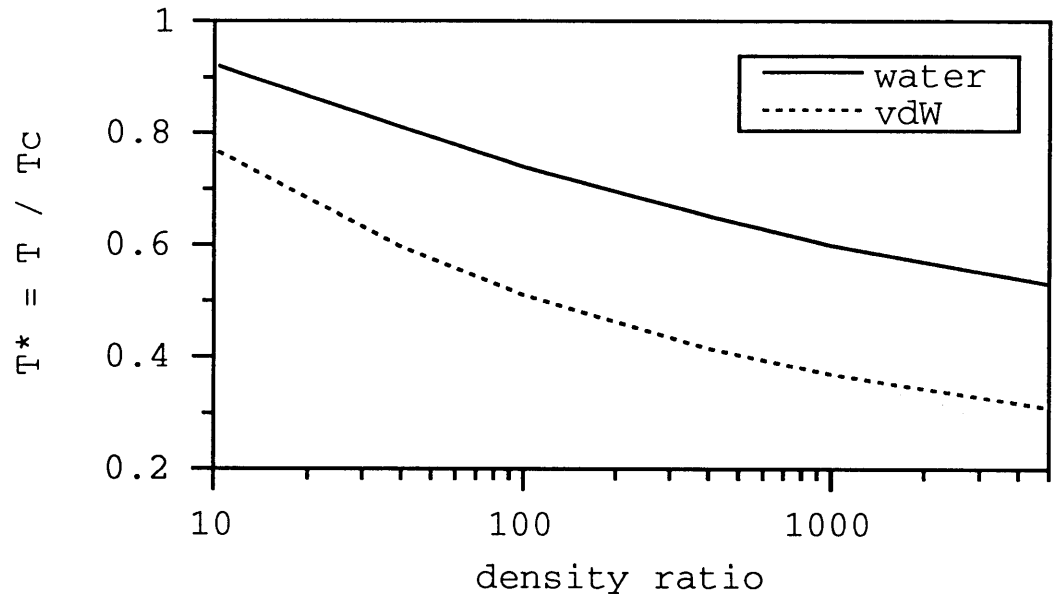

Figure 5.4: Reduced temperature T^* vs. density ratio, comparison between water and van der Waals system.

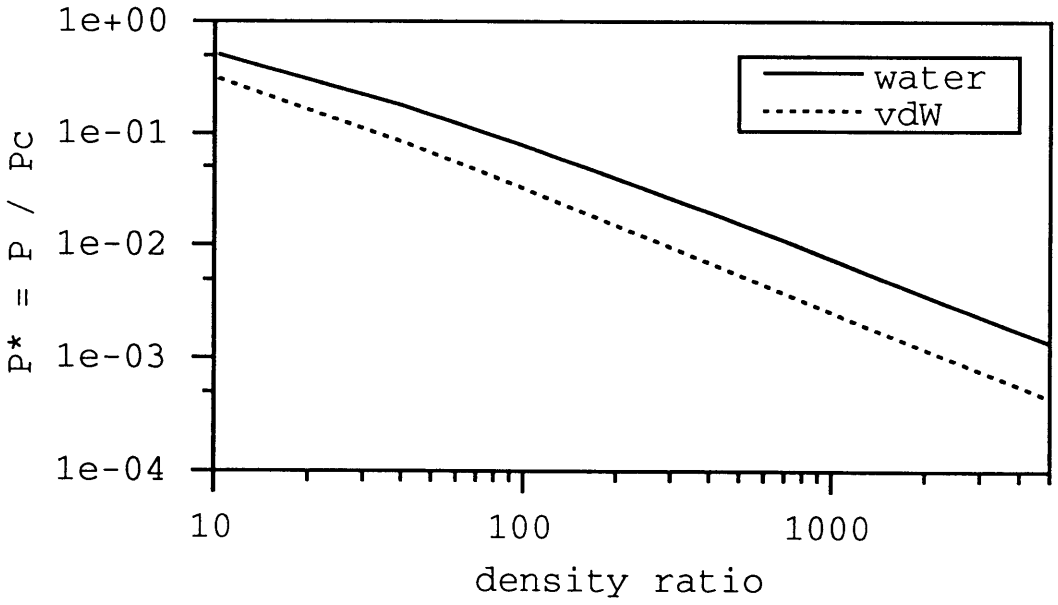

Figure 5.5: Reduced pressure P^* vs. density ratio, comparison between water and van der Waals system.

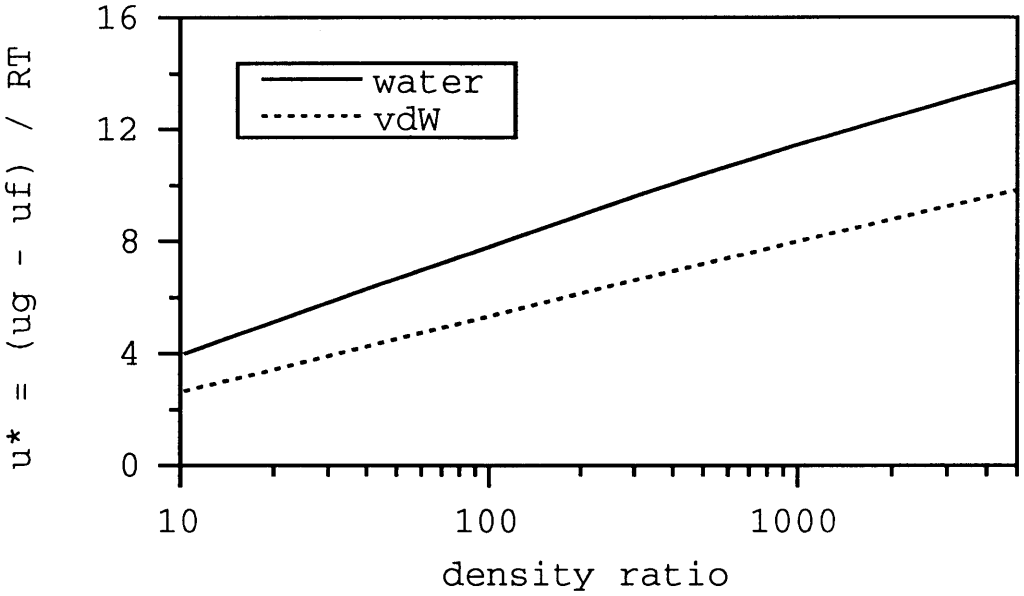

Figure 5.6: Dimensionless latent internal energy of vaporization u^* vs. density ratio, comparison between water and van der Waals system.

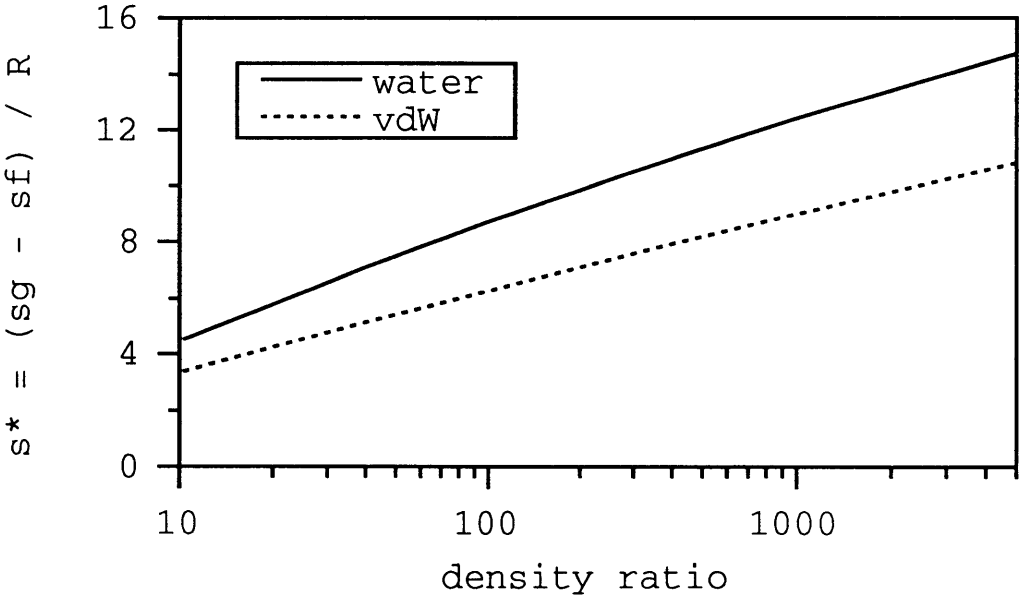

Figure 5.7: Dimensionless latent entropy of vaporization s^* vs. density ratio, comparison between water and van der Waals system.

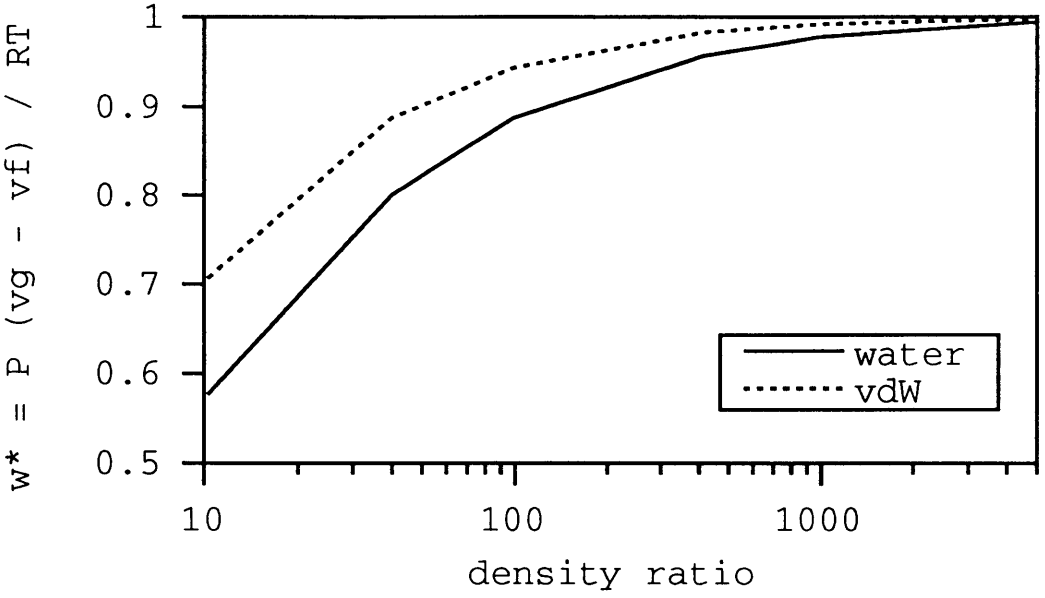

Figure 5.8: Dimensionless latent volume-work of vaporization w^* vs. density ratio, comparison between water and van der Waals system.

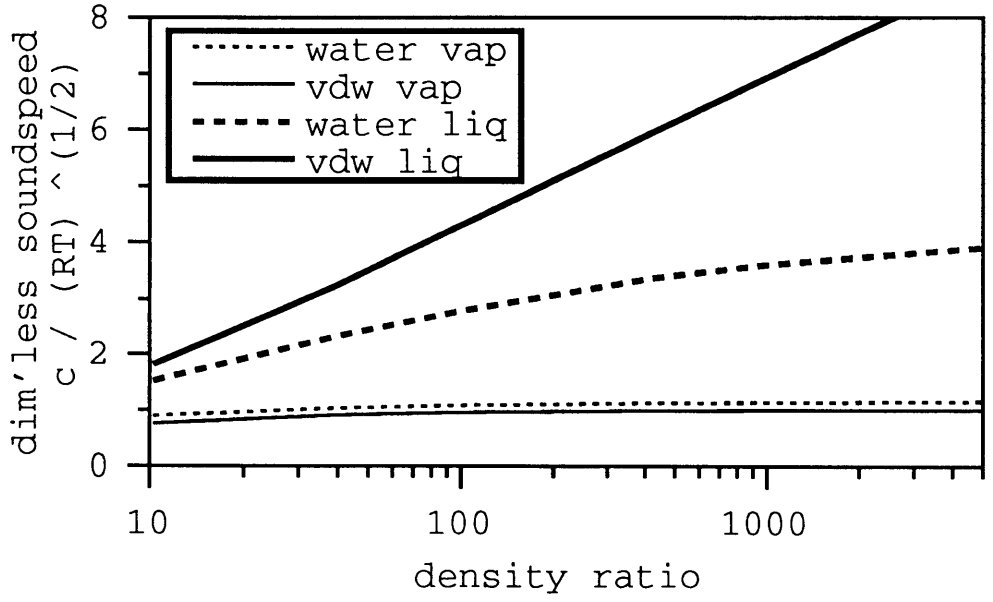

Figure 5.9: Dimensionless liquid and vapor soundspeeds, comparison between water and van der Waals system. Isothermal soundspeeds are used for the latter, calculated as in Section 7.2.

represent the full range of this quantity as it varies from the equilibrium vapor value $\tilde{u}_g$ to that of the liquid $\tilde{u}_f$. Thus the system must be designed to accommodate the dimensionless latent energy of vaporization u^* associated with the desired range of simulation conditions. For example, a system with a density ratio $r_\rho = 40$, which matches that of water at 250 degrees C, will have a dimensionless latent energy of vaporization $u^* = 4.3$ (as seen in Figure 5.6). Recalling that the equilibrium vapor internal energy per unit mass is $\tilde{u}_g \cong 2\tilde{R}\tilde{T}$, then that of the liquid must be $\tilde{u}_f \cong -2.3\tilde{R}\tilde{T}$.

Clearly the required dynamic range of $\tilde{u}$ increases linearly with temperature $\tilde{R}\tilde{T}$, for a given value of u^*. From the point of view of designing a system with adequate dynamic range, it is therefore desirable to have a small value of lattice temperature $\tilde{R}\tilde{T}$. An important consequence of the general dependence of the two-phase properties of a van der Waals system on a single parameter is that it puts no constraint on the choice of the lattice temperature $\tilde{R}\tilde{T}$. This is because for any value of the parameter $Z = a/b\tilde{R}\tilde{T}$, one may always choose van der Waals constants a and b to accommodate any value of $\tilde{R}\tilde{T}$, even while additionally specifying some other (non-dimensionless) property such as the absolute value of the liquid density.

A criterion that can be used in the choice of lattice temperature $\tilde{R}\tilde{T}$ is that the multiphase system should approach the standard system at low density, and the standard system has a dynamic range of $1/3 < \tilde{R}\tilde{T} < 2/3$. It turns out that, in the multiphase system as implemented it in this work, there is an upper limit on temperature $\tilde{R}\tilde{T}$ due to the nature of the solution of the system of constraints. In Section 6.1 it is shown that there is a requirement $\tilde{u} < 1$ (see equation (6.18)). This means that for the vapor, $\tilde{u} = \tilde{u}_g \cong 2\tilde{R}\tilde{T} < 1$, hence there

is an approximate upper limit of $\tilde{R}\tilde{T} \cong 1/2$. There is, however, no corresponding lower limit on temperature. The lattice temperature will therefore be considered an arbitrary parameter in the range $1/3 < \tilde{R}\tilde{T} < 1/2$, and the usual value will be $\tilde{R}\tilde{T} = 0.4$. Physically the absolute value of the lattice temperature has little meaning as an isolated quantity, its relevance is its role as a scaling parameter for the other thermodynamic quantities as shown above. Of key significance, however, is that once a lattice temperature $\tilde{R}\tilde{T}$ and the maximum desired density ratio are chosen, the required range of internal energy per unit mass $\tilde{u}$ is essentially determined. In Section 6.1 it is shown that this in turn determines the amounts of negative microscopic internal energy which need to be included in the choice of particle species.

The liquid to vapor density ratio, as opposed to say the reduced temperature, will continue to be chosen as the basic quantity by which to specify the thermodynamic conditions of the multiphase system. This is done for several reasons. First, the density ratio is important to the flow dynamics, although in cases such as bubbly flow where the vapor can be thought of as void space, it is only necessary to be sure that the density ratio is large. Second, it is a simple but important equilibrium property of a two-phase mixture. Third, there is the upper limit of about 200 discussed above.

In this chapter important thermodynamic and flow properties have been identified, and the means by which to relate the multiphase system to a real fluid has been outlined, particularly for the case of water. The capabilities and limitations for an estimated engineering-scale version of the multiphase system were described, and the potential to accurately simulate bubbly flow for low and high temperature water systems was discussed. In the process the physical mechanisms and dimensionless quantities which are important to the bubbly (and

to some extent slug) flow regime were examined, along with the ranges of these quantities that are accessible to the multiphase system. In Section 8.2, results of 2D single bubble rise simulations are presented which demonstrate the ability of the multiphase system to capture the key physical mechanisms. The next chapter deals with additional theoretical and practical issues involved in arriving at a working implementation of the multiphase system.

Chapter 6

Implementation of the Method

6.1 Solution of the System of Constraints

A specific implementation of the multiphase system requires the selection of particle species. It was previously established that at least four species are needed, and at least one with both kinetic and internal microscopic energy. Specifying a set of particle species allows us, in principle, to attempt to find a solution of the system of constraints (4.58-4.61) as written. Instead, a way to simplify that system so as to make it more tractable is now presented. While an analytical solution will not be found, the system of equations will be more easily solved numerically, and along the way some additional insight will be gained.

The goal is to see how the choice of species affects the dynamic range of the system, i.e. the range of internal energy per unit mass u for which a solution exists. It must be noted

that a solution is only valid if it gives a positive real value for each rate coefficient (including Lagrange multipliers α_0 and β_0 defined previously). While many possible combinations of exotic energy species might be tried, a prudent guiding principle is to minimize the departure from the well-tested standard system. Essentially this means limiting the values of microscopic kinetic energy to zero, one, or two. It was found that using only four different species leads to an undesirable property of the solution that two of the species populations are fixed. Since it is desirable to minimize the number of states and the size of the collision list, a system consisting of five different types of particles will be used[1].

To remain somewhat general, a set of species of the form $(0,0)$, $(1,0)$, $(2,0)$, $(1,-v)$, and $(0,-w)$ is considered, where the notation $(\varepsilon_j^K, \varepsilon_j^I)$ is used to indicate a particle of microscopic kinetic energy ε_j^K and microscopic internal energy ε_j^I. The first three are "purely kinetic" species and are those of the three-speed standard system. The last two are "mixed energy" species, and this combination has been found to yield a favorable solution, one which imparts a substantial range of internal energy per unit mass u. That range will tend to be from an upper value u_{max} of about unity to a lower value u_{min} which scales with the magnitudes of the negative microscopic internal energies. The above species set also lends itself favorably to finding suitable energy exchange collisions.

Recalling the system of constraints written in terms of the zero-velocity distributions, equations (4.53-4.56), it is useful to define the total population of species j per unit mass, $P_j \equiv N_j d_j/\rho = n_j d_j$. Then expanding the sums, putting in values for the microscopic

[1]Systems of six or more types of particles have been investigated with no discernible advantage.

energies, and dividing through by density yields

$$1 = P_0 + P_1 + P_2 + P_3 + P_4 \tag{6.1}$$

$$u = P_1 + 2P_2 + (1 - v)P_3 - wP_4 \tag{6.2}$$

$$(3/2)(P_1 + 2P_2 + P_3)^2 = P_1 + 4P_2 + P_3 \tag{6.3}$$

$$(P_1 + 2P_2 + P_3)(-vP_3 - wP_4) = -vP_3 \tag{6.4}$$

There are five species and only four constraints, but an additional equation will be introduced by defining the rate coefficients.

It is convenient to take advantage of the common appearance of the zero-velocity kinetic and internal energy moments $\langle \varepsilon^K \rangle$ and $\langle \varepsilon^I \rangle$. Defining them per unit mass as K and I,

$$K \equiv \frac{\langle \varepsilon^K \rangle}{\rho} = P_1 + 2P_2 + P_3 \tag{6.5}$$

$$I \equiv \frac{\langle \varepsilon^I \rangle}{\rho} = -vP_3 - wP_4 \tag{6.6}$$

and substituting into the above equations gives

$$1 = K + P_0 - P_2 + P_4 \tag{6.7}$$

$$u = K + I \tag{6.8}$$

$$(3/2)K^2 = K + 2P_2 \tag{6.9}$$

$$KI = -vP_3 \tag{6.10}$$

The following relationships are immediately seen:

$$P_2 = \frac{1}{2}K\left(\frac{3}{2}K - 1\right) \tag{6.11}$$

$$P_3 = -\frac{1}{v}KI = -\frac{1}{v}K(u - K) \tag{6.12}$$

$$P_4 = -\frac{1}{w}I(1 - K) = -\frac{1}{w}(u - K)(1 - K) \tag{6.13}$$

and substituting into equation (6.7),

$$1 = K + P_0 - \frac{1}{2}K\left(\frac{3}{2}K - 1\right) - \frac{1}{w}(u - K)(1 - K) \tag{6.14}$$

Completing the solution requires specifying the "rate structure" of the system, that is to say one must write out explicitly the relationships expressed by equation (4.57). As mentioned, only two of the rates can be independently adjusted. The following rate structure has been found to yield a favorable solution:

$$\begin{aligned} P_0 &= r_0 y \\ P_1 &= dyz \\ P_2 &= dyz^2 \\ P_3 &= dryz^{(1-v)} \\ P_4 &= ryz^{-w} \end{aligned} \tag{6.15}$$

where it has been noted that d_j happens to be the same number of directions, $d = 24$, for each of the moving species, and unity for the two non-moving species. In this formulation, r and r_0 are the independent rates, where $r_3 = r_4 = r$ and $r_1 = r_2 = 1$. An important result of assigning the same rate coefficient to both of the mixed energy species is that their populations tend to vanish together at low density.

By taking the ratios P_2/P_1 and P_3/P_4, equations (6.15) may be rearranged to give

$$z = \frac{P_2}{P_1} = \left(\frac{P_3}{P_4}\right)^{\frac{1}{1-v+w}} \tag{6.16}$$

Using equations (6.5) and (6.11-6.13) to substitute for the populations per unit mass P_1, P_2, P_3, and P_4, yields

$$\frac{3K-2}{8-6K+4(u-K)/v} = \left(\frac{w}{vd}\frac{K}{1-K}\right)^{\frac{1}{1-v+w}} \tag{6.17}$$

and this equation can be solved numerically for its single unknown K. All of the populations per unit mass may then be solved for directly, and they are strictly functions only of the internal energy per unit mass u.

A solution is only valid when all of the associated equilibrium populations have real, positive values; this condition will only be met for some finite range of isotropic kinetic energy moment K corresponding to some finite range of the internal energy per unit mass u, known as the dynamic range. This positivity condition can be applied separately to each species population in order to make some observations about the behavior of the dynamic range of the system.

From equation (6.12),

$$\begin{aligned} P_3 &= -\frac{1}{v}K(u-K) > 0 \\ &\Rightarrow u < K \end{aligned} \tag{6.18}$$

where the fact that $K > 0$ was used, since there are no negative values of microscopic kinetic energy ε_j^K. Equation (6.13) gives

$$\begin{aligned} P_4 &= -\frac{1}{w}(u-K)(1-K) > 0 \\ &\Rightarrow K < 1 \Rightarrow u < 1 \end{aligned} \tag{6.19}$$

and equation (6.11) gives

$$\begin{aligned} P_2 &= \frac{1}{2}K(\frac{3}{2}K - 1) > 0 \\ &\Rightarrow K > 2/3 \end{aligned} \tag{6.20}$$

From equations (6.5), (6.11), and (6.12),

$$\begin{aligned} P_1 &= 2K - \frac{3}{2}K^2 + \frac{1}{v}K(u-K) > 0 \\ &\Rightarrow u > K + \frac{3}{2}vK - 2v \Rightarrow u > \frac{2}{3} - v \end{aligned} \tag{6.21}$$

where $K > 2/3$ from above was used to get the last relation. Thus the dynamic range of the system will be at most $2/3 - v < u < 1$.

A final condition is derived from equation (6.14) by solving for P_0 and setting the result to be greater than zero, which may then be rearranged to give

$$u > \frac{4K - 4K^2 - 4w + 6wK - 3wK^2}{4(1-K)} \tag{6.22}$$

$w\backslash v$	1	2	3	4	5
1		0.980 , -0.080	0.993 , -1.16	0.997 , -1.54	0.998 , -1.88
2	0.568 , -0.333		0.973 , -0.648	0.990 , -2.22	0.996 , -2.61
3	0.583 , -0.333	0.205 , -1.33		0.970 , -1.21	0.988 , -3.24

Table 6.1: Dynamic range (max,min) of internal energy per unit mass u for combinations of microscopic internal energy parameters v and w in the (0, 1, 2, 1-v, -w) 5-species system.

This condition tends to have a very small effect on the upper end of the range, but has a substantial effect on the lower bound u, especially as w becomes small.

The exact dynamic range of internal energy per unit mass u for several sets of parameters v and w, is displayed in Table 6.1. It appears to be desirable to have $v > w$. However, combinations which give $w = v - 1$ are excluded as they lead to solutions which require that two of the species populations are fixed. The values in this table were found by numerically solving equation (6.17) for $K(u)$ and noting the range over which all the populations per unit mass P_j remain positive. Typically the upper bound is limited by P_3 and P_4, which both become negative as the rate coefficient r becomes negative; this is physically consistent as it is expected that the relative fractions of these mixed energy species will dwindle as internal energy per unit mass u increases. The other species populations decline as u decreases, and the lower bound tends to be reached when P_0 becomes negative (as the rate coefficient r_0 goes negative).

For the multiphase system implemented in this thesis, $v = 4$ and $w = 2$ were chosen, which gives a dynamic range $-2.22 < u < 0.990$, and allows a favorable set of interspecies collisions (discussed in Section 6.4). For a lattice temperature $\tilde{R}\tilde{T} = 0.4$, this implies a maximum dimensionless latent energy of vaporization $u^* = \Delta\tilde{u}/\tilde{R}\tilde{T} \cong 7.5$, which is sufficient to model

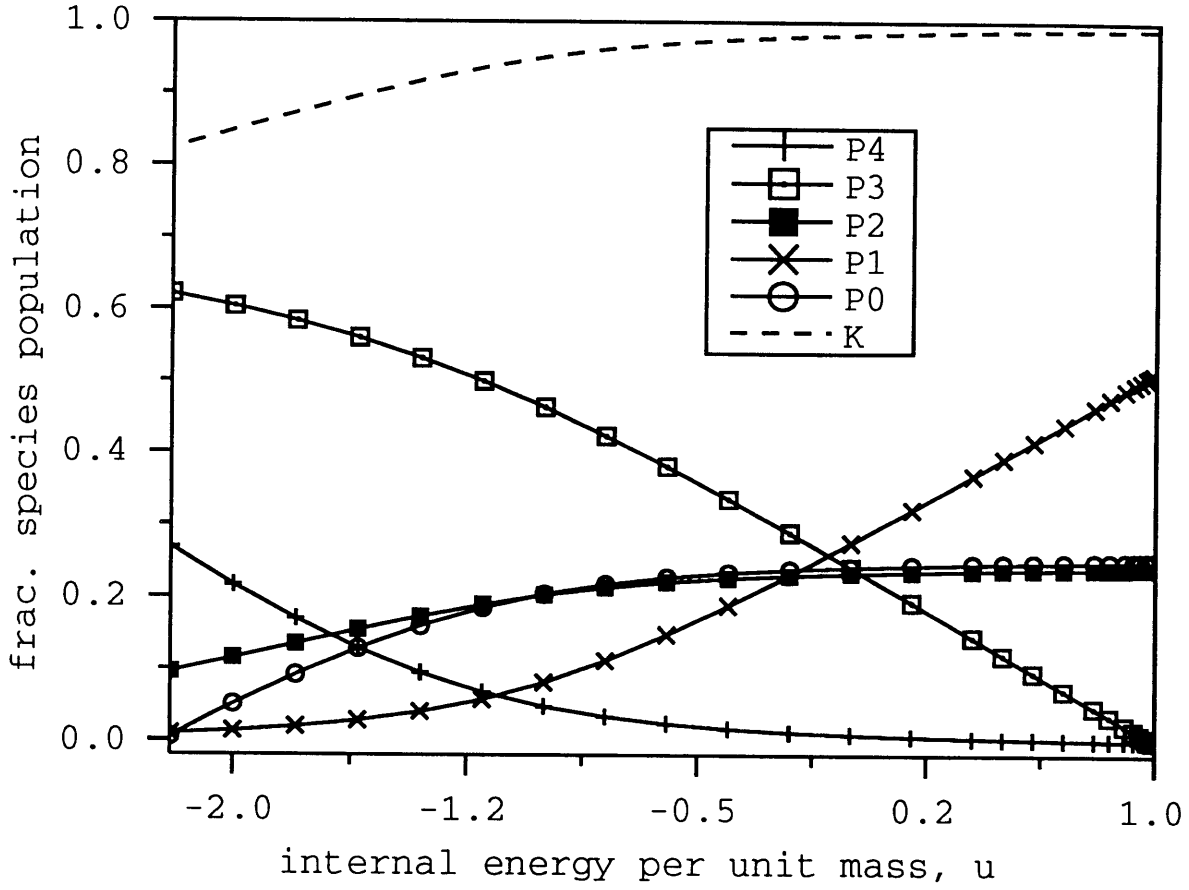

Figure 6.1: Fractional species populations P_j and isotropic kinetic energy moment per unit mass $K = P_1 + 2P_2 + P_3$ vs. internal energy per unit mass u, for the (0, 1, 2, -3, -2) 5-species multiphase system.

a density ratio of up to $r_\rho \cong 700$. This is quite suitable since, as discussed in Section 5.2, there is already an upper limit on density ratio of about 200. The values of the species populations per unit mass P_j in the $v = 4$, $w = 2$ system are plotted as a function of internal energy per unit mass u in Figure 6.1. The isotropic kinetic energy moment per unit mass $K = P_1 + 2P_2 + P_3$ is also shown; it will be seen later that K plays a significant role in certain aspects of system behavior, such as the value of the kinematic viscosity ν.

6.2 Stability of the Dense Phase

It was found that when the multiphase system is implemented in a straightforward manner, the dense phase is not stable with respect to density fluctuations. The amplitude of the fluctuations grows with time, causing a uniform region to rapidly break up into local spots of very high density surrounded by regions of lower density. The pattern itself fluctuates wildly, and the high densities can reach values of several times the expected value of the liquid density. This instability has been observed in the liquid phase of a two phase mixture and for a pure single phase liquid. The rheology of the instability is typically fairly distinct, and different than that observed, for example, in the standard system [71] in the presence of large flow velocities in combination with a high degree of over-relaxation[2]. Indeed, the liquid phase instability is observed even for a system with no flow, no over-relaxation, and fixed rates[3].

The instability is believed to occur because the elevated soundspeed of the liquid violates a kind of Courant condition. The soundspeed is the velocity at which density perturbations are propagated, and thereby represents a rate of travel of information. In a lattice gas, however, the fastest rate of information propagation is the speed of the fastest particles. In this implementation of the multiphase system, the fastest particle speed is two. It is therefore impossible for the system to move mass around in response to fluctuations quickly enough to match the desired rate for a liquid phase with a soundspeed above two. Thus a

[2]Collisional over-relaxation [17, 19] is a technique for reducing the viscosity of the lattice gas, and is detailed further in Sections 6.3 and 6.4.

[3]"Fixed rates" refers to a scheme where the rate coefficients for the energy-exchange collisions are constant for the duration of a simulation, as opposed to dynamic rates which are updated at each time step.

soundspeed of two is expected to be the absolute maximum supported by the multiphase system, although in practice the threshold may be lower, due to other operations which exacerbate the instability, or to the presence of a relatively small fraction of the species which have particle speed two.

Such a limitation would severely hamper the usefulness of the multiphase system. This is apparent from Figure 5.9, which shows the (isothermal) liquid soundspeed of the multiphase system as a function of density ratio. At a density ratio of forty the liquid soundspeed is already above two, and in practice even lower density ratios result in an unstable liquid phase. Also, soundspeed increases with density and pressure, so that liquids at pressures above their saturation pressures have higher soundspeeds. The Courant stability condition is not a problem for the vapor phase, in which the soundspeed is never greater than unity.

The adopted solution is to implement the multiphase system with a reduced time step. The liquid soundspeed will scale with the effective time step, while the actual particle speeds do not change. In this way arbitrarily high liquid soundspeeds can be achieved if one is willing to endure correspondingly small time steps. It turns out that typically only a modest time step reduction is required to achieve a stable bulk liquid phase in the systems of interest in this project. A rough criterion for the expected maximum reduced time step, ω_p^{max}, is simply that the *effective* soundspeed, $\omega_p c_s$, should be no greater than the maximum particle speed of two. Hence the theoretical maximum reduced time step $\omega_p^{max,th}$ is

$$\omega_p^{max,th} = 2/c_s \tag{6.23}$$

The modification of the advection scheme used to achieve a reduced time step is discussed in the next section.

Another important feature of the instability is its sensitivity to collisional over-relaxation. Basically, the problem gets worse as the amount of over-relaxation is increased. This is unfortunate since over-relaxation is typically used in order to reduce the liquid kinematic viscosity. A theoretical analysis of the effect of over-relaxation on the onset of instability is approximate and cumbersome at best, yet some sort of guide is needed by which to choose optimum values of the reduced time step ω_p. An optimum exists because ω_p should be as large as possible to limit the number of steps needed for a given simulation, while allowing a stable liquid phase for a given set of conditions.

Stability tests were conducted by which to determine the maximum allowable value of the reduced time step, ω_p^{max}, for a given liquid soundspeed and a given amount of over-relaxation. In these tests, a 30x30 lattice was seeded with uniform density and velocity, with each state population set to the corresponding equilibrium value, plus a small fluctuation. The level of fluctuation was larger than that due to dithering the populations to integer values, and was even larger than that normally observed in a steady state liquid phase; it was present to help induce unstable behavior for purposes of the test. The lattice velocity components were fixed at $u_x = 0.15$ and $u_y = 0.13$, giving a flow speed $|\mathbf{u}| \cong 0.2$. The instability has been observed to become more severe with increasing velocity; this flow speed value was chosen to give a practical, though not extreme, example of typical operating conditions.

The lattice soundspeed was varied[4] either by adjusting the universal van der Waals param-

[4]Calculation of the soundspeed is detailed in Section 7.2.

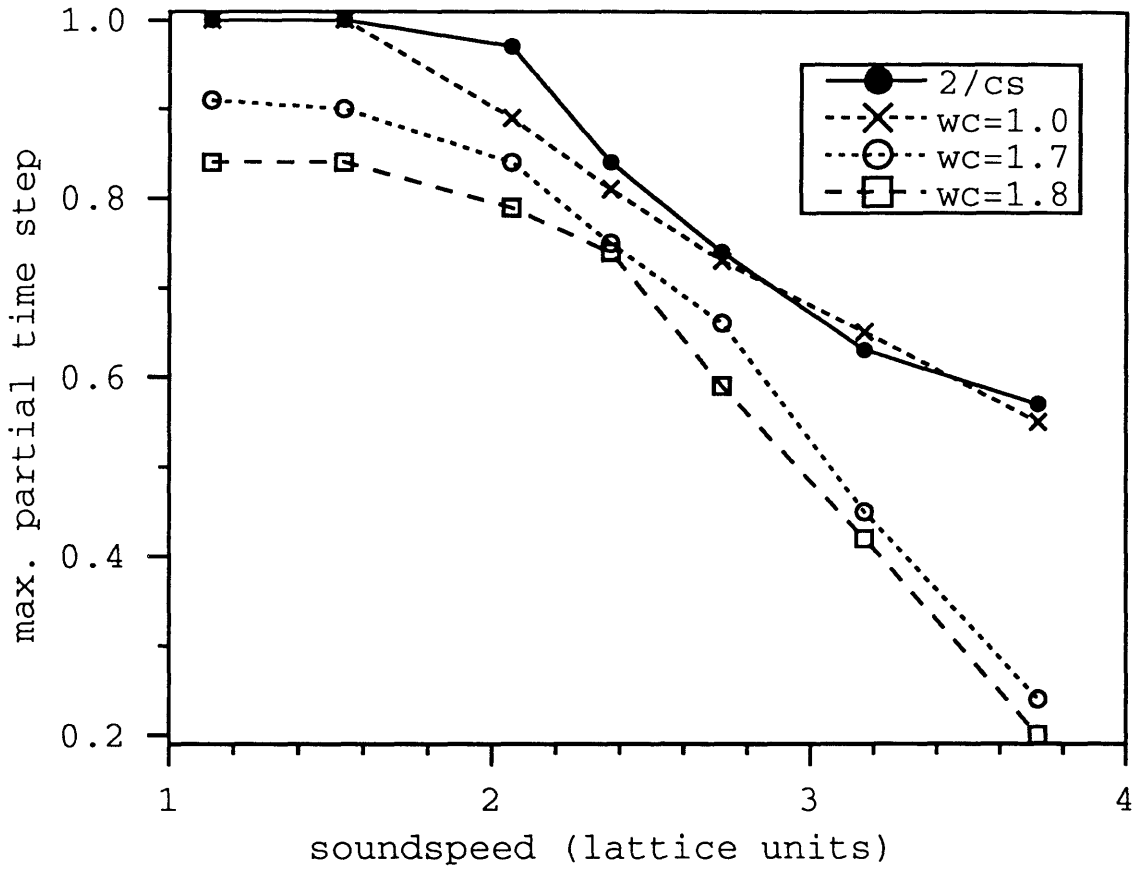

Figure 6.2: Results of liquid phase stability tests to determine maximum allowable partial time step ω_p^{max} as a function of liquid soundspeed c_s. The proposed theoretical value is $\omega_p^{max} = 2/c_s$; however ω_p^{max} is also strongly affected by the collisional over-relaxation parameter ω_c.

eter $Z = a/b\tilde{R}\tilde{T}$, or by increasing the density for a given value of Z; the lattice temperature was kept constant at $\tilde{R}\tilde{T} = 0.4$. The results are shown in Figure 6.2, where the maximum value of the partial time step ω_p^{max} is plotted against soundspeed c_s for several values of the over-relaxation parameter ω_c. The given value of ω_p^{max} indicates the largest partial time step, measured in increments of 0.01, for which the system remained stable. Thus the area to the upper right of a curve represents an unstable region for that value of ω_c. Also plotted is the theoretical maximum partial time step $\omega_p^{max,th} = 2/c_s$; with no over-relaxation ($\omega_c = 1$) it

is in fact a good prediction, and supports the conjecture regarding the Courant condition as the source of the instability. It is clear from the results that over-relaxation contributes significantly to the instability condition.

For purposes of this test the criteria for a system to be considered stable was that the mean square density fluctuations averaged over the lattice had to continually decrease or remain at a constant minimum value for at least 1000 time steps. Growth of the mean density fluctuations in the absence of some external agent is strictly unphysical and is essentially the definition of the instability. While the results of this experiment by no means provide a guarantee that a given set of conditions are stable, it has been found to be a useful guide, especially when a margin of safety is included, such as using a partial time step of $\omega_p = 0.8\omega_p^{max}$. In different situations the liquid phase may require less than twenty or more than a thousand steps to become unstable; however, the onset of instability is always observed to occur faster for increased partial time step or degree of over-relaxation.

6.3 Probabilistic Advection and Recovery of Low Viscosity

A modified advection scheme is now presented by which to reduce the effective time step while preserving the viscosity reduction available through collisional over-relaxation. The new scheme will be referred to as the "probabilistic advection" method[5], and allows a reduced

[5]The concept of probabilistic advection is due originally to Chen, Teixeira, Gang, and Molvig [72], and has been adapted here to create the reduced time step method.

time step ω_p, $0 < \omega_p < 1$, without introducing artifacts into the resulting macroscopic dynamics. In the process of describing probabilistic advection, essential elements of transport theory for the multiphase system will be derived.

A reduced time step has been found to stabilize the dense phase of the multiphase system, as described above. The meaning of a reduced time step is that particles travel, on average, only the fraction ω_p of the distance they normally would based on their current speed. Thus the usual definition of velocity $\mathbf{u}$,

$$\sum_{ji} \mathbf{c}_{ji} N_{ji}^{EQ} = \rho \mathbf{u} \tag{6.24}$$

becomes

$$\sum_{ji} \mathbf{c}_{ji} N_{ji}^{EQ} = \omega_p \rho \mathbf{u} \tag{6.25}$$

Microscopically, however, particles can only travel discrete distances on the lattice. Thus the above condition can be brought about most simply by allowing only $\omega_p N_{ji}^{EQ}$ particles to move for each state ji at each time step. This rule will be referred to as the "partial advection" scheme, and it introduces an extraneous diffusive term which leads to undesirable artifacts. The probabilistic advection scheme, on the other hand, achieves the reduced time step but also introduces an antidiffusive component into the advection process which eliminates these artifacts. It will be shown that partial advection dramatically weakens the ability of over-relaxation to lower the lattice viscosity; it is especially important that the probabilistic advection process does not have this disadvantage, since it usually desirable to lower the lattice viscosity as much as possible in order to boost the accessible range of Reynolds

numbers.

Probabilistic advection is invoked by using a generalized advection process, represented by the following lattice update equation:

$$N_i(\mathbf{x}, t+\omega_p) = \sum_n G_n^i N_i'(\mathbf{x}-\mathbf{c}_n, t) + \omega_p \mathcal{I}_i \tag{6.26}$$

Here n refers to a nearest neighbor, and G_n^i is a transition probability, such that for a state i it is the fraction of the population N_i at site $\mathbf{x}$ which is advected to neighbor $\mathbf{x}+\mathbf{c}_n$ (or equivalently from neighbor $\mathbf{x}-\mathbf{c}_n$ to site $\mathbf{x}$). Note the species index j has been dropped for this discussion, so state ji will just be written as state i. As given, equation (6.26) indicates that the population of state i which ends up at site $\mathbf{x}$ is the sum over the neighborhood of the preadvection state i populations of each neighbor multiplied by a transition probability which depends on the relative location of that neighbor. A single complete update is considered to advance the system from time t to time $t+\omega_p$. Note that in the presence of the reduced time step, the interaction operator must be scaled by ω_p, and this is accounted for in practice in the calculation of the interaction parameter ψ.

The preadvection population N_i' is the post-collision population, which normally is the equilibrium distribution, thus $N_i' = N_i^{EQ}$. This is also true for the multiphase system since, as previously discussed, the momentum and energy pushing operations occur after advection but prior to collision. However when over-relaxation is present, the distributions are driven

beyond equilibrium in the collision process, and the post-collision population is given by

$$N_i' = N_i - \omega_c(N_i - N_i^{EQ}) \tag{6.27}$$

where ω_c is the over-relaxation parameter, and $1 < \omega_c < 2$. The above equation indicates that, for $\omega_c > 1$, the distributions are driven to equilibrium and then beyond by a factor of $(\omega_c - 1)$. We are particularly concerned by the interaction between over-relaxation and the reduced time step.

The mean dynamics of the system are derived in the usual fashion via a Chapman-Enskog type of procedure. Expanding the update equation (6.26) to second order in Knudsen number,

$$N_i + \omega_p \partial_t N_i + \frac{1}{2}\omega_p^2 \partial_t \partial_t N_i = \sum_n G_n^i \left(N_i' - \mathbf{c}_n \cdot \nabla N_i' + \frac{1}{2}\mathbf{c}_n \mathbf{c}_n : \nabla\nabla N_i' \right) + \omega_p \mathcal{I}_i \tag{6.28}$$

Continuity requires that, for each state i, the set of transition probabilities G_n^i obey

$$\sum_n G_n^i = 1 \tag{6.29}$$

and, in light of equation (6.25), the required velocity moment is

$$\sum_n G_n^i \mathbf{c}_n = \omega_p \mathbf{c}_i \tag{6.30}$$

Using these conditions in equation (6.28) gives

$$N_i + \omega_p \partial_t N_i + \frac{1}{2}\omega_p^2 \partial_t \partial_t N_i = N_i' - \omega_p \mathbf{c}_i \cdot \nabla N_i' + \frac{1}{2}\left(\sum_n G_n^i \mathbf{c}_n \mathbf{c}_n\right) : \nabla\nabla N_i' + \omega_p \mathcal{I}_i \qquad (6.31)$$

It is also useful to define the transition probability matrix $\underline{\underline{T}}^i$ for state i,

$$\underline{\underline{T}}^i \equiv \sum_n G_n^i \mathbf{c}_n \mathbf{c}_n \qquad (6.32)$$

Applying the usual Chapman-Enskog formalism, the distributions and the derivatives are expanded by order such that

$$\begin{aligned} N_i &= N_i^{EQ} + \epsilon N_i^{(1)} + \epsilon^2 N_i^{(2)} + \ldots \\ \partial_t &= \epsilon \partial_{t1} + \epsilon^2 \partial_{t2} + \ldots \\ \nabla &= \epsilon \nabla \end{aligned} \qquad (6.33)$$

and the order subscript is dropped for the spatial derivative since no second or higher order gradient terms survive the expansion. Equation (6.31) becomes

$$\begin{aligned} &\omega_p(\epsilon\partial_{t1} + \epsilon^2\partial_{t2})(N_i^{EQ} + \epsilon N_i^{(1)}) + \frac{1}{2}\omega_p^2 \partial_{t1}\partial_{t1}\epsilon^2 N_i^{EQ} \\ &= -\omega_c(\epsilon N_i^{(1)} + \epsilon^2 N_i^{(2)}) - \omega_p \mathbf{c}_i \cdot \epsilon\nabla\left[N_i^{EQ} + \epsilon(1-\omega_c)N_i^{(1)}\right] + \frac{1}{2}\underline{\underline{T}}^i : \nabla\nabla\epsilon^2 N_i^{EQ} + \omega_p \mathcal{I}_i \end{aligned} \qquad (6.34)$$

where substitution was made for N_i' using the relation

$$N_i' = N_i^{EQ} + \epsilon(1-\omega_c)N_i^{(1)} + \epsilon^2(1-\omega_c)N_i^{(2)} \qquad (6.35)$$

which is just the expanded form of equation (6.27).

The first order terms from equation (6.34) give

$$\begin{aligned} \omega_p \partial_{t1} N_i^{EQ} &= -\omega_c N_i^{(1)} - \omega_p \mathbf{c}_i \cdot \nabla N_i^{EQ} + \omega_p \mathcal{I}_i \\ \Longrightarrow \partial_{t1} N_i^{EQ} + \mathbf{c}_i \cdot \nabla N_i^{EQ} &= -\frac{\omega_c}{\omega_p} N_i^{(1)} + \mathcal{I}_i \end{aligned} \tag{6.36}$$

By inspection the mass and momentum moments of this kinetic equation are

$$\partial_{t1} \rho + \nabla \cdot \rho \mathbf{u} = 0 \tag{6.37}$$

$$\partial_{t1} \rho \mathbf{u} + \nabla \cdot \underline{\underline{\Pi}}^{(0)} = 0 \tag{6.38}$$

where $\underline{\underline{\Pi}}^{(0)}$ is the zeroth order momentum flux tensor, which includes the non-local contribution,

$$\begin{aligned} \nabla \cdot \underline{\underline{\Pi}}^{(0)} = \nabla \cdot \sum_i \mathbf{c}_i \mathbf{c}_i N_i^{EQ} - \sum_i \mathbf{c}_i \mathcal{I}_i = \nabla \cdot (\rho \mathbf{u}\mathbf{u} + P_k \underline{\underline{\mathrm{I}}}) + \nabla \cdot P_n \underline{\underline{\mathrm{I}}} \\ \Longrightarrow \underline{\underline{\Pi}}^{(0)} = \rho \mathbf{u}\mathbf{u} + P \underline{\underline{\mathrm{I}}} \end{aligned} \tag{6.39}$$

and substitution was made for the momentum moment of the first order piece of the interaction operator via equations (3.1) and (3.4). As expected the correct mass and momentum transport equations are recovered at the Euler level.

The second order terms in equation (6.34) give

$$\begin{aligned} &\omega_p \partial_{t2} N_i^{EQ} + \omega_p \partial_{t1} N_i^{(1)} + \frac{1}{2} \omega_p^2 \partial_{t1} \partial_{t1} N_i^{EQ} \\ &= -\omega_c N_i^{(2)} - \omega_p \mathbf{c}_i \cdot \nabla [(1 - \omega_c) N_i^{(1)}] + \frac{1}{2} \underline{\underline{T}}^i : \nabla \nabla N_i^{EQ} \end{aligned} \tag{6.40}$$

and now the contribution of the interaction operator has been neglected. It is believed that this will not affect the analysis of the coefficient of shear viscosity, though it will affect the bulk viscosity coefficient. Shear viscosity corresponds to the mean free path of the particles, which will be determined by the "kinetic" part of the microdynamics and should be independent of the "non-local" part. On the other hand, the presence of the interaction operator should affect the bulk viscosity, in analogy to the dependence of this property on the internal structure of molecules in a real fluid. However, evaluation of the second order part of the interaction operator is complex and bulk viscosity is unimportant to the flow dynamics of systems of interest in this work. The results of shearwave tests and soundwave tests (Sections 7.1 and 7.2) will bear out the above assumptions.

Substituting for $N_i^{(1)}$ via equation (6.36) gives

$$\begin{aligned} &\omega_p \partial_{t2} N_i^{EQ} + \omega_p \partial_{t1} \left(-\frac{\omega_p}{\omega_c} \partial_{t1} N_i^{EQ} - \frac{\omega_p}{\omega_c} \mathbf{c}_i \cdot \nabla N_i^{EQ} \right) + \frac{1}{2} \omega_p^2 \partial_{t1} \partial_{t1} N_i^{EQ} \\ &= -\omega_c N_i^{(2)} - \omega_p (1 - \omega_c) \mathbf{c}_i \cdot \nabla \left(-\frac{\omega_p}{\omega_c} \partial_{t1} N_i^{EQ} - \frac{\omega_p}{\omega_c} \mathbf{c}_i \cdot \nabla N_i^{EQ} \right) + \frac{1}{2} \underline{\underline{T}}^i : \nabla \nabla N_i^{EQ} \end{aligned} \tag{6.41}$$

and dividing by ω_p and rearranging,

$$\begin{aligned} &\partial_{t2} N_i^{EQ} + \left(-\frac{\omega_p}{\omega_c} + \frac{1}{2} \omega_p \right) \partial_{t1} \partial_{t1} N_i^{EQ} + \left(\omega_p - 2\frac{\omega_p}{\omega_c} \right) \mathbf{c}_i \cdot \nabla \partial_{t1} N_i^{EQ} \\ &+ \left(\omega_p - \frac{\omega_p}{\omega_c} \right) \mathbf{c}_i \mathbf{c}_i : \nabla \nabla N_i^{EQ} - \frac{1}{2\omega_p} \underline{\underline{T}}^i : \nabla \nabla N_i^{EQ} = -\frac{\omega_p}{\omega_c} N_i^{(2)} \end{aligned} \tag{6.42}$$

The transition probability matrix $\underline{\underline{T}}^i$ can be written strictly as a function of state i by

defining a coefficient q_i such that

$$\underline{\underline{T}}^i = \sum_n G_n^i \mathbf{c}_n \mathbf{c}_n \equiv q_i \mathbf{c}_i \mathbf{c}_i \tag{6.43}$$

It is also assumed that, since a sum over all directions will eventually be taken, the coefficient q_i may as well be a constant, q. Combining the last two terms on the left-hand side of equation (6.42), it may be rewritten as

$$\begin{aligned} \partial_{t2} N_i^{EQ} + \left(-\frac{\omega_p}{\omega_c} + \frac{1}{2}\omega_p\right) \partial_{t1}\partial_{t1} N_i^{EQ} + \left(\omega_p - 2\frac{\omega_p}{\omega_c}\right) \mathbf{c}_i \cdot \nabla \partial_{t1} N_i^{EQ} \\ + \left(\omega_p - \frac{\omega_p}{\omega_c} - \frac{q}{2\omega_p}\right) \mathbf{c}_i \mathbf{c}_i : \nabla\nabla N_i^{EQ} = -\frac{\omega_p}{\omega_c} N_i^{(2)} \end{aligned} \tag{6.44}$$

It is straightforward to take the mass moment of equation (6.44):

$$\begin{aligned} \partial_{t2} \rho + \left(-\frac{\omega_p}{\omega_c} + \frac{1}{2}\omega_p\right) \partial_{t1}\partial_{t1} \rho + \left(\omega_p - 2\frac{\omega_p}{\omega_c}\right) \nabla \cdot \partial_{t1} \rho \mathbf{u} \\ + \left(\omega_p - \frac{\omega_p}{\omega_c} - \frac{q}{2\omega_p}\right) \nabla\nabla : \underline{\underline{\mathbf{\Pi}}}_k^{(0)} = 0 \end{aligned} \tag{6.45}$$

Substituting in for $\partial_{t1}\rho$ from equation (6.37), and noting that in the absence of the interaction operator the zeroth order momentum flux tensor $\underline{\underline{\mathbf{\Pi}}}^{(0)}$ can be replaced with the kinetic part $\underline{\underline{\mathbf{\Pi}}}_k^{(0)}$ in equation (6.38), some additional manipulation gives

$$\partial_{t2} \rho + \frac{1}{2}\left(\frac{q}{\omega_p} - \omega_p\right) \nabla \cdot \partial_{t1} \rho \mathbf{u} = 0 \tag{6.46}$$

or

$$\partial_{t2} \rho + A_0 \nabla \cdot \partial_{t1} \rho \mathbf{u} = 0 \tag{6.47}$$

where $A_0 = (q - \omega_p^2)/2\omega_p$ is an "artifact coefficient." Equation (6.47) shows that the second order mass flux does not vanish unless A_0 vanishes. The condition to avoid this artifact is

$$q = \omega_p^2 \tag{6.48}$$

Note that the partial advection scheme, in which only a fraction ω_p particles in each state move while the rest stay still, is equivalent to having $q = \omega_p$. This can be seen by observing that in this scheme there are only two non-zero transition probabilities, $G_i^i = \omega_p$ and $G_0^i = (1 - \omega_p)$, thus $\underline{\underline{T}}^i = \omega_p \mathbf{c}_i \mathbf{c}_i$. For partial advection, therefore, $A_0 = (1 - \omega_p)/2$, indicating a second order mass flux artifact which goes as $(1 - \omega_p)$.

Taking the momentum moment of equation (6.44) gives

$$\begin{aligned} \partial_{t2}\rho\mathbf{u} + \left(-\frac{\omega_p}{\omega_c} + \frac{1}{2}\omega_p\right)\partial_{t1}\partial_{t1}\rho\mathbf{u} + \left(\omega_p - 2\frac{\omega_p}{\omega_c}\right)\nabla\cdot\partial_{t1}\underline{\underline{\mathbf{\Pi}}}_k^{(0)} \\ + \left(\omega_p - \frac{\omega_p}{\omega_c} - \frac{q}{2\omega_p}\right)\nabla\nabla : \underline{\underline{\underline{B}}} = 0 \end{aligned} \tag{6.49}$$

where the third order tensor $\underline{\underline{\underline{B}}}$ is defined as

$$\underline{\underline{\underline{B}}} = \sum_i \mathbf{c}_i \mathbf{c}_i \mathbf{c}_i N_i^{EQ} \tag{6.50}$$

Using equation (6.38) once again, and defining the coefficient A_1 as

$$A_1 = \frac{\omega_p}{2} - \frac{\omega_p}{\omega_c} \tag{6.51}$$

equation (6.49) becomes

$$\partial_{t2}\rho\mathbf{u} + A_1\nabla\cdot\partial_{t1}\underline{\underline{\Pi}}_k^{(0)} + (A_1 - A_0)\nabla\nabla : \underline{\underline{B}} = 0 \tag{6.52}$$

or

$$\partial_{t2}\rho\mathbf{u} + \nabla\cdot\underline{\underline{\Pi}}_k^{(1)} = 0 \tag{6.53}$$

where the kinetic part of the first order momentum flux tensor $\underline{\underline{\Pi}}_k^{(1)}$ has been defined as

$$\underline{\underline{\Pi}}_k^{(1)} = A_1\partial_{t1}\underline{\underline{\Pi}}_k^{(0)} + (A_1 - A_0)\nabla\cdot\underline{\underline{B}} \tag{6.54}$$

When $q = \omega_p^2$, as required to remove the second order mass flux artifact,

$$\underline{\underline{\Pi}}_k^{(1)} = A_1(\partial_{t1}\underline{\underline{\Pi}}_k^{(0)} + \nabla\cdot\underline{\underline{B}}) \tag{6.55}$$

This is identical to the usual form of the first order momentum flux tensor in the collisional over-relaxation scheme, save for the scaling factor ω_p. Indeed the presence of ω_p is advantageous as it further lowers the value of the lattice viscosity. At this point it can be concluded that the condition $q = \omega_p^2$ is the desired one for the probabilistic advection scheme, as it restores the correct forms of the second order mass and momentum transport. It is still useful to find the viscosity as a function of q in general, to see for example how it behaves for partial advection.

In evaluating the first order momentum flux, only terms through first order in velocity

need to kept. Recalling equation (4.24) for the kinetic pressure P_k,

$$\begin{aligned} \partial_{t1}\underline{\underline{\Pi}}_k^{(0)} &\cong \partial_{t1} P_k \underline{\underline{I}} = \partial_{t1} \frac{1}{2}\langle \varepsilon^K \rangle \underline{\underline{I}} \\ \cong \frac{1}{2} K \partial_{t1} \rho \underline{\underline{I}} &= -\frac{1}{2} K \nabla \cdot \rho \mathbf{u} \underline{\underline{I}} \cong -\frac{1}{2} K \rho \nabla \cdot \mathbf{u} \underline{\underline{I}} = -\frac{1}{2} K \rho \partial_\gamma \mathbf{u}_\gamma \delta_{\alpha\beta} \end{aligned} \tag{6.56}$$

The fact that the isotropic kinetic energy moment per unit mass K is approximately constant has been used. Also the density gradient is of the same order as the velocity, so terms like $\mathbf{u} \cdot \nabla \rho$ are second order in velocity and may be ignored. The term $\underline{\underline{\underline{B}}}$ must be evaluated using the form of the equilibrium distribution N_i^{EQ} shown in Section 4.1,

$$N_i^{EQ} \cong N_j \left[1 + \frac{2\rho}{\langle \varepsilon^K \rangle} (\mathbf{c}_i \cdot \mathbf{u}) + ... \right] \tag{6.57}$$

which gives

$$\begin{aligned} \underline{\underline{\underline{B}}} &= \sum_i \mathbf{c}_i \mathbf{c}_i \mathbf{c}_i N_j \left[1 + \frac{2\rho}{\langle \varepsilon^K \rangle} (\mathbf{c}_i \cdot \mathbf{u}) \right] = \frac{2\rho}{\langle \varepsilon^K \rangle} \sum_i N_j \mathbf{c}_i \mathbf{c}_i \mathbf{c}_i \mathbf{c}_i \cdot \mathbf{u} \\ &= \frac{2\rho}{\langle \varepsilon^K \rangle} \frac{4\langle \varepsilon^K \varepsilon^K \rangle}{D(D+2)} \Delta^{(4)} \cdot \mathbf{u} = \frac{1}{2} \langle \varepsilon^K \rangle \Delta^{(4)} \cdot \mathbf{u} \end{aligned} \tag{6.58}$$

The divergence of $\underline{\underline{\underline{B}}}$ can now be written as

$$\begin{aligned} \nabla \cdot \underline{\underline{\underline{B}}} &= \nabla \cdot \left(\frac{1}{2} \langle \varepsilon^K \rangle \Delta^{(4)} \cdot \mathbf{u} \right) = \partial_\gamma \left[\frac{1}{2} \langle \varepsilon^K \rangle (\delta_{\alpha\beta} \mathbf{u}_\gamma + \delta_{\alpha\gamma} \mathbf{u}_\beta + \delta_{\beta\gamma} \mathbf{u}_\alpha) \right] \\ &= \partial_\gamma \left(\frac{1}{2} \langle \varepsilon^K \rangle \mathbf{u}_\gamma \right) \delta_{\alpha\beta} + \partial_\alpha \left(\frac{1}{2} \langle \varepsilon^K \rangle \mathbf{u}_\beta \right) + \partial_\beta \left(\frac{1}{2} \langle \varepsilon^K \rangle \mathbf{u}_\alpha \right) \end{aligned} \tag{6.59}$$

Terms like $\mathbf{u}_\beta \partial_\alpha \langle \varepsilon^K \rangle$ will be second order in velocity, because the isotropic kinetic energy moment $\langle \varepsilon^K \rangle$ is essentially proportional to density ρ. Thus approximations like $\partial_\alpha (\langle \varepsilon^K \rangle \mathbf{u}_\beta) \cong$

$\langle \varepsilon^K \rangle \partial_\alpha \mathbf{u}_\beta$ are made, and equation (6.59) becomes

$$\nabla \cdot \underline{\underline{B}} \cong \frac{1}{2}\langle \varepsilon^K \rangle (\partial_\gamma \mathbf{u}_\gamma \delta_{\alpha\beta} + \partial_\alpha \mathbf{u}_\beta + \partial_\beta \mathbf{u}_\alpha) \tag{6.60}$$

A complete expression for the kinetic first order momentum flux tensor may now be written out:

$$\underline{\underline{\Pi}}_k^{(1)} = -A_1 \frac{1}{2} K \rho \partial_\gamma \mathbf{u}_\gamma \delta_{\alpha\beta} + \frac{1}{2}\langle \varepsilon^K \rangle (A_1 - A_0)(\partial_\gamma \mathbf{u}_\gamma \delta_{\alpha\beta} + \partial_\alpha \mathbf{u}_\beta + \partial_\beta \mathbf{u}_\alpha) \tag{6.61}$$

which may be rearranged slightly to give

$$\begin{aligned} \underline{\underline{\Pi}}_k^{(1)} &= \frac{1}{2}\langle \varepsilon^K \rangle \left[\frac{2}{D}(A_1 - A_0) - A_0 \right] \partial_\gamma \mathbf{u}_\gamma \delta_{\alpha\beta} \\ &+ \frac{1}{2}\langle \varepsilon^K \rangle (A_1 - A_0) \left(\partial_\alpha \mathbf{u}_\beta + \partial_\beta \mathbf{u}_\alpha - \frac{2}{D} \partial_\gamma \mathbf{u}_\gamma \delta_{\alpha\beta} \right) \end{aligned} \tag{6.62}$$

The transport coefficients, dynamic shear viscosity μ and bulk viscosity η, are defined by

$$\underline{\underline{\Pi}}^{(1)} = -\eta \partial_\gamma \mathbf{u}_\gamma \delta_{\alpha\beta} - \mu \left(\partial_\alpha \mathbf{u}_\beta + \partial_\beta \mathbf{u}_\alpha - \frac{2}{D} \partial_\gamma \mathbf{u}_\gamma \delta_{\alpha\beta} \right) \tag{6.63}$$

Comparing these last two expressions,

$$\eta = -\frac{1}{4} \rho K (A_1 - 3A_0) \tag{6.64}$$

$$\mu = -\frac{1}{2} \rho K (A_1 - A_0) \tag{6.65}$$

As discussed this η does not include the anticipated influence of the interaction operator,

and could be thought of as just the kinetic contribution to the bulk viscosity. The general expression for the kinematic viscosity $\nu = \mu/\rho$ is

$$\nu = \frac{\mu}{\rho} = \frac{1}{2}K(A_0 - A_1) = \frac{1}{2}K\left(\frac{1}{2}\frac{q}{\omega_p} + \frac{\omega_p}{\omega_c} - \omega_p\right) \tag{6.66}$$

When artifact coefficient A_0 vanishes (i.e. $q = \omega_p^2$),

$$\nu = \frac{1}{2}K\omega_p\left(\frac{1}{\omega_c} - \frac{1}{2}\right) \tag{6.67}$$

and the full effect of over-relaxation is recovered. On the other hand for partial advection, when $q = \omega_p$, kinematic viscosity ν' is

$$\nu' = \frac{1}{2}K\left(\frac{1}{2} + \frac{\omega_p}{\omega_c} - \omega_p\right) \tag{6.68}$$

and $\nu' > \nu$ for any combination of $\omega_c > 1$ and $\omega_p < 1$. In particular, as ω_c approaches the limit $\omega_c = 2$, ν becomes very small whereas ν' goes to $K(1 - \omega_p)/4$.

A method for achieving equation (6.43), with a constant q, subject to conditions (6.29) and (6.30), has been adapted from a technique worked out by Chen, Teixeira, Gang, and Molvig [72] (they applied it to irregular lattice geometries rather than a reduced time step). The individual transition probabilities G_n^i are broken into two parts,

$$G_n^i = \bar{G}_n^i + \hat{G}_n^i \tag{6.69}$$

where $\bar{G}_n^i$ represents the expected mean values in the absence of a diffusive term, which corresponds exactly to the partial advection transition probabilities, while $\hat{G}_n^i$ is the diffusive component (which may be positive or negative). Therefore the following system must be solved for the set of unknown $\hat{G}_n^i$:

$$\sum_n \hat{G}_n^i = 0 \tag{6.70}$$

$$\bar{G}_i^n = \left\{ \begin{array}{ll} \omega_p, & \mathbf{c}_n = \mathbf{c}_i \\ (1-\omega_p), & \mathbf{c}_n = 0 \\ 0, & \text{all else} \end{array} \right] \tag{6.71}$$

$$\sum_n \hat{G}_n^i c_n^\alpha = 0 \tag{6.72}$$

$$\sum_n \hat{G}_n^i c_n^\alpha c_n^{\alpha'} + \sum_n \bar{G}_n^i c_n^\alpha c_n^{\alpha'} - q c_i^\alpha c_i^{\alpha'} = 0 \tag{6.73}$$

where α and α' are dimension indices. Clearly this system is highly under-determined, so a Lagrange minimum principle is applied to the set of $\hat{G}_n^i$. The result for the 2D FCHC lattice is

$$\hat{G}_n^i = \frac{q-\omega_p}{1040}\left\{ 26 \sum_{\alpha,\alpha'} c_i^\alpha c_i^{\alpha'} c_n^\alpha c_n^{\alpha'} + \sum_\alpha (c_i^\alpha)^2 \left[7 \sum_\alpha (c_n^\alpha)^2 - 30 \right] \right\} \tag{6.74}$$

6.4 The Multiphase Algorithm

6.4.1 Introduction and System Setup

The multiphase algorithm may be thought of as consisting of three sections: system setup, the main loop, and calculated output. The main loop of course is the heart of the code and contains the major operations performed for each time step: collision, advection, momentum pushing, and energy pushing, in that order. The main loop also contains sitewise measurement of macroscopic variables such as density, temperature, x- and y-components of the velocity, and scalar pressure, and checks on global conservation of mass, momentum, and energy. A flow chart illustrating the overall structure of the algorithm is shown in Figure 6.3; the location of the "measurement" operation is meant indicate that many quantities are monitored dynamically; however, some measurements occur at additional places in the loop.

The present code uses a 31-bit word to represent the population $N_{ji}(\mathbf{x})$ of a state ji at a site $\mathbf{x}$. There are 29 different states for the 2D FCHC lattice with the five species used in the multiphase system. These five different species of particles will be denoted as S_j,

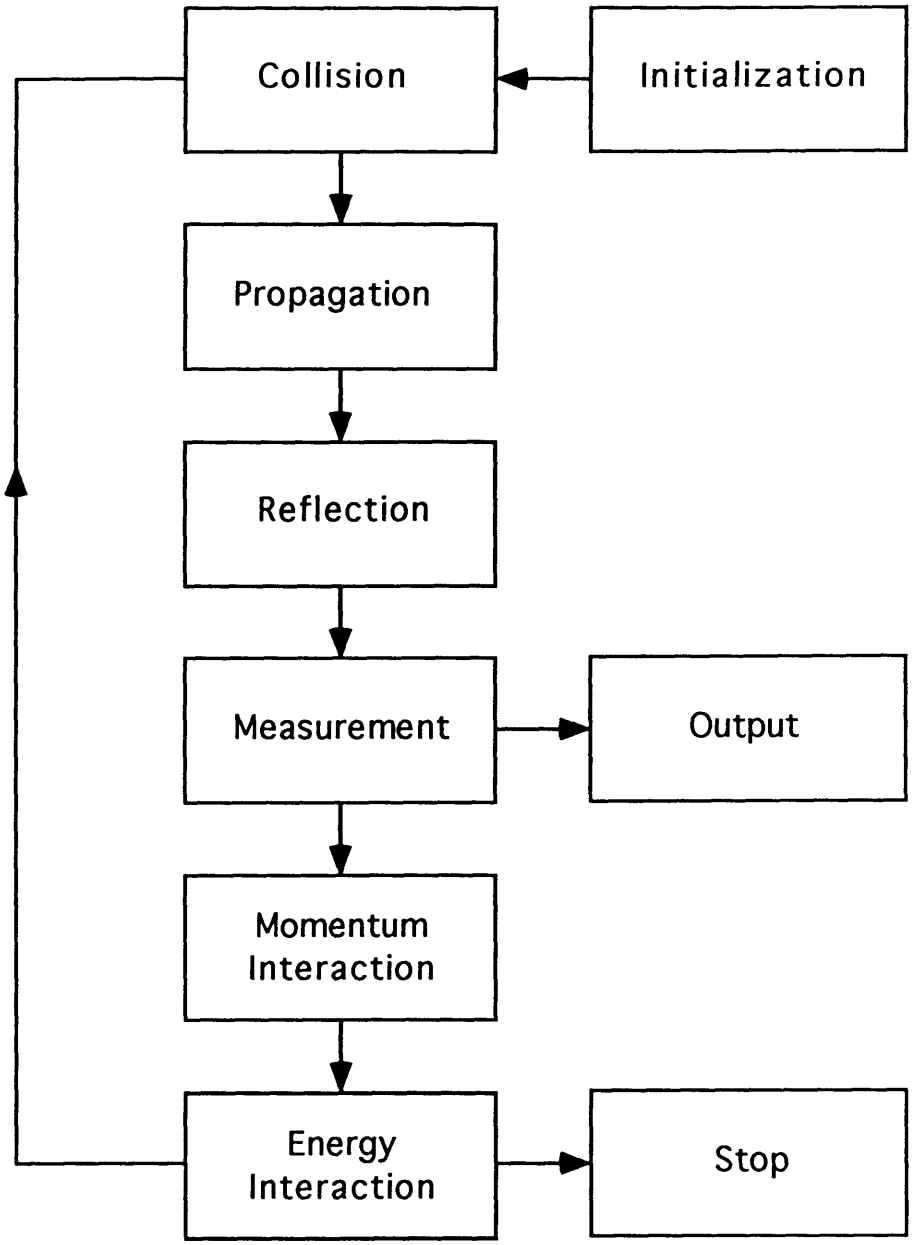

Figure 6.3: Flowchart of algorithm used in implementation of multiphase system.

$j = 0, 1, ..., 4$, and can be thought of in the following way:

$$\begin{aligned} S_0 &= (0,0) \\ S_1 &= (1,0) \\ S_2 &= (2,0) \\ S_3 &= (1,-4) \\ S_4 &= (0,-2) \end{aligned} \tag{6.75}$$

where $S_j = (\varepsilon_j^K, \varepsilon_j^I)$ means that particles of type j have microscopic kinetic energy of ε_j^K and microscopic internal energy of ε_j^I. Species S_3 and S_4 are the new types of species introduced in the multiphase system. There is one state associated with each of the non-moving species S_0 and S_4, and nine states (in 2D) associated with each of the moving species S_1, S_2, and S_3, for a total of 29.

The presence of these species requires six classes of collision rules: one for self-collisions of each of the three moving species, and three energy exchange collisions by which to achieve the desired "rates" governing the relative distribution of particles amongst the five species. The classes of collisions will be denoted as C^α, where C^1, C^2, and C^3 indicate self-collisions of species S_1, S_2, and S_3, respectively, while C^0, C^4, and C^5 indicate energy exchange collisions which will be described momentarily.

In setting up the system, the first step is to use information read from input files to set the microscopic velocity components, weights, and energies of each state, and to form the rule lists for the collision, momentum pushing, and energy pushing operations. Data for determination of the rates is also read in. Key operating variables such as lattice size and

run length are prescribed in a header file.

The matrix $\underline{\underline{G}}$ (i.e. the set of G_n^i) used for the probabilistic advection scheme is constructed, as described in Section 6.3, from the values of the reduced time step ω_p and the collisional over-relaxation parameter ω_c. The geometry of the system is set up in some user specified fashion such that the solid sites are marked as distinct from open (non-solid) sites. Walls are each represented by two rows of solid sites, e.g. at the top and bottom of the lattice.

The next step is the seeding of the lattice, i.e. assigning initial values of the state populations. Seeding is performed by determining the local equilibrium (Boltzmann) distributions N_{ji}^{EQ}, according to equation (4.4), for each site based on assigned values of the following macroscopic properties: density ρ, temperature T, and velocity $\mathbf{u}$. It is also possible to impose a specific level of fluctuations in the initial seeding, and each actual state population is determined from the following algorithm:

$$N_{ji} = N_{ji}^{EQ}(1 - \lambda_f + 2\lambda_f\lambda_r) \tag{6.76}$$

where λ_r is a random number of linear distribution from zero to one. The resulting value is in the range $N_{ji} = N_{ji}^{EQ}(1 \pm \lambda_f)$, and is then dithered to an integer; the fluctuation parameter λ_f is typically set to $\lambda_f = 0.01$.

The most obvious configuration to begin with is uniform density, temperature, and velocity throughout the lattice. Often it is more useful to begin with separate regions of liquid and vapor with densities near the expected equilibrium values. In the shearwave test

(Section 7.1), the initial configuration is uniform density and a sinusoidally varying velocity field. Once the lattice is seeded, initial measurements are made of sitewise properties, and of global properties such as the total system mass, momentum, and energy. System setup is then complete, and the main loop begins.

6.4.2 Collisions

In general, the form of the zero-velocity equilibrium distribution per unit mass $n_j = N_j/\rho$ for species S_j is

$$n_j = r_j y z^{\epsilon_j^T} \tag{6.77}$$

where r_j is a rate coefficient, $y \equiv e^{-\alpha_0}/\rho$, and $z \equiv e^{-\beta_0}$, as shown in Section 4.3. Following equations (6.15), the rate structure may be written in full as

$$\begin{aligned} n_0 &= r_0 y \\ n_1 &= yz \\ n_2 &= yz^2 \\ n_3 &= ryz^{-3} \\ n_4 &= ryz^{-2} \end{aligned} \tag{6.78}$$

where the microscopic internal energy parameters are $v = 4$ and $w = 2$. The rates are implemented through the chemical equilibrium constants, K^α, $\alpha = 0, 1, ..., 5$ (of which again only two can be independently adjusted). There are three energy exchange equilibrium constants, K^0, K^4, and K^5, one for each class of energy exchange collisions. These three

classes of energy exchange collisions are as follows:

$$\begin{aligned} C^0 &: S_{1m} + S_{1n} = S_2 + S_0 \\ C^4 &: S_2 + S_3 = S_1 + S_4 \\ C^5 &: S_{1m} + S_{1n} + S_0 = S_{2m} + S_{2n} + S_4 \end{aligned} \tag{6.79}$$

which may written in terms of the total microscopic energies of each species as

$$\begin{aligned} C^0 &: 1 + 1 = 2 + 0 \\ C^4 &: 2 + -3 = 1 + -2 \\ C^5 &: 1 + 1 + 0 = 2 + 2 + -2 \end{aligned} \tag{6.80}$$

where S_{jm} and S_{jn} in collisions C^0 and C^5 indicate the use of two different states of the same species S_j. The corresponding chemical equilibrium constants are

$$K^0 = \frac{n_2 n_0}{(n_1)^2} = r_0 \tag{6.81}$$

$$K^4 = \frac{n_1 n_4}{n_2 n_3} = 1 \tag{6.82}$$

$$K^5 = \frac{(n_2)^2 n_4}{(n_1)^2 n_0} = \frac{r}{r_0} \tag{6.83}$$

Thus the independent equilibrium constants turn out to be K^0 and K^5. Note that the values of equilibrium constants K^1, K^2, and K^3 for the three classes of self-collisions are always unity.

While it is preferable to use bi-linear collisions whenever possible, the tri-linear collision

C^5 is needed in order to introduce the rate r; for the current choice of species, there is no bi-linear collision which will do so. Indeed collision classes C^0 and C^4 are the only binary energy exchange collisions that exist for this species set, save for the one which may be obtained by "adding" these two collisions to produce the collision C^*:

$$C^* : 1 + -3 = 0 + -2 \tag{6.84}$$

The chemical equilibrium constant for this collision is, however, just r_0 once again, thus collision class C^* is redundant. Any two of the three available bi-linear collisions could be chosen, but another, higher-order collision must be used to complete the set of energy exchange collisions. Collision class C^5 is in fact the only available tri-linear collision whose equilibrium constant contains the rate r.

Each of the zero-velocity equilibrium distributions n_j depends only on the internal energy per unit mass $u = E/\rho$. The system of constraints is solved numerically for many values of u which span the range where a solution exists; in this particular system the range is $-2.2 < u < 0.99$. The result is a set of values of n_j for each species, or alternatively the species populations $P_j = d_j n_j$, as a function of u, as displayed in Figure 6.1. Values of n_j are determined dynamically from this set of values by linear interpolation; if u is somehow out of bounds the values for the near boundary is used. The chemical equilibrium constants are then determined as shown above.

The number of collisions performed for each site was nominally 300, or higher (e.g. 600) for low viscosity simulations ($\nu < 0.04$). There are 157 different collision rules: 14 of class

C^0, 22 each of classes C^1, C^2, and C^3, 33 of class C^4, and 44 of class C^5. For each collision event, a collision rule is chosen at random from the list of 157. Based on the rule selected, and the populations $\{N_a, N_b, ..., N_f\}$ of the states involved in that rule, an N_{scat} is calculated. N_{scat} is the amount of mass pushed out of each of the reactant states and into each of the product states, for the collision "reactions" as written above. For self-collisions [42],

$$N_{scat}(C^j) = \frac{N_a N_b - N_d N_e}{4N_j} \tag{6.85}$$

where N_j still denotes the isotropic distribution (rather than an actual state population). For the energy exchange collisions,

$$N_{scat}(C^0) = \frac{K^0 N_a N_b - N_d N_e}{N_2 + N_0 + 2K^0 N_1} \tag{6.86}$$

$$N_{scat}(C^4) = \frac{K^4 N_a N_b - N_d N_e}{N_1 + N_4 + K^4(N_2 + N_3)} \tag{6.87}$$

$$N_{scat}(C^5) = \frac{K^5 N_a N_b N_c - N_d N_e N_f}{(N_2)^2 + 2N_2 N_4 + K^5[(N_1)^2 + 2N_1 N_0]} \tag{6.88}$$

where individual reactant state populations are indicated by N_a, N_b, and (for collision C^5) N_c, while individual product state populations are indicated by N_d, N_e, and (for collision C^5) N_f. Again the N_j's in the denominators are the isotropic distributions. The first of these energy exchange collisions (C^0) is identical to the one used in the (three speed) standard system [42]. The other two are new, and in particular C^5 is the first use of a tri-linear collision rule. All three are multi-linear processes[6] of the form needed to satisfy a local

[6]Specifically of a type called "smart sandpaper" [18].

H-Theorem [14] and a shot noise theorem [13].

For each chosen rule of the collision process, an N_{scat} is calculated and dithered to integer value, and the corresponding amounts of mass are exchanged between states. If the desired pushing would result in a negative population for one of the states, the rule is skipped. For collisional over-relaxation [17, 19] (i.e. over-relaxation parameter $\omega_c > 1$), the entire cycle of rules for a site is repeated, but with new values of N_{scat} which are just the previous (floating point) N_{scat} values multiplied by $(\omega_c - 1)$ and dithered.

6.4.3 Advection

The traditional advection operation simply rearranges the lattice populations such that

$$N_{ji}(\mathbf{x}) \Longrightarrow N_{ji}(\mathbf{x} + \mathbf{c}_{ji}) \tag{6.89}$$

The more involved but necessary probabilistic advection scheme moves particles such that

$$\sum_n G^n_{ji} N_{ji}(\mathbf{x} - \mathbf{c}_n) \Longrightarrow N_{ji}(\mathbf{x}) \tag{6.90}$$

which may be written in terms of individual events as

$$G^n_{ji} N_{ji}(\mathbf{x}) \Longrightarrow N_{ji}(\mathbf{x} + \mathbf{c}_n) \tag{6.91}$$

where the set of velocity indices n uniquely defines the advection neighborhood. The coefficient G^n_{ji}, an element of the probabilistic advection matrix $\underline{\underline{G}}$, gives the fraction of particles in state ji which are moved in direction n. The set of G^n_{ji} are calculated from equation (6.74). In the case that G^n_{ji} is negative, particles are to be moved into state ji at site $\mathbf{x}$ from state ji at site $\mathbf{x} + \mathbf{c}_n$. The set of n is not generally the same as the set of all particle states ji; in the current system they differ because several sets of states ji have redundant velocity components.

Probabilistic advection is implemented at each site by performing all of the individual scattering events indicated by equation (6.90). However, for each event, it is first determined whether or not that event is eligible for the diffusive component of the probabilistic advection scheme. An event is eligible if both the current site $\mathbf{x}$ and the neighbor site $\mathbf{x} + \mathbf{c}_n$ are non-solid and not part of an interface. A site is considered part of an interface (i.e. not part of a bulk phase) if the density ratio between the site and any of its neighbors is larger than some preset threshold. If the event is eligible, scattering proceeds according to the coefficient G^n_{ji}, such that the dithered value of $G^n_{ji} N_{ji}(\mathbf{x})$ particles are transferred. If not, then the transfer is determined instead by the "partial advection scheme," such that

$$\begin{aligned} \omega_p N_{ji}(\mathbf{x}) &\Longrightarrow N_{ji}(\mathbf{x} + \mathbf{c}_{ji}), \\ (1 - \omega_p) N_{ji}(\mathbf{x}) &\Longrightarrow N_{ji}(\mathbf{x}) \end{aligned} \tag{6.92}$$

Partial advection lacks the diffusive component of probabilistic advection, and is imple-

mented by substituting for the usual value of the coefficient G_{ji}^n in the following way:

$$G_{ji}^n = \left\{ \begin{array}{ll} \omega_p, & \mathbf{c}_n = \mathbf{c}_{ji} \\ (1-\omega_p), & \mathbf{c}_n = 0 \\ 0, & \text{all else} \end{array} \right] \tag{6.93}$$

Each pair of neighbors is considered twice during an advection update; determining the eligibility of each scattering event according to both sites assures that the exchange follows the same advection scheme both times. When the update as described is complete, the desired change in population of each state at each site has been recorded. If for any such state the calculated change in population would result in a negative value, the population $N_{ji}(\mathbf{x})$ of that state is set to zero. The remaining difference is then subtracted from the neighboring populations $N_{ji}(\mathbf{x}+\mathbf{c}_n)$ in randomly chosen scattering events which distribute the burden evenly. This process is continued iteratively until exact mass conservation is recovered without any negative population values.

The final part of advection involves the action taken at solid sites. A "reflection" routine, for example, invokes a simple bounce back rule. The bounce back is implemented by reversing the velocity of each particle at all solid sites in the first layer of a wall, which is adjacent to non-solid sites. Solid sites in the second layer of a wall may be reached by particles of species S_2 which start out next to a wall; these particles are placed back where they started out prior to advection with their velocities reversed. This works because only particles of speed 2 headed directly into the wall can reach the second layer of the wall, and their momentum must carry them a distance of two lattice spacings, which are counted as one to get to the

adjacent solid site and one to get back. In this way the momenta of the solid sites and the mass of the second layer vanish macroscopically, although the solid sites in the first layer do contain finite mass. There are many other possible solid site advection algorithms which could be used to invoke various boundary conditions.

6.4.4 Momentum Pushing

The momentum pushing operation is performed at all open sites. First, all sites are assigned a (floating point) value of the interaction parameter $\psi(\mathbf{x})$, calculated as in equation (3.13). Then for each neighbor pair or "link", the pairwise product of their interaction parameters is calculated and dithered. Finally, a momentum adjustment for each site is calculated and performed according to equation (2.22). The exact integer calculation of the components F_x and F_y of the interaction force at site $\mathbf{x}$ is therefore given by

$$\begin{aligned} F_x &= \sum_m [\psi(\mathbf{x})\psi(\mathbf{x}+\mathbf{c}_m)]c_{mx} \\ F_y &= \sum_m [\psi(\mathbf{x})\psi(\mathbf{x}+\mathbf{c}_m)]c_{my} \end{aligned} \tag{6.94}$$

where the sum is taken over all the sites in the "interaction neighborhood," and the quantities in square braces are first calculated as floating point numbers and then dithered to integer values. In the case that a neighbor $\mathbf{x}+\mathbf{c}_m$ is a solid site, the value of $\psi(\mathbf{x}+\mathbf{c}_m)$ is replaced by that of $\psi(\mathbf{x})$.

The next step is an estimation of the amount of x- and y-momentum which is available for pushing, based on the current populations at site $\mathbf{x}$. If for either component the desired

momentum adjustment cannot be achieved, the amount available is performed, and the remainder is considered the "momentum flip failure" F_x^{fail} or F_y^{fail}. This amount is passed along to the neighbor directly adjacent to $\mathbf{x}$ in the direction of the momentum change, to be performed in a subsequent iteration. That is to say, if $F_x(\mathbf{x})$ is positive, for example, but only an x-momentum change of $F_x^a(\mathbf{x})$ can be achieved, then the value of the burden $F_x^{fail}(\mathbf{x}) = F_x(\mathbf{x}) - F_x^a(\mathbf{x})$ is stored as a momentum adjustment associated with the neighbor directly to the right of site $\mathbf{x}$, but to be carried out in a subsequent run through the lattice which cleans up such momentum flip failures. This procedure is continued iteratively until all momentum flip failures throughout the lattice have been eliminated; in this way momentum is conserved exactly at each time step, even when the desired local momentum change cannot be entirely accomplished.

Finally, the momentum pushing itself is implemented through a sequence of individual scattering events which continues until the calculated momentum adjustments for the current site and current iteration are achieved. These events each alter either x- or y-momentum, thus separate x-pushes and y-pushes are used. In each event, first a random choice is made between an x-push or a y-push, if both are still needed. Then a pushing rule is chosen randomly from a list; there are 23 different x-pushes and the same number of y-pushes. Each push is a unary or binary event in which particles are transferred from one state or pair of states to another state or pair of states of the same species, which is a simple way of automatically conserving energy. The number of particles transferred in each event is determined by an algorithm which attempts to strike a balance between completing the total adjustment quickly and spreading it evenly amongst the available types of pushes.

6.4.5 Energy Pushing

There are two types of energy pushing operations. The first represents contact of the system with a constant temperature reservoir. The second implements the energy adjustment process derived in Section 4.2 by which to eliminate the kinetic pressure artifact for an adiabatic system. All of the two phase simulations in this work were run using the constant temperature algorithm, for the reasons discussed in Section 5.2. However, some of the soundwave tests (Section 7.2) used the adiabatic energy transport algorithm.

In the constant temperature case, each site $\mathbf{x}$ at every time step undergoes an energy change required to set its temperature to that of the reservoir, T_R. This is accomplished by changing the internal energy per unit volume $E(\mathbf{x})$ by an amount

$$\Delta E(\mathbf{x}) = C_v[T(\mathbf{x}) - T_R] = 2\rho[T(\mathbf{x}) - T_R] \tag{6.95}$$

The value of the energy change $\Delta E(\mathbf{x})$ is dithered to an integer, and a sequence of energy pushing events continues until this integer energy adjustment is complete. During the sequence, a pushing rule is chosen randomly from a list. All of the energy pushing rules are binary scattering events which involve pairs of parity states from two different species (a simple way to choose rules which conserve momentum since the momenta of parity states sum to zero); there are 80 of these rules. The number of particles involved in each event is again determined in a way which attempts to minimize the number of events without drastically skewing the resulting distributions.

The other type of energy pushing, used for adiabatic energy transport, requires initial

calculation for each site $\mathbf{x}$ of the value of the interaction energy parameter $Y_{ji}(\mathbf{x})$:

$$Y_{ji}(\mathbf{x}) = \frac{\Gamma}{2}\frac{\psi^2(\mathbf{x})N_{ji}(\mathbf{x})}{\rho(\mathbf{x})} \tag{6.96}$$

as given by equation (4.47); this value is dithered to an integer. Once the complete set of integer Y_{ji}'s is known, an integer energy change is calculated for each site $\mathbf{x}$ by taking the following sum:

$$\Delta E(\mathbf{x}) = \sum_{ji} [Y_{ji}(\mathbf{x}) - Y_{ji}(\mathbf{x} - \mathbf{c}_{ji})] \tag{6.97}$$

as given by equation (4.49). In this operation the sum is taken over the same set of velocity states ji that define the populations N_{ji}, thus the notation is consistent. This energy change $\Delta E(\mathbf{x})$ is now achieved in identical fashion to the method described for the constant temperature case, i.e. via a sequence of energy pushes which are each binary scattering events.

Chapter 7

Basic Simulation Experiments

This chapter presents results of simulation experiments which investigate the basic behavior of the multiphase system and verify the theoretical predictions of the previous chapters. Basic behavior refers to fundamental macroscopic properties which must be properly recovered by the method if it is to be used for simulations of complex flow systems. The key macroscopic properties of a pure fluid (in the context of the current use of the method) are the Galilean invariance coefficient g, the kinematic viscosity ν, the soundspeed c_s, and the pressure $P = P(\rho, u)$ (i.e. the equation of state), while for a phase separated system they also include the equilibrium liquid and vapor densities ρ_f and ρ_g, and the surface tension σ. Additionally there is the gravitational constant, g (this symbol is also used for the Galilean invariance coefficient as they rarely appear together). The following experiments use relatively simple simulation systems to directly or indirectly observe all of these properties for comparison to prediction.

7.1 Momentum Shearwave Decay

The purpose of the "shearwave test"[1] is to measure the Galilean coefficient g and the kinematic viscosity ν. This single phase test verifies that momentum transport has the correct basic form. The Galilean coefficient g should be constant and equal to unity, which implies Galilean invariance and elimination of the dynamic pressure artifact, as shown in Section 4.1. The kinematic viscosity ν should be constant and equal to the predicted value given by the analyses of Section 6.3. Achieving these indications of correct hydrodynamic behavior verifies that the type and number of collisions performed during the collision operation is sufficient to drive the distributions close to equilibrium. In the case of probabilistic advection it also demonstrates the validity of this scheme and its ability to take advantage of collisional overrelaxation to achieve low values of kinematic viscosity. Shearwave test results for both the vapor and liquid phases are presented.

The shearwave test takes advantage of the fact that there is a simple analytical solution to the momentum transport equation for incompressible, isothermal flow with an initial velocity field given by

$$\mathbf{u}(\mathbf{x}, t = 0) = u_{y0}\mathbf{e}_y + u_{x0}\sin(ky)\mathbf{e}_x \tag{7.1}$$

Here $k = 2\pi n_w / L_y$ is the wavenumber of the sinusoidal velocity perturbation, which contains an integer n_w wavelengths. The amplitude of the velocity perturbation is u_{x0}, while u_{y0} is the transverse velocity. The lattice momentum transport equation in this case may be written

[1]The methodology used here follows that of Teixeria [13] who presented shearwave tests for the standard system.

as

$$\partial_t \mathbf{u} + g\mathbf{u} \cdot \nabla \mathbf{u} = \nu \nabla^2 \mathbf{u} \tag{7.2}$$

and the solution is

$$\mathbf{u}(\mathbf{x}, t) = u_{y0}\mathbf{e}_y + u_{x0} \exp(-\nu k^2 t) \sin[k(y - g u_{y0} t)]\mathbf{e}_x \tag{7.3}$$

The shearwave decays exponentially with a time constant that depends on kinematic viscosity ν, and it propagates in the transverse direction at a rate which depends on the Galilean coefficient g. These parameters are solved for by observing that upon taking the Fourier transform of the spatial part of the solution, the *modulus* is given by

$$\ln\left(\frac{2}{u_{x0} L_y}\sqrt{F_{re}^2 + F_{im}^2}\right) = -\nu k^2 t \tag{7.4}$$

while the *phase* is given by

$$\arctan\left(-\frac{F_{re}}{F_{im}}\right) = k g u_{x0} t + \pi/2 \tag{7.5}$$

where

$$F_{re} \equiv \sum_y u_x(y, t) \cos\left(\frac{2\pi k y}{L_y}\right) \tag{7.6}$$

$$F_{im} \equiv \sum_y u_x(y, t) \sin\left(\frac{2\pi k y}{L_y}\right) \tag{7.7}$$

are the real and imaginary components of a discrete version of the transform. The sums are also averaged over the x-direction, in which all behavior should be uniform. Both the

modulus and *phase* should vary linearly with time. Kinematic viscosity ν is taken from the slope of the best fit line of measured values of the *modulus* versus time, and the Galilean coefficient g is taken from the slope of the best fit line of measured values of the *phase* versus time.

Results are presented for the nominal system, over a range of kinematic viscosities, for both the pure liquid and pure vapor, and for both partial and probabilistic advection schemes. The parameters chosen were a perturbation wavelength $n_w = 1$, velocity components $u_{x0} = 0.15$ and $u_{y0} = 0.13$, and lattice size 50 by 50. The nominal multiphase system uses a lattice temperature of $\tilde{R}\tilde{T} = 0.4$, with a van der Waals parameter $Z = 5.66$, corresponding to a two-phase mixture of density ratio 40 (although these experiments are strictly single phase). For liquid systems an equilibrium liquid density $\rho_f \cong 4(10^5)$ was used, and for the vapor systems an equilibrium vapor density $\rho_g \cong 10^5$ was used. Hence different van der Waals constants were used for liquid and vapor, though temperature and parameter Z were the same.

Table 7.1 summarizes the shearwave decay results. Tests were performed for partial time step ω_p equal to 0.5 or 0.2, and over-relaxation parameter ω_c equal to 1, 1.7, or 1.85. Care was taken to avoid regions of liquid phase instability indicated in Figure 6.2 (the liquid soundspeed for this system is $c_s = 2.06$). Advection type "0" means partial advection, while "1" indicates the probabilistic advection scheme was used. The theoretical values of viscosity ν_{th} are calculated from equation (6.68) for the former and equation (6.67) in the latter case. The theoretical value of the Galilean coefficient g is unity. Normally the number of collisions performed during the collision process was $N_{coll} = 300$, but to achieve low viscosities a

case				liquid			vapor		
ω_p	ω_c	Adv	N_{coll}	ν_{th}	ν_{exp}	g_{exp}	ν_{th}	ν_{exp}	g_{exp}
0.5	1	0	300	0.239	0.244	0.990	0.248	0.255	0.993
0.5	1	1	300	0.119	0.123	0.989	0.123	0.130	0.991
0.5	1.7	0	300	0.140	0.145	0.991	0.145	0.152	0.992
0.5	1.7	1	300	0.0210	0.0248	0.987	0.0218	0.0273	0.988
0.5	1.7	1	1000	0.0210	0.0214	0.985	0.0218	0.0224	0.986
0.2	1.7	0	300	0.199	0.204	0.987	0.206	0.210	0.988
0.2	1.7	1	300	0.00842	0.0104	0.985	0.00873	0.0158	0.985
0.2	1.85	1	1000	0.00387	0.00461	0.985	unstable		

Table 7.1: Shearwave test results.

greater number may be desired.

The results show that the Galilean coefficient g tends to be slightly less than unity, but never by more than two percent. In fact additional tests showed that for the standard system or for a vapor in the multiphase system where the time step could be set to $\omega_p = 1$, the deviation in g becomes substantially smaller ($\sim \pm 0.5\%$). The $1 - 2\%$ deviations seen here, particularly in the presence of the probabilistic advection scheme, were similarly observed for a related probabilistic advection method used to implement the standard system on an irregular (parallelepiped) lattice geometry [72]. Moreover, the deviations were substantially reduced in the irregular lattice geometry case by adding a small empirical correction factor to the advection transition probabilities (see Section 6.3), which could similarly be done for the current method.

Strong agreement between the measured and predicted values of the viscosity for $\nu > 0.03$, for both partial and probabilistic advection, indicate that the analysis of Section 6.3 is valid and that these schemes have been properly implemented. The degradation of viscosity at low

values indicates that too few collisions are being performed to achieve the desired degree of over-relaxation. This is verified by the improvement shown for the test cases where a greater numbers of collisions were used. In every case, even when ν_{exp} deviated quite a bit from ν_{th}, the correct Galilean coefficient (to within acceptable error) was achieved and the slope of the *modulus* and *phase* were both observed to remain linear. These are key indications that the system is behaving hydrodynamically. An example of the experimental results is given in Figure 7.1, which shows the *modulus* and *phase* versus time, along with the best fit lines, for the fairly low viscosity case of the liquid with $\omega_c = 1.7$, $N_{coll} = 1000$, $\omega_p = 0.2$ (and probabilistic advection).

Also of primary importance is that even when there is some viscosity degradation, viscosities below $\nu = 0.01$ are still achieved by using probabilistic advection in conjunction with over-relaxation. This is a reduction in viscosity by a factor of 10-20, or more, compared to cases without probabilistic advection or without over-relaxation. This viscosity reduction is important because it increases the value of the Reynolds number which can be achieved by the system, and therefore the range of flow conditions which can be simulated for a given system size.

Shearwave tests for the vapor with $\omega_c = 1.85$ were not be performed because of an instability that occurs in this case. The instability is not the Courant condition violation shown for the liquid; rather it is a well-known phenomenon observed for the standard system [71] in the presence of aggressive flow velocities, a high degree of over-relaxation, and dynamic updating of the energy-exchange collision rate coefficients (also called "dynamic rates"). The use of "advected rates," [71], in which local values of the rate coefficients propagate with the

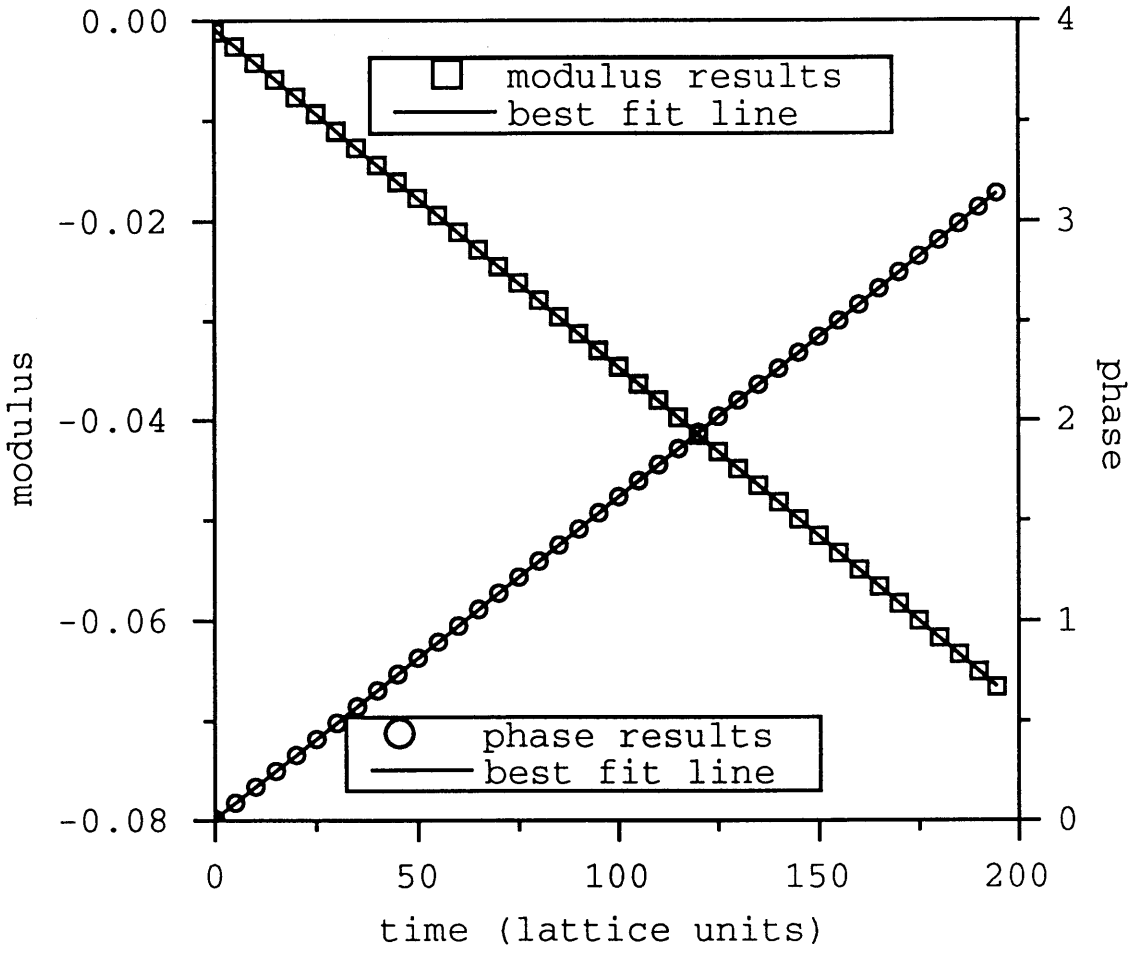

Figure 7.1: Example of shearwave test results – modulus and phase of decaying shearwave vs. time. Slopes of best fit lines indicate lattice viscosity $\nu = 0.0214$ and Galilean coefficient $g = 0.985$; theoretical values are $\nu = 0.210$ and $g = 1$.

flow velocity, has been shown to greatly extend the parameter ranges for which the standard system is stable. Indeed the above case ($\omega_c = 1.85$, $|\mathbf{u}| \cong 0.2$, dynamic rates) for the standard system is known to be stable when advected rates are used, and this scheme would be simple to include in the multiphase system.

It is interesting that the liquid phase remains stable for high flow velocity and low viscosity conditions even in the absence of advected rates. The reason for the apparent stability

improvement associated with the liquid compared to the vapor (and the standard system) is most likely that the momentum and energy pushing operations of the non-local interaction tend to disrupt the feedback mechanism that leads to the growth of a regular spatial pattern through which this type of instability manifests itself. One could take advantage of the fact that the liquid is less prone to instability by using different amounts of over-relaxation in the liquid and vapor phases, especially in situations where the viscosity of the vapor phase is not important to the flow behavior. This will be true when the vapor may be treated as void space, in which case the dynamic viscosity of the vapor should merely be much smaller than that of the liquid (thus the density ratio must be much larger than the kinematic viscosity ratio of the two phases).

7.2 Soundwave Propagation

An important fluid property is the soundspeed. The speed of sound reflects the compressibility of a substance, and is the rate at which small disturbances are propagated through a fluid. A basic general property of liquids is that they have greater soundspeeds than gases. For example, the soundspeed of saturated liquid water at 250 C is 2.3 times as great as that of its equilibrium vapor, and this ratio increases to 3.5 at 20 C.

The speed of sound for a fluid in the multiphase system can be measured by simulation. A simple "soundwave test" consists of perturbing an otherwise uniform system in a particular fashion and observing the response, similar to the "shearwave test." Since the soundspeed is easily derived from the equation of state and the energy transport equation, the soundwave

test provides a convenient way to verify that the multiphase system behaves in agreement with the predicted forms of these relations. The following analysis will focus on the liquid soundspeed, which plays an important role in the experimental observations presented in this chapter and the next.

Soundspeeds can be predicted and measured for the three different lattice energy transport equations identified previously. These energy transport equations and the types of systems they result in will be referred to as: (1) isothermal, (2) adiabatic, and (3) kinetic pressure artifact. The isothermal condition is required to stabilize an interface, as already noted, and is therefore a necessary approximation generally used in the multiphase system; it is not necessary when only a single phase is present. The adiabatic condition, obtained by implementing the local energy adjustment procedure described in Section 4.2, gives the true behavior of a fluid. The adiabatic condition may be used in the soundwave test since there is a single phase fluid and therefore no interface. When neither of these conditions are used to adjust the local macroscopic energy, the system has the kinetic pressure artifact, as described in Section 4.2, where the true pressure is replaced by the kinetic pressure in the energy transport equation.

The soundwave test involves initializing a system with a slightly nonuniform density, which gives rise to soundwaves or "waves of expansion." The nonuniformity, and all resulting variations, may be restricted to one dimension for simplicity, and will be taken to occur in the x-direction. It is convenient to define the fractional density variation $s(x,t)$ from the the constant mean density ρ_0:

$$\rho(x,t) = \rho_0[1 + s(x,t)] \tag{7.8}$$

Denoting the velocity in the x-direction as v, and neglecting second and higher order terms in the perturbative quantities, the mass and momentum transport equations take a 1D linearized form,

$$\frac{\partial s}{\partial t} + \frac{\partial v}{\partial x} = 0 \tag{7.9}$$

$$\frac{\partial v}{\partial t} = -\frac{1}{\rho_0}\frac{\partial P}{\partial x} + b\frac{\partial^2 v}{\partial x^2} \tag{7.10}$$

The coefficient b of the viscous damping term should depend on both the shear viscosity and the bulk viscosity; although a theoretical prediction for the bulk viscosity has not been derived (see Section 6.3), b is expected to be of the same order as the kinematic shear viscosity[2] ν, and it has the same units.

Taking the time derivative of equation (7.9) and the spatial derivative of equation (7.10) and combining them to eliminate the cross-derivative of the velocity v gives

$$\frac{\partial^2 s}{\partial t^2} - \frac{1}{\rho_0}\frac{\partial^2 P}{\partial x^2} + b\frac{\partial^3 v}{\partial x^3} = 0 \tag{7.11}$$

The variation in pressure P with respect to density ρ is the square of the soundspeed c_s:

$$\partial P = \frac{dP}{d\rho}\partial\rho = c_s^2\partial\rho \tag{7.12}$$

Thus equation (7.11) becomes a 1D damped wave equation,

$$\frac{\partial^2 s}{\partial t^2} - c_s^2\frac{\partial^2 s}{\partial x^2} - b\frac{\partial^3 s}{\partial x^2 \partial t} = 0 \tag{7.13}$$

[2]This is also true of real fluids [73].

where equation (7.9) has been used to substitute into the viscous term. Alternatively the time derivative of equation (7.10) may be taken, and replacing the pressure via equation (7.12) gives

$$\frac{\partial^2 v}{\partial t^2} = -c_s^2 \frac{\partial^2 s}{\partial x \partial t} + b \frac{\partial^3 v}{\partial x^2 \partial t} \tag{7.14}$$

and once again using equation (7.9),

$$\frac{\partial^2 v}{\partial t^2} - c_s^2 \frac{\partial^2 v}{\partial x^2} - b \frac{\partial^3 v}{\partial x^2 \partial t} = 0 \tag{7.15}$$

The soundspeed c_s is a strong function of density, but in equations (7.13) and (7.15) it was assumed that the density variations are small enough that the soundspeed may be approximated as constant.

To conduct the experiment a system of length L is initialized in such a way that it evolves according to a single dominant eigenmode. To proceed a solution is assumed which corresponds to a traveling wave,

$$s(x,t) = s_0 \exp(-ikx - i\omega t) \tag{7.16}$$

and likewise for the velocity,

$$v(x,t) = v_0 \exp(-ikx - i\omega t) = \frac{v_0}{s_0} s(x,t) \tag{7.17}$$

If one initial condition is a sinusoidal density perturbation of one complete wavelength, then

$$s(x,0) = s_0 \cos(2\pi x/L) \tag{7.18}$$

which is consistent with equation (7.16) if s_0 is real and $k = 2\pi/L$. The latter is consistent with the periodic boundary conditions $s(0,t) = s(L,t)$ and $v(0,t) = v(L,t)$. From equation (7.9),

$$-i\omega s = ikv = ik\frac{v_0}{s_0}s \Longrightarrow v_0 = -\frac{\omega}{k}s_0 \tag{7.19}$$

Substituting the assumed solution, equation (7.16), back into the governing equation (7.13), gives

$$-\omega^2 + c_s^2 k^2 - ib\omega k^2 = 0 \Longrightarrow \omega = -\frac{1}{2}ibk^2 \pm kc_s \tag{7.20}$$

The real part of the density variation is then

$$s(x,t) = s_0 \exp\left(-\frac{1}{2}bk^2 t\right) \cos k(x \pm c_s t) \tag{7.21}$$

and the real part of the solution for the velocity is

$$v(x,t) = -\frac{\omega}{k}s(x,t) = -s_0 \exp\left(-\frac{1}{2}bk^2 t\right)\left[-\frac{1}{2}bk \sin k(x \pm c_s t) \pm c_s \cos k(x \pm c_s t)\right] \tag{7.22}$$

where $k = 2\pi/L$. It is expected, however, that the condition $bk << c_s$ will always hold, thus the first term in the square brackets is small compared to the second, which gives

$$v(x,t) = \mp cs(x,t) \tag{7.23}$$

where the sign indicates the direction of the traveling wave. The velocity field must therefore be initialized according to

$$v(x,0) = \mp cs(x,0) = \mp cs_0 \cos\frac{2\pi x}{L} \tag{7.24}$$

which forms another initial condition of the soundwave system.

So far energy transport has been ignored, since it need not be considered for the isothermal system. For the non-isothermal systems the temperature field will also evolve and must be initialized properly to yield the desired single eigenmode solution. The temperature variation $z(x,t)$ from the constant mean temperature T_0 can be defined as

$$T(x,t) = T_0[1 + z(x,t)] \tag{7.25}$$

Let E_0 and $\hat{P}_0$ be the internal energy per unit volume and pressure corresponding to mean density ρ_0 and mean temperature T_0, where $\hat{P}$ is the true pressure P for the adiabatic system, and is the kinetic pressure P_k in the artifact system. The 1D linearized energy transport equation may be written as

$$\frac{\partial E}{\partial t} + (E_0 + \hat{P}_0)\frac{\partial v}{\partial x} = 0 \tag{7.26}$$

Dissipative terms, which should only contribute to damping of the temperature variations, have been ignored. Recalling that internal energy per volume in the multiphase system is $E = \rho(2T - a\rho)$,

$$E = 2\rho_0 T_0(1 + s + z) - a\rho_0^2(1 + 2s) \tag{7.27}$$

for small perturbations, and

$$E_0 = 2\rho_0 T_0 - a\rho_0^2 \tag{7.28}$$

Dividing through by ρ_0, equation (7.26) becomes

$$2T_0\left(\frac{\partial s}{\partial t} + \frac{\partial z}{\partial t}\right) - 2a\rho_0\frac{\partial s}{\partial t} + 2T_0\frac{\partial v}{\partial x} - a\rho_0\frac{\partial v}{\partial x} + \frac{\hat{P}_0}{\rho_0}\frac{\partial v}{\partial x} = 0 \tag{7.29}$$

and noting from above that $\partial s/\partial t = -i\omega s$ and $\partial u/\partial x = i\omega s$,

$$2T_0\frac{\partial z}{\partial t} + a\rho_0 i\omega s + \frac{\hat{P}_0}{\rho_0}i\omega s = 0 \tag{7.30}$$

or

$$\frac{\partial z}{\partial t} = -\frac{i\omega s}{2T_0}\left(a\rho_0 + \frac{\hat{P}_0}{\rho_0}\right) \tag{7.31}$$

Direct integration gives

$$z(x,t) - z(x,0) = -\frac{i\omega}{2T_0}\left(a\rho_0 + \frac{\hat{P}_0}{\rho_0}\right)\left(-\frac{1}{i\omega}\right)[s(x,t) - s(x,0)] \tag{7.32}$$

or, defining the coefficient $\xi \equiv (a\rho_0 + \hat{P}_0/\rho_0)/2T_0$,

$$z(x,t) - z(x,0) = \xi[s(x,t) - s(x,0)] \tag{7.33}$$

Thus the temperature variation $z(x,t)$ will follow the density variation $s(x,t)$ if the initial temperature variation is

$$z(x,0) = \xi s(x,0) = \xi s_0 \cos 2\pi x/L \tag{7.34}$$

When the above analysis holds the values of the soundspeed c_s (and the viscous damping coefficient b) can be extracted from measurements of the perturbed quantities, by taking the Fourier transform of the spatial component of the solution (as in the shearwave test analysis). Using the density variation $s(x,t)$, the real and imaginary parts of the transform are defined as

$$F_{re} = \sum_{x=0}^{L} s(x,t) \cos 2\pi x/L \tag{7.35}$$

$$F_{im} = \sum_{x=0}^{L} s(x,t) \sin 2\pi x/L \tag{7.36}$$

According to the predicted solution (7.21), the *modulus* will be

$$\ln\left(\frac{1}{s_0}\sqrt{F_{re}^2 + F_{im}^2}\right) = -\frac{1}{2}bk^2t \tag{7.37}$$

and the *phase* will be

$$\arctan\left(\frac{-F_{im}}{F_{re}}\right) = \pm kc_st \tag{7.38}$$

Thus a plot of the *modulus* versus time should be a straight line with slope $(-bk^2/2)$, and a plot of the *phase* versus time should be a straight line with slope $(\pm kc_s)$.

So far a general soundspeed c_s and temperature variation coefficient ξ, which depend on the nature of the energy transport equation, have been used. These quantities are now derived for each of the three systems identified above. The physical significance of the energy equation with regard to soundspeed is that local density variations are accompanied by local variations in energy, and thus variations in temperature. In principle this provides a driving force for heat transfer between neighboring fluid regions. In a real fluid, however, density

fluctuations occur much too quickly for local thermal equilibrium to be established [73], and instead almost no such heat transfer has a chance to take place. Hence the process is essentially adiabatic, and therefore isentropic; this is found to be an excellent assumption for real materials, and the soundspeed of a fluid is normally defined according to the isentropic variation of pressure with respect to density,

$$c_{sa}^2 = \left[\frac{dP}{d\rho}\right]_S \tag{7.39}$$

and c_{sa} will be referred to as the adiabatic soundspeed. If one could somehow find a way to cause very slow perturbations of a fluid, such that local thermal equilibrium always existed, the fluid would behave with what will be referred to as the isothermal soundspeed c_{si},

$$c_{si}^2 = \left[\frac{dP}{d\rho}\right]_T \tag{7.40}$$

Finally, the soundspeed corresponding to the energy transport equation which includes the kinetic pressure artifact will be referred to as c_{sk}; it is the adiabatic soundspeed when the real pressure is replaced by the kinetic pressure of the lattice gas, and has no physical significance. It is interesting to predict and measure this quantity for the sake of showing that the system does indeed behave with the expected artifact.

In the isothermal system, temperature variations vanish and so does the temperature variation coefficient ξ; the soundspeed c_{si} is found simply from the van der Waals equation,

$$c_{si}^2 = \left[\frac{\partial P}{\partial \rho}\right]_T = \frac{RT}{(1-\rho b)^2} - 2a\rho \tag{7.41}$$

More generally the soundspeed may be derived by considering the total variation in the pressure $P = P(\rho, T)$:

$$dP = \left[\frac{\partial P}{\partial \rho}\right]_T d\rho + \left[\frac{\partial P}{\partial T}\right]_\rho dT \tag{7.42}$$

The internal energy per unit volume is $E = E(\rho, T)$, thus

$$dE = \left[\frac{\partial E}{\partial \rho}\right]_T d\rho + \left[\frac{\partial E}{\partial T}\right]_\rho dT \tag{7.43}$$

which gives

$$dP = \left[\frac{\partial P}{\partial \rho}\right]_T d\rho + \left[\frac{\partial P}{\partial T}\right]_\rho \left[\frac{\partial T}{\partial E}\right]_\rho \left(dE - \left[\frac{\partial E}{\partial \rho}\right]_T d\rho\right) \tag{7.44}$$

To proceed a relationship between $d\rho$ and dE is required which, as mentioned, comes from the energy transport equation. Using $\hat{P}$ as in equation (7.26), the energy transport equation may be written in terms of total differentials as

$$dE = \frac{E + \hat{P}}{\rho} d\rho \tag{7.45}$$

Hence the soundspeed may be written in general as

$$c_s^2 = \left[\frac{dP}{d\rho}\right]_S = \left[\frac{\partial P}{\partial \rho}\right]_T + \left[\frac{\partial P}{\partial T}\right]_\rho \left[\frac{\partial T}{\partial E}\right]_\rho \left(\frac{E + \hat{P}}{\rho} - \left[\frac{\partial E}{\partial \rho}\right]_T\right) \tag{7.46}$$

where only the first term on the right hand side survives if the system is isothermal.

Using the van der Waals forms for the pressure P and internal energy per unit volume E

energy transport mode	theoretical soundspeed c_s	temperature variation coefficient ξ
isothermal	$\frac{RT}{(1-\rho b)^2} - 2a\rho$	0
adiabatic	$\frac{3}{2}\frac{RT}{(1-\rho b)^2} - 2a\rho$	$\frac{1}{2(1-\rho b)}$
kin. P artifact	$\frac{RT}{(1-\rho b)^2} - 2a\rho + \frac{a\rho + K/2}{2(1-\rho b)}$	$\frac{a\rho + K/2}{2T}$

Table 7.2: Analytical form of parameters needed in soundwave test.

to evaluate the partial derivatives, equation (7.46) becomes

$$c_s^2 = \frac{RT}{(1-\rho b)^2} - 2a\rho + \frac{1}{2(1-\rho b)}\left(a\rho + \frac{\hat{P}}{\rho}\right) \tag{7.47}$$

(the subscript "0" has been dropped and it is understood that mean quantities are being used). The last term is similar to that in the definition of the coefficient ξ, and depends on whether the adiabatic or kinetic pressure artifact system is present. For the former, $\hat{P} = P(\rho, T)$ gives

$$c_{sa}^2 = \frac{3}{2}\frac{RT}{(1-\rho b)^2} - 2a\rho = c_{si}^2 + \frac{RT}{2(1-\rho b)^2} \tag{7.48}$$

and

$$\xi = \frac{1}{2(1-\rho b)} \tag{7.49}$$

In the latter case, $\hat{P} = P_k = \langle \varepsilon^K \rangle / 2 = \rho K/2$, where K is the isotropic kinetic energy moment per unit density, as defined in Chapter 6. The parameter K is a function of the internal energy per unit mass u, and can have values in the range 0.82-0.99 (see Figure 6.1,

density ratio	energy transport mode	L	ω_p	$c_{s,th}$	$c_{s,exp}$
10	isothermal	50	0.65	1.13	1.12
10*	isothermal	50	0.65	1.54	1.54
40	isothermal	50	0.65	2.06	2.05
40*	isothermal	50	0.65	2.37	2.36
100	isothermal	50	0.65	2.72	2.71
100*	isothermal	50	0.4	3.17	3.18
400	isothermal	50	0.4	3.72	3.73
10*	isothermal	100	0.65	1.54	1.55
100	isothermal	100	0.65	2.72	2.71
10	adiabatic	50	0.5	1.76	1.82
40	adiabatic	50	0.5	2.85	2.95
100	adiabatic	50	0.5	3.64	3.80
40	kin. P artifact	50	0.4	3.02	3.03
40	kin. P artifact	100	0.4	3.02	3.03

Table 7.3: Soundwave test results for liquid soundspeed. Density was equal to the equilibrium liquid density for a system with the given density ratio, except * indicates somewhat higher density (and hence greater soundspeed). System size L, partial time step ω_p, and energy transport mode were varied as well.

but it is approximately constant for small density variations. Hence the kinetic pressure soundspeed is

$$c_{sk}^2 = \frac{RT}{(1-\rho b)^2} - 2a\rho + \frac{a\rho + K/2}{2(1-b\rho)} = c_{si}^2 + \frac{a\rho + K/2}{2(1-b\rho)} \tag{7.50}$$

and for the temperature variation coefficient,

$$\xi = \frac{a\rho + K/2}{2T} \tag{7.51}$$

Table 7.2 summarizes the theoretical results needed for the soundwave test.

The measured soundspeeds and comparison to theory for a number of soundwave tests are given in Table 7.3. Systems of size $L = 50$ and $L = 100$ were used to verify the correct

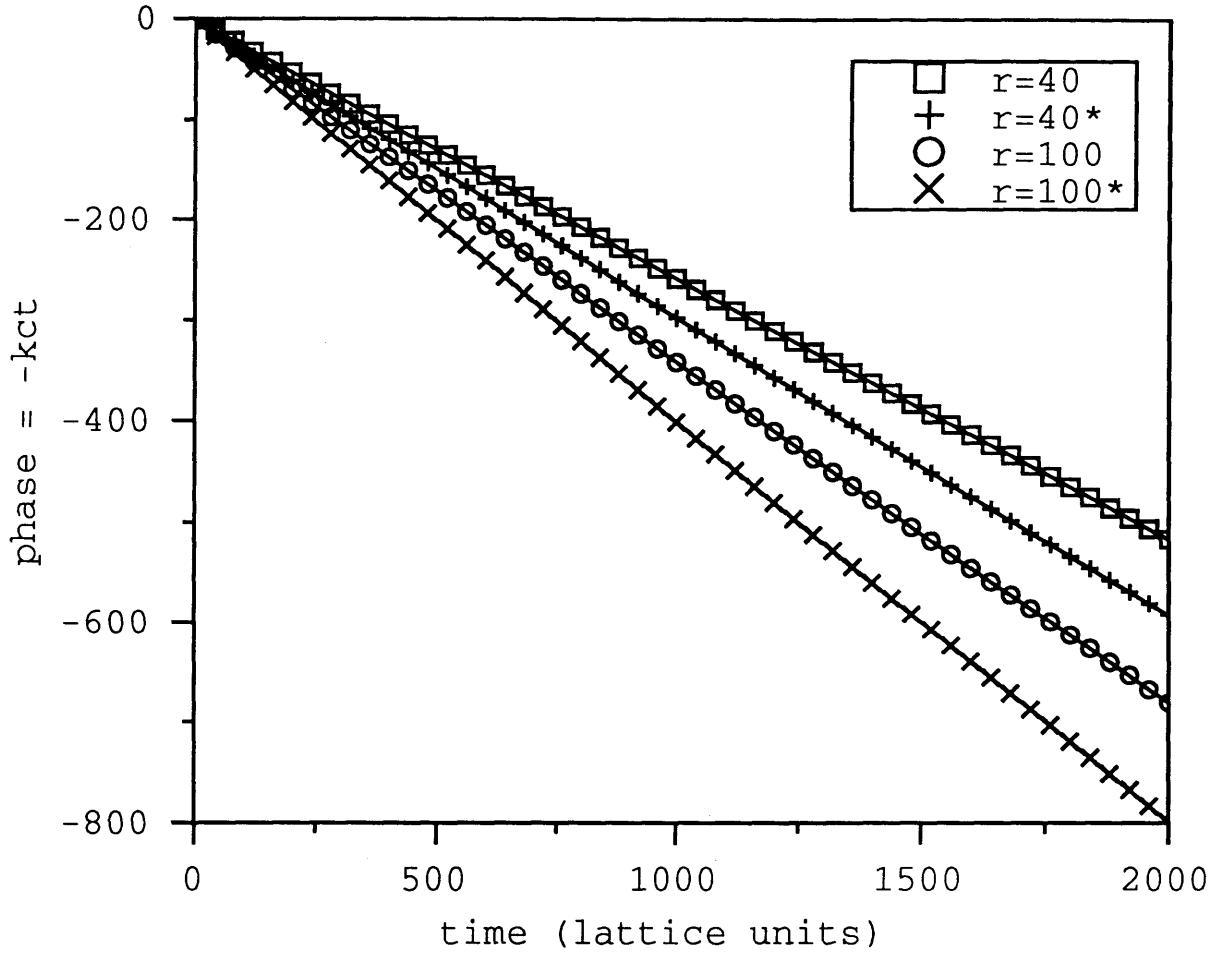

Figure 7.2: Examples of soundwave test results - phase vs. time for four of the cases in Table 7.3, with $L = 50$ and equation of state as indicated by density ratio r. Slopes of best fit lines (solid) equal to $kc_{s,exp}$.

dependence on L; the number of cells in the inert direction was 20. The equation of state was adjusted and is characterized by the varying equilibrium liquid to density ratio, in order to test a range of soundspeeds. To accomplish this the lattice temperature remained fixed at $\tilde{R}\tilde{T} = 0.4$, while the van der Waals constants a and b were varied. The resulting equilibrium liquid density was used in some cases, while in others the liquid density was increased above the equilibrium value in order to further vary the soundspeed. The latter cases are indicated by a * next to the density ratio in Table 7.3.

Excellent agreement between the results and the theory presented in this section is seen for the isothermal and kinetic pressure artifact systems. Good agreement is also seen for the adiabatic system. The noticeable discrepancy there is believed to be due to errors in the calculation of local quantities during the energy adjustment process, because there is a certain subtlety involved in how to properly evaluate the instantaneous particle distributions. It was observed that plots of the *modulus* versus time had significant nonlinearity, which is to be expected since soundwaves of finite amplitude become distorted due to the variation in soundspeed within the wave itself. Nevertheless the behavior of the *phase*, from which the soundspeed is calculated, was observed to be quite linear. This can be seen in Figure 7.2, where the simulation results for four of the isothermal, $L = 50$ cases are plotted, along with the best fit lines.

7.3 Liquid Column with Gravity

Another simple but compelling demonstration that the fluids of the multiphase system obey the expected equation of state can be made by measuring the vertical density profile for a column of fluid in a gravitational field. The fluid at the bottom of the column must be at a higher density and pressure due to the weight of the fluid above it. For a liquid the density gradient will be very small relative to that of a vapor, but the experiment can be still be conducted for a liquid column of moderate height because there is a great deal of flexibility in setting the gravitational constant $\tilde{g}$ of the lattice system. The approximate fractional change in density over the total height of the column L_y is (for small values) given by the

dimensionless quantity $D_g = gL_y/c_s^2$.

The theoretical density profile for a fluid at rest is obtained from the differential force balance,

$$dP = \rho g dy \tag{7.52}$$

Integrating from the bottom h_0 to a height h, and using the van der Waals equation to substitute for dP, gives (for an isothermal fluid)

$$\int_{P_0}^{P} \frac{dP}{\rho} = g(h - h_0) = \int_{\rho_0}^{\rho} \left[\frac{RT}{\rho(1-\rho b)^2} - 2a \right] d\rho \tag{7.53}$$

where P_0 and ρ_0 are the pressure and density at the bottom of the column. Direct integration gives

$$RT \left[\ln\left(\frac{\rho}{\rho_0} \frac{1-\rho_0 b}{1-\rho b} \right) + \frac{1}{1-\rho b} - \frac{1}{1-\rho_0 b} \right] + 2a(\rho_0 - \rho) = g(h - h_0) = gL_y \tag{7.54}$$

An experiment was conducted for a liquid column, with solid top and bottom boundaries and periodic boundaries at the sides. The initial density was uniform and very close to that of the saturated liquid, and the nominal thermodynamic system with van der Waals parameter $Z = 5.66$ was used. The height of the column was $\tilde{L}_y = 200$, with gravitational constant $\tilde{g} = 0.0002$. The system was allowed to relax for 2500 steps, and measurements were taken and averaged for the final 500 steps. Initially there is a pair of small pressure waves formed when the system readjusts the densities at the top and bottom boundaries (which occurs due to imperfect seeding), and the waves travel up and down the column at

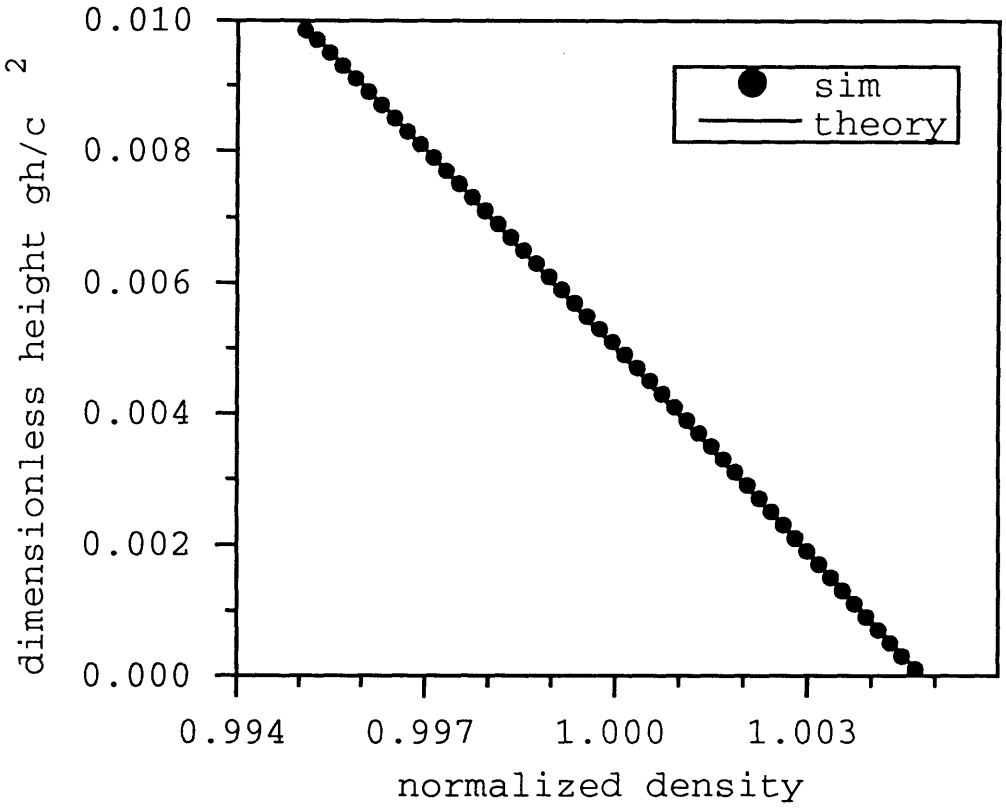

Figure 7.3: Density profile of liquid compressed by gravity (column height was $L = 200$ cells).

the soundspeed until they dissipate away. The reason for waiting a couple thousand steps to begin measurements is both to allow the system time to adjust to the presence of gravity, and to allow the pressure waves to dissipate enough so that they don't affect the results (a relaxation period of this nature was used with many of the other experiments as well).

The results are shown in Figure 7.3. The circles show the height as a function of the measured density, and the solid line represents equation (7.54). The value of height is expressed in the dimensionless form of D_g given above, and density is normalized by the initial uniform value. The strong agreement of the density profile with prediction indicates that the liquid has the correct isothermal compressibility, and verifies that the algorithm

implementing gravity works properly. Measurements were averaged over the width of the column, $L_x = 100$, although it has been found that much smaller widths, as low as $L_x = 6$, may be used with no significant loss in experimental accuracy. Since the soundspeed of this system is predicted to be $c_s = 2.06$, the estimated fractional density change is $D_g = gL_y/c_s^2 = 0.00943$. This compares well to the measured fractional density change over the column of $\Delta\rho/\rho_0 = 0.00962$.

The quantities of this experiment can be converted to real units for a column of water. For example, Figure 5.3 indicates that on the basis of density ratio, the saturation temperature of water corresponding to $Z = 5.66$ is 250 C, and the system is essentially saturated liquid, which at that temperature has a soundspeed of 1145 m/s. Thus with $g = 9.8$ m/s^2, the height of the column can be calculated in meters,

$$L_y = \frac{D_g c_s^2}{g} = 1253 \tag{7.55}$$

which indicates a length conversion of 1253/200 or about 6 meters per lattice cell. This is not surprising since it should take a considerable head of water to produce a density change on order of one percent. If this experiment were to represent a smaller real column, it would have to correspond to a proportionally larger real gravitational field. The relationship between the lattice system and the "real world" is especially simple to establish in this case because there is only one relevant dimensionless quantity, D_g.

7.4 Spontaneous Phase Separation

The experiments described so far were used to observe behavior and verify theory for a single pure phase. The rest of the results are concerned with systems which involve the presence of a liquid region and a vapor region, and a distinct, explicit interface which separates them. Perhaps the most natural starting point is to try to observe the evolution of two phases from a single phase system. If one were working with real materials, they might begin with a liquid, heat it to the saturation point, and then beyond to cause the formation of some amount of vapor. Given the current capabilities of the multiphase system, a similar but more convenient experiment is to initialize the lattice in such a way that it represents a thermodynamically metastable state, then watch it evolve. The system is seeded at a uniform density which lies somewhere on the negative-slope part of the theoretical $P - \rho$ isotherm. This initial metastable density is represented, for example, by point C in Figure 3.1. The thermodynamic conditions are constant temperature and volume, so in order to minimize its free energy, the system should spontaneously separate into a vapor region represented by point A and a liquid one represented by point B (as determined from equations (3.15) and (3.16)). The isothermal condition ensures that evolution of the system will proceed along the given isotherm, adding heat to or removing it from the "temperature reservoir" as needed. If the system were adiabatic instead of isothermal, it would have to be seeded with the correct total energy (rather than temperature) for a given equilibrium state.

An experiment was performed on a 200 square lattice for the nominal thermodynamic system ($Z = 5.66$, equilibrium density ratio $r_\rho = 40$), with an initial uniform density $\rho_0 =$

$0.75\rho_f$, where ρ_f is the predicted equilibrium density of the liquid. The results are shown as a series of snapshots in Figure 7.4. At time $t = 0$ only tiny density variations due to seeding exist. The system quickly breaks up into distinct regions of high and low density. The small regions coalesce and larger, circular vapor bubbles are formed. These coalesce further into very large bubbles, since the vapor volume fraction is about 0.25. The interfaces appear sharp; they are actually about four cells thick. Figure 7.5 shows the evolution of the average bulk phase densities. The liquid reaches a density very close to the predicted equilibrium value almost immediately. A vapor value does not appear right away because it takes some time for enough vapor to accumulate such that it is recognized by the phase identification algorithm. After a couple hundred steps the vapor also reaches a density very close to its predicted equilibrium value.

7.5 Oscillations of the Initially Phase Separated System

As seen from the spontaneous phase separation results it is possible to initialize a system far from thermodynamic equilibrium and allow it to approach equilibrium spontaneously. In many simulations, however, it is desirable to save time by starting out with two regions in a particular spatial configuration which already have the expected equilibrium liquid and vapor densities for the given conditions. We have found this approach to work well, but there are some aspects of it that deserve discussion.

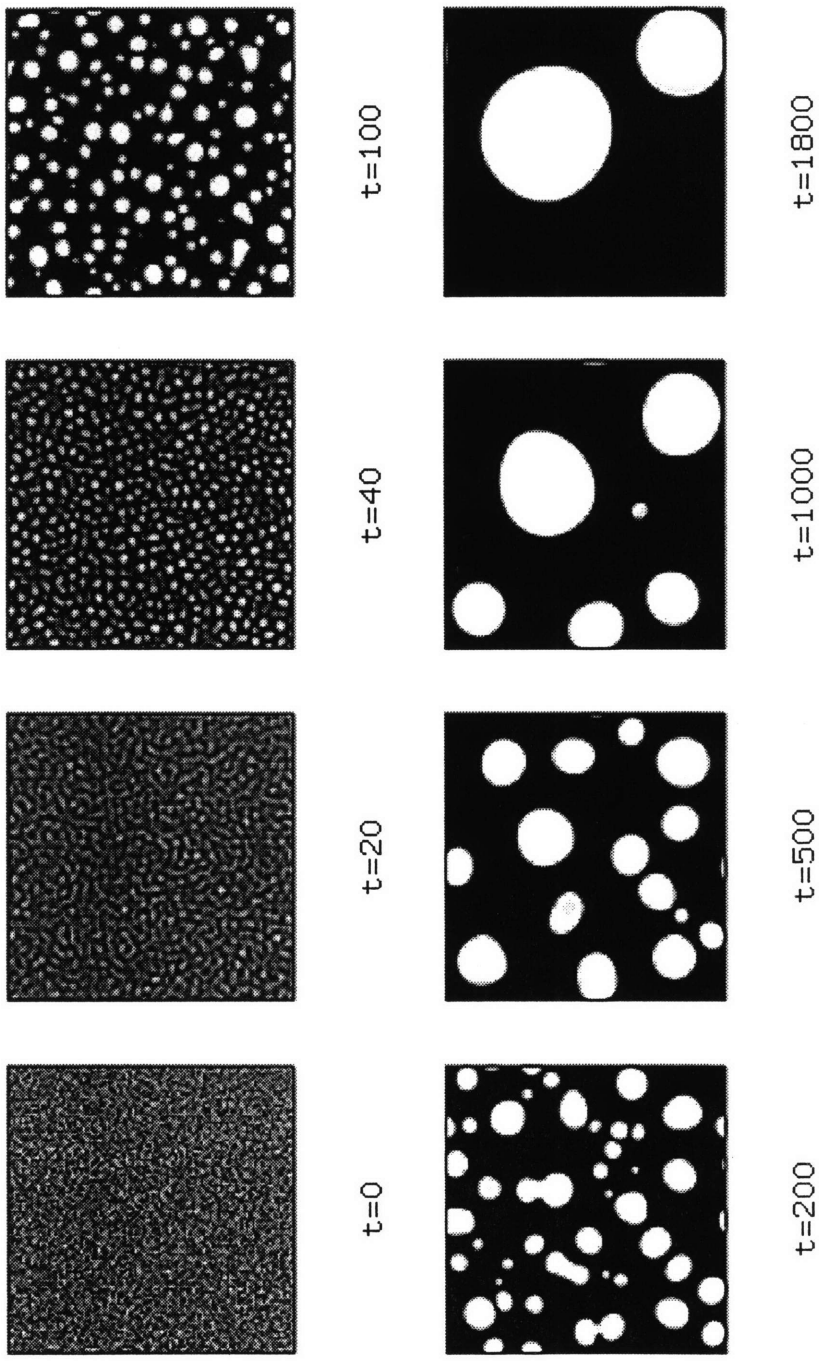

Figure 7.4: Spontaneous phase separation.

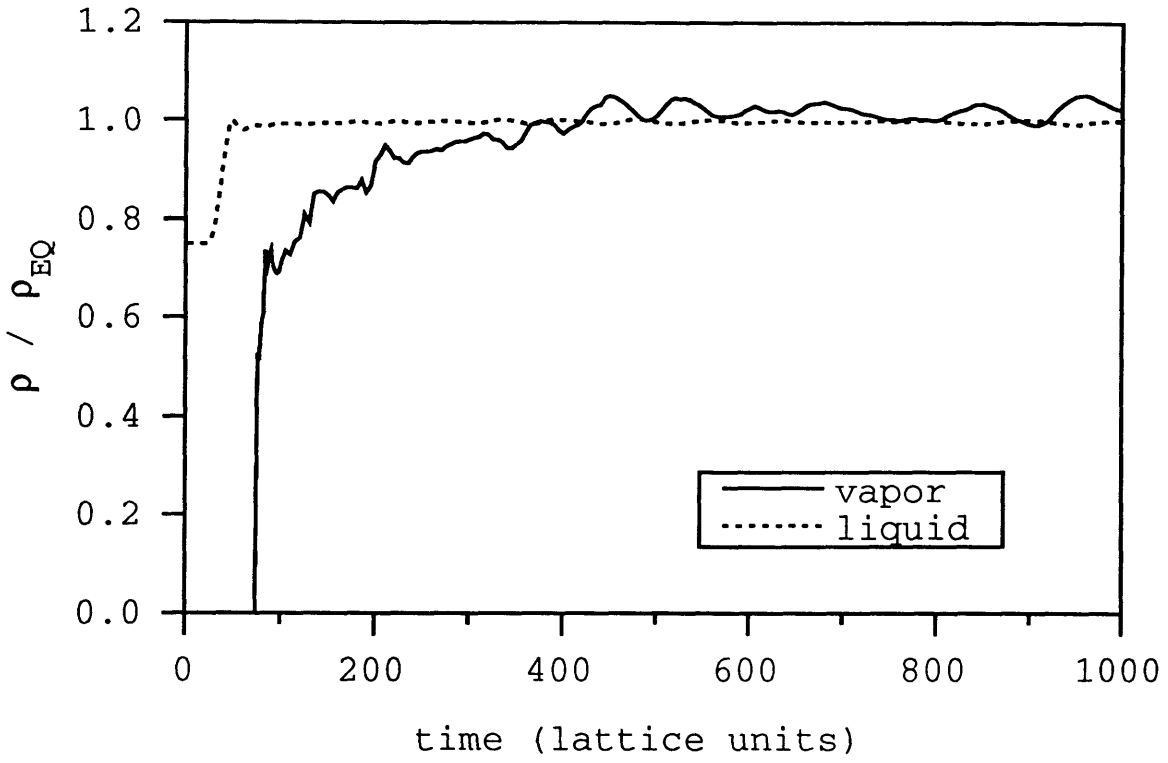

Figure 7.5: Liquid and vapor phase average densities during spontaneous phase separation.

In the first place, even when the equilibrium densities of the bulk phases are successfully predicted, it is difficult to precisely predict the "steady state" interfacial density profiles, especially for arbitrary interface shape. It has been found, however, that even when regions of uniform density representing liquid and vapor are initialized directly adjacent to each other, an interface forms quickly and the regions remain generally intact. Within about ten update steps the presence of an interfacial region of about 3-4 lattice cells in width is clearly visible, and the interface appears to take about 30-50 steps to become fully formed. Judging by density alone the steady state interface is typically about 4-5 cells in width, for liquid to vapor density ratios of about 10 and above[3].

[3]At low density ratio such as 2, the interface thickness is about 6 cells.

Also visible during this early stage is a substantial deficit in the density of the liquid in the region immediately adjacent to the new interface, which apparently borrows mass as needed while forming. The depleted liquid region recovers quickly, becoming uniform right up to the interface within a few tens of time steps. It is believed that the recovery of the depleted region contributes to the formation of a pressure wave. This wave then propagates about the system and causes apparent oscillations in the measured values of the bulk average pressures and densities of each phase. The values of these quantities, which are spatially averaged over the entire regions comprising each phase, appear to undergo damped oscillations about their eventual steady state values. This is always observed, even when the initial bulk phase densities are very close to their final steady state values, but the initial oscillation amplitudes are larger when they are not as close. These oscillations are small to moderate in magnitude, except in the case of the liquid phase pressure because of its sensitivity to density. They may persist for several thousand time steps, before dissipating to magnitudes on the order of noise.

The soundwaves caused by the formation of the liquid-vapor interface, like the soundwaves generated at solid boundaries (mentioned in Section 7.3), are created due to imperfect seeding at locations where a large density gradient exists. When the system relaxes the resulting pressure waves cause time or space averaged quantities such as average phase density to oscillate. This is physically correct since any pressure disturbance should be propagated at the soundspeed and rattle around until it dissipates due to viscosity. It is therefore expected that the frequency of the bulk phase density oscillations should correspond to the soundspeed and the system size. This was investigated for a system configured as equal sized regions of

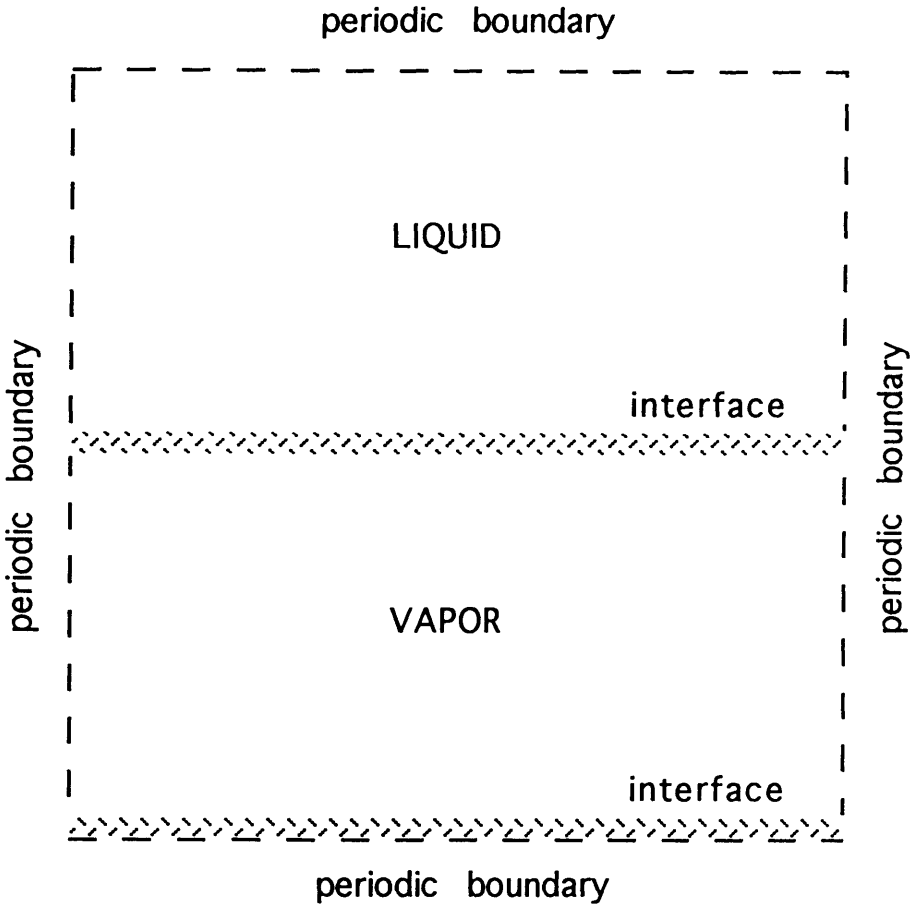

Figure 7.6: Configuration of planar two phase system, consisting of flat interfaces and approximately equal phase volumes.

liquid and vapor separated by a pair of parallel flat interfaces, as shown in Figure 7.6; this will be referred to as a "planar" two phase system. The system was initialized with the top half at the equilibrium liquid density and the bottom half at the equilibrium vapor density (and no gravity force). A single layer of cells with density half the value of the liquid was included in between the phases; it was hoped that this sandwich layer would reduce the size of the initial perturbation, but in fact it did not seem to help much.

It is thought that the soundwaves essentially come to form a standing wave with a wavelength equal to the system size L, causing the liquid density and pressure to oscillate out

of phase with those of the vapor. The liquid phase contains almost all of the mass, and it is therefore expected that the liquid soundspeed will control the oscillation frequency. Defining $s_L(t) \equiv [\rho_L(t) - \rho_0]/\rho_0$ to be the fractional departure of the bulk average liquid phase density $\rho_L(t)$ from its constant steady state value ρ_0, it should be given by integrating the density variation due to a soundwave over the liquid portion of the system (in the x-direction). Equation (7.21) gives the appropriate form of the density variation $s(x,t)$ for a 1D soundwave, and assuming the liquid occupies exactly half the system,

$$s_L = \int_0^{L/2} s_0 \exp\left(-\frac{1}{2}bk^2t\right) \cos k(x \pm c_s t)dx = \mp\frac{2}{k} s_0 \exp\left(-\frac{1}{2}bk^2t\right) \sin kc_s t \qquad (7.56)$$

where s_0 is the initial perturbation amplitude, $k = 2\pi/L$ is the wavenumber, b is the viscous damping coefficient, and c_s is the liquid soundspeed.

Experiments were conducted in which density oscillations were observed for systems with density ratios $r_\rho = 10, 40, 100$ and system sizes $L = 100, 200$. An example of the behavior of the fractional liquid density variation $s_L(t)$ is shown in Figure 7.7 for the system with $r_\rho = 40$ and $L = 100$. Also shown is the corresponding fractional vapor density variation $s_G(t)$. After some initial nonlinearity the phase averaged density clearly varies with time in a damped sinusoidal fashion.

From the form of the right-hand side of equation (7.56) we predict an oscillation frequency $f_{th} = kc_s = 2\pi c_s/L$. The measured oscillation frequency f_{exp} was determined in each case by consecutively numbering each wave peak, plotting the peak number versus the time at which it occurred, and finding the slope of the best fit line. Examples are shown in Figure 7.8,

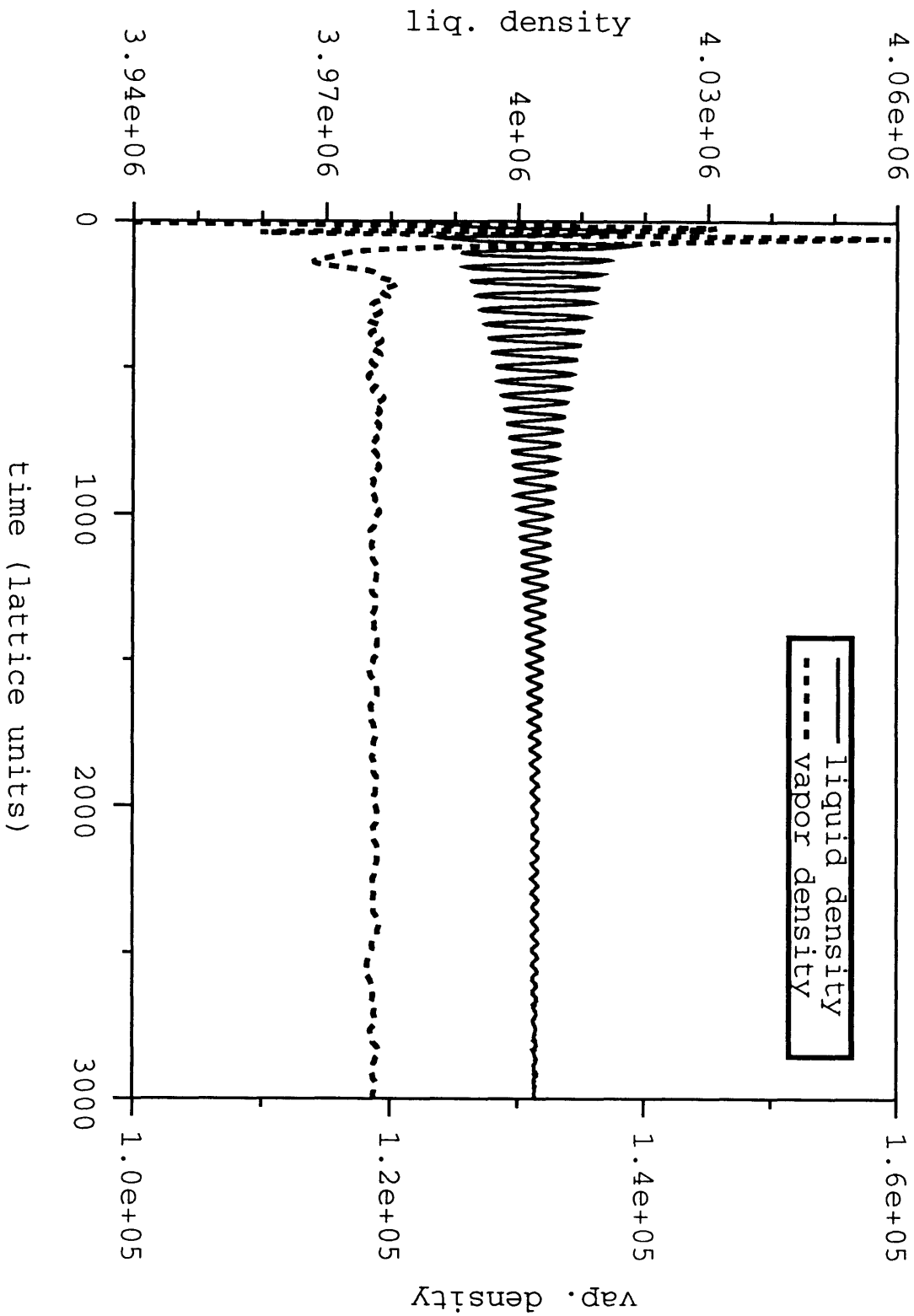

Figure 7.7: Density oscillations in initially phase separated system; $r = 40$, $L = 100$ case.

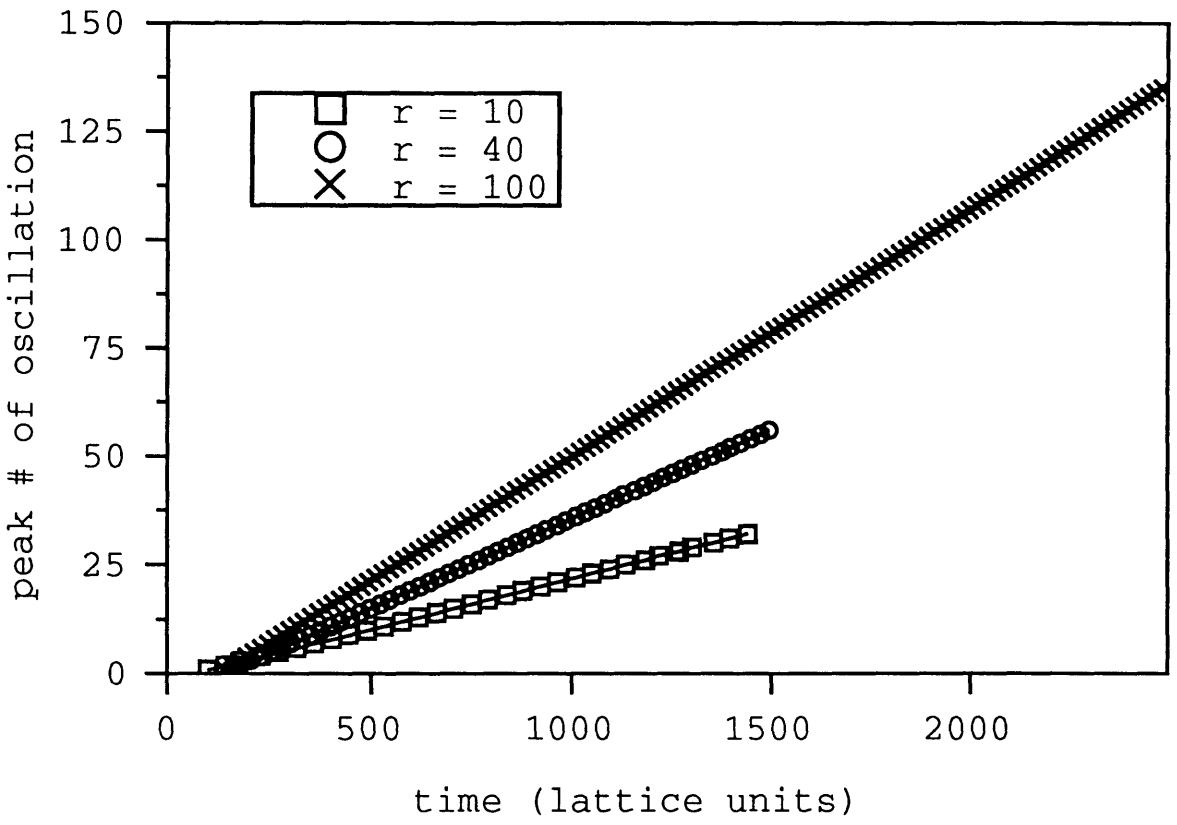

Figure 7.8: Examples of oscillation frequency results - extremum (crests and troughs), vs. time, of phase average liquid density oscillations for the $L = 100$ cases in Table 7.4. Slopes of best fit lines (solid lines) give twice the frequency. Symbols indicate results, r is equilibrium density ratio.

where the results from the three $L = 100$ systems are plotted. Since both crests and troughs were included, the slope is twice the frequency.

Results of these experiments are given in Table 7.4. The measured frequencies f_{exp} agree well with the theoretical values $f_{th} = kc_s$. The isothermal liquid soundspeed c_s is predicted as described in Section 7.2 (where it was verified that the soundspeeds in the simulation agree with prediction). Thus the oscillations, though unwanted, are a manifestation of the physically realistic nature of the system.

r_ρ	L	$f_{th} = 2\pi c_s/L$	f_{exp}
10	100	0.0722	0.0727
40	100	0.129	0.129
100	100	0.170	0.180
10	200	0.0361	0.0366
40	200	0.0647	0.0649
100	200	0.0851	0.0897

Table 7.4: Results of oscillation frequency measurement in initially phase separated planar systems of equilibrium density ratio r_ρ and length L.

7.6 Two Phase Equilibrium Pressure and Density

Once the soundwave-induced oscillations presumably due to interface formation have died down, the planar two phase system is a convenient way to measure the equilibrium (i.e. steady state) properties of the multiphase system. Specifically, the densities and pressures of the liquid and vapor phases can be measured and compared to the theoretically predicted values. Since the interface is flat, there should be no effect of surface tension on pressure, thus the pressures of the two phases should be equal.

A common way to represent two phase equilibrium data is a P-V diagram in which pressure versus volume is plotted for several isotherms which extend from the liquid to the vapor region. The equilibrium values of pressure and density (or specific volume) for the various isotherms form the coexistence curve of the substance. Within the two phase coexistence region bounded by the coexistence curve, the pressure along an isotherm is constant. The peak of the coexistence region is the critical point.

A P-V diagram including the coexistence curve is shown in Figure 7.9. The lines on the diagram represent isotherms for a van der Waals system with van der Waals constants

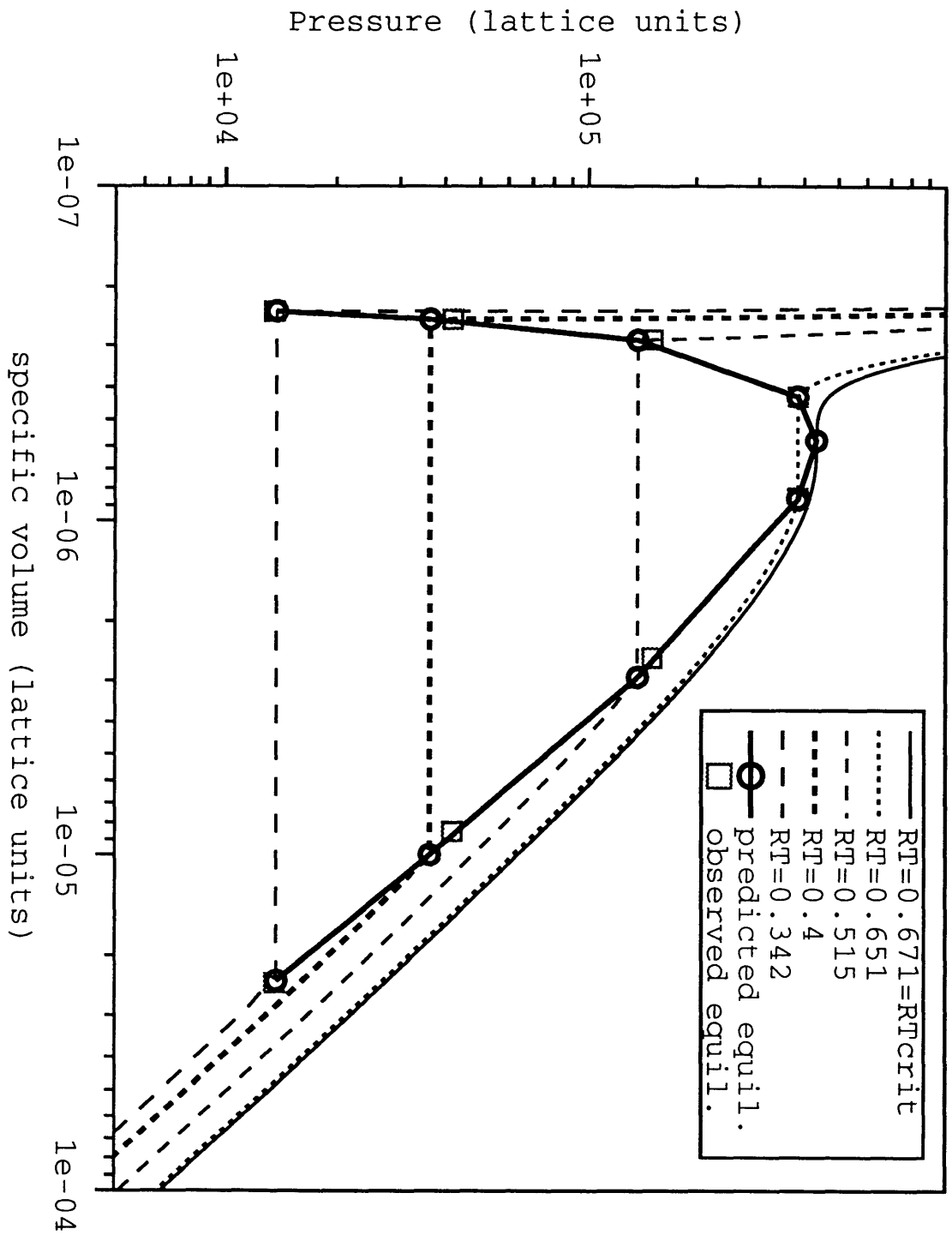

Figure 7.9: Pressure-volume diagram of van der Waals substance with $a = 4.37(10^{-7})$ and $b = 1.93(10^{-7})$ (in lattice units). Comparison of theoretical values (circles) and simulation results (squares) for equilibrium liquid and vapor densities and pressures for several isotherms.

$a = 4.37(10^{-7})$ and $b = 1.93(10^{-7})$ in lattice units. These are commonly used values for the multiphase system, where the densities in terms of particles per site are large, hence the specific volumes are small in these units. The isotherms represent several values of lattice temperature $\tilde{R}\tilde{T}$; a discussion of lattice temperature and its physical meaning was given in Section 5.6. The isotherms are calculated from the equation of state and the Maxwell construction, as discussed in Section 3.1 (and also in Appendix A). Hence they represent the predicted behavior of the multiphase system. The critical temperature for the above van der Waals constants happens to be $\tilde{R}\tilde{T} = 0.671$, and this isotherm is also plotted in Figure 7.9.

Simulations were performed on a 200x200 lattice initialized as a planar two phase system, with $\omega_c = 1$ in each case, and $\omega_p = 1$ for $\tilde{R}\tilde{T} = 0.651$, $\omega_p = 0.7$ for $\tilde{R}\tilde{T} = 0.515$, and $\omega_p = 0.4$ for $\tilde{R}\tilde{T} = 0.4$ and $\tilde{R}\tilde{T} = 0.342$. Different reduced time steps were used due to the different soundspeeds for these systems. The simulation results are plotted in Figure 7.9 as squares; they should be compared to the circles, which denote the equilibrium values bounding the predicted coexistence curve for each given temperature below the critical point. Agreement is quite good; however, some deviation from theory is seen for the vapor phase density and equilibrium pressure in two cases. Indeed it was generally observed in experiments of this nature that the steady state pressure reached by the simulation depends weakly on the over-relaxation parameter ω_c and the partial time step ω_p.

It is likely that these parameters affect the balance maintained within the interface between the advection step, in which there is a net flux of particles towards the vapor, and the momentum-flipping step, in which there is a net change in momentum towards the liquid. This in turn influences the structure of the interface, and therefore the $\psi(\partial^2\psi/\partial n^2)$ term in

equation 3.53 for the force due to interfacial tension $\mathbf{F}_\sigma$. Therefore it is conjectured that the equilibrium pressure has some dependence on this interfacial property, causing the small deviations from thermodynamic prediction. In all cases, however, the pressures of the two phases were equal to each other (to well within experimental error), as physically required by the condition of mechanical equilibrium. Furthermore, the agreement of the results with theory is quite adequate from the viewpoint of hydrodynamic simulation.

7.7 Surface Tension

Two methods were employed for measuring the coefficient of surface tension in the multiphase system, based on two common formulas for surface tension. The first is Laplace's Law, which states that the coefficient of surface tension gives the relationship between the pressure difference ΔP inside and outside of a bubble and the radius of the bubble R_b. For a 2D bubble[4], $\Delta P = \sigma\rho_f/R_b$, where σ is the coefficient of surface tension divided by the liquid density.

To measure the surface tension via Laplace's law, the system was initialized in the configuration of a vapor bubble and allowed to relax for several thousand time steps to avoid measurement error due to pressure oscillations. Bubbles of radii 15, 20, 25, and 30 were each used in three different systems with density ratios 10, 40, and 100. System size varied but the volume fraction of vapor was never allowed to exceed 0.25. The steady state phase average pressures of vapor and liquid were measured (using equation (3.41)), and the results are

[4]This is just a special case of the Young-Laplace equation, $\Delta P = \kappa\sigma\rho_f$, and κ is $1/R$ for a circle.

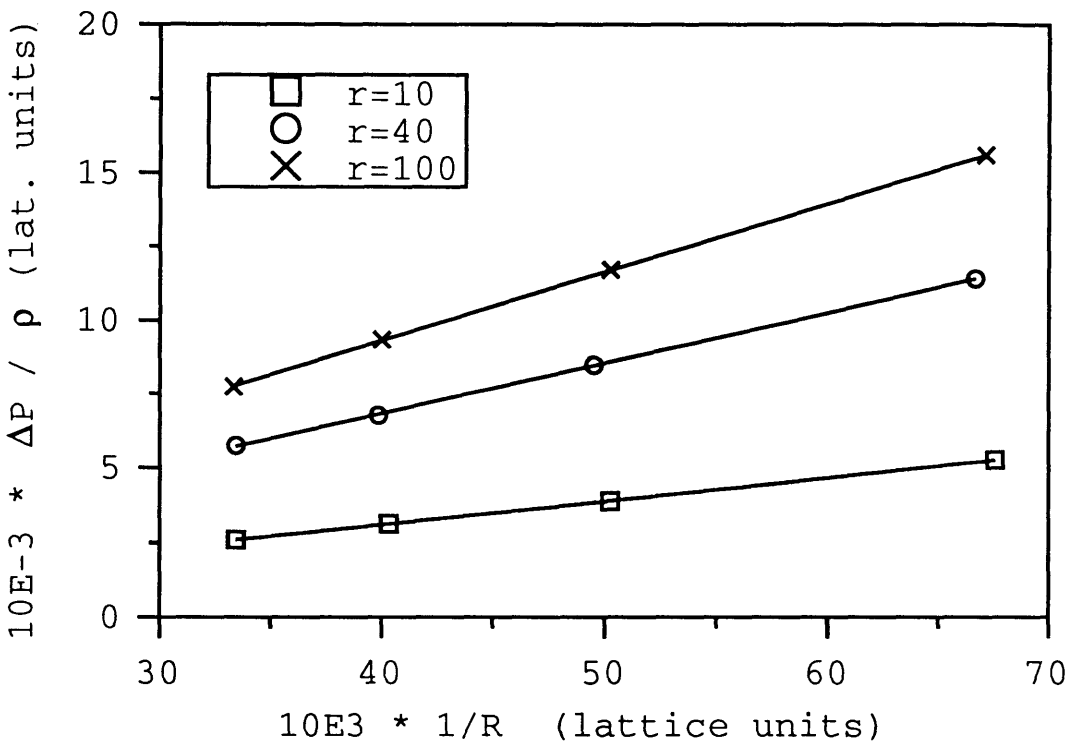

Figure 7.10: Verification of Laplace's Law for vapor bubbles (of radius R) in three systems with density ratios $r = 10$, 40, and 100. Symbols are simulation results, lines are best fits, slopes give coefficients of surface tension (per unit liquid density) of 0.078, 0.17, and 0.23 (in lattice units) respectively.

shown in Figure 7.10 as a plot of ΔP versus $1/R_b$. The linear relationship verifies Laplace's law, and the slopes of the best fit lines indicate surface tensions of 0.078, 0.17, and 0.23 (in lattice units) for systems with density ratio 10, 40 and 100 respectively.

The other method for determining the coefficient of surface tension employs the relation [55],

$$\sigma \rho_f = \int_{z_g}^{z_f} (P_N - P_T) dz \tag{7.57}$$

which is the difference between the normal and tangential components of the pressure tensor, P_N and P_T (see Section 3.3), integrated over a flat interface. The pressure components are

defined as $P_N = \hat{\mathbf{n}}\hat{\mathbf{n}} : \underline{\underline{\mathrm{P}}}$ and $P_T = \hat{\mathbf{t}}\hat{\mathbf{t}} : \underline{\underline{\mathrm{P}}}$, where the zero-velocity pressure tensor $\underline{\underline{\mathrm{P}}}$ is determined according to equation (3.41), and $\hat{\mathbf{n}}$ and $\hat{\mathbf{t}}$ are the unit normal and tangent vectors. Taking the z-direction as normal to the interface and the y-direction as parallel, the vapor and liquid boundaries of the flat interface are z_g and z_f respectively. These are the z-locations on either side of the interface at which the density gradient essentially vanishes and $P_N = P_T$.

Noting the form of equation (3.41), the pressure components at a site $\mathbf{x}(y, z)$ in the flat interface can be written as

$$P_N = P_{zz} = \sum_{ji} \left[N_{ji}(\mathbf{x}) c_{jiz}^2 - \frac{1}{2} \sum_{ji} \psi(\mathbf{x}) \psi(\mathbf{x} + \mathbf{c}_{ji}) c_{jiz}^2 \right] \tag{7.58}$$

and

$$P_T = P_{yy} = \sum_{ji} \left[N_{ji}(\mathbf{x}) c_{jiy}^2 - \frac{1}{2} \sum_{ji} \psi(\mathbf{x}) \psi(\mathbf{x} + \mathbf{c}_{ji}) c_{jiy}^2 \right] \tag{7.59}$$

where c_{jiz} and c_{jiy} are the z and y components of velocity vector $\mathbf{c}_{ji}$. Then the formula for surface tension appropriate for this experiment can be written in discrete form as

$$\sigma \rho_f = \frac{1}{N_y} \sum_{z=z_g}^{z_f} \sum_{y=1}^{N_y} \sum_{ji} \left\{ \left[N_{ji}(\mathbf{x}) - \frac{1}{2} \psi(\mathbf{x}) \psi(\mathbf{x} + \mathbf{c}_{ji}) \right] \left[c_{jiz}^2 - c_{jiy}^2 \right] \right\} \tag{7.60}$$

where N_y is the number of sites (width of the system) in the direction parallel to the interface.

Surface tension was measured in this fashion by setting up planar systems (Figure 7.6), once more with density ratios of 10, 40, and 100, and again they were allowed to relax for several thousand time steps. System size was $L_z = 100$ (normal to the flat interfaces)

and $L_y = 10$. The resulting steady state profiles of the quantity $(P_N - P_T)$ across an interface are shown in Figure 7.11 (where the axis labeled "x" is in fact the z-axis). The pressure components are equal as expected in the bulk regions, but are significantly different through the interface. Theoretically the normal pressure component P_N should be constant (due to the requirement of mechanical equilibrium), while the tangential pressure component decreases substantially. This was observed to be approximately true in the simulation results; some deviation from uniformity occurred for P_N, while nearly all of the difference $(P_N - P_T)$ was due to a large decrease in P_T. The fluctuations in P_N are mainly responsible for the structure which is observable several nodes into the liquid region (to the right of the interface). Values of surface tension calculated from equation (7.60)[5] were found to be 0.079, 0.18, and 0.22 for systems with density ratio 10, 40, and 100 respectively. These are in fine agreement with the values obtained from Laplace's Law. The corresponding density profiles for the interfaces in these systems are shown in Figure 7.12. It is interesting that in all three cases most of the density change occurs over about four cells.

[5]Or by taking the areas under the curves in Figure 7.11.

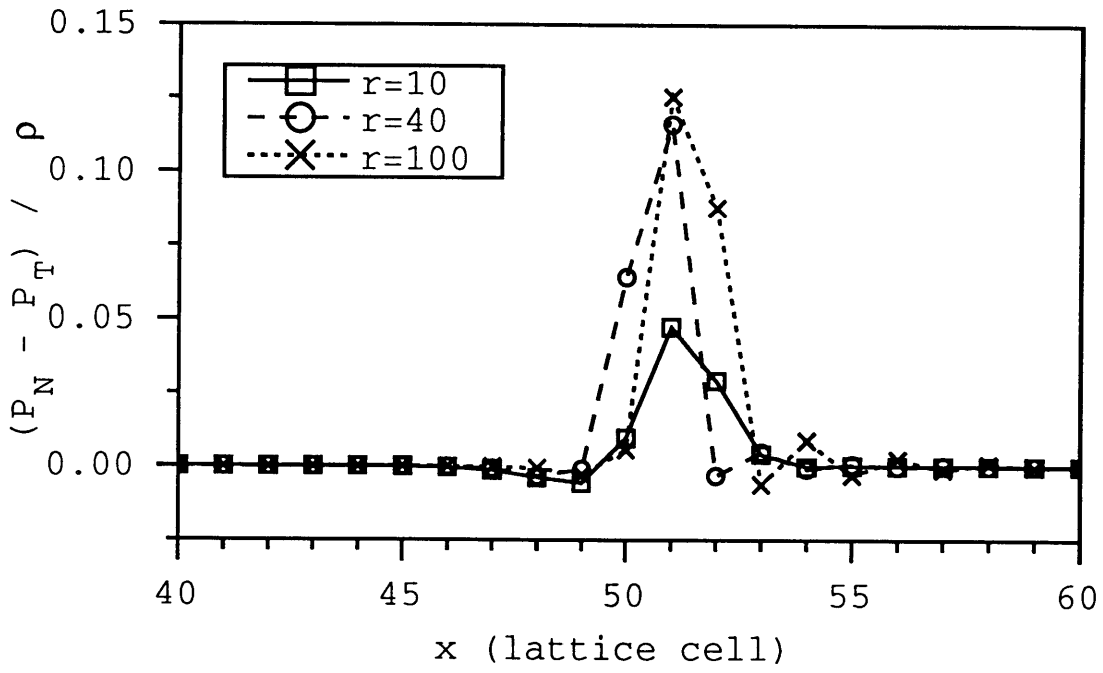

Figure 7.11: $(P_N - P_T)$ across a flat interface; P_N and P_T are normal and tangential components of the pressure tensor. Areas under the curves give surface tension (per unit liquid density) σ: 0.079, 0.18, and 0.22 for systems of density ratio $r = 10$, 40, and 100.

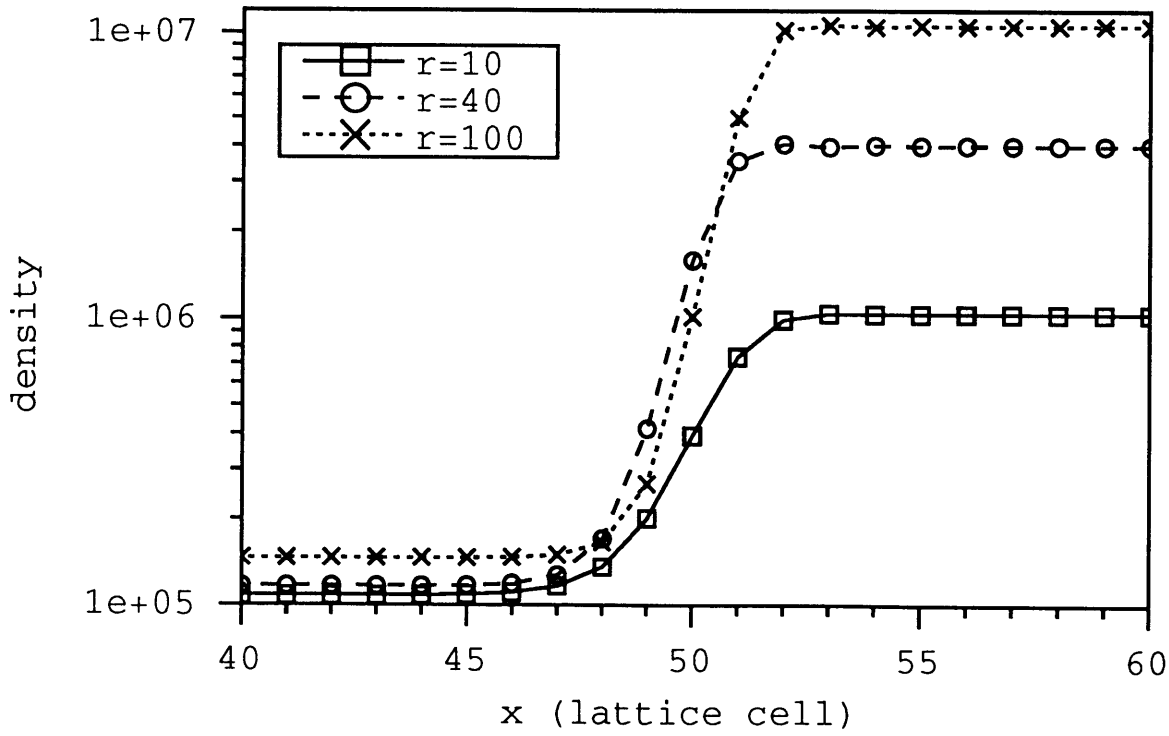

Figure 7.12: Density profile across a flat interface for systems of density ratio $r = 10$, 40, and 100.

Chapter 8

Dynamic Two Phase Experiments

This chapter presents results of simulation experiments for two common dynamic systems in which the interface evolves in space and time. The first involves the Rayleigh-Taylor instability, and the second is a single vapor bubble rising in an otherwise stagnant liquid. These two experiments were chosen because they are compatible with relatively small lattice sizes and very simple boundary conditions, but at the same time involve interactions between some of the key forces which influence two phase flow. They are also systems which are actively investigated in order to better understand the complex dynamics which take place. In the case of Rayleigh-Taylor instability, simulation results may be directly compared with the analytical results of small perturbation theory for the instability threshold of a 2D interface. For the bubble rise system, qualitative comparisons can be made to experimentally known behavior, and major features such as variations in bubble shape can be probed.

8.1 Rayleigh-Taylor Instability

As described by Sharp [74], "The Rayleigh-Taylor instability is a fingering instability of an interface between two fluids of different densities, which occurs when the light fluid is pushing the heavy fluid." For example imagine a tube, closed at the top, and open to the atmosphere at the bottom, with a slug of water occupying all the space between the top and the midpoint. The tube is wide enough such that surface effects are negligible. The water may fall out of the tube, but not because of its weight, which is easily supported by atmospheric pressure. Rather, the air-water interface is unstable to perturbations, such that a small deviation from flatness is able to grow with time into fingers of upward flowing air and downward flowing water. However not all perturbation wavelengths are unstable, only those greater than a threshold size determined by the fluid properties (and the strength of gravity). Hence if the tube is small enough, perturbations of wavelength above the threshold cannot exist, and the water will not fall.

For an inviscid fluid resting on a fluid of much lower density, the threshold or critical wavelength is [56]

$$\lambda_{cr} = 2\pi\sqrt{g/\sigma} \tag{8.1}$$

where σ is once again the usual coefficient of surface tension divided by density. For a one-dimensional interface, its length L is equal to the maximum wavelength it can support. Thus for a given fluid there is a critical system size $L_{cr} = \lambda_{cr}$ for which the interface is Taylor unstable. The situation can be represented non-dimensionally with the Bond number,

$Bo = gL^2/\sigma$. Then the instability condition is simply

$$Bo \geq 4\pi^2 \tag{8.2}$$

The Bond number is essentially the ratio of gravity forces to surface tension forces; the critical Bond number for this system may be defined as $Bo_{cr} = 4\pi^2$. The above relations show that gravity drives the instability, while surface tension acts as a restoring force, because it tends to flatten out the interface.

The Rayleigh-Taylor instability was explored for an interface in the 2D multiphase system. The main purpose was to compare the observed critical Bond number for onset of instability to the theoretical value. Systems of fixed size and constant fluid properties were used, and the gravitational constant was altered in order to vary the Bond number. Lattice systems with top and bottom walls and periodic boundaries at the sides were initialized in a planar configuration (see Figure 7.6) with the liquid occupying the top half and the vapor on the bottom half. The initial densities of each phase were uniform and set to their theoretical equilibrium values.

As expected, the presence of gravity caused the density of each phase to vary with height, and the weight of the liquid increased the average density of the vapor phase. However, it was found that the initially perfectly flat interface that formed between the liquid and vapor would remain so, even for Bond numbers well above Bo_{cr}. This was not true if a very small disturbance, such as a brief density or velocity perturbation, was provided somewhere along the interface. Once an irregularity existed it was observed to damp out or grow with time

depending on whether or not the interface was Rayleigh-Taylor unstable.

A set of experiments was performed on a lattice of 100 cells in width (i.e. L=100) and 120 cells in height (hence each phase was only about 60 cells deep). The nominal thermodynamic parameters were used, so the predicted density ratio was 40 (large enough to justify the assumption $\rho_f >> \rho_g$) and the surface tension was $\sigma = 0.17$. The predicted threshold value of the gravitational constant was therefore $g_{cr} = 4\pi^2\sigma/L^2 = 0.00067$. This prediction assumes a perfectly inviscid liquid; the fluids in the simulation must have finite viscosity, and it was set to $\nu \cong 0.1$. This is low enough to make viscous effects small, as can be seen through the relevant dimensionless combinations, for example, the ratio of viscous to buoyancy forces, $\nu^2/[g_{cr}(L/2\pi)^3] \simeq 10^{-3}$.

In the first experiment the gravitational constant was set to $g = 0.0008$. A perturbation was applied to a small region of the interface; this region was 6 cells wide (in the direction parallel to the interface) by 8 cells high (centered on the interface), and for the first 20 time steps of the simulation, gravity at these sites was increased to $g = 0.005$. The results of this experiment are shown in Figure 8.1 as a series of snapshots of the system as it evolves in time. Initially the perturbation is barely detectable, only the slightest irregularity at the center of the interface is visible. This is still true at time step $t = 200$, as seen in the first frame. The perturbation was observed to spread, eventually forming a sinusoidal shape of wavelength $\lambda = L$. The lower hanging part of the interface then grew until it became a large column of liquid which pushed the vapor out of the way and splashed onto the bottom wall. Almost all of the liquid drained through the column, which became thinner as the top layer of liquid depleted. A small amount of liquid remained on the top wall, first as a thin film,

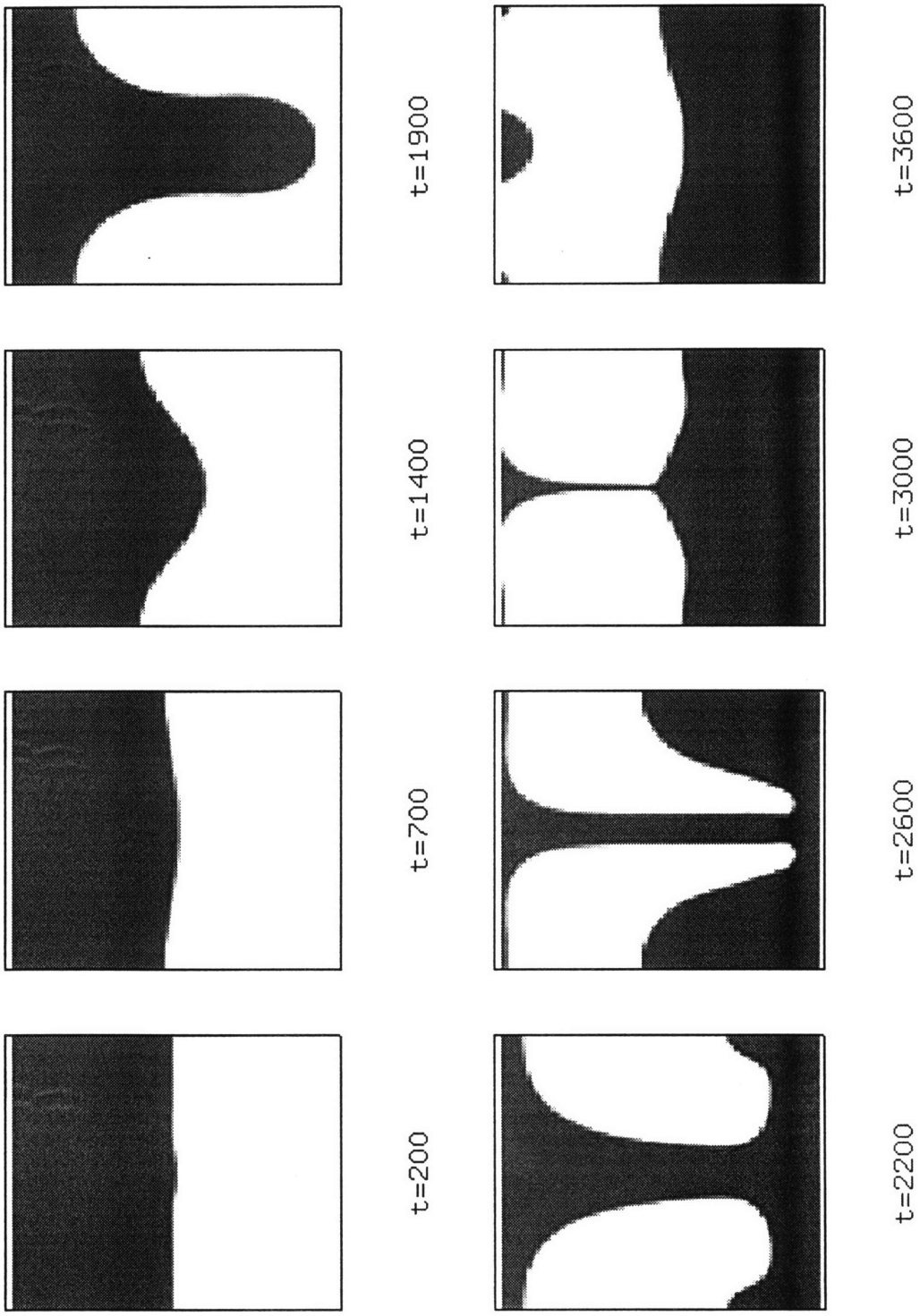

Figure 8.1: Evolution of Rayleigh-Taylor unstable system; $g = 0.0008$ (lattice units), $Bo = gL^2/\sigma = 47$.

then as two small hanging droplets. The rest of the liquid settled on the bottom with the vapor now on top and a wavy surface separating them.

The experiment was repeated with gravitational constant g set to 0.0007, 0.0006, 0.0005, and 0.0004. Everything else was identical in each case, including the initial perturbation. The $g = 0.0007$ system was also observed to be Rayleigh-Taylor unstable, while the other three cases were not. These results agree with the prediction of the critical value of the gravitational constant $g_{cr} = 0.00067$. The entire set of experiments was repeated for an even smaller amplitude initial sinusoidal perturbation of one wavelength. Again the $g = 0.0008$ and $g = 0.0007$ cases exhibited the instability, while for the lower g cases the perturbation died out and the interface remained flat. Based on these results the critical Bond number for the system must have been somewhere between 35 and 41, and hence matches the predicted value of about 39 to within 10% or better.

8.2 2D Bubble Rise Simulations

The theory of a single bubble rising in a column of liquid was discussed in detail in Chapter 5. Here the results of bubble rise simulations performed with the multiphase system are presented. The experiments used systems with top and bottom walls and periodic left and right boundaries. A system was initialized with a uniform density set to the predicted equilibrium value of the liquid, except for a circular region near the bottom where the density was set to the predicted equilibrium value of the vapor. The system was then allowed to relax, in the absence of gravity, to reduce initial pressure oscillations. Once steady state was

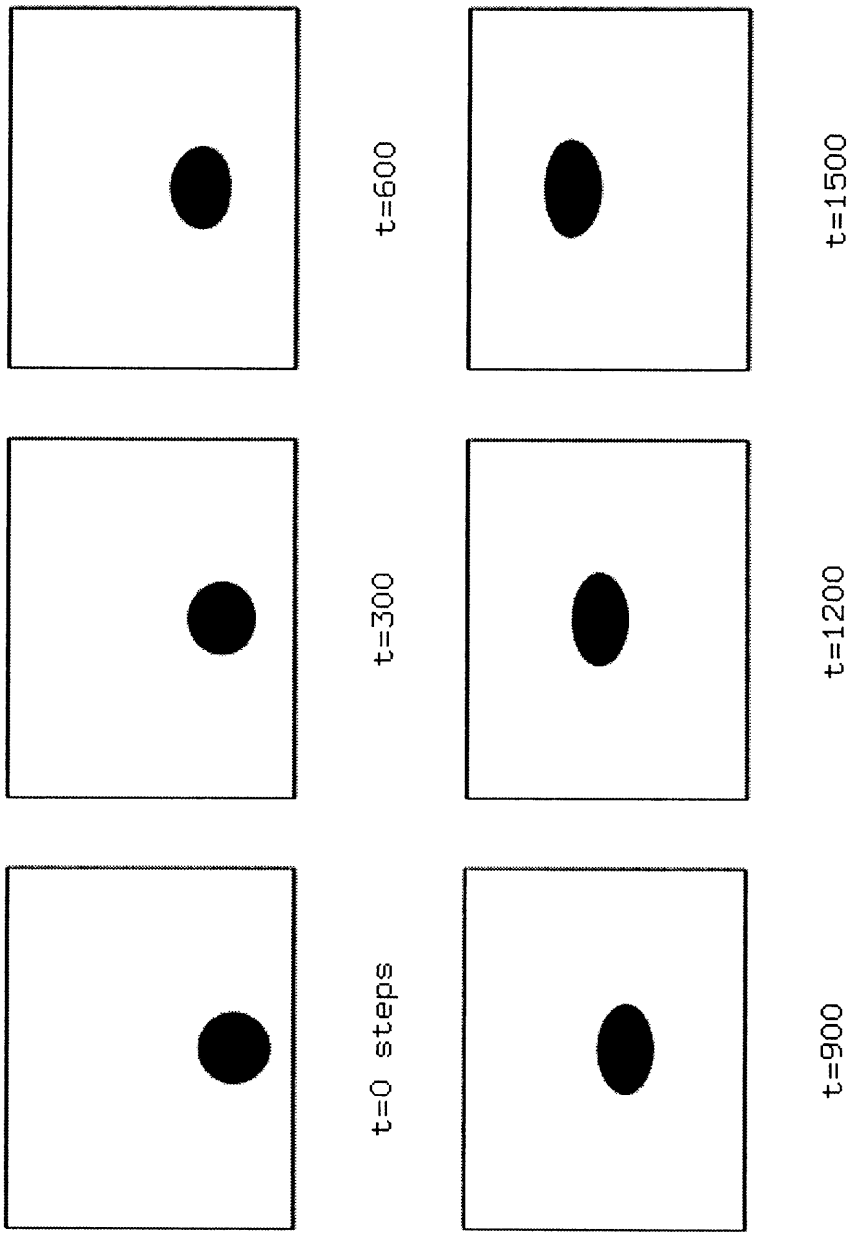

Figure 8.2: Example of 2D bubble rise simulation (corresponds to case J in Table 8.1). Snapshots of density image plot at several times (given in lattice units). Vapor is dark ($\rho \cong 10^5$) and liquid is light ($\rho \cong 4(10^6)$).

well established, gravity was turned on, the liquid pressure became non-uniform with height, and the vapor bubble began to rise. The position of the center of mass of the bubble was recorded as a function of time, as was the area and horizontal cross-sectional width of the 2D bubble. Snapshots (i.e. density maps) of the evolution of one of these experiments is shown in Figure 8.2. In this example the bubble, which began as a perfect circle, became ellipsoidal as its velocity and drag increased, until a steady state (terminal) rise velocity and shape were reached.

Before discussing the results at length, some key experimental details are described. Due to the finite thickness of the interface, measurement of the bubble size is not trivial. The area of the bubble A_b was taken to be the number of sites occupied by vapor, A_G, plus half the number of sites occupied by the interface, A_I; this is illustrated in Figure 8.3 (in which the size of the interfacial region is exaggerated). Hence the equivalent bubble diameter was calculated as

$$d_e = \sqrt{\frac{4}{\pi} A_b} = \sqrt{\frac{4}{\pi}\left(A_G + \frac{1}{2}A_I\right)} \tag{8.3}$$

In order to have a quantitative indication of shape, the width of the bubble projected onto the horizontal plane, d_h, was also measured. Again an average was used, this time between the distance separating the leftmost and rightmost vapor sites, d_{hG}, and the distance separating the leftmost and rightmost interfacial sites, d_{hI}. Hence $d_h = d_{hG} + 0.5\, d_{hI}$; these quantities are also diagrammed in Figure 8.3. The distinction between vapor, interface, and liquid is accomplished by the phase-identification algorithm discussed in Section 6.4[1].

[1]The phase-identification algorithm checks to see that the ratio of the density of a site to that of each of its neighbors is within a threshold range; typically the maximum neighbor-pair density ratio allowed to be considered a member of either phase was 0.9.

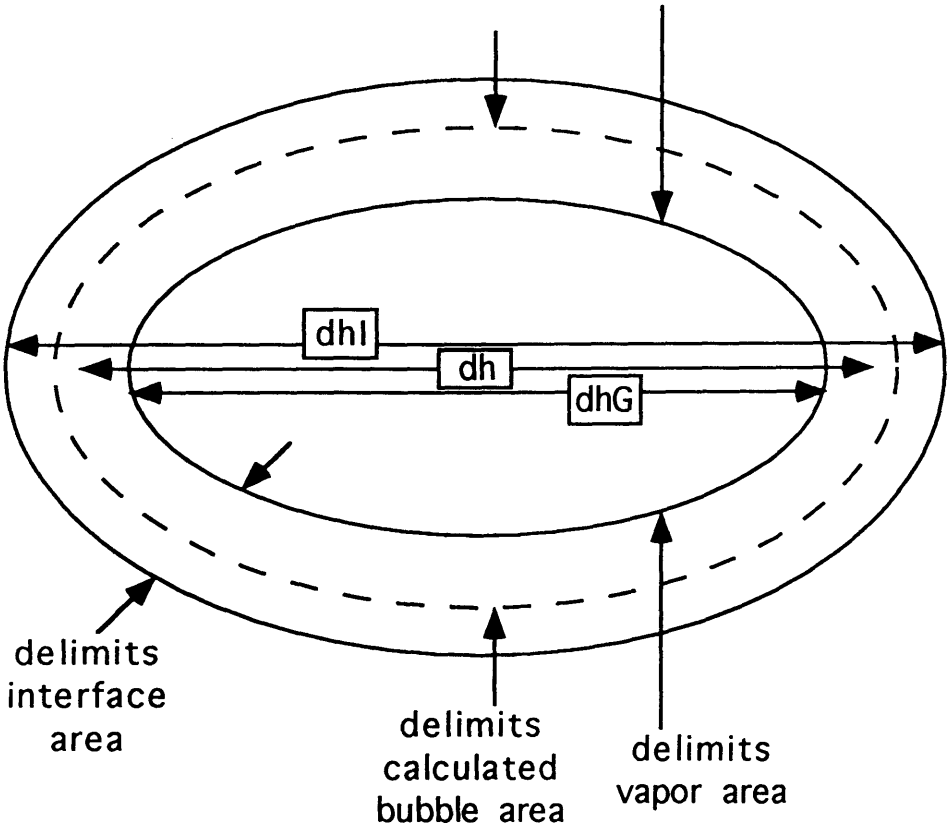

Figure 8.3: Illustration of bubble size determination – calculation of bubble area, and horizontal cross-sectional width.

The purpose of these experiments is to find the terminal velocity of a bubble as a function of its size and the properties of the liquid. When the density and viscosity of the vapor are small relative to those of the liquid, it may be thought of essentially as void space and its properties do not affect the rise velocity. The theoretical equilibrium density ratio in all of the bubble rise simulations was 40, and the actual densities were measured in each case and found to give a density ratio between 36 and 40. Hence the low vapor density approximation was always a good one. Other investigators [10] note that increasing liquid to vapor density ratio above 40 has no significant effect.

The heights of the liquid columns varied with initial bubble size and were chosen so as to

minimize simulation time while still allowing the bubble an opportunity to reach terminal velocity. Typically experiments were run until a reasonably steady velocity was observed, as measured by the slope of the plot of height versus time. Eventually the bubble would approach the top wall and slow down; a significant decrease in velocity could be seen when the top of the bubble was about one to one and a half bubble diameters from the top of the column. The widths of the liquid columns were chosen to be five times the equivalent bubble diameter; hence the nominal blockage was always 20%, but actually more for bubbles which became non-circular. This is a significant amount of blockage, but was necessary to keep simulation times manageable.

Results were obtained for many bubble rise simulations, with bubbles of several sizes, liquids with varying kinematic viscosity, and different values of the gravitational constant. Values of initial bubble diameter were 20, 30, 40, 50, or 60 lattice cells, for which the column sizes were 100x150, 150x150, 200x200, 250x200, and 300x300, respectively. Bubbles smaller than 20 cells in diameter were considered to have too large a ratio of mean bubble diameter to interface thickness, while bubbles larger than 60 cells required correspondingly larger system size and simulation time. The predicted equilibrium values of the liquid and vapor phase densities were always $4(10^6)$ and $1(10^5)$ particles per lattice site, respectively. This corresponds to the "nominal" thermodynamic system, where the van der Waals constants are $a = 4.37(10^{-7})$ and $b = 1.93(10^{-7})$, and the lattice temperature is $\tilde{R}\tilde{T} = 0.4$. Therefore, as shown in Section 7.7, the surface tension coefficient was always taken to be $\sigma = 0.17$.

For a given simulation the predicted lattice viscosity $\tilde{\nu}$ of the liquid is basically a function of the collisional over-relaxation parameter ω_c and the partial time step ω_p, as shown in

Section 6.3. It was seen in Section 7.1, however, that the actual viscosity could deviate somewhat from the theoretical value, and the amount of deviation depends on the number of collisions used in the collision process. Therefore for cases with low lattice viscosity ($\tilde{\nu} < 0.1$), a shearwave test was conducted where the viscosity was measured using precisely the same values of ω_c, ω_p, and number of collisions as in the bubble rise simulation. This viscosity was then used when determining the Reynolds and Morton numbers for the simulation.

Values of the important parameters used in each experiment are given in Table 8.1 (in lattice units, and the $\tilde{}$ is dropped for the moment). These are the gravitational constant g, kinematic viscosity ν, and nominal initial bubble diameter d_o (i.e. the diameter of the circle initially seeded with the equilibrium vapor density). The next columns give the results in the form of the measured quantities mentioned above. These are the equivalent diameter d_e, horizontal cross-section d_h, and terminal rise velocity U_b of the bubble (also in lattice units).

The terminal velocity was taken to be the slope of the best fit line for the height of the bubble (based on its center of mass) plotted against time, taken over a region of the plot which was very linear. This is illustrated in Figure 8.4, which contains the height versus time results for the simulation pictured in Figure 8.2, and which corresponds to case J in Table 8.1. The linear region was selected by eye, and typically there was no discernible deviation from the best fit line for small bubbles (larger bubbles tended to wobble in shape and velocity, as shown below). The time span used in the calculation of the terminal velocity for each case was also used in determining the time-averaged values of d_e and d_h.

Table 8.1 also shows for each case the key dimensionless quantities of the bubble rise problem: Eotvos number $Eo = gd_e^2/\sigma$, Morton number $M = g\nu^4/\sigma^3$, and Reynolds number

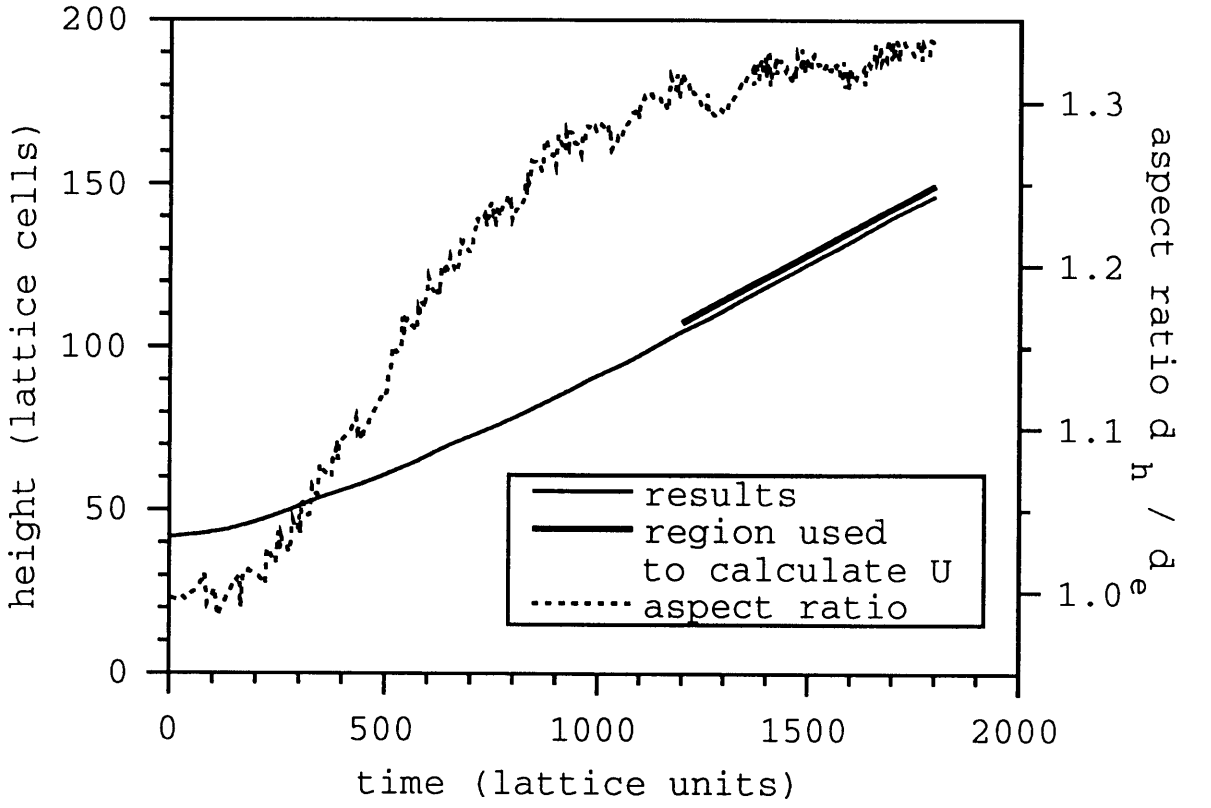

Figure 8.4: Example of bubble height and aspect ratio vs. time results, and terminal velocity calculation, using ellipsoidal bubble of Figure 8.2 (case J).

$Re = d_e U_b/\nu$. Another interesting quantity is the aspect ratio, defined here as d_h/d_e, also plotted in Figure 8.4. It was decided that the bubbles began to look ellipsoidal rather than circular when the aspect ratio was greater than 1.03. Hence the distinction between these shapes as given in Table 8.1 has a quantitative basis (of course the threshold of 1.03 is subjective). The shape was determined to be spherical cap if the bubble became hemispherical for at least part of its journey. Eotvos numbers large enough to achieve true spherical caps were not reached, but there was still a clear distinction between the hemisphere-cap and the ellipsoid shapes.

The results of cases H, K, M, and P are displayed in more detail in Figures 8.5, 8.6, 8.7,

case	g	ν	d_o	d_e	d_h	U_b	M	Eo	Re	d_h/d_e	shape
A	$5(10^{-5})$	0.147	20	16.3	16.1	0.0079	$5(10^{-6})$	0.078	0.88	0.988	sph
B	$5(10^{-5})$	0.147	40	36.9	37.2	0.0210	$5(10^{-6})$	0.40	5.3	1.008	sph
C	$5(10^{-5})$	0.147	50	47.5	49.3	0.0289	$5(10^{-6})$	0.66	9.3	1.038	elp
D	$5(10^{-5})$	0.147	60	58.0	62.5	0.0342	$5(10^{-6})$	0.99	14	1.078	elp
E	$2(10^{-4})$	0.147	20	15.8	16.1	0.0266	$2(10^{-5})$	0.29	2.9	1.019	sph
F	$2(10^{-4})$	0.147	40	39.2	47.0	0.0587	$2(10^{-5})$	1.8	16	1.199	elp
G	$2(10^{-4})$	0.147	50	49.4	64.5	0.0537	$2(10^{-5})$	2.9	18	1.306	elp
H	$2(10^{-4})$	0.0521	20	16.5	17.0	0.0375	$3(10^{-7})$	0.32	12	1.030	sph
I	$2(10^{-4})$	0.0521	40	38.0	42.0	0.0689	$3(10^{-7})$	1.7	50	1.105	elp
J	$2(10^{-4})$	0.0521	50	48.4	63.8	0.0698	$3(10^{-7})$	2.8	65	1.318	elp
K	$2(10^{-4})$	0.0521	60	58.6	82.3	0.0719	$3(10^{-7})$	4.0	81	1.404	elp
L	$1(10^{-4})$	0.0616	20	16.4	16.6	0.0221	$3(10^{-7})$	0.16	5.9	1.012	sph
M	$4(10^{-4})$	0.0442	60	57.6	83.8	0.0870	$3(10^{-7})$	7.8	113	1.455	cap
N	$2(10^{-4})$	0.0144	30	27.5	29.0	0.0554	$2(10^{-9})$	0.89	106	1.055	elp
O	$2(10^{-4})$	0.0144	50	47.5	60.0	0.0669	$2(10^{-9})$	2.7	221	1.263	elp
P	$4(10^{-4})$	0.0126	50	47.6	71.1	0.0767	$2(10^{-9})$	5.3	290	1.494	cap
Q	$2(10^{-4})$	0.0220	20	16.5	17.5	0.0420	$1(10^{-8})$	0.32	32	1.061	elp
R	$3(10^{-4})$	0.0200	60	58.0	82.2	0.0651	$1(10^{-8})$	5.9	189	1.417	cap

Table 8.1: 2D bubble rise simulation results.

and 8.8, respectively. The left side of each figure shows bubble height versus time results, where the length and time scales have also been converted to real units (the conversion procedure will be described momentarily). The right side shows density contours for several simulation times, which are indicated by the symbols on the height-time plots. The contours indicate density equal to half that of the liquid phase (thus midway through the interface) and show the evolution of the bubble shape over the course of the simulation. We see that a bubble starts off at rest and accelerates due to buoyancy. As its velocity increases it may or may not deform due to drag, depending on Eotvos number and Morton number. The bubble in Figure 8.5 remains spherical, while that in Figure 8.6 becomes ellipsoidal, in fact it could be called a "wobbling" ellipsoid. Perhaps a better example of an ellipsoidal bubble (i.e.

more symmetrical about its horizontal axis) is the one shown in Figure 8.2. The bubbles in Figures 8.7 and 8.8 are cap shaped, or at least they are part of the time. It is apparent that the shapes of the bubbles in the latter three simulations underwent substantial variation, even after a fairly steady velocity was attained. This is quite consistent with experimental observations of large bubbles.

The conversion from lattice units to real units in presenting the simulation results can be done in a straightforward manner by choosing a real liquid with the same Morton number as that of a given simulation. The formalism introduced in Chapter 5 is revisited, where $x^* = \tilde{x}/x$, i.e. the starred quantity gives the lattice value of a quantity x in lattice units divided by the real world value in SI units. By specifying a liquid based on Morton number, real values of surface tension and viscosity are identified; σ^*, ν^*, and g^* are therefore known, and the length, time, and velocity conversions d^*, t^*, and U^* may be calculated. Take for example case P (Figure 8.8). In this simulation the lattice values were $\tilde{\nu} = 0.0126$, $\tilde{g} = 0.0004$, and (as for all the cases) $\tilde{\sigma} = 0.17$. These give a Morton number $M = 2(10^{-9})$, which is the same as that of turpentine (at room temperature). The real values for turpentine are then used: $\nu = 1.6(10^{-6})$, $\sigma = 3.2(10^{-5})$, and of course $g = 9.8$. These give $\nu^* = 7.9(10^3)$, $\sigma^* = 5.3(10^3)$, and $g^* = 4.1(10^{-5})$. Since $g^*(d^*)^2/\sigma^* = 1$ (as shown in Section 5.5), the length conversion is $d^* = \sqrt{\sigma^*/g^*} = 1.1(10^4)$ lattice cells / meters, or about 11 cells/mm. Another dimensionless combination gives $U^*\nu^*/\sigma^* = 1$, hence $U^* = 0.67$ (cells/step) / (meters/sec). The time conversion is then found simply as $t^* = d^*/U^* = 1.6(10^4)$ time steps per second. Due to their Morton number, cases H, K, and M (Figures 8.5, 8.6, and 8.7) were assumed to be isoamyl alcohol, for which $\nu \cong 5.4(10^{-6})$ and $\sigma \cong 3.0(10^{-5})$ (hence $M \cong 3(10^{-7})$). Unit

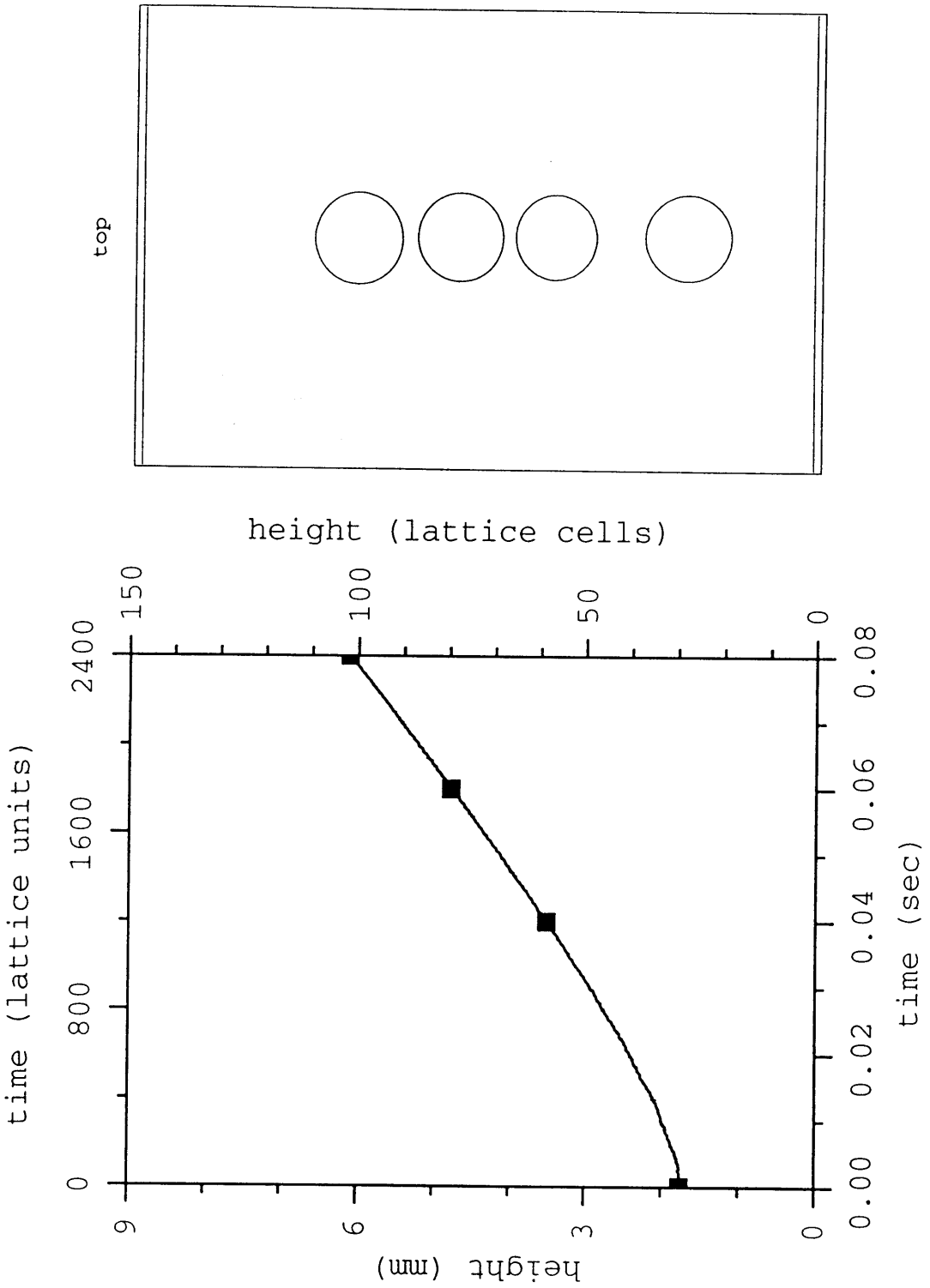

Figure 8.5: Contour snapshots and bubble height vs. time results for case H, where $M = 3(10^{-7})$, $Eo = 0.32$, and $Re = 12$ at terminal velocity. Symbols indicate snapshot times.

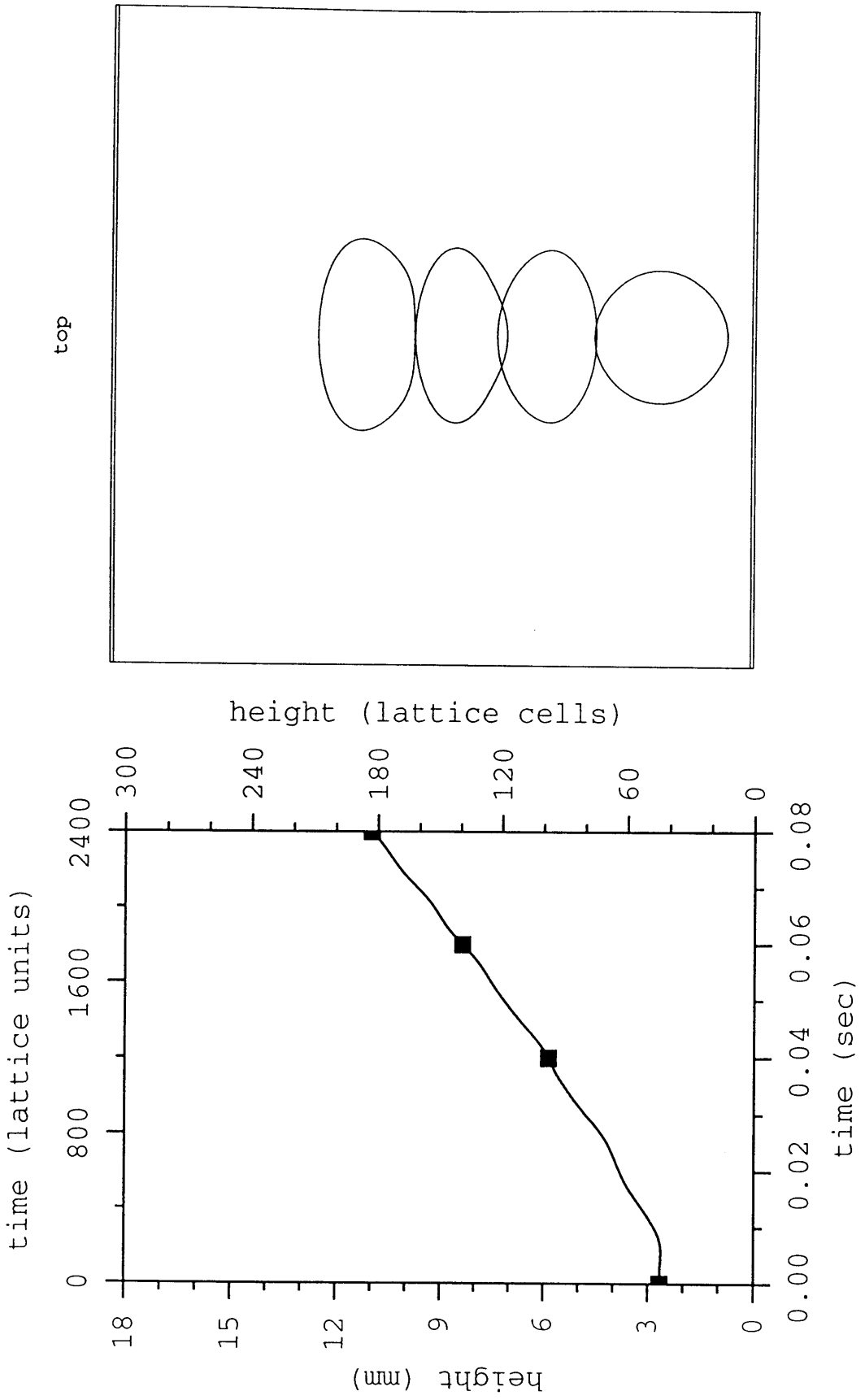

Figure 8.6: Contour snapshots and bubble height vs. time results for case K, where $M = 3(10^{-7})$, $Eo = 4.0$, and $Re = 81$ at terminal velocity. Symbols indicate snapshot times.

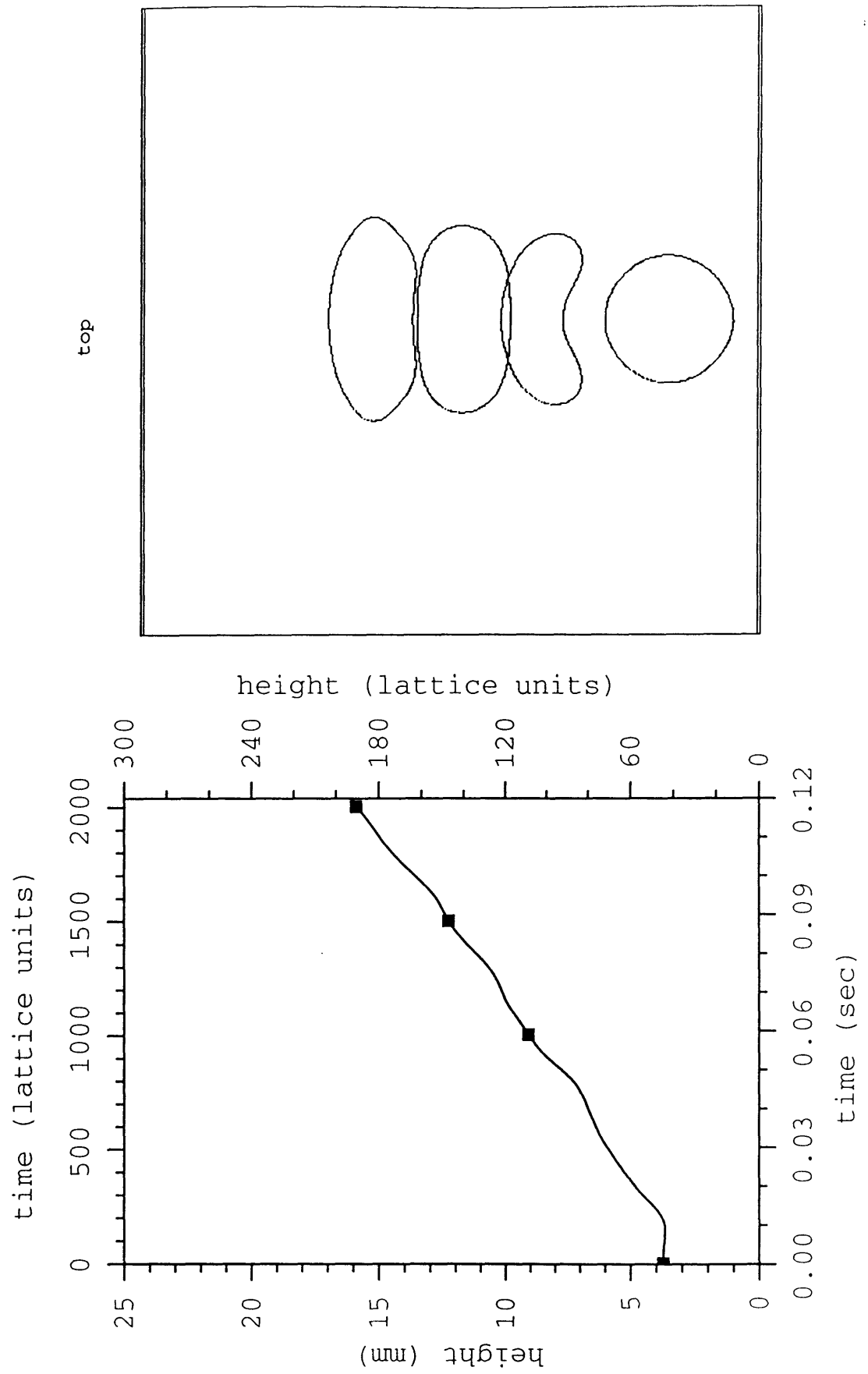

Figure 8.7: Contour snapshots and bubble height vs. time results for case M, where $M = 3(10^{-7})$, $Eo = 7.8$, and $Re = 113$ at terminal velocity. Symbols indicate snapshot times.

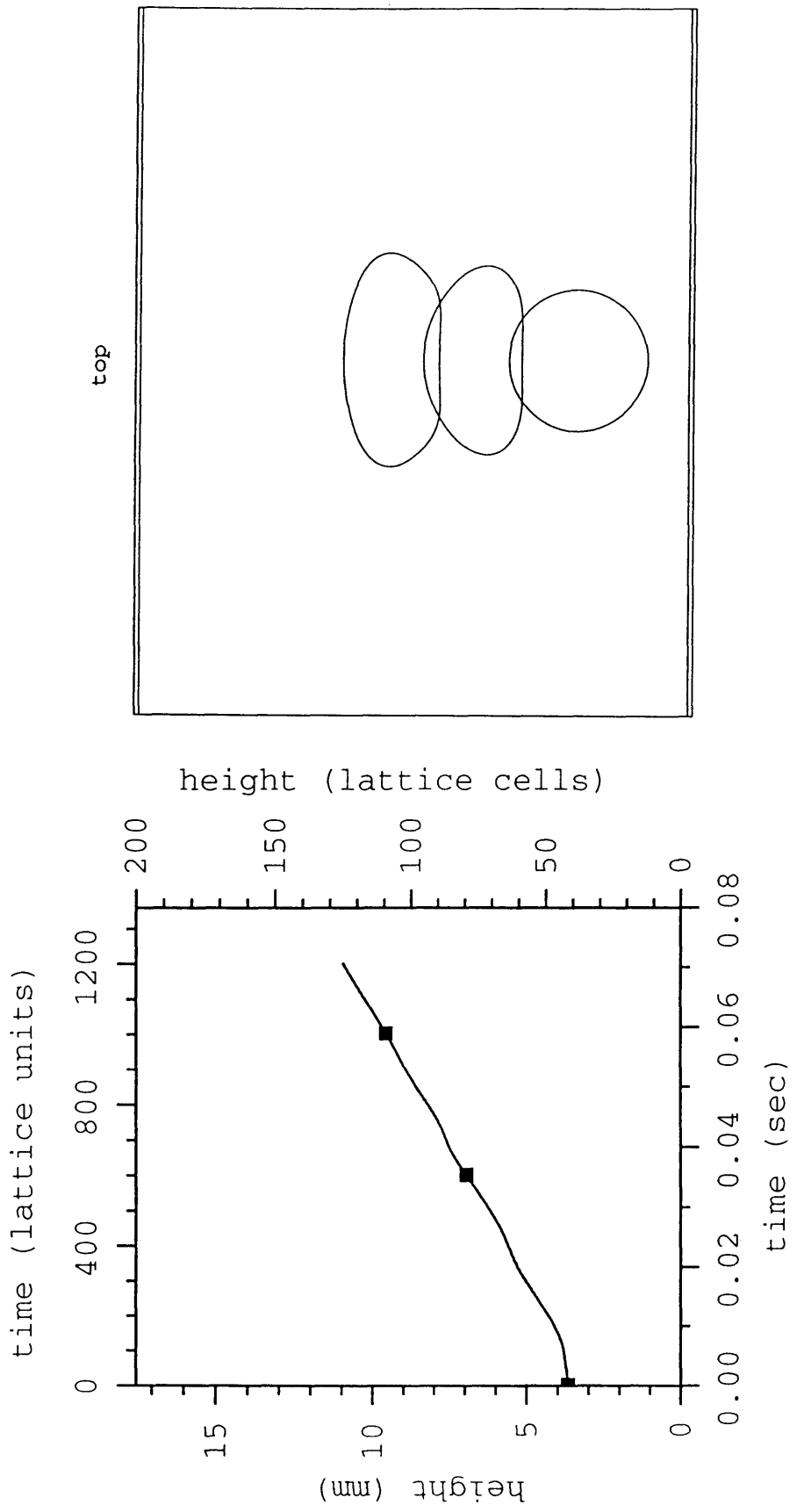

Figure 8.8: Contour snapshots and bubble height vs. time results for case P, where $M = 2(10^{-9})$, $Eo = 5.3$, and $Re = 290$ at terminal velocity. Symbols indicate snapshot times.

conversions were then determined in the manner just outline.

Although these simulations are 2D, the results may be compared to real bubble rise data with the intent of verifying that the correct trends are present for bubble shape and rise velocity. There are two common ways of presenting the data graphically. The first is to plot the terminal rise velocity against the bubble size; this is common for experiments with a single fluid, where properties such as surface tension and viscosity are constant. When a variety of fluids are employed it is convenient to use a dimensionless analysis by plotting the Reynolds number as a function of the Eotvos and Morton numbers, as exemplified by the graphical correlations of Grace [62] and Bhaga and Weber [63]. One of the useful features of these "dimensionless maps" of bubble rise behavior is that regions of expected bubble shape are identified. A dimensionless characterization is especially useful for the present simulation results as not only are the fluid properties varied but the strength of gravity is varied as well.

A plot of the first kind, velocity U_b versus equivalent diameter d_e in lattice units, is shown in Figure 8.9 for two sets of constant fluid properties (and gravity). The symbols indicate simulation results, while the lines are constructed using the semi-empirical wave analogy correlation introduced in Section 5.4 and detailed in Appendix B. The solid line and square symbols correspond to cases where the lattice gravitational constant was $\tilde{g} = 5(10^{-5})$ and the lattice viscosity was $\tilde{\nu} = 0.147$, hence the Morton number was $M \cong 5(10^{-6})$. The dashed line and circle symbols correspond to $\tilde{g} = 2(10^{-4})$ and $\tilde{\nu} = 0.0521$, and thus a Morton number $M \cong 3(10^{-7})$. Near each symbol is the letter of the case it represents. Agreement with the predictions of the correlation is quite good, despite the fact that the simulation was 2D. The deviation for small spherical bubbles is expected, because the correlation goes over to Stokes

equation for flow past a sphere in this limit, but the drag on a 2D bubble (i.e. a cylinder) of equivalent diameter will be smaller and yield a higher velocity [75]. These results are replotted in Figure 8.10 with real units instead of lattice units.

In Figure 8.11, all of the results in Table 8.1 are plotted in the form of a dimensionless map. Lines are again calculated from the wave analogy correlation; each line gives Reynolds number versus Eotvos number for a constant value of Morton number (thus representing a particular fluid). Predictions and results for five different Morton numbers are shown. The shape of a symbol indicates the Morton number for that simulation. Near each data point is a letter indicating the observed shape of the bubble: "s" for spherical, "e" for ellipsoidal, and "c" for cap. Regions of the map corresponding to each of the three main shapes can be identified on the basis of the simulation results. These regions are demarcated in Figure 8.11 via thick dashed lines. The agreement of the results with the correlation again appears quite reasonable. At low Eo, the positive deviation of the simulation Reynolds numbers corresponds to the lower drag on a cylinder compared to a sphere, as mentioned.

Of main importance is the correct variation in bubble shape with bubble size and fluid properties. The simulation results verify that small bubbles tend to be spherical, intermediate bubbles are ellipsoidal, and large bubbles become caps. Moreover, it is seen that certain key trends are obeyed. For example: bubbles with the same Eotvos number, $Eo \sim 0.3$, are spherical at higher Morton numbers and ellipsoidal at lower Morton numbers; bubbles with Reynolds number on order 100 are ellipsoidal at lower Eo but form caps at higher Eo. These observations agree with experimental data [62]. The positions of the lines separating regions of bubble shape are not the same in Figure 8.11 as in the literature [62, 63]. For

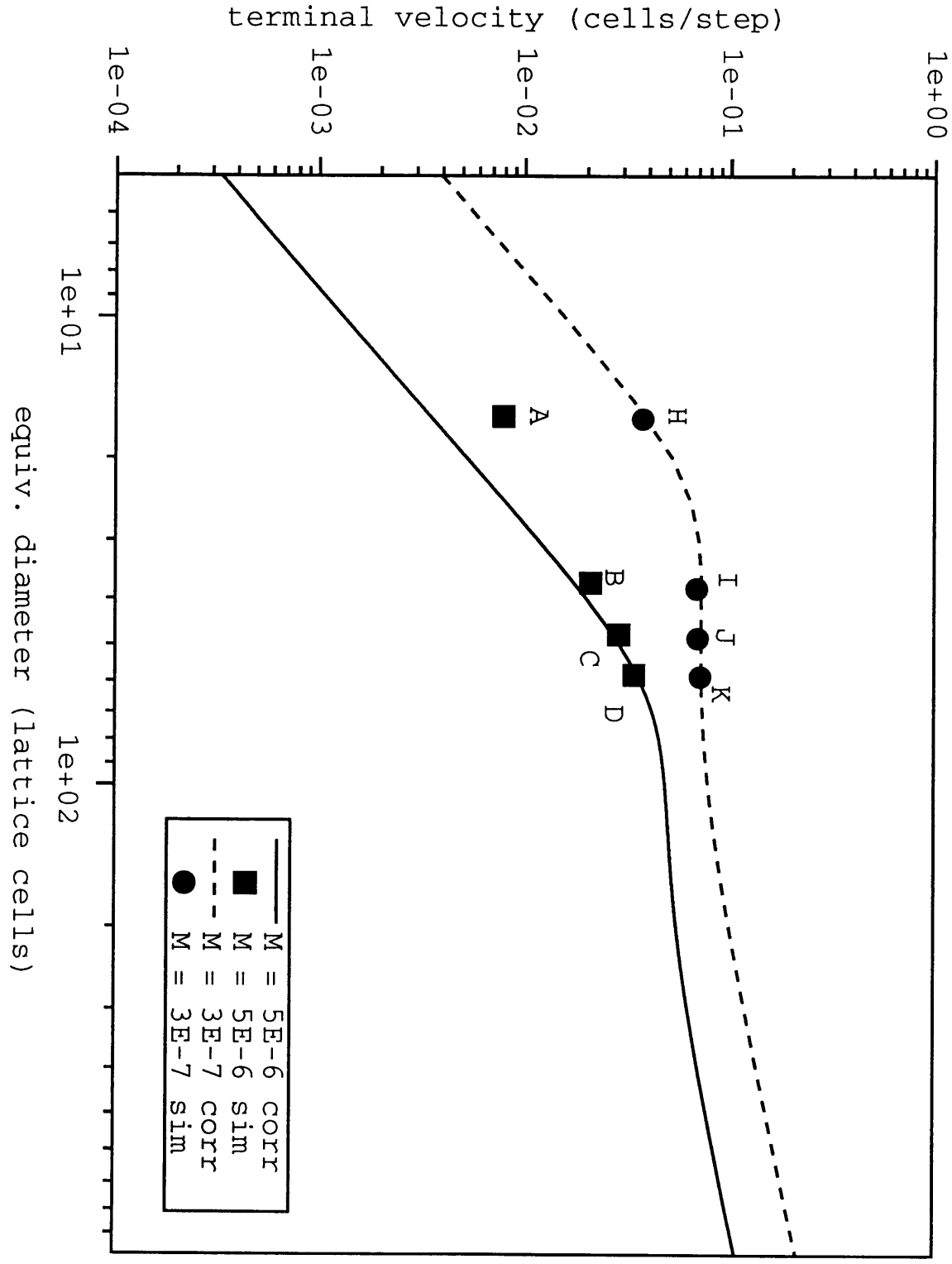

Figure 8.9: Terminal velocity U_b vs. equivalent bubble diameter d_e (in lattice units), simulation results compared to prediction of wave analogy correlation.

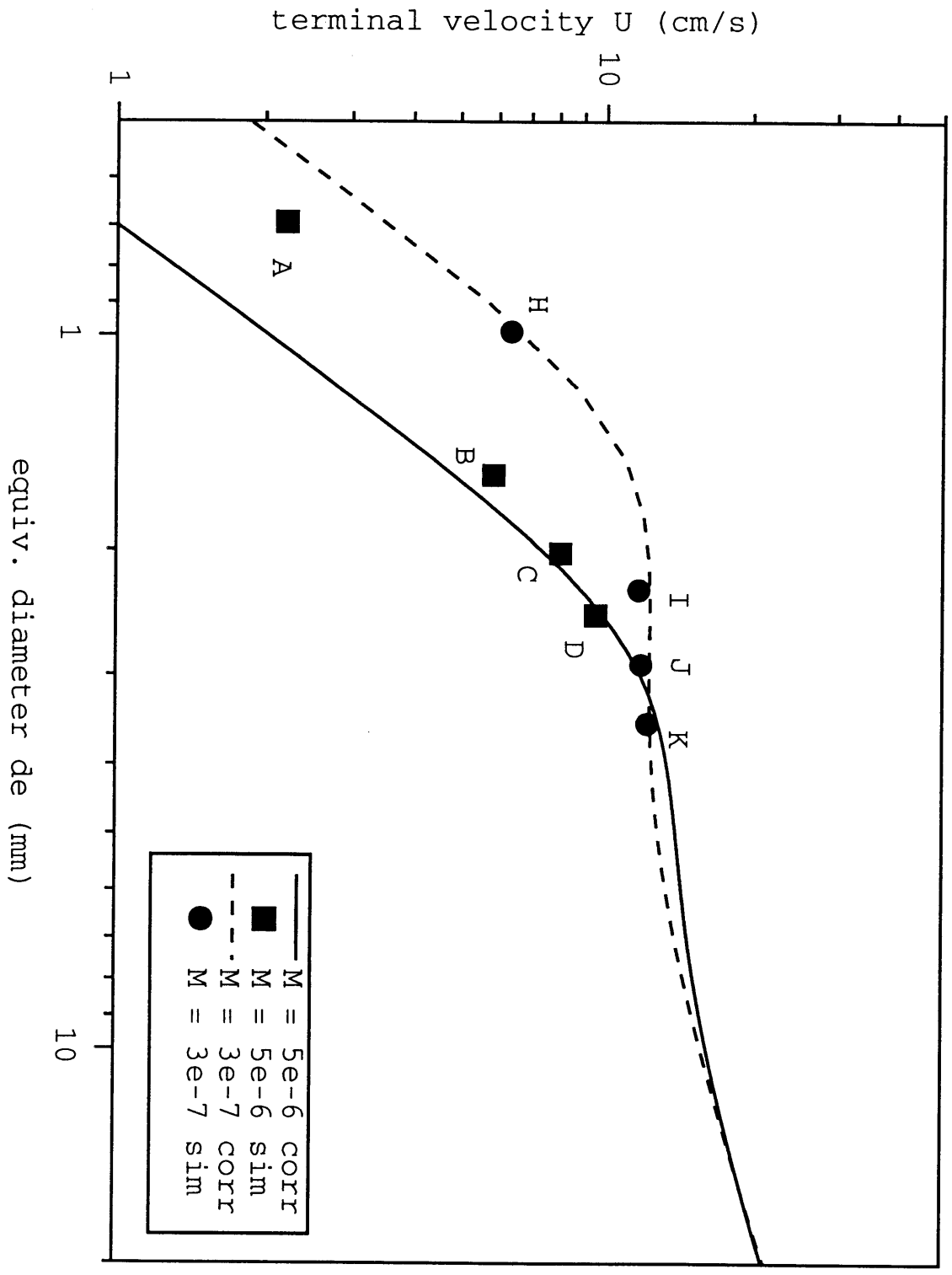

Figure 8.10: Terminal velocity U_b vs. equivalent bubble diameter d_e (converted to real units), simulation results compared to prediction of wave analogy correlation.

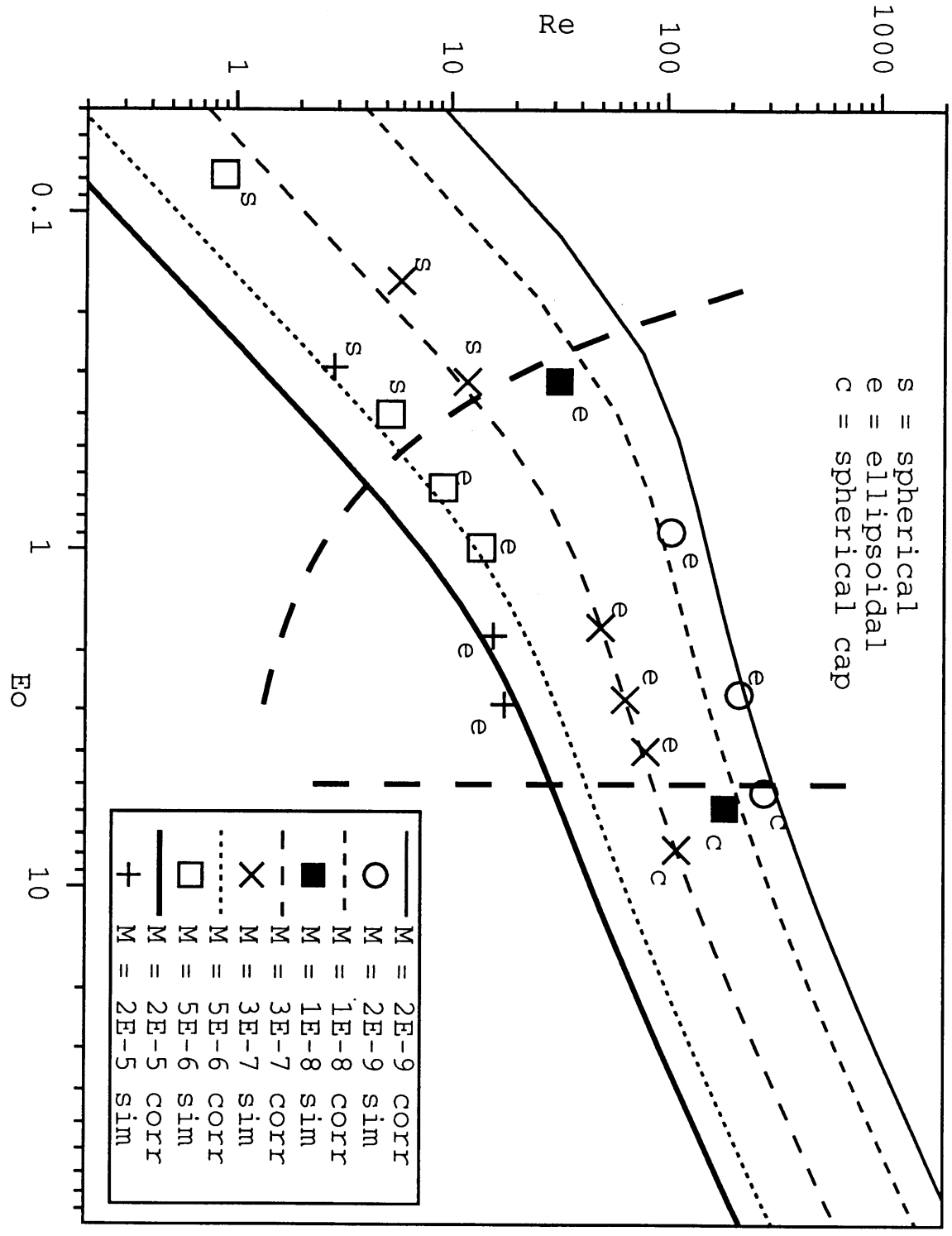

Figure 8.11: Dimensionless map of bubble rise behavior, comparison of simulation results to wave analogy correlation.

the spherical-ellipsoidal transition there is a slight difference, while for the ellipsoidal-cap transition there is a larger difference. These are due, at least in part, to the subjectivity involved in identifying the shape of a bubble.

A few additional comments are in order. A possible source of error in the simulation results (besides its 2D nature) involves the blockage correction. The blockage due to finite column width in the simulations was accounted for in the predictions of the wave-analogy correlation in a fashion suggested by Maneri [76]; details are supplied in Appendix B. Maneri also investigated plane bubbles, i.e. flat bubbles rising between closely spaced plates, approximating a 2D situation. He found that terminal velocity versus bubble volume behavior for plane bubbles was very similar to that of 3D bubbles, and concluded that the wave analogy correlation is also directly applicable to 2D media. In light of this finding it is not as surprising that strong agreement was obtained between the 2D bubble rise simulations of this thesis and a correlation for real 3D bubbles.

Chapter 9

Conclusions

Digital Physics, an outgrowth of lattice gas automata, has already advanced the state of the art for accurate and efficient hydrodynamic simulation of an isothermal ideal gas, appropriate for applications such as the flow of air around a moving automobile. The success of Digital Physics raises the question of whether similar gains can be achieved for hydrodynamic simulation of complex fluids such as multiphase flows.

In this work, an extension to the current Digital Physics method has been developed which allows flow simulation of non-ideal-gas fluids and, most significantly, liquid-vapor mixtures. The resulting method, referred to as the Digital Physics *multiphase system*, provides detailed flow simulation including the explicit presence of interfaces. The present implementation is particularly suitable for applications where the dynamics of the liquid phase are dominant, such as in the bubbly and slug flow regimes.

The heart of the multiphase system is a non-local interaction step, which occurs in addition to the usual propagation and collision steps of the multispeed lattice gas, and the addition of microscopic internal energy to the microphysical system. The general theory describing these features has been developed. It includes the procedure for removing artifacts from the lattice transport equations, such that correct hydrodynamics is recovered. It also shows how a suitable empirical thermodynamical system, governing the two phase equilibrium properties and the equations of state of each phase, is obtained.

A two dimensional implementation of the multiphase system following a van der Waals thermodynamics was created. This "lab-scale" version of the method was used to verify the basic theoretical predicitions for the behavior of the system. It was then used to perform simulations of Rayleigh-Taylor instability and single vapor bubbles rising in liquid. These experiments demonstrated the ability of the multiphase system to capture the dynamical interplay between viscous forces, inertial forces, bouyancy forces, and surface tension forces, which are some of the key physical mechanisms of two phase flow in general.

It is estimated that the multiphase system can improve upon the range of flow systems accessible to detailed flow simulation. An "engineering-scale" version of the method would be a 3D simulation code with optimized algorithms running in a high performance computing environment. Based on current Digital Physics capabilities, it is predicted that bubbly flow simulations of a 100 cubic centimeter test section with Reynolds numbers on order 10^4 and Morton numbers on order 10^{-11} could be performed. Thus the effects of turbulence could be investigated, and at Morton numbers representative of water. Both of these conditions are currently unattainable in detailed numerical simulations of bubbly flow.

The extension to three dimensional simulations is quite straightforward. No additional theory is required, only a few specific changes to the implementation, such as additional velocity states and collision rules for those states. Heat transfer, on the other hand, cannot be included in the present multiphase system due to an isothermal requirement related to the microdynamics of the interface. There is also an upper limit on the liquid to vapor density ratio of about 200, above which the exact-integer algorithms for the non-local interaction begin to fail at the interface. Hence the multiphase system can achieve the correct density ratio for pressurized water, i.e. $P > 9$ atm., but not for water at atmospheric conditions, where the density ratio is about 1000. However, in systems such as bubbly flow where the dynamics of the vapor phase are not a significant influence, it is sufficient to merely have a simulation density ratio much larger than unity, which was demonstrated to be easily achieved in the multiphase system.

I believe it may be possible to improve upon the Digital Physics multiphase system developed here through further extensions of the non-local microdynamics. One idea is to develop an interaction algorithm which recovers a non-ideal-gas equation of state and correct adiabatic energy transport, simultaneously, through the lower order gradient expansion terms. The higher order terms would then be used to control the effects of interfacial tension, providing direct representation of the surface excess free energy which is thermodynamically predicted to exist within the interfacial region of a two phase mixture. Another possible approach would be to construct an algorithm allowing simultaneous exchange of mass, momentum, and energy, such that the net non-local mass exchange is only non-vanishing in the interfacial region, where it would effectively provide a surface excess free energy. It is hoped

that such concepts will, in the near future, lead to removal of the isothermal requirement, control of the surface tension coefficient, and manipulation of the interfacial density profile, which would allow heat transfer, greater ranges of key dimensionless quantities, and very large densities ratios, respectively.

Appendix A

Dimensionless Analysis of van der Waals Thermodynamics

We wish to show that specification of one dimensionless quantity, such as the density ratio r_ρ, determines the others in a van der Waals system. To begin, the thermodynamic relations which determine the two-phase equilibrium properties, equations (3.15) and (3.16), are rewritten:

$$P = \frac{\rho_g RT}{1-\rho_g b} - a\rho_g^2 = \frac{\rho_f RT}{1-\rho_f b} - a\rho_f^2 \tag{A.1}$$

$$\int_{\rho_g}^{\rho_f} \left(\frac{RT}{\rho(1-\rho b)} - a - \frac{P}{\rho^2} \right) d\rho = 0 \tag{A.2}$$

where the van der Waals equation (3.12) was used for $P(\rho, T)$ in the expression for the Maxwell equal area rule. Direct integration and division by RT gives

$$\ln\left(\frac{\rho_f}{\rho_g}\frac{1-\rho_g b}{1-\rho_f b}\right) + \frac{P}{RT}\left(\frac{1}{\rho_f} - \frac{1}{\rho_g}\right) + \frac{a}{RT}(\rho_g - \rho_f) = 0 \tag{A.3}$$

Recalling the entropy relation (3.31), the first term in the above equation is just the dimensionless latent entropy of vaporization s^* defined in Section 5.6. The second term is the dimensionless volume-work of vaporization w^*, and the third term is the dimensionless latent energy of vaporization u^*. Thus equation (A.3) is identical to the requirement that the chemical potentials of the coexisting phases are equal, and may be rewritten simply as

$$Ts^* - Pv^* - u^* = 0 \tag{A.4}$$

Rearranging equation (A.1) gives

$$\frac{\rho_f}{\rho_g}\frac{1-\rho_g b}{1-\rho_f b} = 1 + \frac{a\rho_f}{RT}(1-\rho_g b)\left(\frac{\rho_f}{\rho_g} - \frac{\rho_g}{\rho_f}\right) \tag{A.5}$$

Substituting for the entropy term in equation (A.3), and employing the definitions of u^* and r_ρ, gives

$$u^* = \ln\left[1 + \frac{a\rho_f}{RT}(1-\rho_g b)\left(r_\rho - \frac{1}{r_\rho}\right)\right] + \frac{P}{RT}\left(\frac{1}{\rho_f} - \frac{1}{\rho_g}\right) \tag{A.6}$$

We are generally interested in systems with a large density ratio, $r_\rho >> 1$, and it is most straightforward to continue the exercise with this assumption. In this case, the vapor phase

behaves like an ideal gas, and the ideal gas law $P \cong \rho_g RT$ can be used. Also, the van der Waals constant b is of order $1/\rho_f$, which implies $\rho_g b << 1$. Noting that $u^* \cong a\rho_f/RT$ and $1/\rho_g >> 1/\rho_f$, equation (A.6) becomes

$$u^* = \ln(1 + u^* r_\rho) - 1 \tag{A.7}$$

or using the fact that $r_\rho u^* >> 1$,

$$u^* \cong \ln(r_\rho u^*) - 1 \tag{A.8}$$

Thus $u^* = u^*(r_\rho)$, hence the dimensionless latent energy of vaporization may indeed be written as a function solely of the density ratio. The same may also be said for the dimensionless latent entropy of vaporization and the dimensionless volume-work of vaporization:

$$s^* \cong \ln r_\rho u^* = s^*(r_\rho) \tag{A.9}$$

$$w^* \cong 1 \tag{A.10}$$

and in fact w^* is exactly unity in the limit of large density ratio.

Returning once more to the entropy term in equation (A.3), and noting equation (A.9),

$$\begin{aligned} s^* &\cong \ln\left(r_\rho \frac{1}{1-\rho_f b}\right) \cong \ln r_\rho u^* \\ &\Longrightarrow u^* \cong \frac{1}{1-\rho_f b} \end{aligned} \tag{A.11}$$

which means that even the dimensionless quantity $\rho_f b$ is specified for a given density ratio. Therefore

$$\frac{u^*}{\rho_f b} = \frac{a\rho_f}{RT\rho_f b} = \frac{a}{bRT} = Z(r_\rho) \tag{A.12}$$

which combined with equation (A.11) gives

$$Z = \frac{(u^*)^2}{u^* - 1} \tag{A.13}$$

This equation can be solved explicitly for $u^*(Z)$, and combined with an explicit solution of equation (A.8) for $r_\rho(u^*)$, to give an expression for $r_\rho(Z)$:

$$r_\rho = \frac{\exp\left[1 + \frac{1}{2}(Z + \sqrt{Z(Z-4)})\right]}{\frac{1}{2}(Z + \sqrt{Z(Z-4)})} \tag{A.14}$$

It is also well known that for a van der Waals system the critical temperature and pressure are

$$RT_{crit} = \frac{8}{27}\frac{a}{b} \tag{A.15}$$

$$P_{crit} = \frac{1}{27}\frac{a}{b^2} \tag{A.16}$$

which may be derived from the conditions defining the critical point:

$$\left[\frac{\partial P}{\partial \rho}\right]_T = \left[\frac{\partial^2 P}{\partial \rho^2}\right]_T = 0 \tag{A.17}$$

Thus the reduced temperature T^* is

$$RT^* = \frac{RT}{RT_{crit}} = \frac{27bRT}{8a} = \frac{27}{8}\frac{1}{Z} \tag{A.18}$$

and for the reduced pressure P^*,

$$P^* = \frac{P}{P_{crit}} = \frac{27b^2\rho_g RT}{a} = \frac{u^*}{r_\rho Z^2} \tag{A.19}$$

It necessarily follows that $T^* = T^*(r_\rho)$ and $P^* = P^*(r_\rho)$.

Finally the soundspeed, essentially the isentropic compressibility, is

$$c_s^2 = \left[\frac{\partial P}{\partial \rho}\right]_S = \frac{3}{2}\frac{RT}{(1-\rho b)^2} - 2a\rho \tag{A.20}$$

This is the adiabatic soundspeed; however, for the isothermal version of the multiphase system, the relevant soundspeed will be

$$c_s^2 = \left[\frac{\partial P}{\partial \rho}\right]_T = \frac{RT}{(1-\rho b)^2} - 2a\rho \tag{A.21}$$

and this isothermal soundspeed is somewhat smaller than the corresponding adiabatic soundspeed. The dimensionless soundspeed of the liquid (squared) is

$$\frac{c_{s,f}^2}{RT} = \frac{1}{(1-\rho_f b)^2} - 2\frac{a\rho_f}{RT} \cong u^*(u^* - 2) \tag{A.22}$$

and that of the gas is

$$\frac{c_{s,g}^2}{RT} = \frac{1}{(1-\rho_g b)^2} - 2\frac{a\rho_g}{RT} \cong 1 - \frac{2}{r_\rho}u^* \tag{A.23}$$

Also, the liquid to vapor soundspeed ratio r_c

$$r_c \equiv \frac{c_{s,f}}{c_{s,g}} \cong \sqrt{\frac{u^*(u^*-2)}{1-2u^*/r}} \tag{A.24}$$

Thus the set of dimensionless quantities relevant to to the thermodynamics of a two phase system (as listed in Section 5.6) is fully determined by specifying any one of them. While this has been shown for the high liquid to vapor density ratio approximation, it is in fact rigorously true for the van der Waals system, but much more tedious to prove analytically without the approximation.

Appendix B

The Wave-Analogy Correlation for Prediction of Terminal Velocities of Rising Bubbles

The wave analogy is a simple, elegant, physically motivated theory of bubble dynamics. It was originally proposed by Mendelson [65], who suggested that due to the "inviscid nature of the motion of large bubbles," they "may be thought of as merely interfacial disturbances, whose dynamic behavior should be similar to those of waves on an ideal fluid." When the depth of the liquid is large compared to the wavelength λ of the surface wave, its wave velocity c_w is given by

$$c_w = \sqrt{\frac{2\pi\sigma}{\lambda} + \frac{g\lambda}{2\pi}} \tag{B.1}$$

As usual σ is taken to be the coefficient of surface tension divided by the density of the liquid. Mendelson suggested using the equivalent circumference of the bubble as the wavelength, $\lambda = \pi d_e$, in equation (B.1) to give the terminal velocity of the bubble U_b^w:

$$U_b^w = \sqrt{\frac{2\sigma}{d_e} + \frac{g d_e}{2}} \tag{B.2}$$

This equation is for single bubbles rising in infinite media, and which are large enough to be non-spherical such that viscous drag is small compared to inertial drag. These are bubbles corresponding to regions III and IV in the discussion of bubble rise behavior given in Section 5.4. Note that squaring equation (B.2) and dividing through by the last term gives

$$\frac{8/3}{C_D} = \frac{4}{Eo} + 1 \tag{B.3}$$

where drag coefficient C_D and Eotvos number Eo are given by equations (5.12) and (5.9). Hence the wave analogy for the rise of large bubbles is essentially a relationship between the two relevant dimensionless parameters of this system.

A method to extend the wave analogy to include small bubbles was given by Jamialahmadi, Branch, and Müller-Steinhagen [66]. They propose that the terminal velocity U_b of a bubble of any size is

$$U_b = \frac{U_b^s U_b^w}{\sqrt{(U_b^s)^2 + (U_b^w)^2}} \tag{B.4}$$

where U_b^s is the terminal velocity of a small spherical bubble. U_b^s is found by equating the

buoyancy force to Stokes equation for drag force on a sphere, and may be written as

$$U_b^s = \frac{1}{18}\frac{g d_e^2}{\nu} \tag{B.5}$$

Hadamard [68] showed that for a non-rigid interface where internal circulation of the bubble occurs, a correction is needed. When the vapor viscosity is much smaller than that of the liquid, the rise velocity is 3/2 larger than that given by equation (B.5). Most real systems, however, contain surface active agents (especially aqueous systems) which cause the interface to be rigid, so the small bubbles tend to obey equation (B.5).

Equation (B.4) is the wave analogy correlation (for infinite media) referred to in Chapters 5 and 8. It asymptotically approaches the original wave analogy velocity U_b^w for large bubbles, and goes over to the Stokes velocity U_b^s in the limit of small bubbles. In applying the wave analogy correlation, equation (B.5) was used without Hadamard's correction because it is suspected that the interface of the multiphase system is rigid with respect to internal slip. It is interesting to note that the characteristic rise curves of Figures 5.1 and 5.2, which plot equation (B.4) for water at 20 C and 250 C, follow the Stokes equation far beyond $Re_b = 1$. This represents an approximation due to the form of the wave analogy correlation for the range of Reynolds numbers greater than that of true Stokes flow ($Re < 1$), but less than that required for surface tension forces to have a strong affect. Nevertheless Jamialahmadi, Branch, and Müller-Steinhagen [66] showed that equation (B.4) agrees favorably with experimental data for a wide range of fluids and bubble sizes.

When the motion of a rising bubble is influenced by the walls of a container, the infinite

media approximation is invalid. Let the characteristic length of the width of the container be D. As the fractional blockage $\beta = d_e/D$ due to the presence of the boundaries increases, the drag effectively increases and the terminal velocity decreases for a bubble of given size. Maneri [76] recognized the existence of a wave analogy for finite media due to the general expression for the velocity of a wave on an interface between two fluids (e.g. vapor and liquid) of different depths h_1 and h_2 and different densities ρ_1 and ρ_2:

$$c_w = \left[\frac{g\bar{\lambda}(\rho_2 - \rho_1) + \rho_2\sigma/\bar{\lambda}}{\rho_1 \coth(h_1/\bar{\lambda}) + \rho_2 \coth(h_2/\bar{\lambda})}\right]^{1/2} \tag{B.6}$$

where $\bar{\lambda} = \lambda/2\pi$. Hence equation (B.1) is a special case for $h_1/\lambda,\ h_2/\lambda >> 1$ and $\rho_2 >> \rho_1$. When the liquid to vapor density ratio remains large but the depth of the liquid is finite (and the depth of the vapor is not very small), equation (B.6) becomes

$$c_w = \left[\frac{g\bar{\lambda} + \sigma/\bar{\lambda}}{\coth(h/\bar{\lambda})}\right]^{1/2} \tag{B.7}$$

where h is the depth of the liquid. Replacing wavelength as above, the finite media terminal bubble velocity U_{bf}^w is

$$U_{bf}^w = \sqrt{\left(\frac{gd_e}{2} + \frac{2\sigma}{d_e}\right)\tanh\frac{2h}{d_e}} = U_b^w\sqrt{\tanh\frac{2h}{d_e}} \tag{B.8}$$

Now an assumption must be made to determine h in a bubble rise system. For application to plane bubbles, Maneri takes h to be proportional to the channel half-width b, $h = c_1 b$, and determines the constant c_1 essentially from the condition that in the limit of large bubbles,

the slug terminal velocity U_s is reached. That is to say, when $d_e/2 = \beta_s b$, then $U_{bf}^w = U_s$, where β_s is the fractional blockage at which the bubble becomes a slug. Thus

$$U_{bf}^w(d_e = 2\beta_s b) = U_s = U_b^w \sqrt{\tanh \frac{c_1}{\beta_s}} \tag{B.9}$$

which may be solved for c_1,

$$c_1 = \beta_s \tanh^{-1} \left(\frac{U_s}{U_b^w} \right)^2 \tag{B.10}$$

Maneri goes on to give an empirical expression for the slug rise velocity U_s, and estimates $\beta_s = 0.235$, based on results for large plane bubbles rising in low viscosity fluid (i.e. water). These are not likely to be valid over the whole range of parameters used in the present bubble rise simulations, and in any case the expression for U_s involves the thickness of the duct spacing, the effect of which cannot be estimated for the 2D multiphase system. Instead it is assumed that the ratio of slug velocity to infinite media velocity is about a half, and occurs at a blockage of about 40%; these are rough estimates based on relatively few simulation results, but are quite plausible. Thus $U_s/U_{bf}^w = 0.5$ and $\beta_s = 0.4$, which substituted into equation (B.10) gives $c_1 = 0.10$. Noting that $\beta = d_e/D = d_e/2b = c_1 d_e/2h$, equation (B.8) becomes

$$U_{bf}^w = U_b^w \sqrt{\tanh \frac{0.1}{\beta}} \tag{B.11}$$

In all of the simulations for which results are presented in Chapter 8, the blockage was $\beta = 0.2$, which yields $U_{bf}^w = 0.68 U_b^w$. It is further assumed that this constant blockage correction can applied to the general velocity U_b rather than just the "wave" part of the

correlation, since a small bubble with velocity U_b^s is also affected by containing walls. This implies

$$U_{bf} = 0.68U_b = 0.68\frac{U_b^s U_b^w}{\sqrt{(U_b^s)^2 + (U_b^w)^2}} \tag{B.12}$$

where U_b^s is determined from equation (B.5) and U_b^w is determined from equation (B.2). The curves of predicted bubble rise behavior in Figures 8.9-8.11 for comparison to the simulation results were plotted via equation (B.12).

Bibliography

[1] G. F. Hewitt. Introduction to two phase flow problems in the process industry. In *Two-Phase Flow and Heat Transfer in the Power and Process Industries*, chapter 17, page 508. Hemisphere Publishing Corporation, 1981.

[2] N. E. Todreas and M. S. Kazimi. *Nuclear Systems I.* Hemisphere Publishing Corporation, 1990.

[3] M. Ishii and G. Kocamustafaogullari. Two-phase flow models and their limitations. In *Advances in Two-Phase Flow and Heat Transfer*, volume 1, page 1. NATO Advanced Research Workshop, Martinus Nijhoff Publishers, 1983.

[4] Y. Taitel, D. Bornea, and A. E. Dukler. Modelling flow pattern transitions for steady upward gas-liquid flow in vertical tubes. *AIChE J.*, 26(3):345, 1980.

[5] G. B. Wallis. *One-Dimensional Two-Phase Flow.* McGraw-Hill, Inc., 1969.

[6] K. E. Carlson et al. *RELAP5-MOD3 Code Manual.* Nuclear Regulatory Commission, NUREG/CR-5535, 1990.

[7] C. W. Hirt and B. D. Nichols. Volume of fluid (VOF) method for the dynamics of free boundaries. *J. Comp. Phys.*, 39:201, 1981.

[8] A. Tomiyama, A. Sou, H. Minagawa, and T. Sakaguchi. Numerical analysis of a single bubble by VOF method. *JSME Int. J.*, Series B, 36(1):51, 1993.

[9] A. Tomiyama, I. Zun, A. Sou, and T. Sakaguchi. Numerical analysis of bubble motion with the VOF method. *Nuclear Engineering and Design*, 141:69, 1993.

[10] S. O. Unverdi and G. Tryggvason. A front-tracking method for viscous, incompressible, multi-fluid flows. *J. Comp. Phys.*, 100:25, 1992.

[11] A. Tomiyama, A. Sou, I. Zun, and T. Sakaguchi. Three-dimensional detailed numerical simulation of bubbly flow in a vertical square duct. In *Proc. Japan-German Seminar on Multiphase Flow, KfK-5389*, page 487, 1994.

[12] K. Molvig, P. Donis, J. Myczkowski, and G. Vichniac. Removing the discreteness artifacts in 3D lattice-gas fluids. In *Discrete Kinetic Theory, Lattice Gas Dynamics and Foundations of Hydrodynamics.* World Scientific, 1988.

[13] C. Teixeira. *Continuum Limit of Lattice Gas Fluid Dynamics.* PhD thesis, Massachusetts Institute of Technology, September 1992.

[14] H. Chen. H-Theorem and generalized semi-detailed balance condition for lattice gas systems. *J. Stat. Phys.*, 81:347, 1995.

[15] K. Molvig and G. Papadopoulos. Particle interaction processing system. US Patent #5,432,718, issued 7/11/95.

[16] H. Chen, P. Churchill, R. Iannucci, K. Molvig, G. Papadopoulos, S. Remondi, C. Teixeira, and K. R. Traub. Computer system for simulating physical processes using multiple-integer state vectors. US Patent #5,594,671, issued 1/14/97.

[17] K. R. Traub, T. F. Knight, Jr., K. Molvig, and C. Teixeira. Viscosity reduction in physical process simulation. US Patent #5,606,571, issued 2/25/97.

[18] K. Molvig, C. Teixeira, and K. R. Traub. Collision operators in physical process simulation. (patent pending).

[19] H. Chen, C. Teixeira, and K. Molvig. Digital Physics approach to computational fluid dynamics: Some basic theoretical features. *Int. J. Mod. Phys. C*, (in press).

[20] U. Frisch, B. Hasslacher, and Y. Pomeau. Lattice-gas automata for the Navier-Stokes equations. *Phys. Rev. Lett.*, 56:1505, 1986.

[21] D. d'Humières and P. Lallemand. Lattice gas automata for fluid mechanics. *Physica A*, 140:326, 1986.

[22] C. Burges and S. Zaleski. Bouyant mixtures of cellular automaton gases. *Complex Systems*, 1:31, 1987.

[23] A. J. C. Ladd and M. E. Colvin. Application of lattice-gas cellular automata to Brownian motion of solids in suspension. *Phys. Rev. Lett.*, 60:975, 1988.

[24] M. Hénon. Optimazation of collision rules in the FCHC lattice gas, and addition of rest particles. In *Discrete Kinetic Theory, Lattice Gas Dynamics and Foundations of Hydrodynamics*. World Scientific, 1989.

[25] R. Kapral, A. Lawniczak, and P. Masiar. Oscillations and waves in a reactive lattice-gas automaton. *Phys. Rev. Lett.*, 66:2539, 1991.

[26] D. H. Rothman and S. Zaleski. Lattice-gas models of phase separation: Interfaces, phase transitions, and multiphase flow. *Rev. Mod. Phys.*, 66(4):1417, 1994.

[27] S. Wolfram. Cellular automaton fluids I: Basic theory. *J. Stat. Phys.*, 45:471, 1986.

[28] J. Salem and S. Wolfram. *Theory and Applications of Cellular Automata*, page 382. World Scientific, 1986.

[29] J. P. Boon. Statistical mechanics and hydrodynamics of lattice gas automata: An overview. *Physica D*, 47:3, 1994.

[30] T. R. Kirkpatrick and M. H. Ernst. Kinetic theory for lattice-gas cellular automata. *Phys. Rev. A*, 44:8051, 1991.

[31] L. G. Kadanoff, G. McNamara, and G. Zanetti. From automata to fluid flow: Comparisons of simulation and theory. *Phys. Rev. A*, 40:4527, 1989.

[32] D. d'Humières, P. Lallemand, and Y. H. Qian. Review of flow simulations using lattice gases. In *Proceedings of the International Seminar on Hyperbolic Problems*, page 57. Springer-Verlag, 1988.

[33] H. A. Lim. Lattice-gas automaton simulations of simple fluid dynamical problems. *Mathl. Comp. Modelling*, 14:720, 1990.

[34] T. Toffoli, N. Margolus, and G. Vichniac. Cellular automata supercomputers for fluid-dynamics modeling. *Phys. Rev. Lett.*, 56:1694, 1986.

[35] U. Frisch, B. Hasslacher, P. Lallemand, Y. Pomeau, D. d'Humières, and J. P. Rivet. Lattice gas hydrodynamics in two and three dimensions. *Complex Systems*, 1:649, 1987.

[36] G. R. McNamara and G. Zanetti. Use of the Boltzmann equation to simulate lattice-gas automata. *Phys. Rev. Lett.*, 61:2332, 1988.

[37] F. J. Higuera and J. Jiménez. Boltzmann approach to lattice gas simulations. *Europhys. Lett.*, 9:663, 1989.

[38] R. S. Benzi, S. Succi, and M. Vergassola. The lattice Boltzmann equation: Theory and applications. *Phys. Rep.*, 222:145, 1992.

[39] G. D. Doolen, editor. *Lattice Gas Methods for Partial Differential Equations.* Sante Fe Institute Studies in the Sciences of Complexity. Allan M. Wylde, 1990.

[40] R. Monaco, editor. *Discrete Kinetic Theory, Lattice Gas Dynamics and Foundations of Hydrodynamics.* World Scientific, 1988.

[41] F. Mujica. Lattice gas wind tunnel. Master's thesis, Massachusetts Institute of Technology, February 1991.

[42] H. Chen, K. Molvig, and C. Teixeira. Collision operator properties. EXA Corporation internal memorandum, 1994.

[43] A. Anagnost, A. Alajbegovic, H. Chen, D. Hill, C. Teixeira, and K. Molvig. Digital Physics analysis of the morel body in ground proximity. SAE Technical Paper 970139, Society of Automotive Engineers, 1997.

[44] C. Teixeira. Digital Physics simulation of lid-driven cavity flow. *Int. J. Mod. Phys. C*, (in press).

[45] D. H. Rothman and J. M. Keller. Immiscible cellular-automaton fluids. *J. Stat. Phys.*, 52:1119, 1988.

[46] M. R. Swift, W. R. Osborn, and J. M. Yeomans. Lattice Boltzmann simulation of nonideal fluids. *Phys. Rev. Lett.*, 75:830, 1995.

[47] C. Appert and S. Zaleski. Lattice gas with a liquid-gas transition. *Phys. Rev. Lett.*, 64:1, 1990.

[48] A. K. Gunstensen. *Lattice-Boltzmann Studies of Multiphase Flow Through Porous Media.* PhD thesis, Massachusetts Institute of Technology, 1992.

[49] A. K. Gunstensen and D. H. Rothman. A Galilean invariant immiscible lattice gas. *Physica D*, 47:53, 1991.

[50] D. Grunau, S. Chen, and K. Eggert. A lattice Boltzmann model for multiphase fluid flows. *Phys. Fluids A*, 5(10):2557, 1993.

[51] X. Shan and H. Chen. Lattice Boltzmann model for simulating flows with multiple phases and components. *Phys. Rev. E*, 47:1815, 1993.

[52] J. D. Sterling and S. Chen. Stability analysis of lattice Boltzmann methods. *J. Comp. Phys.*, 123:196, 1996.

[53] H. B. Callen. *Thermodynamics.* John Wiley and Sons, Inc., 1960.

[54] E. Fermi. *Thermodynamics.* Dover Publications, Inc., 1936.

[55] J. S. Rowlinson and B. Widom. *Molecular Theory of Capillarity.* Clarendon Press, 1982.

[56] V. P. Carey. *Liquid-Vapor Phase-Change Phenomena.* Hemisphere Publishing Corporation, 1992.

[57] C. Teixeira and K. Molvig, 1996 (private communication).

[58] M. Ishii. *Thermo-Fluid Dynamic Theory of Two-Phase Flow.* Eyrolles (Paris), 1975.

[59] J. Hoch and K. Molvig, 1997 (private communication).

[60] R. Clift, J. R. Grace, and M. E. Weber. *Bubbles, Drops, and Particles.* Academic Press, 1978.

[61] G. B. Wallis. The terminal speed of single drops or bubbles in an infinite medium. *Int. J. Multiphase Flow*, 1:491, 1974.

[62] J. R. Grace. Shapes and velocities of bubbles rising in infinite liquids. *Trans. Instn Chem. Engrs*, 51:116, 1973.

[63] D. Bhaga and M. E. Weber. Bubbles in viscous liquids: Shapes, wakes, and velocities. *J. Fluid Mech.*, 105:61, 1981.

[64] W. L. Haberman and R. K. Morton. An experimental study of bubbles moving in liquids. *Trans. Amer. Soc. Civil Eng.*, 121:227, 1956.

[65] H. D. Mendelson. The prediction of bubble terminal velocities from wave theory. *AIChE J.*, 13(2):250, 1967.

[66] M. Jamialahmadi, C. Branch, and H. Müller-Steinhagen. Terminal bubble rise velocities in liquids. *Trans. IChemE*, 72:119, 1994.

[67] G. G. Stokes. On the effect of the internal friction of fluids on the motion of pendulums. *Trans. Cambridge Phi. Soc.*, 9:8, 1851.

[68] J. Hadamard. *Compt. Rend. Acad. Sci. Paris*, 152:1735, 1911.

[69] R. M. Davies and G. Taylor. The mechanics of large bubbles rising through extended liquids and through liquids in tubes. *Proc. Royal Soc. (London)*, 200A:375, 1950.

[70] I. Zun. The transverse migration of bubbles influenced by walls in vertical bubbly flow. *Int. J. Multiphase Flow*, 6:583, 1980.

[71] H. Chen, C. Teixeira, and K. Molvig, 1996 (private communication).

[72] H. Chen, C. Teixeira, F. Gang, and K. Molvig, 1996 (private communication).

[73] H. Lamb. *Hydrodynamics.* Cambridge University Press, 6th edition, 1932.

[74] D. H. Sharp. An overview of Rayleigh-Taylor instability. *Physica D*, 12:3, 1984.

[75] G. K. Batchelor. *An Introduction to Fluid Dynamics.* Cambridge University Press, 1967.

[76] C. C. Maneri. New look at wave analogy for prediction of bubble terminal velocities. *AIChE J.*, 41(3):481, 1995.